UNIVERSITÀ DEGLI STUDI DELL'INSUBRIA

Facoltà di Scienze Matematiche, Fisiche e Naturali

Anno Accademico 2010-2011

Dottorato in Fisica XXIII ciclo

EXPERIMENTAL TECHNIQUES FOR DEFLECTION AND RADIATION STUDIES WITH BENT CRYSTALS

Author: Said Hasan

Tutor: Dr. Michela Prest
Università degli Studi dell'Insubria
Cotutor: Dr. Erik Vallazza
INFN sezione di Trieste

Contents

Introduction **5**

1 Overview on channeling and related effects **7**
1.1 Bent crystals in a nutshell . . . 7
1.2 Applications . . . 12
1.2.1 Crystal collimation . . . 12
1.2.1.1 Crystal assisted beam extraction . . . 18
1.2.2 Beam splitting . . . 21
1.2.2.1 Beam attenuator . . . 22
1.2.2.2 Microbeam . . . 24
1.2.3 Radiation emission related applications . . . 28
1.3 The theory behind bent crystals . . . 32
1.3.1 The continuum approximation . . . 33
1.3.2 Channeling . . . 37
1.3.2.1 Dechanneling . . . 40
1.3.3 Bent crystals . . . 42
1.3.4 Volume effects . . . 46
1.3.4.1 Volume capture . . . 47
1.3.4.2 Volume reflection . . . 49

2 Bent crystal measurements **55**
2.1 Experimental setup . . . 55
2.1.1 Basic concepts . . . 56
2.1.2 The goniometer . . . 57
2.1.3 The full tracking system . . . 58
2.1.4 The DAQ . . . 62
2.1.5 The bent crystals . . . 64
2.1.5.1 Strip crystals . . . 64
2.1.5.2 Quasimosaic crystals . . . 65
2.1.6 The beam . . . 65
2.1.7 The experimental procedure . . . 67

2.2 Single crystal characterization 69
2.2.1 The crystal torsion 71
2.2.2 Channeling 76
2.2.3 Volume reflection 83
2.2.4 Negative particles 86
2.2.5 Going to lower energy 90
2.2.6 Summarizing 98

3 Radiation emission in channeling and VR 101
3.1 A physical model 102
3.1.1 Channeling 102
3.1.2 Volume reflection 109
3.2 The experimental test 113
3.2.1 A setup add-on for the radiation tests 113
3.2.1.1 Spectrometer 114
3.2.1.2 Primary beam calorimeter 120
3.2.1.3 The γ-calorimeters 121
3.2.1.4 The Rino calorimeter 123
3.2.1.5 The Willie calorimeter 125
3.2.1.6 The 2010 beam test (the Jack calorimeter) . . . 128
3.2.2 Analysis and results 133
3.2.3 Crystals and background 133
3.2.4 Channeling 135
3.2.5 Volume Reflection 138
3.2.6 Conclusion 141

4 Advanced bent crystals 145
4.1 Multi VR in a sequence of crystals 145
4.1.1 The measurements 147
4.2 Axis related effects 153
4.2.1 Skew planes 153
4.2.2 Axial channeling 156
4.2.2.1 Results with positive and negative particles . . . 159
4.2.3 Multi VR in One Crystal (MVROC) 164
4.2.3.1 Experimental meausurements on MVROC . . . 166
4.2.4 Summarizing 171

Conclusion and outlooks 178

List of figures 184

List of tables **185**

List of acronyms **185**

The bibliography **195**

Introduction

What happens when a high energy charged particle crosses an amorphous material? It loses energy by ionization and its trajectory is affected by the multiple Coulomb scattering, being these phenomena originated by uncorrelated collisions with the atoms. If the atoms of the target were distributed according to an ordered scheme, the uncorrelated collisions would turn into a coherent interaction with the whole atomic structure. This is the case of an aligned crystal that, depending on the orientation, is seen as a set of atomic planes or strings by the impinging particles. Planes and strings produce potential wells able to confine the charged particles in a transversal region of the crystal, in the so called channeling condition, so that, bending the crystal, particles are forced to follow the curvature, being deflected.
This simple and powerful idea, dating 1979, is at the basis of many theoretical and experimental studies that have proven its effectiveness, described the possible applications and optimized the deflection performances.
The contribution of this thesis locates itself in this field as an attempt to provide a picture of the experimental techniques and the analysis procedures developed to investigate bent crystals in the last years.

In this period, bent crystal physics has witnessed a tremendous progress characterized by the increase of performances and the discovery of new phenomena. The driving forces of this process have been essentially three: bent crystals have been identified as a possible solution of the LHC collimation problem, bringing considerable resources to their research field; new bending techniques exploiting secondary deformations have been implemented and, finally, the single particle track reconstruction has become the core of the crystal testing procedures, making the measurements faster and more precise.

This thesis is a bridge across two complementary fields, that is the experimental techniques applied in the crystal study and the description of the observed phenomena from the phenomenological point of view as well as from the microscopic theoretical one, resulting in a complete overview on the bent crystal physics.

The bent crystals features are presented in the very beginning of the thesis, with the key elements of the research field described in the first chapter before go-

ing to an overview on the most important applications to show how bent crystals can be exploited in accelerator physics. The last section of the chapter focuses on the microscopic bent crystal behaviour to describe the physics behind the effects induced by the crystal on the charged particles crossing it. The second chapter describes the state of the art of the bent crystals characterization and test. The first section presents the experimental setup, from the inspiring concepts to the description of the single components and procedures. The setup basic idea is that the combination of a silicon microstrip tracking system with a multi-stage goniometer allows to measure the relative alignment between the beam and the crystal as well as the crystal deflection angle.
The second section is dedicated to the analysis methods used to characterize the single crystal behaviour in terms of the channeling and the volume reflection phenomena. The described procedures are applied in a wide range of beam conditions from 13 GeV to 400 GeV of energy with positive and negative particles; all the data have been acquired at CERN on different beamlines during the past three years.

The third chapter explores a different bent crystal aspect, that is the radiation emission. Coherent interaction with atoms, in fact, does not only mean deflection capabilities but also quasi-periodic trajectories that, in turn, produce an enhancement of the emitted electromagnetic radiation.
The description of the theoretical bases of this phenomenon both in channeling and volume reflection is presented in the first section of the chapter, while the second one is dedicated to the setup and the results obtained with a 120 GeV/c positron beam.

The last chapter goes back to the bent crystals deflection issue; going beyond channeling and volume reflection, it shows innovative bent crystals deflection schemes, developed in the last years in order to enhance the efficiency and the angular acceptance provided by channeling. This result can be achieved creating a sequence of aligned crystals to increase the deflection angle induced by volume reflection as shown in the first section or exploiting the interaction with a crystalline axis that, as described in the second section, originates new phenomena such as the multi volume reflection in one crystal (MVROC) and the axial channeling able to deflect both positive and negative particles with high efficiency.

Chapter 1

Overview on channeling and related effects

This chapter presents an introduction to bent crystals, providing an overview on this research field that goes from the theoretical bases of the coherent interaction between charged particles and crystals to the possible applications in high energy physics.

Sec. 1.1 tries to present bent crystals, skipping the details of their microscopic properties and jumping directly to the phenomenological aspects. In this way some of the key concepts of the thesis will be introduced from the beginning.
While this prologue intends to arise the curiosity of the reader on these peculiar devices, sec. 1.2 will present a number of applications in which bent crystals can play an innovative role: from the hadron collimation to the production of high energy photons and positrons.

Finally sec. 1.3 will enter inside the bent crystal, providing a detailed description of the theoretical laws behind the macroscopic phenomena they induce.

1.1 Bent crystals in a nutshell

The comparison in fig. 1.1 summarizes the charm of the bent crystal research field: bent crystals are devices developed to deflect relativistic charged particles, producing the same effect of a huge magnetic field, thanks to the coherent interaction of particles with the ordered crystalline structure.

The comparison between a standard bending magnet and a bent crystal is somewhat provocative, since there is a fundamental difference: while in a bending magnet particles can travel in vacuum (inside a beam pipe), in a crystal the presence of nuclei and electrons cannot be avoided resulting in a certain amount of scattering, which, in turn, perturbs the particle trajectory and produces a de-

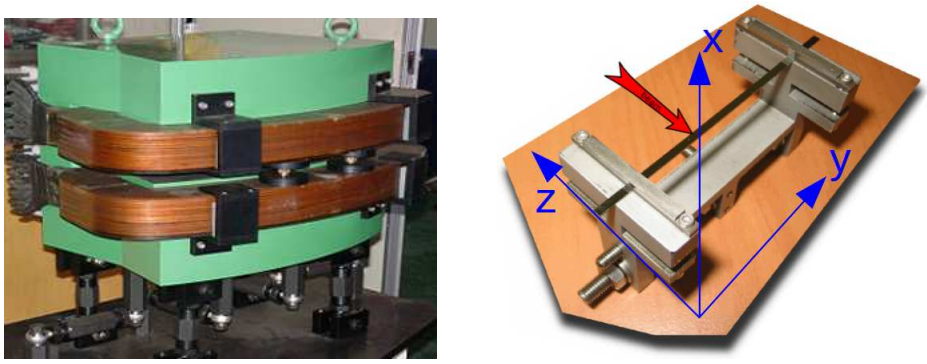

(a) (b)

Figure 1.1: (a) A bending magnet: it is a bulky device commonly used to deflect charged particle beams thanks to the magnetic field induced by the current injected in its coils; the most advanced bending magnets (superconducting devices) can generate magnetic fields up to 8 Tesla [1]. (b) A bent silicon crystal (strip type, sec. 2.1.5): it is mounted on an aluminium holder that provides the curvature; its dimensions are 0.5 mm (x) $\times$ 7 cm (y) $\times$ 2 mm (z, beam direction). The particles are deflected exploiting the electric field generated at the atomic scale by the crystalline planes; in this way an equivalent magnetic field of hundreds of Tesla can be produced [2].

flection efficiency smaller that 100%. This is the reason why, at the moment, it is impossible to imagine a replacement of bending magnets with bent crystals. Despite this consideration, bent crystals have a great potentiality for many applications, such as beam collimation, beam steering, photon production and many more; the studies performed in the last years have shown a considerable improvement in the deflection efficiency and have revealed many deflection effects that, with their pros and cons, can be exploited in the different situations [3].

The physical principle at the basis of bent crystals is the following: when a charged particle travels almost aligned with respect to an atomic plane, the plane behaves as a continuous charge distribution able to reflect the charged particle. In this way, two neighboring planes can confine the particle trajectory between themselves, in the so called *channeling* condition. In 1976 E. Tsyganov proposed to bend a crystal and to use the confinement due to channeling to deflect particles [4, 5] as it is schematically shown in fig. 1.2; his pioneering idea was experimentally confirmed in 1979 [6] at the JINR [7].

The physical observables that have to be measured to study a bent crystal are the alignment of the crystal planes with respect to the particle direction and the deflection angle produced by the crystal on the particle trajectory. In sec. 2.1 the experimental setup developed to perform this measurement is described in detail; in short, it is formed by a tracking system which reconstructs the trajectory before

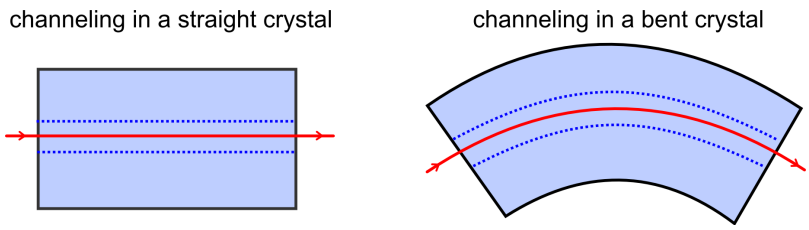

Figure 1.2: The basic principle of channeling in bent crystals: on the left side, a particle in channeling in a straight crystal; on the right side, the crystal is bent (together with its atomic planes) so that the channeled particle is forced to follow the curvature, being deflected.

and after the crystal and by a high precision goniometer that rotates the crystal. Fig. 1.3 shows the result of the measurement[1]: a plot where on the horizontal axis there is the crystal misalignment with respect to the beam direction (α), and on the vertical one the deflection angle produced by the crystal itself (ϕ). In this coordinate system, $\alpha = 0$ indicates the perfect alignment between the crystal planes and the beam, while $\phi = 0$ means that there is no deflection. In the external regions of the plot ($\alpha < -250$ μrad, $\alpha > 50$ μrad) the distribution of the particles is centered around $\phi = 0$ because the crystal is misaligned and thus behaves like an amorphous material.

When the crystal is rotated so that its planes are aligned with the beam ($\alpha = 0$), a part of the beam is captured in channeling being deflected, as schematically shown in the first sketch of fig. 1.4. Fig. 1.5a shows the deflection angle distribution corresponding to this alignment ($\alpha = 0$, yellow histogram), compared with the amorphous one (gray histogram). The mean angular position of the channeled particles is $\phi_{ch} \simeq$182 μrad. This angle allows to compute the curvature radius (R) of the crystal; being its curvature circular, the following holds: $\phi_{ch} = l/R$, where $l = 2$ mm is the crystal length along the beam. In this case R=11.0 m.

Considering the spot formed by the channeled particles in the scatter plot (fig. 1.3), the limited channeling angular acceptance can be noted; if the alignment interval for channeling is $-\alpha_c < \alpha < \alpha_c$, in this case $\alpha_c \simeq 20$ μrad. The theoretical formula which determines this value is computed in sec. 1.3.2 where the dependence of the angular acceptance on the crystal material and on the particle energy will be pointed out.

Fig. 1.5a shows that not all the particles are channeled even for $\alpha = 0$: some remain in the "amorphous" angular region while some others are located between the channeling peak and the amorphous one. The particles that are still in the amorphous region constitute the channeling inefficiency caused by the fact that

[1] More details on the same data will be given in chap. 2.

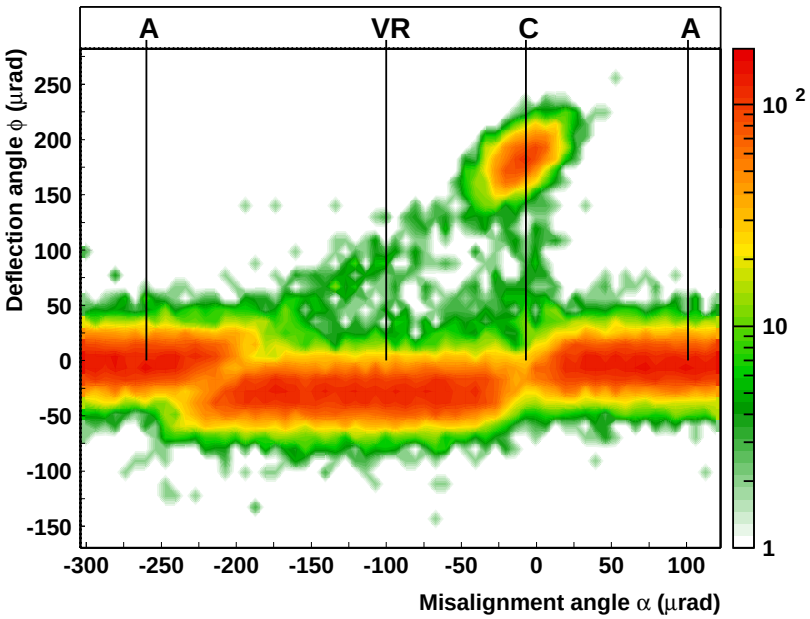

Figure 1.3: Scatter plot of the deflection angle produced by the crystal as a function of its alignment with respect to the particles; it is obtained rotating the crystal with a goniometer. The letters indicate the different regions: *A*-amorphous, *VR*-volume reflection, *C*-channeling.

not all the space in the crystal is available for channeling: the nuclear layers, which confine the particles motion, in fact, have a finite thickness so that, if a particle enters the crystal approaching the edge of a channel, it cannot be channeled. For what concerns the particles between the amorphous peak and the channeling one, they are *dechanneled*, which means that, although initially channeled, due to scattering with the crystalline medium (nuclei and electrons), they are expelled from the channel. Therefore, as schematically shown in the second sketch of fig. 1.4, their deflection angle is smaller than the channeling one (the dechanneling effect is treated in sec. 1.3.2.1).

Fig. 1.3 shows that, in a bent crystal, channeling is not the only phenomenon able to deflect charged particles. In the range -182 μrad$< \alpha < 0$ μrad in fact, an angular shift of almost the whole beam on the opposite direction with respect to the channeling side can be noted: this effect is called *volume reflection*. Considering that ϕ_{ch} =182 μrad corresponds to the crystal bending angle, this angular region covers the range in which the particle trajectories become parallel with the channel inside the crystal "volume", being reflected by the crystal plane, as it is

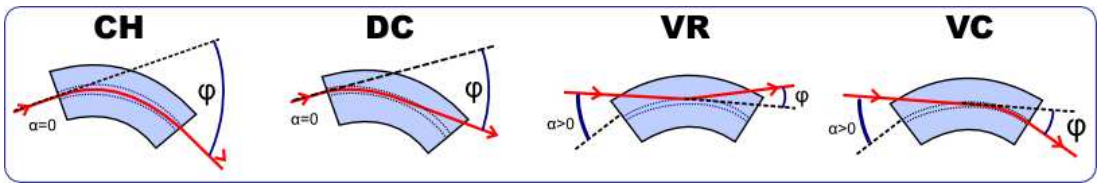

Figure 1.4: Schematic description of the different deflection effects in a bent crystal: **CH**-channeling, **DC**-dechanneling, **VR**-volume reflection, **VC**-volume capture.

shown in the third sketch of fig. 1.4.
Fig. 1.5b presents the deflection angle distribution in the "volume" region; the reflected beam (yellow histogram) is compared with the "amorphous" one (gray histogram). The deflection angle is $\phi_{VR} = 29.7\ \mu$rad that is in agreement with the expected value $\phi_{VR} = 1.5\ \alpha_c$. The theoretical reason at the basis of this value is given in sec. 1.3.4.2 but, from an intuitive point of view, the relation between the channeling angular acceptance and the volume reflection angle can be figured out thinking that both of them are linked to the strength of the interaction between the crystalline planes and the charged particle: in the channeling case, this strength keeps the particle confined; in the volume reflection one, it changes its direction.
Fig. 1.5b points out that there is a small percentage of particles deflected towards

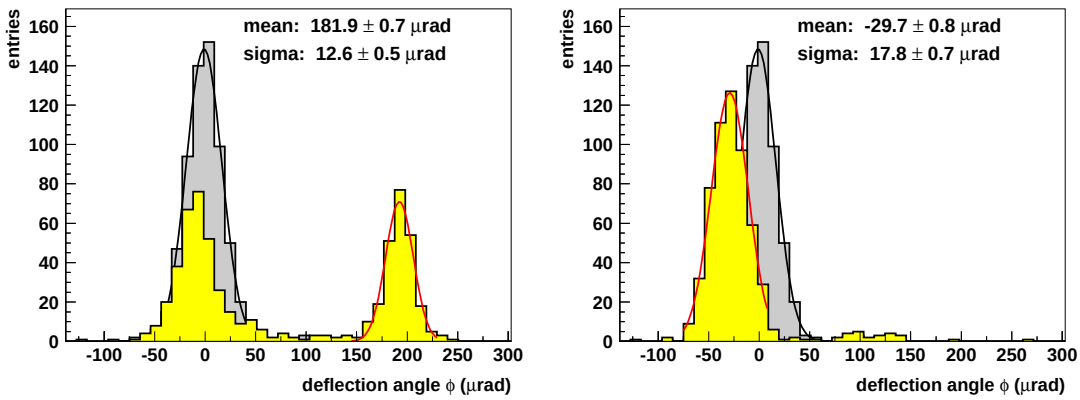

(a) (b)

Figure 1.5: Deflection angle profiles of the particles that cross the crystal in the amorphous condition (gray histograms) compared to the channeling one (yellow histogram (a)) and the volume reflection one (yellow histogram (b)). The fits performed with gaussian functions allow to estimate the channeling angle ϕ_{ch} and volume reflection one ϕ_{vr} (indicated with "mean" in the plots).

the "channeling side" around $\phi = 90\ \mu$rad; they are the so called *volume captured* particles which in fig. 1.3 fill the diagonal region of the plot connecting the channeling peak with the end of the reflected region.
The volume capture effect takes place when a particle reaches the tangency point with the channel inside the crystal, just as in the reflection case, but in this position it is captured in the channel instead of being reflected. As it happens for the dechanneling effect, volume capture takes place because the crystal is not an empty region: fluctuations in the particle trajectory, due to scattering, are present and they can take the particle out (dechanneling) or bring it into (volume capture) the channeling condition. Dechanneling and volume capture are in fact strictly related as it is explained in sec. 1.3.4.1.

1.2 Applications

The brief phenomenological description of bent crystals given in the previous section has probably impressed the reader who has never heard about them before. Bent crystals, in fact, open the way to the possibility of using totally new beam steering techniques increasing the achievable deflection angles, reducing the steering device dimensions and power consumption.
Although, at the current state of knowledge, these progresses still represent a far goal, there are several fields in which bent crystals can be applied, improving the present performance and allowing new possibilities.
This section will present an overview on the most studied bent crystal applications providing a selection of the interesting experimental results obtained in the last years.
Among the different applications, a special role has to be assigned to beam collimation (sec. 1.2.1) and beam extraction (sec. 1.2.1.1): the collimation represents the current hot topic, that, due to the relevance of the LHC collimation issue, leads and inspires most of the present bent crystals research (including this thesis work); on the other side, beam extraction is historically the most studied application and thus the most exploited at the moment.

1.2.1 Crystal collimation

The collimation system is an essential apparatus in a particle accelerator. Its role is to reduce the beam halo, that is the external beam region, populated by particles which are leaving the nominal accelerator orbit because of phenomena connected with the beam dynamics, such as: the scattering on the residual gas; the beam-beam interaction which takes place in colliders; the non linearity field errors of the superconducting magnets.

The beam halo represents an increasing concern for modern accelerators since it causes: equipment damages, residual radiation and large experimental backgrounds [8].
To keep these effects under control, complex multi-stage collimation systems have been developed in order to absorb the high energy halo particles: a first stage intercepts the primary halo and generates a secondary halo composed of particles with a larger misalignment with respect to the nominal beam trajectory; most of this secondary halo is then stopped by secondary collimators, that are bulk absorbers (fig. 1.6a).

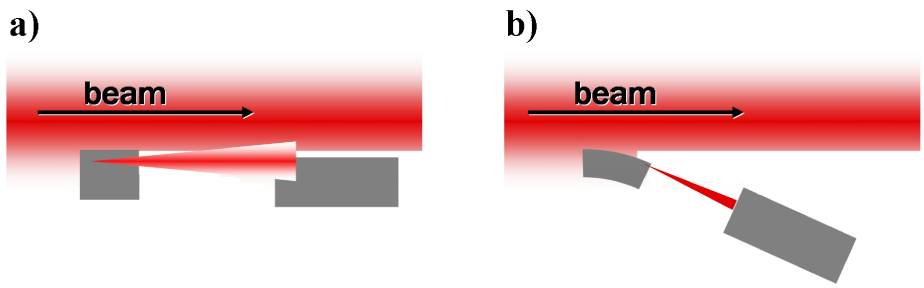

Figure 1.6: a) Traditional multi-stage collimation system: an amorphous target spreads the primary halo (creating the secondary halo) so that most of it can be intercepted by a more distant, with respect to the beam, secondary collimator; note that a real collimation system can present further collimation stages as well as shields to protect the equipment from the escaping particles. b) Crystal based collimation: a bent crystal acts as a smart primary collimator deviating (through channeling) the beam halo into the absorber.

In 1991 it was proposed, for the first time, to use bent crystals for halo collimation in SSC (Superconducting Super Collider) [9]. The basic idea was that a bent crystal used as a primary collimator should extract the incident halo particles directing them onto a secondary collimator (fig. 1.6b). In this way the collimation efficiency increases, because the channeled particles are deflected towards the center of the absorber rather than to its edge, thus avoiding particles backscattering in the beam. Moreover the wide angular shift provided by the bent crystal allows to keep the secondary collimator farther from the beam reducing its beam coupling impedance.
Although the SSC accelerator has never been built, the need of an efficient and robust collimation system in hadron colliders has kept the interest in crystal collimation alive. Experiments have been performed at the RHIC [10] (BNL) and at the U70 (IHEP) [3] accelerators during the past few years, while at the moment there are studies addressed to develop a collimation system for the Tevatron [11] (FNAL) and the LHC (CERN) accelerators.

Among the studies on crystal collimation, the one addressed to LHC certainly has had a leading role given the complexity and importance of the whole LHC project. The LHC collimation represents, in fact, a very difficult task, because of the huge stored beam energy, with an unprecedented transverse energy density (fig. 1.7a) and the use of superconducting magnets which can undergo quenching. As shown in fig. 1.7b, the proton loss rate for a realistic beam lifetime is from 10^3 to 10^4 times larger than the magnet quench limit, meaning that out of 10^4 lost protons no more than a few are allowed to escape from the collimators [12].

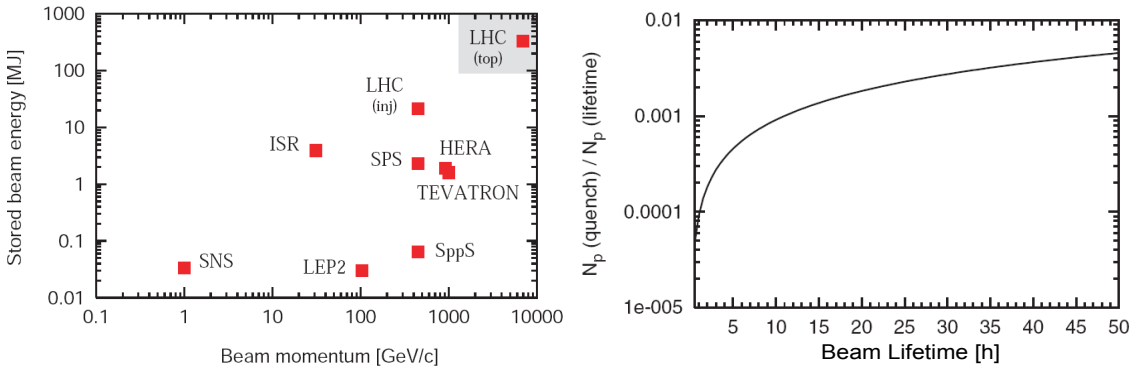

(a) (b)

Figure 1.7: a) Stored beam energy versus beam momentum for various past, present and future high power accelerators. b) Quench limit over the number of lost particles as a function of the beam lifetime [13].

The study performed on the LHC collimation did not produce a single solution that fulfills all the machine design goals. The collimation system will be implemented in different phases so that the difficulties and the performance goals will be distributed in time, following the natural evolution of the LHC performance. The first phase [13] (which is operating at the moment) is designed to be fail proof requiring a minimum number of interventions in the high LHC radiation environment. This collimation system limits the LHC luminosity to 40% of the nominal one thus it should be modified to reach the nominal machine performance, with the help of a new generation of collimators which is not decided yet [14].
In this framework, crystal collimation represents an appealing solution [15], so that an intense research program has started in 2006 with the goal of: improving the knowledge on bent crystals, increasing their performance and proving their effectiveness as collimators with dedicated tests on a circular accelerator.
The first point of this program has led to the development of a refined experimental technique that in turn has allowed to understand many of the scientific and technological aspects related to bent crystals going far beyond the LHC collima-

tion issue. The description of the developments obtained in this context represents the core of this thesis work and will be presented in the next chapters.
In parallel to this research activity on the extracted beamlines, a crystal collimation test on a circular accelerator has started at CERN under the name UA9 [16].
The UA9 experiment is performed at the CERN SPS accelerator (that is the LHC injector) at an energy of 120 GeV; fig. 1.8 presents the setup layout, whose main elements are: the C1-C2 bent crystals[2] assembled on two goniometers, inside a vacuum tank (fig. 1.9a) and the TAL secondary collimator, a 60 cm long tungsten absorber (fig. 1.9b).

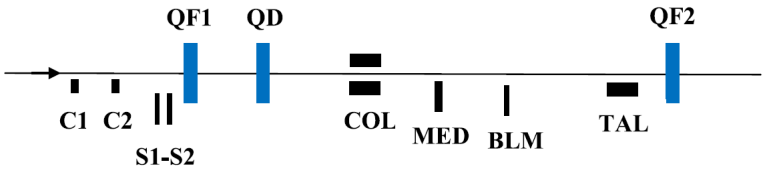

Figure 1.8: The layout of the UA9 experiment: the bent crystals **C1-C2**; the scintillator detectors **S1-S2**; the quadrupole magnets **QF1, QF2, QD**; **COL** is a LHC collimator prototype with two 1 m long graphite jaws that can be moved to intercept the deflected beam; **BLM** is a beam loss monitor that measures the radiation level outside the beam pipe and **TAL** is the tungsten absorber.

Fig. 1.10 describes the alignment technique used during the UA9 experiment, a method already exploited during the Tevatron [11] and RHIC [10] collimation tests both to find the correct crystal orientation and to measure its performances.
A radiation sensitive detector (in UA9 a couple of scintillators) measures the rate of particles scattered at large angles by the crystal. The rate of these events, that are produced by close inelastic interactions with the crystal nuclei, strongly decreases when the crystal is in the channeling orientation for two reasons: the channeled particles trajectories are far from the nuclear planes (sec. 1.3.2) and the effective number of collisions with the crystal decreases given the channeled particles are immediately expelled from the beam thus not impinging on the crystal in the following turns.
This second effect is partially present also in volume reflection: the VR deflection angle, in fact, is larger than the one given by multiple scattering (in the amorphous orientation), so that a volume reflected particle performs less turns than an amorphous interacting one.
Therefore the dip (marked with **CH**) in fig. 1.10b is a hint of the channeling ori-

[2]They are respectively a strip crystal and a quasimosaic one (sec. 2.1.5), 2 mm long, with a bending angle of about 145 μrad.

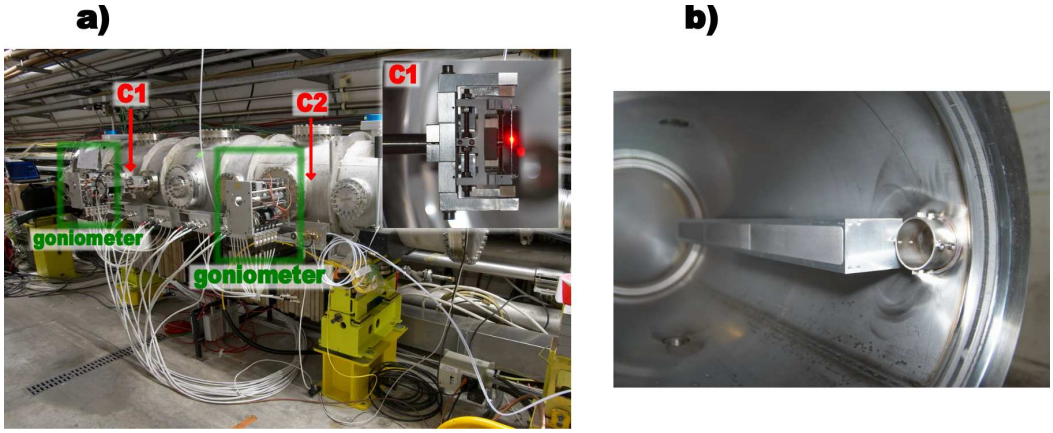

Figure 1.9: a) The so called “first station” consisting of a vacuum tank in which (box at the top right) the bent crystals are mounted; the external part of the goniometers (green box) is visible. b) The “second station” consisting of a smaller vacuum tank containing the tungsten absorber.

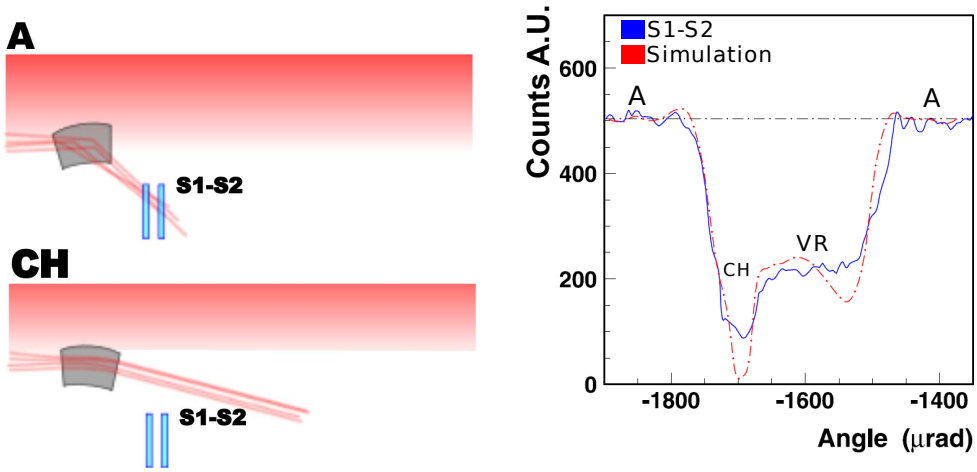

(a) (b)

Figure 1.10: a) Schematic description of the UA9 crystal alignment technique: in the top plot, the crystal is misaligned (**A** stands for amorphous) and scatters some particles at large angles towards the scintillator detectors; in the bottom plot, the crystal is in channeling and the particles are directed towards the **TAL** absorber. b) The **S1-S2** scintillator counts as a function of the crystal misalignment angle: the amorphous, channeling and volume reflection orientations are respectively marked with **A**, **CH** and **VR** [16].

entation and the shoulder at its right can be interpreted as the **VR** region. The

agreement between data and simulation is rather good and the discrepancy in the minimum value of the nuclear interaction in channeling is probably due to a torsion of the crystal (sec. 2.2.1) resulting in a different orientation as a function of the vertical impact position on the crystal surface.

Once the channeling orientation was found, the LHC COL and the following BLM (Beam Loss Monitor) were used to measure the deflection efficiency of the crystal. As shown in fig. 1.11a, the collimator is progressively moved towards the beam so that, at a certain point, it intercepts the channeled particles. The BLM, detecting some of the particles scattered by the collimator, provides a signal proportional to the number of particles impinging on the collimator, so that moving the collimator, the integral shape of the deflected beam is given by the BLM signal.
Fig. 1.11b shows the result of a collimator scan. The increase in the BLM signal ($\sigma_{coll} = -7.5$ mm) corresponds to the "integration" of the channeling peak and the fit performed with an error function (the gaussian integral) provides information on the channeling peak; for instance, the plateau level is proportional to the channeling peak intensity. Once the channeling peak is crossed by the collimator (that is the plateau level is reached), the BLM signal slightly increases because of the dechanneled particles integration (sec. 1.3.2.1), till the sharp rise detected at $a_{coll} \simeq -3$ mm, that indicates the collimator has touched the secondary halo created by non-channeled particles undergoing multiple scattering in the crystal. Beyond this position, the collimator passes the crystal touching the beam so that the BLM signal becomes proportional to the number of particles impinging on the crystal itself. The crystal deflection efficiency can be estimated as the ratio of the error function plateau value to the maximum value at the scan edge (as indicated by the right vertical scale in fig. 1.11b) obtaining $P_{ch} = 75 \pm 4\%$.

New UA9 runs have been planned for 2011, with the goal to improve some key features of the setup:

- the goniometric system has to be improved: the recorded channeling efficiency in fact does not correspond to the perfect crystal alignment that, according to simulation, would produce an efficiency $P_{ch} \sim 95\%$.

- the collimation efficiency, intended as the ratio between the particles impinging on the TAL absorber to the ones lost along the accelerator should be measured.

- from the bent crystals point of view, the efforts will be directed firstly to the correction of the torsion (sec. 2.2.1), whose presence could limit the channeling efficiency and thus the collimation one, and secondly to the test of new collimation schemes such as the use of volume reflection or of the multi volume reflection (sec. 4.1) in place of channeling as shown in fig. 1.12.

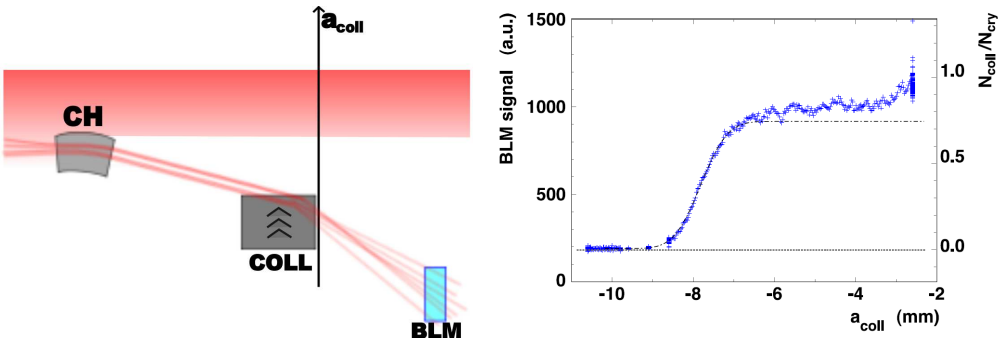

(a) (b)

Figure 1.11: a) The procedure used to measure the channeling efficiency in the UA9 experiment: the LHC COL is progressively moved towards the beam, intercepting the deflected particles so that the signal of the following BLM is proportional to the number of particles impinging on the collimator. b) The BLM signal as a function of the horizontal collimator position, during the scan towards the beam with the crystal in channeling ($a_{coll} = 0$ represents the center of the orbit). The dashed blue line indicates the error function fit [16].

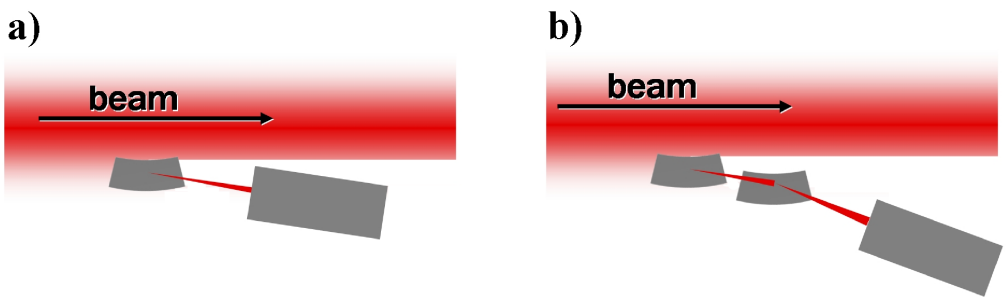

Figure 1.12: a) Crystal collimation using the VR effect with a single crystal and b) with a series of crystals to increase the final deflection angle (sec. 4.1 will present an experimental study on the multi-crystal systems).

1.2.1.1 Crystal assisted beam extraction

Particle extraction from circular accelerators allows to produce high energy beams that can be used either in fixed target experiments, including the production of secondary particle beams such as the gamma and neutrino ones, or to test instrumentation.
The classic slow extraction method consists of a system of electrostatic and magnetic septa: usually the electrostatic septum (a long array of thin wires) deviates the particles from the nominal orbit towards the field region of a magnetic sep-

tum [17] that, producing a further deflection, steers the particles towards the external beamline.

A bent crystal can be used in particle extraction as a compact and passive septum characterized by a strong electric field (of the order of $10^9 - 10^{11}$ Vm) with a very small entrance wall that, ideally, can be just a single atomic layer.
The scheme of the crystal assisted extraction is similar to the crystal collimation one: a crystal intercepts the beam halo deviating it from the circular trajectory but, differently from collimation, the extracted beam is not lost in an absorber but sent to bending magnets that bring it to the experimental areas.
Depending on the required extracted beam intensity, crystal extraction can work in a "parasitic" mode, exploiting the "natural" beam halo, or in an "active" one, in which the beam halo is stimulated to increase its intensity.
Crystal extraction presents several benefits with respect to the classic extraction method [3]:

- working in parasitic mode, it allows at the same time the operation of a collider and the production of an extracted beam.
- the time structure of the extracted beam is almost flat, since the extraction mechanism does not use a resonant method.
- the extracted beam has a small size and a regular shape.
- the polarization of the main beam is preserved during the extraction.

Given these advantages, crystal extraction has been identified as one of the most promising applications of bent crystals since their first years of study. The first successful test was performed in 1985 at Fermilab increasing the maximum momentum of the delivered particles from the magnetic septum limit of 225 GeV/c to the primary beam momentum of 400 GeV/c [18].
In 1989 a wide crystal extraction test program started at the IHEP laboratory (Protvino, Moscow), exploiting the U70 accelerator that accelerates protons up to 70 GeV. Among the other results, this research program represents the first regular application of crystal extraction: the installed crystal has been delivering the extracted beam since 10 years, but with an efficiency smaller than 1% [19].
In the 1990s, CERN carried out a R&D program called RD22 to investigate the possible implementation of an extracted beamline from the LHC accelerator, using bent crystals [8]. This experiment tested bent crystals on the SPS circulating beam recording an extraction efficiency of $\sim 10 - 20\%$ (fig. 1.13a). In the late 1990s it was the turn of the FNAL laboratory succeeding in extracting 900 GeV protons from the Tevatron accelerator with an efficiency of 30% [20].
The SPS and Tevatron tests gave an important contribution demonstrating that the

extraction efficiency can increase a lot exploiting the so called multi-turn effect: being in a circular accelerator, a particle can impinge on the crystal more than once increasing the resulting channeling probability. The experimental proof of this phenomenon, already predicted in [21], led to the development of shorter crystals in order to enhance efficiency: the shorter the crystal, the lower the intensity of multiple scattering for the particles crossing it in the "amorphous" condition, so that these particles are not expelled from the nominal beam and have a second chance to be channeled.
Specific bending techniques have been developed to produce short bent crystals (the most important are described in sec. 2.1.5) and a new series of tests has been performed at the IHEP laboratory. Fig. 1.13b presents a summary of the results obtained over a decade of experiments: the extraction efficiency shows a large increase when reducing the crystal length and the percentage of extracted particles exceeds 80%.
The studies performed on crystal assisted extraction have turned the IHEP U70

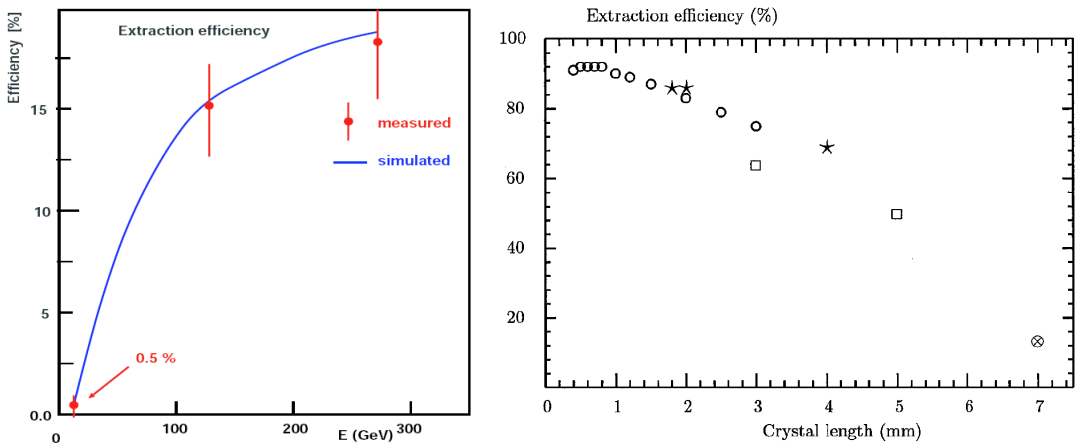

(a) (b)

Figure 1.13: a) Extraction efficiency measured at the SPS as a function of the beam energy [8]. b) The extraction efficiency measured for 70 GeV protons as a function of the crystal length at the U70 accelerator, with different kinds of bent crystals: the strip and quasimosaic ones are presented in sec. 2.1.5 while a description of the O-shaped bending technique can be found in [22].

accelerator in a largely "crystallized" [23] beam facility, where bent crystals are routinely used for beam extraction. Fig. 1.14a presents a schematic view of the U70 accelerator with its crystal stations: the Si_{106}, Si_{19}, Si_{22} crystals (the number refers to the position in the accelerator) extract the circulating beam towards the physics experiments; Si_{30} splits (sec. 1.2.2) the beam originally extracted for

beamline number 8 directing a fraction of it towards beamline 22. In addition, two more stations, Si_{84} and Si_{86}, are used to test the crystals before the installation and for channeling research, in particular for the beam collimation studies (sec. 1.2.1). Fig. 1.14b presents one of the extraction schemes used at IHEP: the circulating beam is brought to the crystal, acting on the field of the two bending magnets placed before it: the channeled particles (red curve) receive a deflection of 1.7 mrad, so that they enter in the aperture of the OM24 magnet avoiding its septum wall and after the following deviation in the OM26 magnet leave the accelerator vacuum chamber reaching the external beamline.

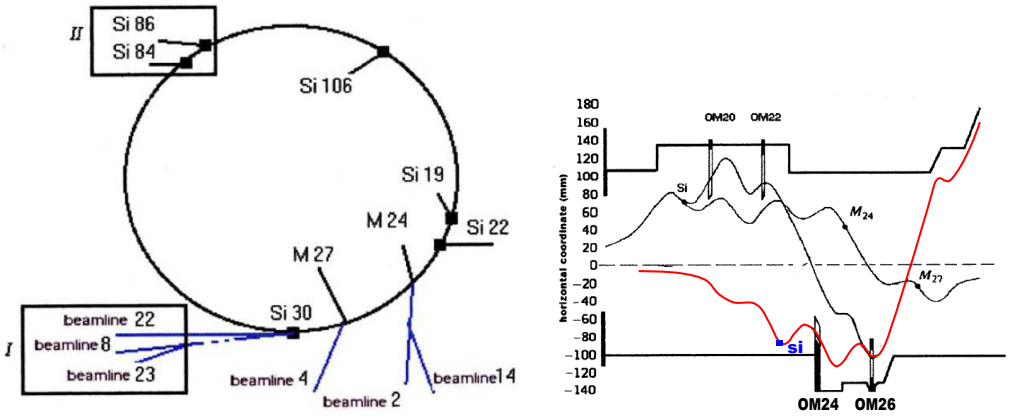

(a) (b)

Figure 1.14: a) Beam extraction schemes at the U70 accelerator: the *SiX* silicon crystal stations, two internal targets M_{24}, M_{27}, the experimental area (*I* box) and the crystal test one (*II* box) are indicated. b) An example of extraction scheme (red trajectory) that exploits the old magnetic septa (OM24 and OM26) to increase the crystal angular kick [23].

1.2.2 Beam splitting

The beam extracted from a circular or linear accelerator can be further divided in order to carry out several physics experiments simultaneously. Usually a beam is split by an electrostatic or a magnetic splitter [2]. This is a technically complex approach that requires a considerable space since the deflection angles provided by the conventional splitters are small. On the other hand a compact beam split method can be based on bent crystals that provide large deflection angles in a very small space.

The first crystal beam-splitting station [2] began to operate at the end of 1988 at the IHEP laboratory, when the installation of a new booster and the consequent increase of the beam intensity in the U70 accelerator allowed to share the beam

with a larger number of experiments. For this reason several magneto-optic beamlines were built in the limited space of the old experimental areas, so that the use of bent crystals to deliver the beam became very attractive.
The layout of the first crystal beam-splitting station is shown in fig. 1.15. The crystal splitter was placed inside a pre-existing bending magnet (M4) and it was aligned in channeling, so that a small part of the beam, directed to beamline 23 (for tagged neutrino beam study), was deflected of α =59 mrad towards beamline 21, designed for hadron studies. Placing the crystal in the halo of the primary beam that had an intensity of $I_{23} = 10^{13}$ protons per cycle, beamline 21 achieved an intensity of $I_{21} = 10^{7}$ protons, keeping the particle loss in the main line below the limit of $\sim 10^{10}$ protons per cycle, corresponding to 0.1%.

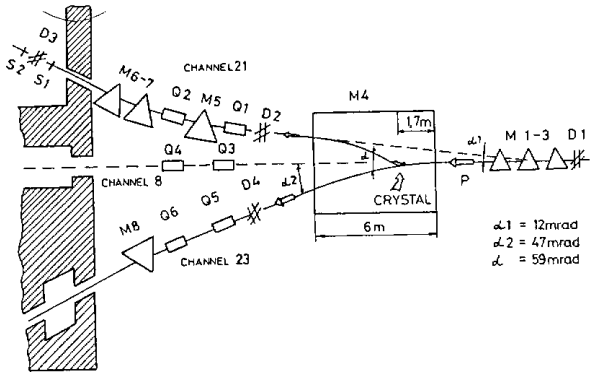

Figure 1.15: The scheme of the first crystal beam-split station installed at the IHEP laboratory. M1-9 are bending magnets; Q1-6 are quadrupole magnets; D1-4 are beam profilometers and S1-2 are scintillator counters.

The crystal features determine the characteristics of the secondary beam: for example decreasing the transversal dimension of the crystal it is possible to have a very small beam spot (<100 μm), useful to test position sensitive detectors. In the next sections three specific applications of a bent crystal splitter will be briefly described.

1.2.2.1 Beam attenuator

It happens that the nominal intensity of an extracted beam has to be reduced by orders of magnitude, usually because the instrumentation under test is not able to withstand a large particle intensity.
In these cases the standard approach consists in decreasing the aperture of the beamline collimators. But collimators are heavy objects and thus difficult to control; moreover they become the source of secondary particles and create a beam halo.
A bent crystal can be used to select a small portion of the beam, with a known divergence (of the order of the crystal critical angle, sec. 1.3.2) and with a size determined by the crystal width.

An example of this application is provided by the NA48 CERN experiment, in which simultaneous beams of K_L and K_S have to be produced to measure the CP violation parameter ε'/ε[3]. The two beams have to be simultaneous because the decays of the K_L and K_S are detected at the same time to minimize the systematic uncertainties.
Fig. 1.16 shows the layout of the NA48 kaon beams production setup. The primary beam ($1.5{\cdot}10^{12}$ protons per SPS pulse) impinges on a first target, producing K_Ls, that move towards the decay region while the charged particles created during the interaction with the target are deviated by a sweeping magnet. Among these particles there are $\sim 6 \cdot 10^{11}$ primary protons that impinge on a bent crystal that deflects just a small part of them ($\sim 5 \cdot 10^{-5}$% corresponding to $\sim 3 \cdot 10^{7}$ protons) deviating their trajectory of 9.6 mrad. The recovered proton beam is then transported (using a bending magnet) in parallel with the K_L one and driven towards a second target (120 m far from the first one) where the K_Ss are produced.

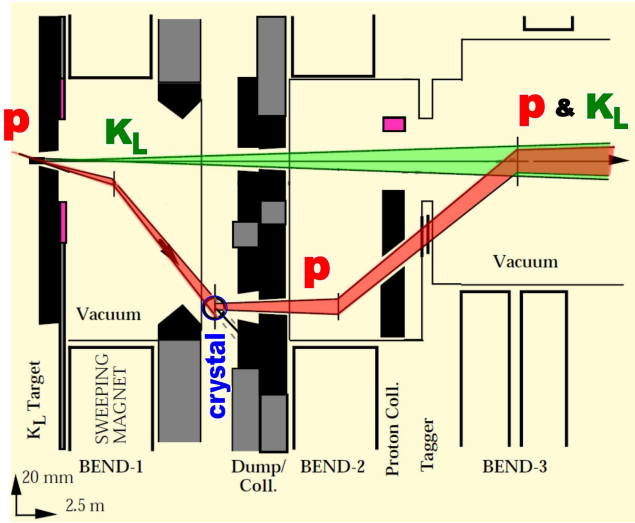

Figure 1.16: Layout of the NA48 kaon beams production setup.

The authors of [25] summarize the advantage of using a bent crystal in the NA48 experiment, with respect to a bending magnet, in three points:

- the flux of the transmitted beam is reduced by more than four orders of magnitude without deteriorating the beam quality.

[3]The parameter of interest is related to the measured double ratio of the $K^0 \to \pi\pi$ decay rates: $\varepsilon'/\varepsilon = \frac{1}{6}\left[1 - \frac{\Gamma(K_L^0 \to \pi^0\pi^0 \to \gamma\gamma)}{\Gamma(K_L^0 \to \pi^+\pi^-)} \cdot \frac{\Gamma(K_S^0 \to \pi^+\pi^-)}{\Gamma(K_S^0 \to \pi^0\pi^0 \to \gamma\gamma)}\right]$ [24] with high precision [24]

- the resulting beam has a small and well defined emittance[4] in both planes.
- the effect of the previous sweeping magnet is not reduced, while the simulation showed that a bending magnet with the same bending power of the crystal would lead to a tenfold increase in the flux of background muons through the NA48 detectors.

To conclude, it should be noted that the NA48 experiment provides the most complete information on the crystal lifetime in a radioactive environment as it has operated with the same crystal for years, achieving an irradiation of $5{\cdot}10^{20}$ protons/cm^2 that produced only a decrease of 30% in the deflection efficiency which means $\sim$100 years of lifetime in the intense beam of the NA48 experiment [26].

1.2.2.2 Microbeam

The term microbeam refers to a particle beam of small size, ranging from some mm^2 to the nanometer scale.
Microbeams are frequently used in medicine and biology research to study the effects of ionizing radiation on a single cell or on a small group of cells [27] both to improve the radiotherapy techniques (whose goal is the destruction of the cancerous cells) and to understand the effects of a low radiation dose on the human body [28].
Moreover, microbeams are applied in the so called PIXE (Particle Induced X-ray Emission) in which a low intensity and low energy (MeV range) proton beam is focused on targets, so that characteristic X-rays are generated and detected by a Si detector providing the element analysis of the sample. This technique has a wide range of applications from the environmental field (e.g. the storm water analysis [29]) to the artistic and historical ones (e.g. the element study of the ink of ancient manuscripts [30]).
Microbeams are usually formed by charged-particles, low energy X rays and low energy electrons; in particular, the majority of microbeams use light ions, such as protons or helium nuclei because of their large linear energy transfer (LET[5]) and large relative biological effectiveness (RBE[6]). A typical setup used to produce a ion microbeam is shown in fig. 1.17.

[4]The emittance is an important beam quality concept: it is defined as the area covered (at one σ) by the beam profile in the phase space of the angle as a function of the transversal position of the particles. It is measured in rad·mm.

[5]LET is the rate at which energy is transferred from ionizing radiation to matter; it is expressed in MeV/mm.

[6]RBE is a measurement of the capability of a specific ionizing radiation to produce a specific biological effect.

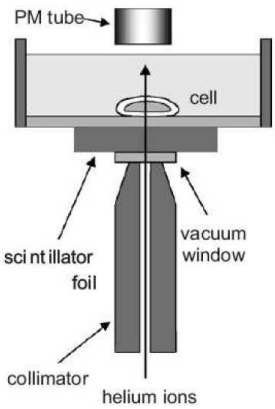

Figure 1.17: A standard method to produce a light ion microbeam: protons and light ions are accelerated with a 4 MV Van der Graaf accelerator and then steered vertically towards the cell irradiation apparatus. The microbeam is provided by a 1 μm diameter bore silica capillary collimator; the particles scattering inside cells are detected by a photomultiplier tube (PMT).

The channeling effect can be used to produce a microbeam [30] either exploiting a silicon crystal, bent to focus the incident beam in a small spot, or by means of nanotube structures as briefly described in the following.

Beam focusing

The idea of crystal focusing consists in bending a crystal in such a way that the directions of the crystalline planes converge towards a focal point. In this way, the deflection angle acquired by the crossing particles becomes a function of their horizontal coordinate, as shown in fig. 1.18a.
The first experimental proof of the crystal focusing capabilities dates back to 1985 [31] when a 1 GeV proton beam was focused by a crystal curved into a cylinder of 2 m radius. In this way a 15.4$\pm$0.05 mm FWHM beam was brought into a 0.65$\pm$0.05 mm FWHM distribution.

More recently [32] a series of bent crystals with a focal length F ranging from 0.5 m to 3.5 m has been tested with a 70 GeV proton beam at the IHEP laboratory. An interesting characteristic of this crystal is that the channeled and focused beam is deflected by the crystal and thus it separates from the unchanneled one reducing the background.
Fig. 1.18b shows the shape of the beam transmitted by the crystal: the spot on the left is the focused beam while the dashed rectangle on the right represents the crystal cross-section in the undeflected one.
The width of the focused beam is determined by the divergence of the channeled particle (that is given by the α_c Lindhard critical angle, eq. 1.12) multiplied by the focal length F. The crystal used in the example (fig. 1.18b), that has $F = 0.5$ m, should provide a beam spot of 12 μm RMS, while the measured value was slightly larger, 21 μm, due to aberration.

Nanotube channeling

The developments in the field of nanotechnology materials can open interest-

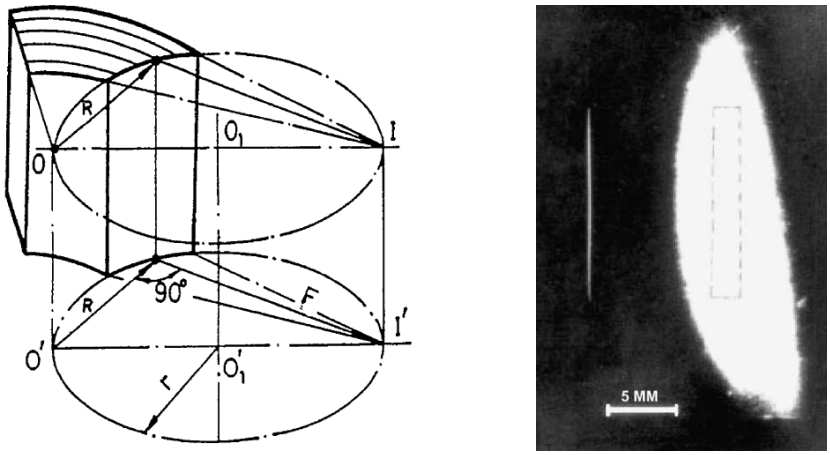

(a) (b)

Figure 1.18: a) The principle of beam focusing with a bent crystal. b) The profile of the deflected and focused beam is on the left, while the dashed rectangle on the right represents the crystal cross-section [32].

ing possibilities for channeling, especially if the microbeam application is concerned [33]. Carbon nanotubes could in fact satisfy the ideal channeling request to trap the particles in two directions inside large channels with the walls made of densely packed atoms. Carbon nanotubes are cylindrical molecules (fig. 1.19) with a typical diameter of the order of 1 nm (single-wall nanotube) or tens of nanometer (multi-wall nanotubes) and with a length of several microns.

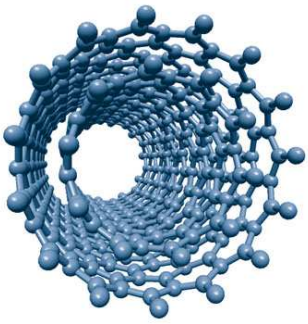

Figure 1.19: Schematic view of a multi-wall nanotube.

The channeling phenomena in nanotube structures occur with the particle confinement in a 2D potential which is located very close to the wall as shown in fig. 1.20a. In order to deflect these particles, a nanotube should be bent; the potential well is thus modified by the centrifugal force (sec. 1.3.3). Fig. 1.20b shows the potential well of a bent nanotube (with $pv/R = 1$ GeV/cm, corresponding to 300 Tesla, where R is the curvature, p the particle momentum and v its velocity).

It is clear that most of the nanotube cross section is still available for channeling.

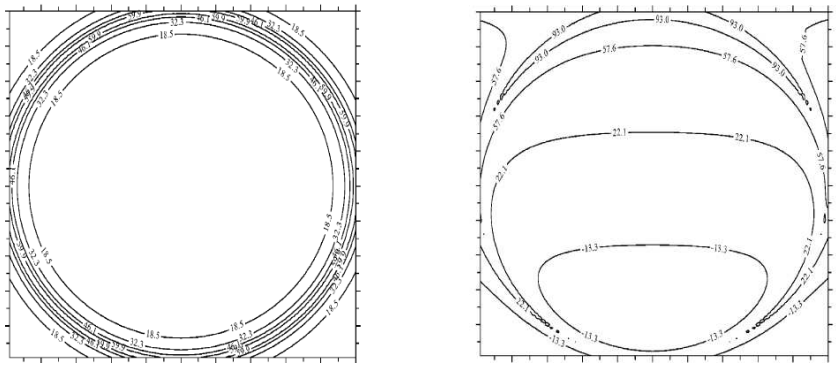

(a) (b)

Figure 1.20: a) The continuous potential within a carbon nanotube of 1.1 nm. b) The same nanotube bent with: pv/R = 1 GeV/cm [33].

To understand the bent nanotube efficiency, Montecarlo simulations of positive particle channeling have been performed: fig. 1.21 shows the number of channeled particles as a function of the nanotube curvature for different nanotube structures (single-wall and multi-wall) revealing values comparable to the Si (110) crystal ones.

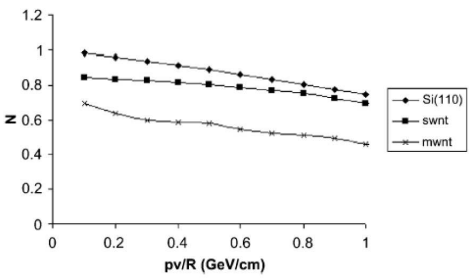

Figure 1.21: Simulation of the nanotube efficiency compared with the silicon crystal one: number of channeled particles as a function of the nanotube curvature for single-wall (SWNT) and multi-wall (MWNT) nanotubes and for a silicon crystal aligned along the (110) planes [33].

Two approaches can be considered to create a microbeam with nanotubes: the trapping of a small fraction of the incident beam, which is then steered away to reduce the emittance with well-defined sharp edges or the arrangement of a focusing array of bent channeling nanotubes that focus the channeled particles into a small spot. The first solution seems to guarantee better results: some experiments in IHEP have evaluated the nanotube performances in terms of efficiency and radiation hardness with good results [33].

1.2.3 Radiation emission related applications

The coherent aspects, characterizing the charged particles interaction with crystals, do not affect only the particle trajectory but also the way it loses energy inside the crystalline medium. In channeling, for example a positive particle is confined in the region between the crystalline planes where the electron density is small, so that the collision probability with the electrons and the corresponding energy loss become lower than in an amorphous material [34].
When it comes to light particles (electrons and positrons) most of the energy lost during the interaction with an amorphous medium does not depend on the electron collisions but on the emission of the bremsstrahlung radiation that is determined by the multiple Coulomb scattering with the nuclei.
A particle crossing a crystal in channeling condition is not subject to multiple scattering with the nuclei but, oscillating in a quasi harmonic potential, emits an intense radiation whose spectrum, depending on the particle energy, can present peaks, corresponding to the different harmonics of the oscillation. Also the particles that form a small angle with the crystalline planes but not small enough to be captured in channeling emit a strong radiation called coherent bremsstrahlung determined by the periodic crossing of the crystalline planes.

The radiation emission in bent crystals, both in channeling and volume reflection (that can be considered as an extension of the coherent bremsstrahlung), is investigated from the theoretical and experimental point of view in chap. 3, while this section will briefly describe the implications in the application field. There are, in fact, several proposals to exploit the enhancement of the radiation emission in aligned crystals in applications such as:

- *the production of high energy photons.*
  High energy gamma beams are commonly produced deflecting high energy electrons in bending magnets; the intensity and the spectral characteristics of the obtained beam depend on the type of used magnet. In fact, besides the standard dipoles [35], dedicated undulator and wiggler magnets [36] have been developed to produce an oscillating trajectory that, due to coherent effects, increases the intensity and the monochromaticity of the emitted photons. Moreover, the bremsstrahlung phenomenon can be exploited to create photons of higher energy but with lower intensity: an electron impinges on a target emitting the photon whose energy can be computed measuring the energy lost by the primary electron [37]. In this scheme an aligned crystal can substitute the standard amorphous target in order to exploit coherent effects which increase the photon intensity preserving the very high energy of the emitted gammas. In addition to that, depending on the used effect, the spectral distribution can present a peaked structure and a high degree of polarization. As an example, a polarized photon beam facility, with an en-

ergy range of 25-70 GeV, has been developed at CERN [38] using a crystal aligned for coherent bremsstrahlung, starting from a pre-existing bremsstrahlung facility [39].

- *the particle identification.*
  The traditional methods (Cherenkov counters and TRDs, Transition Radiation Detectors) developed to identify particles cannot be used at very high energies. For this reason, in 1976 M. A. Kumakhov [40], predicting the existence of channeling radiation, suggested the use of channeling radiation itself to identify electrons and positrons. The principle is the following: an aligned crystal is inserted in a charged beam and the light particles are identified according to their radiation emission as the channeling radiation strongly depends on the particle mass. The radiation intensity enhancement in channeling (compared with bremsstrahlung) has the advantage of allowing the use of a thin target but given that the channeling critical angle (determining the channeling acceptance) is small, the method can be applied only to highly collimated beams. Recently an experimental program called PICH (Particle Identification with CHanneling radiation) has started to test this method [41]. Fig. 1.22 shows the experimental results obtained at CERN with a 5 GeV/c (a) [41] and a 20 GeV/c (b) [42] hadron and light lepton beam.

- *the positron production.*
  The next e^+/e^- colliders (future linear colliders and B factories) will require an increased beam intensity that in turn will need the development of more powerful positron sources. In a conventional positron source, positrons are produced by high-energy electrons hitting a heavy-metal target, and then are captured and accelerated. The maximum positron production efficiency, for 4-8 GeV incident electrons, is obtained with an optimized target thickness of 4-5 X_0 (radiation length) and selecting the outcoming positrons in the 5-25 MeV/c momentum range. The positron intensity can be enhanced, increasing the incident electron beam intensity and energy but there are limits given by the allowable heat load on the target caused by the beam power of the incident electrons. In 1989 R. Chehab [43] proposed to use a crystal oriented in channeling as a positron source. The idea is that, in an aligned crystal, both the photo production and the gamma conversion in pairs (that can be seen as its inverse process) are enhanced, resulting in a “compact” electromagnetic shower that allows to increase the number of emitted positrons without depositing more energy in the medium. Tests on the crystal positron source have been carried out bringing successful results [44] [45], so that, this positron production scheme has been applied to the KEKB injector

linac [46] increasing the positron yield of $\sim 25\%$ and reducing at the same time the steady state heat load on the target of $\sim 20\%$ as shown in fig. 1.23.

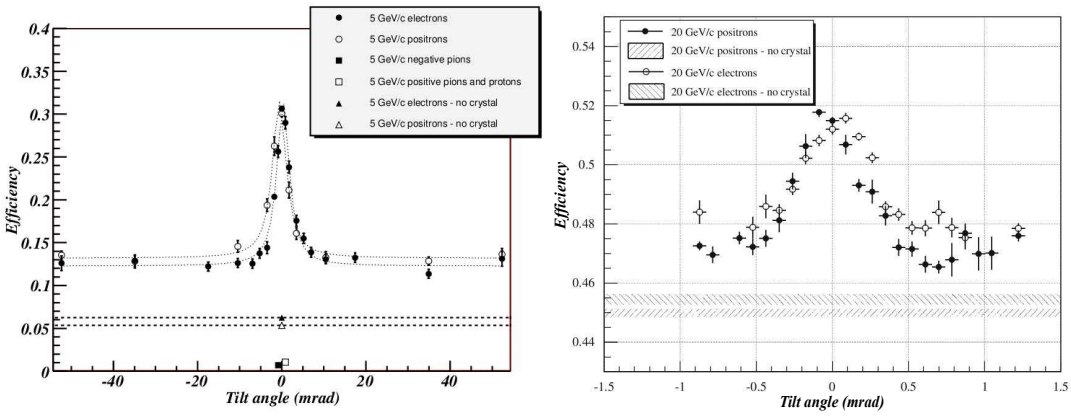

(a) (b)

Figure 1.22: Experimental results of the PICH (Particle Identification with CHanneling radiation) program: the photon efficiency, defined as the number of particles, that emit a detected radiation, over the total acquired one, as a function of the misalignment between the crystal and the beam for a 5 GeV/c beam (a) and a 20 GeV/c one (b). At small angles a clear enhancement in the emitted radiation can be seen for electrons and positrons.

The crystal applications described in this section exploit the radiation emission properties of aligned crystals and are originally thought to work with straight crystals; nevertheless bent crystals could offer some advantages:

- *tagging capabilities.*
  One of the main issues working with aligned crystals is the constant control of the percentage of particles undergoing a certain effect, trying to increase it, optimizing the alignment between the crystal and the beam. Moreover it can be useful to tag whether or not the single particle is subject to a given effect. These operations result to be greatly simplified using bent crystals since the deflection can be exploited as a reference to properly align the crystal and as an indicator of the regime in which the single particle has crossed the crystal.

- *increased angular acceptance.*
  In a bent crystal new phenomena appear such as volume reflection and volume capture. One of their main characteristics is the increased angular acceptance, with respect to channeling, given by the curvature of the crystalline planes. Since the radiation emission of these effects is enhanced, as

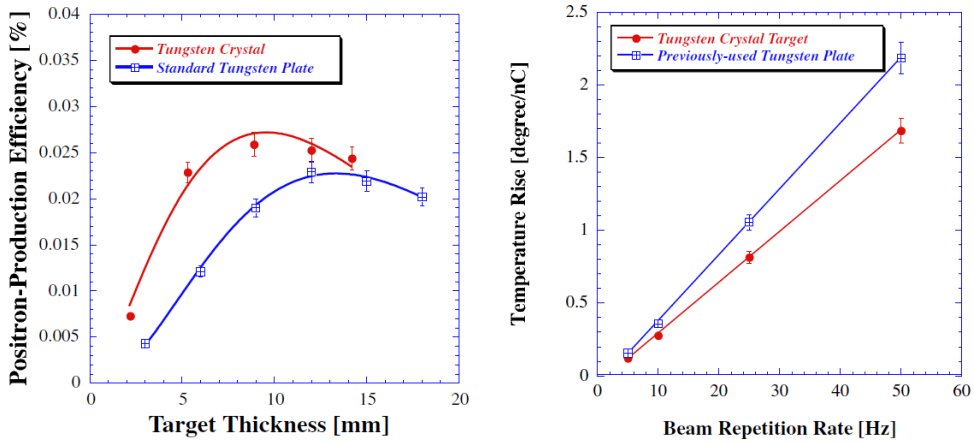

(a) (b)

Figure 1.23: The crystalline positron source used at KEKB [46] compared with a standard one: a) positron production efficiency, measured for the tungsten crystal and the standard tungsten plate, as a function of their thickness (the incident electron energy and positron momentum were 4 GeV and 20 MeV/c, respectively); b) targets temperature rise as a function of the beam repetition rate (the temperature rise is normalized by the average beam charges of the primary electron beam).

well as in the channeling case, they could be exploited to increase the angular acceptance and apply the described technique to low collimated beams.

- *new radiation production schemes.*
  Bent crystals are able to produce a macroscopic particle deflection that itself generates a characteristic radiation emission. For example in sec. 3.1.1 the channeling radiation in a bent crystal is described as consisting of two components: a hard one, given by the particle oscillations in the channel (present also in straight crystals) and a soft one, generated by the crystal curvature. This second component has usually a low intensity but it can be increased using the so called undulator crystal [47]. The undulator crystal is bent in a way that its channels have a sinusoidal shape that coherently increases the radiation emission due to the curvature (fig. 1.24) as well as in an undulator magnet. Differently from the magnet case, in which the oscillation length is limited to several millimeters, in a crystal the sub millimeter range becomes accessible, allowing a strong increase of the emitted photons energy [7].

[7] The energy of a photon emitted by an undulator crystal (magnet) is $E_\gamma = \frac{h\gamma^2 c}{L}$ where γ is the Lorentz factor and L is the undulator period.

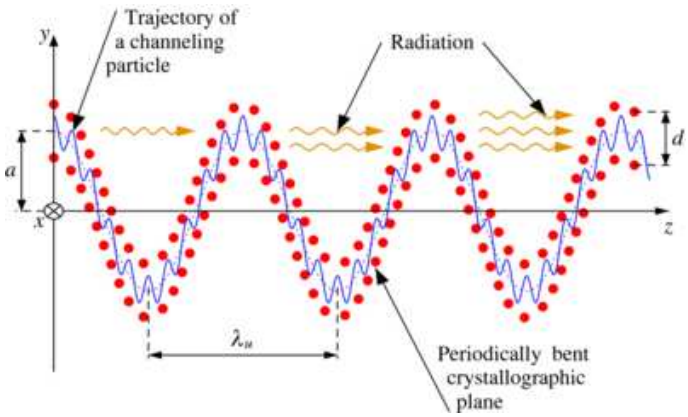

Figure 1.24: The undulator crystal working principle: the red dots represent the nuclei forming the bent crystalline planes, the blue line is the trajectory of the channeled particle, a is the oscillation amplitude and λ_a the oscillation period. The radiation emitted at each oscillation adds coherently.

1.3 The theory behind bent crystals

This section presents the theoretical bases of the coherent interaction in bent crystals. A crystal is a regular arrangement of atoms located in a lattice, so that, depending on the orientation, the atoms are placed in strings or planes, as shown in fig. 1.25.

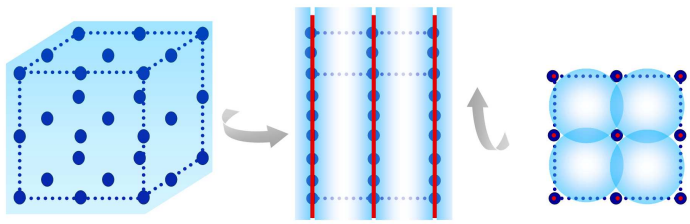

Figure 1.25: The crystalline structure; depending on the orientation, the atoms appear: (left) in a non-ordered structure; (center) arranged in planes, after a rotation around the horizontal axis; (right) arranged in strings after a subsequent rotation around the vertical axis.

A crucial assumption for the charged particle interaction in amorphous materials is that the collisions with the atoms are not correlated. This results in a variety

of different impact parameters, which in turn determine many physical processes: from Rutherford scattering to δ-ray emission, from ionization to X-ray production.
When a charged particle is aligned with a crystal plane or axis, this crucial condition is no more verified. As stated by J. Lindhard [48], the collisions with the crystal atoms are correlated, as if the crystalline plane or axis were physical objects formed by a continuous charge distribution (obtained by smearing the atomic charge along the crystal plane or string). The periodicity of these planar (axial) charge distributions forms a series of potential-wells which are able to confine the charged particles in channeling.
In this section an approximated form of the planar and axial potentials is computed starting from the single atom potential and allowing to derive the main features of the channeling effect that is its angular acceptance and efficiency, the curvature influence on the particle motion and the dechanneling phenomenon.
The last part of the section is dedicated to the so called "volume" effects which take place (only in bent crystals) when a particle becomes tangent to the crystalline plane inside the crystal itself: at this point it can be either captured in channeling (volume capture) or reflected by the potential barrier (volume reflection).

1.3.1 The continuum approximation

When a charged particle crosses a crystal with a small angle with respect to the crystallographic axis (or plane), its motion is determined by the coherent effect of the atomic axis or plane. In this condition the single atoms potential can be approximated by an average potential generated by the axis (plane) as if the charge inside the crystal had a continuum distribution, invariant with respect to the axis (plane) direction; thus the name continuum approximation [2].

The continuum approximation can be figured out considering a particle traveling inside a crystal almost aligned with a regular sequence of atoms (a crystal axis or plane). As shown in fig. 1.26, the angle α between the particle momentum and the atoms direction is small ($\alpha \ll 1$); thus, considering the two momentum components (the parallel one, p_l, and the orthogonal one, p_t, with respect to the atoms direction), since $\alpha = p_t/p_l$, it results that $p_t/p_l \ll 1$. This means that the transversal motion of the particle, compared with the longitudinal one, is very slow; indeed, a long distance in the longitudinal direction and the interaction with a large number of atoms correspond to a short movement in the transversal one. For this reason the particle trajectory is determined by the average effect of many atoms.

Let's take the case of a particle traveling inside a crystal aligned with one of its planes (but not with the axis) as shown in fig. 1.27a; in this condition, if $V(x,y,z)$ is the electric potential between the particle and the single atom, the interaction

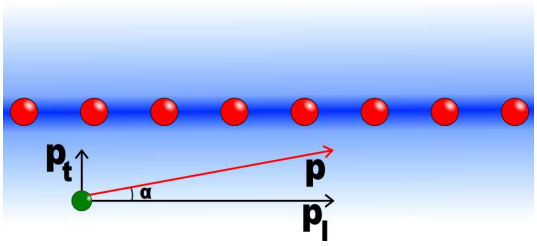

Figure 1.26: Schematic description of the motion of a particle (green dot) that is quasi aligned with a series of atoms inside a crystal (the red dots represent their nuclei). p is the particle momentum, p_l its parallel component and p_t its perpendicular one with respect to the atomic series.

can be represented using an average potential computed as follows:

$$U_{pl}(x) = Nd_p \int_{-\infty}^{\infty}\int_{-\infty}^{\infty} V(x,y,z)\mathrm{d}y\mathrm{d}z \tag{1.1}$$

where N is the number of atoms per unit volume, d_p is the interplanar spacing, so that $N \cdot d_p$ represents the planar atom density.

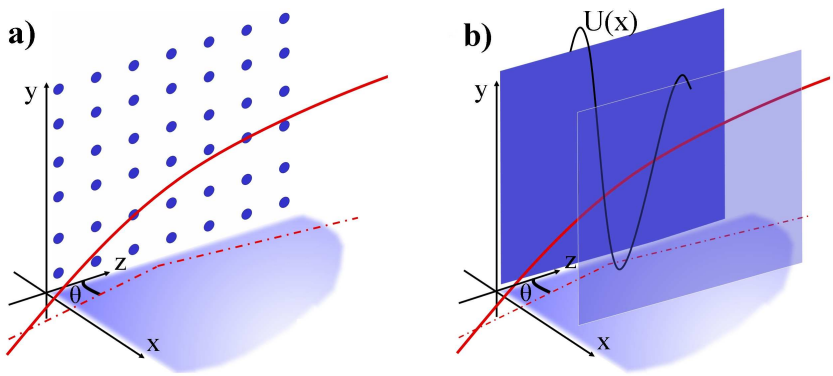

Figure 1.27: a) A particle (red line) moving in a crystal at a small angle with respect to the crystalline plane (placed in the $z-y$ plane). b) The particle experiences an average potential $U(x)$, due to the planes, represented by the black line.

There are different ways to approximate $V(x,y,z)$, that in general can be a quite complicated function depending on several parameters; Lindhard [48] used the Thomas-Fermi model:

$$V(r) = \frac{Z_i Z e^2}{r}\Phi\left(\frac{r}{a_{TF}}\right) \tag{1.2}$$

where Z_i is the atomic number, Ze the charge of the particle and r the distance between the particle and the atom; the first factor is the potential of the point like charge, while $\Phi(r/a_{TF})$ is the screening function which takes into account the charge distribution; a_{TF} is the Thomas Fermi screening radius ($a_{TF} = 0.8853 \cdot a_B \cdot Z^{-1/3}$, $a_B = 0.529$ Å).
A widely used analytical form for Φ is given by Molière [49]:

$$\Phi\left(\frac{r}{a_{TF}}\right) = \sum_{i=1}^{3} \alpha_i e^{\frac{\beta_i}{a_{TF}}} \tag{1.3}$$

where α=(0.1, 0.55, 0.35) and β=(6.0, 1.2, 0.3). Lindhard proposed an alternative form:

$$\Phi\left(\frac{r}{a_{TF}}\right) = 1 - \left(1 + \frac{3(a_{TF})^2}{r^2}\right)^{-1/2} \tag{1.4}$$

which convolved with eq. 1.1 and eq. 1.2 gives the following approximation of the continuous potential generated by a single crystal plane:

$$U_{pl}(x) = 2\pi Z_i Z e^2 N d_p \left(\sqrt{x^2 + 3(a_{TF})^2} - x\right) \tag{1.5}$$

where x is the distance from the plane, so that $x = 0$ represents the plane position and (for positive particles) corresponds to the maximum value of the potential. This value, being proportional to Z and N (the atomic number and the atomic density), depends on the crystal material and, for a given crystal, changes as a function of the interplanar distance d_p so that the wider the channel the greater its confinement strength.
As shown in fig. 1.27b, a particle which is crossing the crystal will feel the effect of all the crystalline planes but the contribution of the two nearest ones will be dominant; therefore:

$$U(x) \simeq U_{pl}\left(\frac{d_p}{2} - x\right) + U_{pl}\left(\frac{d_p}{2} + x\right) - 2U_{pl}\left(\frac{d_p}{2}\right) \tag{1.6}$$

in which the origin of the transversal coordinate x is placed in the middle of the two planes, where the potential value is fixed to zero ($U(0) = 0$).
The most used crystals for channeling investigation in high energy experiments are made of silicon [2] (more rarely germanium) thanks to the high standards reached by the semiconductor technology in terms of quality of the crystals. Silicon crystals belong to the diamond group and they are characterized by a covalent bond: each atom is linked to four neighbours forming a regular tetrahedron with a face centered cubic (fcc) crystalline structure. Fig. 1.28 shows the principal planes of the fcc structure indicated by the Miller indices; the planes useful for channeling are (110) and (111) while (100) generates a too small potential to be of any

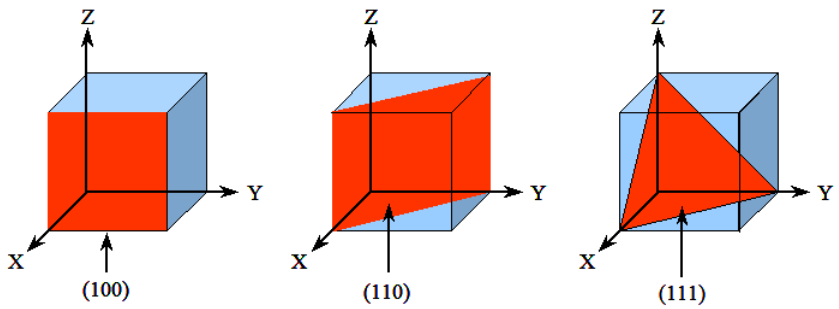

Figure 1.28: Orientation of the most important crystallographic planes in the cubic lattice system, indicated by the Miller indices.

interest in this frame. In fig. 1.29 the interplanar potential $U(x)$ for the (110) and (111) planes in silicon is shown: the (110) orientation has a regular structure with a constant interatomic distance ($d_p = 1.92$ Å) that produces a single potential well of about 22 eV; the (111) one is more complex as it has a variable interatomic distance, a long one ($d_p^L = 2.35$ Å) and a short one ($d_p^S = 0.78$ Å) that origin a couple of potential wells, the deepest one being of about 25 eV. The dashed line in fig. 1.29a is the harmonic approximation that, fitting the interplanar potential rather well, can be used for the analytical computation as it will be shown in sec. 1.3.2.

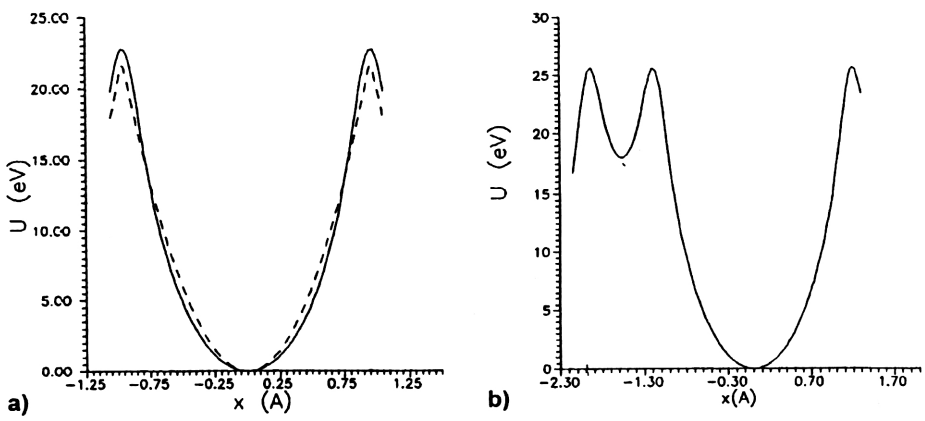

Figure 1.29: The interplanar Molière potential for: a) the (110) Si channel and b) the (111) Si channel which is characterized by two potential wells corresponding to its two interplanar distances. The dashed line is the harmonic potential approximation.

1.3.2 Channeling

A charged particle trapped in the potential well between two crystalline planes is said to be in planar channeling; this happens if the transversal component of the particle momentum (see fig. 1.26) is not enough to overcome the barrier.
In this condition, the particle experiences a series of correlated collisions; although these are quantum events, the particle motion can be described in the classical mechanics frame, thanks to the large number of energetic levels accessible in the interplanar potential.
Taking into account the harmonic potential approximation $U(x) = U_0 \left(x\frac{2}{d_p}\right)^2$, the energy spacing between the levels is $\hbar\left(\frac{8U_0}{d_p^2 M_o}\right)^2$ where M_o is the oscillating mass; so the classical approximation is valid if:

$$N_o = \frac{d_p}{\hbar\sqrt{8}}\sqrt{U_0 M_o} \gg 1 \tag{1.7}$$

where N_o is the number of the accessible energetic levels for the trapped particle. Condition 1.7 is always fulfilled for heavy particles (protons) while for light ones (electrons and positrons), the classical approach becomes valid in the 10-100 MeV range.

In the framework of the continuum approximation (sec. 1.3.1), the transversal momentum is much smaller than the parallel one ($p_t \ll p_l$) and thus the total energy of the system can be approximated as follows:

$$E = \sqrt{p_t^2 + p_l^2 + m^2c^2} + U(x) \simeq \frac{p_t^2c^2}{2E_l} + E_l + U(x) \tag{1.8}$$

where $E_l = \sqrt{p_l^2c^2 + m^2c^4}$; p_l is not affected by the potential so it is conserved, meaning that E_l is conserved and thus $\frac{p_t^2c^2}{2E_l} + U(x)$ is conserved too, due to the energy conservation principle. This quantity defined as the particle transversal energy E_t can be expressed in terms of the misalignment angle between the particle trajectory and the crystal planes ($\alpha = p_t/p_l$):

$$E_t = \frac{p_l^2c^2}{2E_l}\alpha^2 + U(x) \simeq \frac{p^2c^2}{2E}\alpha^2 + U(x) = \text{const.} \tag{1.9}$$

where, in the second equality, according to the condition $p_t/p_l \ll 1$, p_l has been approximated with the total momentum p, and E_l with the total energy E.
According to eq. 1.9, each particle entering the crystal has a transversal energy

value, which is a function of its alignment with respect to the crystal plane (α) and of its position in the channel (x), as it is shown in fig. 1.30.

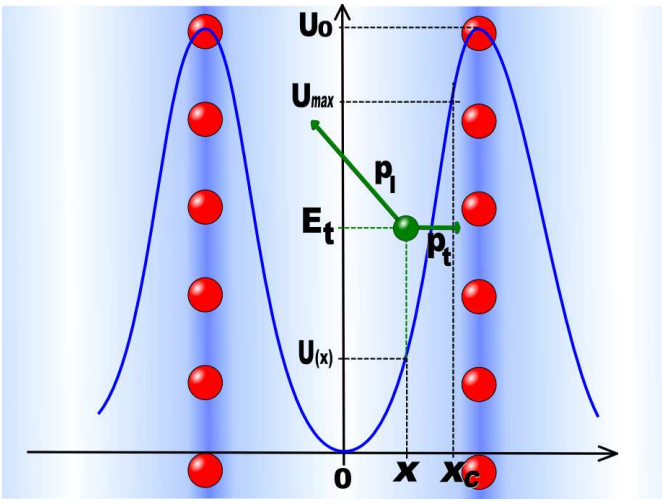

Figure 1.30: Schematic description of the interplanar potential: the two vertical series of red dots represent the atomic nuclei and the blue line is the potential shape $U(x)$. The green dot represents a particle with a transversal energy E_t that, being lower than $U_{max} = U(x_c)$, keeps the particle trapped in the channel.

The particle is trapped in the channel if its transversal energy is smaller than the maximum value of the potential barrier, that is $E_t < U_{max}$; the condition that defines the possible values of α and x for a channeled particle is then:

$$\frac{p^2c^2}{2E}\alpha^2 + U(x) \leq U_{max} \tag{1.10}$$

Although the maximum of the potential is reached at the plane itself ($x = d_p/2$), in this position the particle would be quickly removed from the channel by the scattering with the nuclei; indeed the stable channeling condition (sec. 1.3.2.1) is achieved only when $x < x_c$, where x_c is the critical approaching distance, and thus $U_{max} = U(x_c)$. The distance $p_w = d_p/2 - x_c$ can be imagined as the intrinsic width of the plane where the nuclei density is large. This density decreases from the plane center according to a gaussian distribution whose σ is $\rho_\perp = \sqrt{2}\rho$, being ρ the RMS amplitude of the atomic thermal vibration (the ρ value in silicon at room temperature is 0.075Å). The experimental data [50] show that a good approximation for p_w is 2.5ρ which gives $U_{max} \simeq 16$ eV for the (110) orientation in silicon and 19 eV for the (111) one.

Taking into account the relation $pc^2 = vE$ (vE is the product between the particle velocity and its energy), eq. 1.10 becomes:

$$E_t = \frac{pv}{2}\alpha^2 + U(x) \tag{1.11}$$

that for $E_t = U_{max}$ (critical value of the transversal energy) and $x = 0$ (minimum value of the interplanar potential $U(0) = 0$)[8] gives the maximum misalignment angle that still allows channeling, the so called critical angle:

$$\alpha_c = \sqrt{\frac{2U_{max}}{pv}} \tag{1.12}$$

For a silicon crystal $U_{max} \approx 20$ eV, thus α_c is 280 μrad at 500 MeV, 9.42 μrad at 450 GeV and 2.39 μrad at 7 TeV. It has to be noted that the critical angle decreases as the square root of the energy, while the multiple scattering as the energy of the incoming particles; therefore, the effects due to multiple scattering which (as will be shown) reduce the channeling efficiency become less important at high energy.

The angle α can be expressed as $\frac{\mathrm{d}x}{\mathrm{d}z}$ where dx and dz are the infinitesimal increases in the transversal and longitudinal spatial directions; with this substitution, eq. 1.11 gives the following differential equation which describes the particle motion in the channel:

$$E_t = \frac{pv}{2}\left(\frac{\mathrm{d}x}{\mathrm{d}z}\right)^2 + U(x) \tag{1.13}$$

Differentiating with respect to z:

$$pv\frac{\mathrm{d}^2x}{\mathrm{d}z^2} + U'(x) = pv\frac{\mathrm{d}^2x}{\mathrm{d}z^2} + U_0\frac{8x}{d_p^2} = 0 \tag{1.14}$$

whose solution gives the particle trajectory in space, which in fact corresponds to a sinusoidal oscillation:

$$x = \frac{d_p}{2}\sqrt{\frac{E_t}{U_0}}\sin\left(\frac{2\pi \cdot z}{\lambda} + \phi\right) \tag{1.15}$$

The length of the oscillation period is:

$$\lambda = \pi d_p\sqrt{\frac{pv}{2U_0}} \tag{1.16}$$

For example for a 400 GeV/c proton in silicon $\lambda \sim 25.5$ μm.

[8] corresponding to the particles which enter the channel in its center.

1.3.2.1 Dechanneling

In the particle trajectory derivation (sec. 1.3.2), the transversal energy conservation is assumed, which in real crystals is not exactly true because of the scattering processes with electrons and nuclei as well as the difference between the real potential and the continuum approximation and the possible crystal lattice defects. These events can produce either an instant change or a progressive growth of the transversal energy that, overcoming the interplanar potential barrier, causes the release of the particle from the channeling state, the so called dechanneling.

Dechanneling is a complex phenomenon and its full description, which includes the scattering effects in the real crystal, is achieved through Montecarlo computer simulations [51]. However a simplified dechanneling model can be developed taking into account two fundamental aspects: the multiple scattering on the nuclei (MSN) and the one on the electrons (MSE) [52].
MSN takes place during the first phase of the crystal crossing in channeling and it concerns only the particles which have a high initial transversal energy value ($E_t > U(x_c)$ in fig. 1.30): these particles, moving near the crystal planes where the nuclear density is high, are quickly dechanneled.
On the contrary, given that the electrons distribution is more uniform than the nuclear one, MSE concerns all the channeled particles; it produces a slow transversal energy growth (compared to MSN) and thus has a negligible effect in the first phase of the crystal crossing.
From a practical point of view, MSN is dominant in short crystals (the last generation ones with a length of the order of 1 mm, sec. 2.1.5) while it is almost hidden in long crystals, where the unstable channeling region represents just a small fraction of the crystal itself, and where the observed dechanneling is mainly due to MSE.

In principle the reduction of the number of channeled particles as a function of the crystal depth can be approximated by an exponential decay both for the MSN case and the MSE one but characterizing the two phenomena with their own dechanneling length L_D according to the following equation: [2]:

$$N(z) = N_0 \cdot e^{-\frac{z}{L_D}} \tag{1.17}$$

where $N(z)$ is the number of channeled particles at the z position along the crystal ($z \leq$ crystal length) and N_0 is the number of channeled particles at the crystal entry face.

For what concerns MSN, an estimation of the specific dechanneling length (L_{Dn}) can be provided [53] considering the average distance required to increase the particle transversal energy of about $E_{gap} = U_0 - U_{max}$ (see fig. 1.30) because of the Coulomb multiple scattering.
The relation between the transversal energy E_t and the misalignment angle α is

$\Delta E_t = pv/2 \cdot \Delta\alpha^2$ (eq. 1.11); assuming that α increases following the multiple scattering formula given in [54] (neglecting the logarithmic part), the increase of the transversal energy as a function of the z coordinate is obtained:

$$\Delta E_t(z) = \frac{pv}{2} \cdot \Delta\alpha(z)^2 = \frac{pv}{2} \cdot \frac{E_c^2}{p^2v^2}\frac{z}{X_0} = \frac{E_c^2}{2pv}\frac{z}{X_0} \tag{1.18}$$

where X_0 is the radiation length (9.37 cm in silicon), E_c =13.6 MeV. When the transversal energy overcomes the potential barrier ($\Delta E_t(z_c) = E_{gap}$) the particle is dechanneled ($L_{Dn} = z_c$) so:

$$L_{Dn} = E_{gap} \cdot pv \cdot \frac{2X_0}{E_c^2} \tag{1.19}$$

Taking into account that in silicon $E_{gap} \simeq 5$ eV, at an energy of 400 GeV $L_{Dn} \simeq$ 2 mm. This is a rough estimate since it does not take into account the specific trajectory of the channeled particle; nevertheless, it is interesting to note that the nuclear dechanneling length is proportional to the energy of the particle; for a more accurate estimation, a Montecarlo simulation is needed.

MSN affects only the particles with a high initial E_t. However also the particles with $E_t < U_{max}$ can be dechanneled due to the scattering with the electrons; this phenomenon is slower and therefore it is characterized by a longer dechanneling length [2]:

$$L_D = \frac{256}{9\pi^2}\frac{pv}{\ln(2m_ec^2\gamma I^{-1}) - 1}\frac{a_{TF}}{Z_i r_e m_e c^2} \tag{1.20}$$

where I is the ionization potential (for silicon $\simeq$ 172 eV), m_e is the electron mass at rest, r_e the classical electron radius and Z_i the charge number of the particle. Eq. 1.20 states that the electron dechanneling length, as well as the nuclear one, linearly increases with the energy, but its numerical value far exceeds the nuclear one (for example at 400 GeV in silicon L_{De} =21.9 cm). For this reason the MSE effect is negligible in short crystals, like the ones described and analyzed in this thesis work. Nevertheless these crystals represent the last generation of bent crystals, therefore eq.1.20 has been experimentally verified in the past with long crystals as shown in fig. 1.31.

The given dechanneling description is valid for positive charged particles which are channeled in the central region of the crystalline plane far from the nuclei. On the contrary, negative particles are channeled around the atomic plane as their potential well minimum corresponds to the nuclei positions. The large electron and nuclear densities in this region, increasing the scattering probability, make the dechanneling length much shorter with respect to the positive particles one.

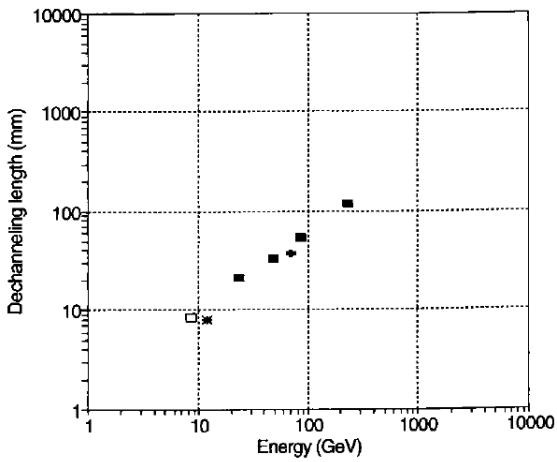

Figure 1.31: Measurements of the electron dechanneling length in long silicon crystals; the symbols refer to several experiments [55].

1.3.3 Bent crystals

The channeling phenomenon can be exploited to deflect high energy charged particles; the motion of a channeled particle is, in fact, confined between the crystalline planes; therefore, if the crystal is bent, the channel is curved and the captured particle is forced to follow the curvature being deflected.
Fig. 1.32a shows the scheme of a bent crystal: the red line represents the particle trajectory which is deviated of the angle $\phi_c = l/R$ (where l is the crystal length and R its bending radius), while an example of bending through a mechanical holder is presented in fig. 1.32b.

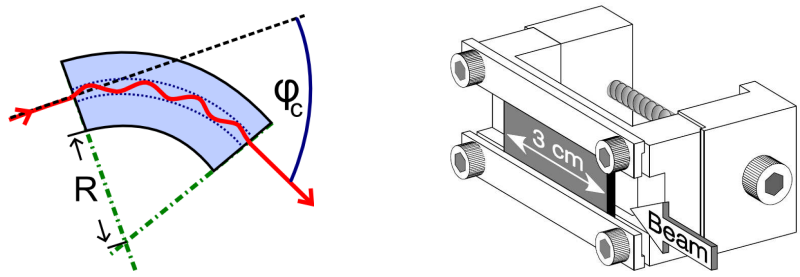

(a) (b)

Figure 1.32: a) The bent crystal working principle; b) an example of a bending device.

The description of the interplanar potential given in sec. 1.3.1 is still valid in a bent crystal since a macroscopic curvature of the crystal (that is a curvature radius of the order of several meters) has a negligible effect on the microscopical crystalline structure (Angstrom scale) itself.
However a particle trapped in a bent channel feels a centrifugal force in addition

to the planar potential, as described in fig. 1.33, where the condition of an ideal particle which enters the crystal in the center of a channel, perfectly aligned to the planes (with zero transversal energy, $E_t = 0$) is shown both in the laboratory inertial frame (plot a) and in the non inertial frame that rotates following the crystal curvature (plot b). In the reference system rotating along the crystal (plot b) a

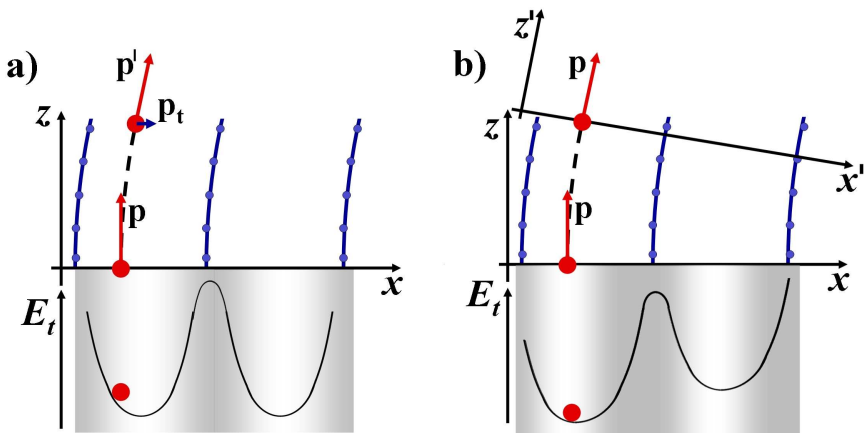

Figure 1.33: A particle with zero transversal energy in channeling in a bent crystal: a) in the laboratory inertial frame, the particle assumes an angle with respect to the planes direction which is curved, thus its equilibrium position in the potential is no more in the channel center; b) in the non inertial frame which rotates with the particle; the centrifugal force appears and modifies the interplanar potential.

centrifugal force directed towards the external side of the channel appears and its contribution should be added to eq. 1.14 which expresses the equilibrium of the forces applied on the particle:

$$pv\frac{\mathrm{d}^2x}{\mathrm{d}z^2} + U^{'}(x) + \frac{pv}{R(z)} = 0 \tag{1.21}$$

where $R(z)$ is the curvature radius as a function of the position in the channel; if it is constant ($R(z) = R$), the crystal curvature is an arc of circumference (as in the bent crystal described in sec. 2.1.5) and the effective interplanar potential $U_{eff}(x)$ has the following analytical form:

$$U_{eff}(x) = U(x) + \frac{pv}{R}x \tag{1.22}$$

The expressions given in sec. 1.3.2 which describe the particles motion for an arbitrary interplanar potential $U(x)$ remain valid with the substitution with $U_{eff}(x)$. According to eq. 1.22, as the curvature (R^{-1}) increases, the minimum

of the potential is shifted towards the outer planes (negative x values) and the potential well depth is reduced, as shown in fig. 1.34 where the interplanar potential is computed for 3 different curvature radii.

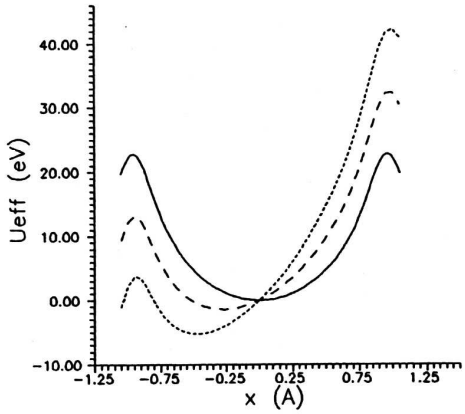

Figure 1.34: The interplanar silicon ((110) planes) potential computed in the Molière approximation for: the straight crystal (solid line), a pv/R of 1 GeV/cm (dashed line) and 2 GeV/cm (dotted line).

When the centrifugal force equals the electric field produced by the atomic plane at the critical distance x_c (that delimits the region with high nuclear density, see fig. 1.30):

$$\frac{pv}{R_c} = U'(x_c) \tag{1.23}$$

channeling is no longer possible; therefore R_c represents the critical curvature radius (Tsyganov critical radius): for R smaller than this value, capture is no longer stable. According to Lindhard potential (eq. 1.4), an approximate expression of R_c can be computed:

$$R_c = \frac{pv}{U'(x_c)} \simeq \frac{pv}{\pi N d_p Z_i Z e^2} \tag{1.24}$$

In deriving this expression, the contribution of the single plane is taken into account; being the x_c position close to an atomic plane, the contribution to the potential from the other planes can be neglected. Given that in silicon $U'(x_c) \simeq 5\,\mathrm{GeV/cm}$, the critical curvature radius for relativistic particles of energy E ($pv \simeq E$) is approximately $R_c^b = \dfrac{E[\mathrm{GeV}]}{5}$ cm.

Since the maximum transversal energy value for a fixed momentum particle decreases with the curvature (fig. 1.34) and indicating with U_{max} the transversal energy limit for channeling in a straight crystal, this limit will assume a different value $U_{max}^b(R) < U_{max}$ in a crystal bent with a curvature radius R.
This affects the critical angle given in eq. 1.12 which becomes:

$$\alpha_c^b = \sqrt{\frac{2U_{max}^b(R)}{pv}} < \alpha_c \tag{1.25}$$

An approximated value of U^b_{max} as a function of the curvature radius can be computed taking into account the harmonic approximation, according to which the effective potential of eq. 1.22 becomes:

$$U_{eff}(x) = U_0 \cdot \left(\frac{x}{x_c}\right)^2 + \frac{pv}{R}x \tag{1.26}$$

As shown in sec. 1.3.1, the interplanar potential has been defined in order to have the minimum in the middle of two atomic planes and to reach the U_{max} value in the critical positions $-x_c$, x_c. Eq. 1.26 shows that if $U(x)$ is harmonic, $U_{eff}(x)$ is harmonic too, but the centrifugal force shifts the minimum position to $x_{min} = -\frac{pvx_c^2}{2RU_0}$; thus the height of the potential barrier will be:

$$U^b_0 = U_{eff}(x_c) - U_{eff}(x_{min}) = U_0 - \frac{pv}{R}x_c + \frac{1}{2U_0}\left(\frac{pv}{R}x_c\right)^2 \tag{1.27}$$

According to eq. 1.24, the critical radius in the harmonic approximation is $R^h_c = \frac{pvx_c}{2U_0}$ so the potential barrier can be expressed as:

$$U^b_0 = U_0\left(1 - 2\frac{R^h_c}{R} + \left(\frac{R^h_c}{R}\right)^2\right) = U_0\left(1 - \frac{R^h_c}{R}\right)^2 \tag{1.28}$$

For a curvature radius tending to infinity, which means in a straight crystal, $U^b_0 = U_0$; if the curvature radius increases, U^b_0 decreases as expected (note that only the region $R > R^h_c$ is considered). Thus the critical angle α_c in a bent crystal with a R^{-1} curvature becomes:

$$\alpha^b_c = \alpha_c\left(1 - \frac{R^b_c}{R}\right) \tag{1.29}$$

As it was already mentioned, the effective potential in a bent crystal is still harmonic, so the particle trajectories in the channel have the same shape of the ones in a straight crystal (eq. 1.3.1):

$$x = -x_c\frac{R_c}{R} + x_c\sqrt{\frac{E_t}{U^b_0}}\sin\left(\frac{2\pi \cdot z}{\lambda} + \phi\right) \tag{1.30}$$

In fact, they have the same period λ but the oscillation takes place around a new equilibrium point, $x_{min} = -x_cR_c/R$. This shift corresponds to a change of the particle distribution in the channel: the channeled particles are shifted towards the atomic plane so they experience a larger electron density with respect to the straight crystal. This should increase the dechanneling probability (sec. 1.3.2.1)

but, as the valence electrons in silicon and germanium have a roughly uniform distribution in the channel, the electron scattering probability of a channeled particle is almost insensitive to the crystal curvature for curvature radii $R \geq 2R_c$.
This effect is indeed hidden by the greater influence on the dechanneling yield of the reduction of the potential well; as already observed in sec. 1.3.2.1 in fact, the dechanneling length is proportional to the maximum transversal energy, so if L is the dechanneling length in a straight crystal, when the crystal is bent it becomes:

$$L^b = L\left(1 - \frac{R_c^h}{R}\right)^2 \tag{1.31}$$

In addition, the dechanneling length in a crystal with a given curvature is no more a linear function of the particle pv as shown in sec. 1.3.1: in the effective potential, the curvature radius R appears always in the denominator $\left(\frac{pv}{R}\right)$; the critical radius has been defined for a fixed particle energy but, in the same way, once the curvature radius is fixed, a critical particle energy pv_c can be defined. Eq. 1.31 becomes:

$$L_D^b = L_D\left(1 - \frac{pv}{pv_c}\right)^2 \propto pv\left(1 - \frac{pv}{pv_c}\right)^2 \tag{1.32}$$

Using the L_D dependence from pv (eq. 1.20), the dechanneling length in a bent crystal is no more a monotonic function of the energy but has a maximum value for $pv = 1/3 \cdot pv_c$ which is the optimal choice to minimize the dechanneling losses in a bent crystal.

1.3.4 Volume effects

In a bent crystal the direction of the atomic plane changes as a function of the position inside it: a channeled particle is forced to follow this change, so its motion does not differ substantially from the one in straight crystals. When a particle crosses the crystal, not in channeling, its motion is approximately straight (apart from the multiple scattering) therefore the alignment between the particle trajectory and the crystalline plane varies during the motion. In particular there is a range of initial alignment positions that will result in the particle trajectory becoming tangent with the crystal plane inside the crystal itself. When this happens, there are two possible effects: either the particle is captured in the channel continuing its motion in channeling (*volume capture*, sec. 1.3.4.1) or it is reflected by the potential barrier in the opposite direction with respect to the channeling deflection (*volume reflection*, sec. 1.3.4.2).

1.3.4.1 Volume capture

In sec. 1.3.2.1 it has been pointed out that the scattering effects can modify the particle transversal energy resulting in a finite probability for the confined particle to leave the channel: this phenomenon is called dechanneling.
For any given particle trajectory in the crystal, the reverse one is possible (Lindhard reversibility rules [48]), meaning that a reverse dechanneling mechanism should exist: a particle with a transversal energy above the critical value can lose part of the energy because of multiple scattering and can be captured in the channel; this phenomenon is called *feed-in* or *volume capture* in the bent crystal frame.
In a straight crystal, the dynamics of the two beam populations, the channeled particles and the random ones (in amorphous condition), is determined by the two opposite mechanisms (dechanneling and feed-in), so that the effective dechanneling can be defined as the total fraction of particles which leave the channel. Fig. 1.35a-top shows a possible particle trajectory in a straight crystal: the initially channeled particle is first *dechanneled* and, at a certain point, re-captured in a channel (*feed-in*). The feed-in mechanism in a straight crystal is possible since the trajectories of the dechanneled particles remain quasi parallel to the crystal planes; in other words the transversal energy fluctuates around the confinement threshold (fig. 1.35a-bottom).
The equivalent process in a bent crystal is shown in fig. 1.35b; in this case, the dechanneling takes place but in the meanwhile the channel rotates its direction as the particle moves forward in the crystal itself. Therefore the particle misalignment with the channel rapidly increases and the transversal energy of the particle moves away from the confinement threshold because of the effective potential shape (fig. 1.35b-bottom). For this reason, the feed-in is very unlikely and gives a negligible contribution to the effective dechanneling probability in bent crystals.

According to the reversibility principle, the inverse of the dechanneling process should exist also in bent crystals. In fact, it can be obtained considering the reversed trajectory of a dechanneled particle: the particle enters the crystal, misaligned with respect to the channel ($\alpha > \alpha_c$), and it is progressively aligned by the crystal curvature, as schematically shown in fig. 1.36. From the transversal energy point of view (right side of the figure), during this phase the distance from the capture threshold is decreasing; thus near the tangency point with the channel its fluctuation allows the capture in the potential well; from this point on the particle behaves as a channeled one. Given the capture happens inside the crystal, that is in its volume, the process is called *volume capture*.
Volume capture is strictly related to dechanneling, as they both depend on the scattering probability; in fact, the probability to be dechanneled (P_D) crossing a crystal length dz is equal to the probability of an almost aligned particle to be

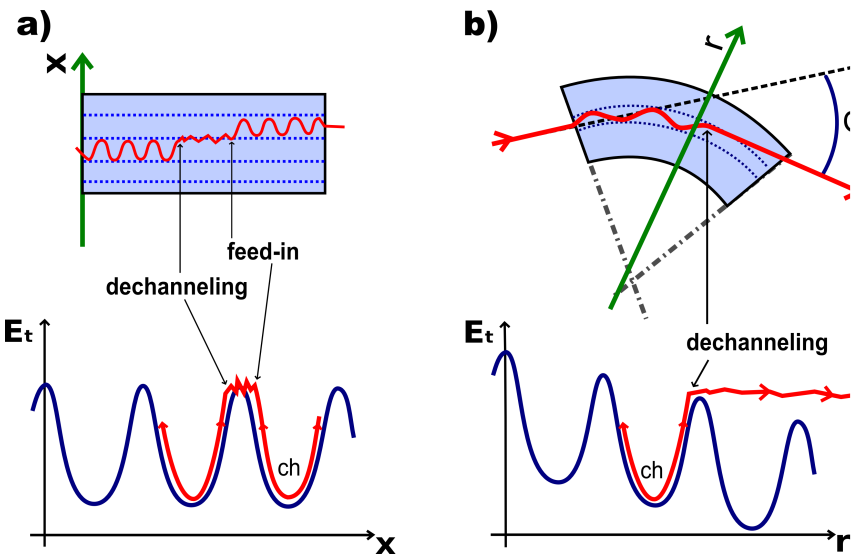

Figure 1.35: a) A possible particle trajectory in a straight crystal: the particle is first dechanneled and subsequently re-channeled (feed-in); b) a similar trajectory in a bent crystal: after the dechanneling the feed-in probability rapidly decreases as the particle is no more aligned with the channel. In the bottom part of the figure the evolution of the particle transversal energy in the interplanar potential is shown for both cases.

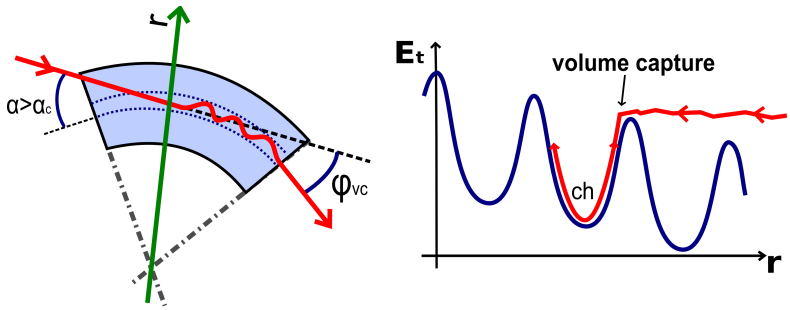

Figure 1.36: The volume capture process in a bent crystal: left) a possible trajectory is given, with a particle which is progressively aligned with the channel due to the crystal curvature and near the tangency point with the channel is captured in channeling; right) the trajectory is represented in the phase space (transversal energy versus radial position); note that it is the reverse process with respect to the dechanneling one (fig. 1.35b-bottom).

captured in the channel (P_{VC}), crossing the same crystal length dz:

$$P_{VC}(\mathrm{dz}) = P_D(\mathrm{dz}) = \frac{\mathrm{dz}}{L_D} \tag{1.33}$$

where dz is the infinitesimal increment in the longitudinal direction and L_D is the dechanneling length (sec. 1.3.2.1). This happens because the two processes require a change of the same amount of transversal energy to take place: an increase for dechanneling and a decrease for volume capture.
To compute the total volume capture probability, an estimation of the length during which the particle is almost aligned and thus can be captured is needed; considering that α_c gives the angular scale allowing channeling, this length can be approximated by $\delta z = \alpha_c R$, resulting in the following estimation for the volume capture probability:

$$P_{VC} \simeq \frac{R\alpha_c}{L_D} \tag{1.34}$$

Considering the trajectories reversibility in the crystal, a more rigorous formula (that introduces a numerical correction factor) for P_{VC} can be derived [2]:

$$P_{VC} = \frac{\pi}{2}\frac{R\alpha_c}{L_D} \tag{1.35}$$

The volume capture trend as a function of the beam energy can be computed, considering that $\alpha_c \propto \sqrt{pv}$ and $L_D \propto pv$ (if the logarithmic correction is neglected):

$$P_{VC} \propto \frac{R}{(pv)^{3/2}} \tag{1.36}$$

1.3.4.2 Volume reflection

The *volume reflection* phenomenon represents the particle deviation in a single point inside the crystal due to the elastic scattering with the atomic potential barrier; it was considered for the first time in computer simulations [56] and then experimentally observed [57].
As well as the volume capture effect, volume reflection takes place when a particle enters the crystal with an angle larger than the critical one α_c so that the transversal energy overcomes the potential barrier and the particle is not channeled. In this condition it crosses the crystal approaching the tangency point with the channel (fig. 1.37) with a trajectory similar to the volume capture one; but in this case the transversal energy fluctuations are not able to cause the particle confinement and the radial coordinate r_t, corresponding to the tangency point, is reached. In this point the particle has no longer a transversal kinetic energy thus it reverses the motion under the influence of the interplanar potential. This phenomenon is called *volume reflection* and produces a deflection angle ϕ_{VR} of the particle trajectory.

To estimate the reflection angle the particle trajectory has to be considered in detail. Fig. 1.37(left) presents a simplified volume reflection trajectory formed by two straight lines connected in a single reflection point; this is an approximation

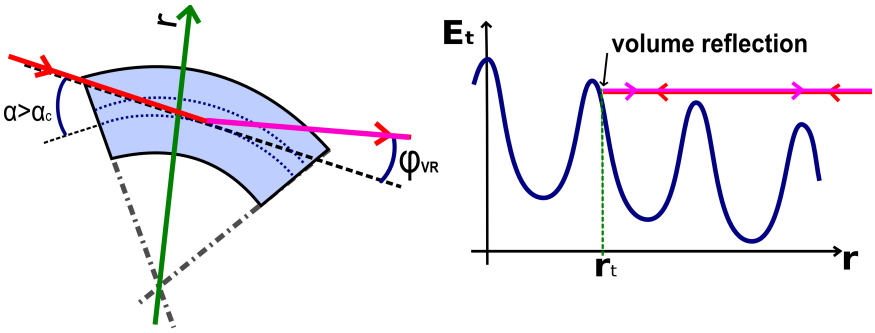

Figure 1.37: Volume reflection of a charged particle in a bent crystal at the turning radial coordinate r_t: on the left side a schematic view of the crystal and on the right one the particle transversal energy and the effective potential as a function of the radial coordinate.

that neglects the oscillations due to the crystalline potential. These oscillations (fig. 1.38a) depend on the fact that the transversal energy is the sum of a kinetic and a potential component, $E_t = \frac{pv}{2}\alpha^2 + U(x)$: when the particle crosses the crystal and thus the different channels, $U(x)$ oscillates from its maximum to its minimum and since the transversal energy is constant also the angle α should oscillate. Fig. 1.38b shows the oscillations of the particle momentum direction as a function of the position inside the crystal. In the first half of the plot the amplitude of the oscillations increases as long as the channel is getting parallel to the particle trajectory; when the tangency position is reached, the particle reverses its motion and the oscillations start again with a decreasing amplitude corresponding to the progressive misalignment. Fig. 1.38b shows that the reflection angle basically depends on the amplitude of the last oscillation (the one with the turning point, indicated in red); during this oscillation the potential component of the transversal energy varies of about $2U_{max}$ (box at the top right in the figure). Therefore, due to the transversal energy conservation (eq. 1.11), the angular variation is:

$$\Delta\alpha \simeq 2\sqrt{\frac{2U_{max}}{pv}} = 2\alpha_c \tag{1.37}$$

$\Delta\alpha$ gives the order of magnitude of the VR deflection angle ϕ_{VR} but it does not take into account two factors which contribute to slightly decrease its mean value:

- *the channel position in which the particle enters and leaves the crystal.* This effect can be appreciated considering the oscillations in fig. 1.38b: the points of maximum represent the points in which the particle is in the center of the channels, while the "valleys" represent the edge of two consecutive channels. If the starting and the end point of the trajectory are the center of

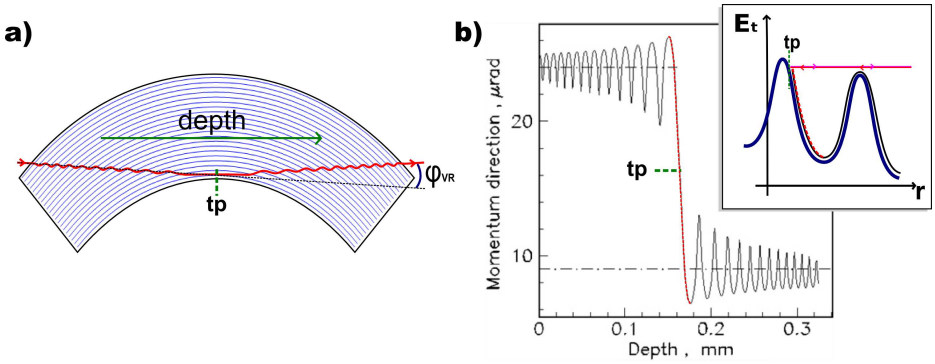

Figure 1.38: a) A detailed scheme of the volume reflection process inside a bent crystal: the particle oscillates while it is crossing the crystal planes. b) The same trajectory in the phase space of the deflection angle as a function of the position inside the crystal; the red line underlines the region in which the reflection takes place; this portion of the trajectory is also shown in the box representing the transversal energy-radius phase space.

the channels, the deflection angle will be larger than if they correspond to the edge of the channels. Since for a macroscopic (with respect to the plane scale) beam the distribution of the entrance and exit points in the channel is equiprobable, this effect produces a decrease of the ϕ_{VR} mean value and an increase of its spread.

- *the bending of the crystal that deforms the effective potential.*
  Computing $\Delta\alpha$, a variation of the transversal energy of $2U_{max}$ has been assumed; this is true only in the limit of $R \gg R_c$ (a crystal with a small curvature). Fig. 1.39 shows the reflection process in terms of the transversal energy in a crystal bent with a large curvature; the variation of the potential component of the transversal energy is $2U_{ref}$, a value between $2U_{max}$ and $2U_{min}$ (where U_{min} is given by eq. 1.28). Since $U_{ref} < U_{max}$, it turns out that $\phi_{VR} < 2\alpha_c$; moreover when a large number of particles is considered, U_{ref} will assume all the possible values producing a spread in the resulting reflection angle distribution.

A better estimation that takes into account all the possible trajectories and the crystal bending can be found in [53] giving $\phi_{VR} = 1.5\ \alpha_c$. This is an indicative average value, as the volume reflection angle depends on the bending radius. For this reason a study has been carried out to characterize the volume reflection behaviour as a function of the crystal curvature [58]. The test has been performed at 400 GeV/c with a silicon strip crystal (sec. 2.1.5) bent with different curvature radii.

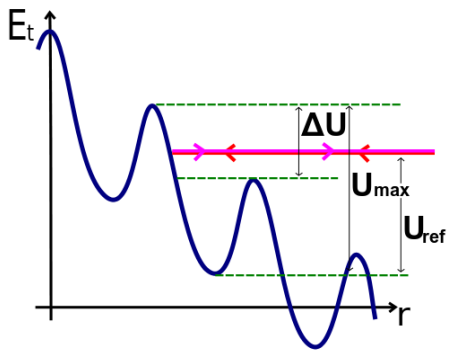

Figure 1.39: The interplanar potential in a crystal with a small bending radius. The volume reflection angle of the single particle, ϕ_{VR}, depends on the specific value of U_{ref} corresponding to the point in which the particle changes direction.

The results are presented in fig. 1.40:

- (a) the volume reflection angle ϕ_{VR} and its RMS (σ_{VR}) spread are plotted as a function of the bending radius. As expected, ϕ_{VR} increases with the bending radius because a lower deformation of the interplanar potential (see fig. 1.39) corresponds to a smaller curvature so that U_{ref} gets nearer to U_{max} increasing the average ϕ_{VR} angle; for the same reason ΔU becomes smaller thus reducing the RMS of the deflection angle distribution, σ_{VR}.

- (b) The volume reflection inefficiency: ε_2 represents the percentage of particles that are captured in the channel reaching its end (volume capture); ε_1 is the total VR inefficiency that adds to ε_2 the contribution of the particles that even being captured in the channel are immediately dechanneled. Both the curves linearly increase with the bending radius in agreement with eq. 1.36.

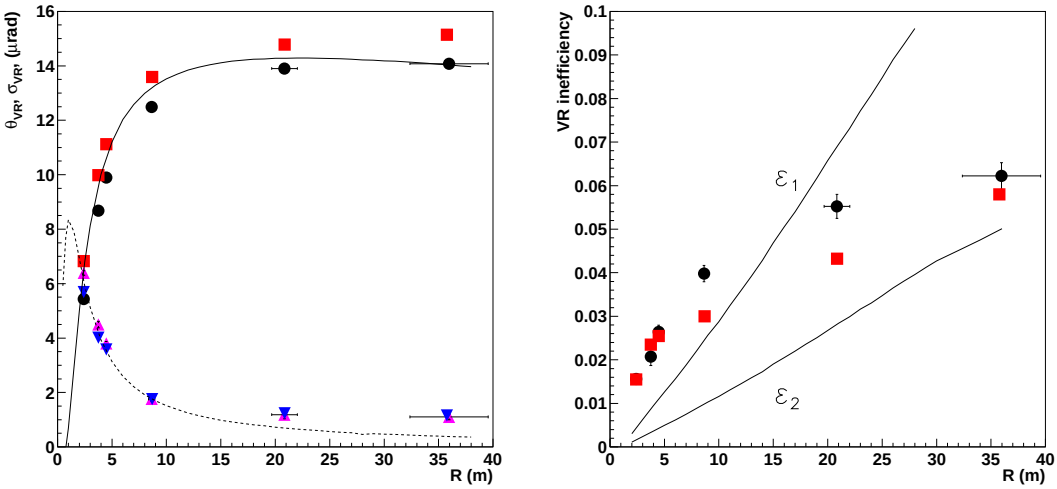

(a) (b)

Figure 1.40: a) The mean volume reflection angle ϕ_{VR} and its RMS σ_{VR} [58]: comparison between experimental data (black dots for the mean and pink triangles for the RMS), simulation data (red squares and blue triangles) and the analytical curves (continuous for the mean and dashed for the RMS). b) The volume reflection inefficiency [58]: comparison between experimental data (black dots), simulation data (red squares) and the analytical curve ε_1; the other curve, ε_2, represents the probability to enter in the stable channeling regime (volume capture).

Chapter 2

Bent crystal measurements

This chapter will review the state of the art of the experimental and analysis techniques used in the bent crystals studies. Its main goal is providing the reader with a complete overview on the method developed to characterize a bent crystal: from its assembly on the goniometer to the detailed analysis of its deflection features.

Sec. 2.1 will describe the different components of the experimental setup (the bent crystals, the detectors and the particle beam) showing how they have been integrated, during the past four years, optimizing the performances in terms of resolution, speed and versatility.

The data collected by means of the setup described in sec. 2.1 need a non trivial analysis to be exploited. The analysis procedure is presented in sec. 2.2, in which the methods developed to extract the interesting crystal parameters are applied to the bent crystals tested in various situations: energies ranging from 13 to 400 GeV with positive and negative particles.

2.1 Experimental setup

The setup used in bent crystal measurements is the result of a multi-stage process, that has registered a turning point in 2006 when, for the first time, the H8RD22 collaboration has used a real time system based on microstrip silicon detectors able to reconstruct the single particle track [59]. The previous channeling experiments, in fact, were based on beam profile integrated measurements to estimate the deflection angles and the efficiencies of the various crystal effects.
The single particle tracking introduced in 2006 has improved the resolution on the measured parameters and has allowed the angular information to be correlated with the impact position on the crystal surface.
The 2006 setup can be defined as a “half tracking system” as it measured the particle track only after the crystal crossing. In this section an improved “full tracking

system", that measures the particle trajectory before and after the crystal, will be described; the performances of this system in terms of resolution are very good (close to the physical limit of this kind of measurement) and the system itself allows a greater adaptability to the different beam conditions.
This section, starting from the basic concepts that guided the development of the setup, will provide a detailed description of all its components, concluding with the experimental procedure that goes from the crystal assembly to the high statistics data taking in the under-study angular position.

2.1.1 Basic concepts

The investigation of the bent crystal effects needs high precision angular measurements. These effects, in fact, are identified by relatively small deflections and occur for small angular acceptances, being their order of magnitude defined by the critical angle (α_c given in eq. 1.12) that, for example, is $\simeq$10 μrad at 400 GeV/c. The small angular acceptances require the use of an active alignment system to rotate the crystal; for this purpose precise goniometric systems are used as the one exploited in this setup which is described in sec. 2.1.2.
For what concerns the particles detection, two different strategies can be adopted:

- the first one needs an almost parallel and narrow beam, which means a divergence smaller than the critical angle and a dimension smaller than the crystal size. With such a beam the setup can be the one described in fig. 2.1a: the beam impinges on the crystal which rotates till it reaches the correct alignment; at this point the beam is split in different angular components which separate in space going farther from the crystal. If a position sensitive detector acquires the beam profile at the distance where the effects are separated, the crystal behaviour can be reconstructed.

- the second strategy can be applied even if the beam conditions are far from the ideal ones, that is a beam divergence larger than the critical angle and a beam dimension larger than the crystal one. The method is based on the capability to measure the single particle track before and after the crystal. This is described in fig. 2.1b: several position sensitive detectors determine the single particle position before and after the crystal so that it is possible to select the particles which impinge on the crystal with a certain angle and to compute the deflection produced by the crystal itself.

The second strategy (for a practical example see sec. 2.1.3) has two clear advantages with respect to the first one: 1) it is more versatile with respect to the beam conditions; 2) it is able to correlate the angular information with the

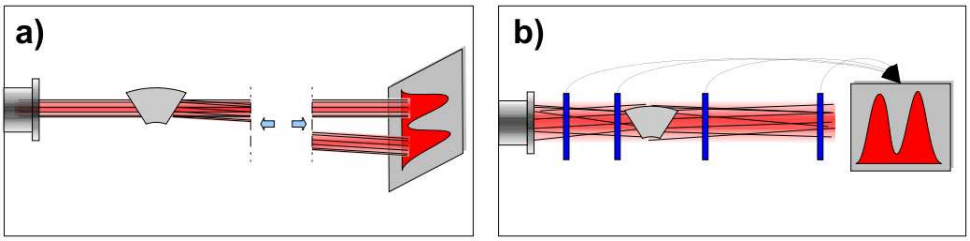

Figure 2.1: Schematic description of the two possible experimental setups for the crystal channeling measurements: a) it can be used if the beam is narrow and parallel (compared with the crystal dimension and angular acceptance); b) it is more complex from the detector point of view, being based on the track reconstruction but can be used also if the beam conditions are far from the ideal ones; in addition it is usually more compact.

impact point on the crystal, allowing to study the uniformity of the crystal behaviour, which in turn affects the crystal performances in terms of deflection (see sec. 2.2.1).

However, from the resolution point of view, that is the capability to distinguish the different crystal effects, both the setups present pros and cons. If the distance between detectors is large enough, the contribution of the intrinsic detector resolution can be neglected and the deflection angle resolution is determined either by the beam size and divergence (first case) or by the multiple scattering (second case). Even if the optimal measurement setup should be chosen on a test by test basis, it is clear that, since the multiple scattering increases linearly with the inverse of the energy, the tracking system strategy is not ideal at low energy.
To give an example, sec. 2.2.5 will show how the performances of a tracking system (designed to work in the hundreds of GeV range) worsen when it is used at about 10 GeV.
The conclusion is that to perform bent crystal measurements in the sub GeV range, the first strategy should be used. In this case the beam geometrical features, if necessary, could be modified, with adequate collimators [60].

2.1.2 The goniometer

The study of channeling phenomena requires a very accurate alignment system to orient the crystals with respect to the charged particles beam.
Furthermore, this alignment system should be remotely controlled by the DAQ (Data AcQuisition) and ensure a very good reproducibility, given that the crystal studies require first the investigation of wide angular ranges and subsequently high statistics data taking in the interesting angular positions (sec. 2.1.7).

The measurements described in this work use a high precision goniometric

system that, besides the angular alignment, is designed to allow the precise positioning of the crystal on the beam. It consists of different stages (as shown in fig. 2.2):

- a linear one to put the goniometer on the beam.
- a rotational one to align the crystal with respect to the beam on the horizontal plane.
- a second linear stage to put the crystal holder on the rotational axis.
- a second rotational stage (the craddle) to orient the crystal with respect to the axis direction.

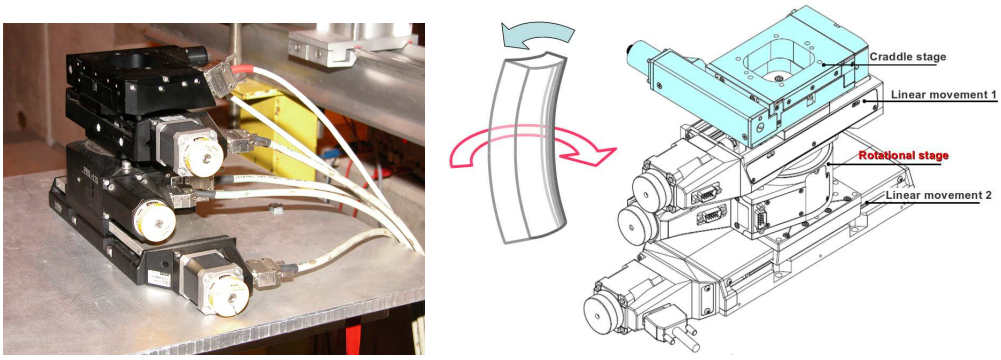

(a) (b)

Figure 2.2: b) A photo of the goniometric system during the operation on the H8 beamline. a) A schematic of the system.

All the stages are equipped with two-phase microstep motors and mechanical limit switches are integrated in the two linear stages. The control of the angular rotation is provided by an optical encoder and closed loop mechanism, which guarantees the required angular accuracy and repeatability. The goniometer is remotely controlled by the DAQ system and the motor positions are stored in the data file and in dedicated control files. The performances of the different stages are summarized in tab 2.1.

2.1.3 The full tracking system

As already mentioned in sec. 2.1.1, a “full tracking system” is a setup able to measure both the incoming and outgoing angle of the particle with respect to the crystal.

	Accuracy	*Repeatability*	*Resolution*	*Range*
Linear stage 2	1.5 μm	2 μm	5 μm	102 mm
Rotational stage	1 μrad	2 μrad	5 μrad	360°
Linear stage 1	1.5 μm	2 μm	5 μm	52 mm
Craddle stage	1 μrad	1 μrad	5 μrad	± 6 °

Table 2.1: Performances of the different stages of the goniometric system.

Fig. 2.3 shows the scheme of the setup on which this thesis work is based: $\mathbf{Ds}_{1-4}$ are double sided silicon microstrip detectors for the track reconstruction while $\mathbf{S}_{1-2}$ are the scintillators for the trigger.

The choice of the silicon microstrip detectors and in particular of double sided ones for the tracking has been determined by the following features:

- a good spatial resolution both in the horizontal and in the vertical direction, allowing to reach a high angular resolution with a compact system.
- a small amount of material in the beam direction, ensuring a limited multiple scattering contribution.
- the compactness of the detectors (readout by VLSI electronics) that allows the installation on different beamlines (sec. 2.1.6) without substantial changes in their layout.

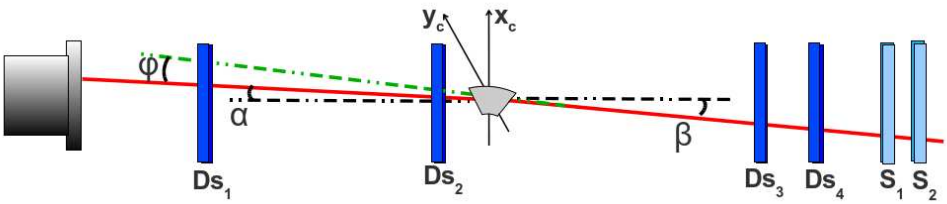

Figure 2.3: Scheme of the tracking system used for the crystal channeling measurements.

One of the four silicon microstrip detectors is shown in fig. 2.4. They have been originally developed by INFN Trieste [61]; each module (the box is 12×50 cm^2 and 4 cm thick) consists of a double sided silicon strip detector (1.92×1.92 cm^2, 300 μm thick) and its frontend electronics. The p-side of the detector has a p+ implantation strip every 25 μm and a readout pitch of 50 μm while the n-side (which is perpendicular to the p-one) has n+ implantation strips with a pitch

of 50 μm, separated by p+ blocking strips. Each silicon side is readout by three VA2[1] 128 channel ASICs (Gamma Medica-IDEAS, Norway), built with a 1.2 μm N-well CMOS technology. Each ASIC channel consists of:

- a low-noise/low power charge sensitive preamplifier.
- a CR-RC shaper.
- a sample & hold circuit.

The 128 output signals are multiplexed on a single output line with a maximum frequency for the readout clock of 10 MHz. The three ASICs are AC coupled to a CSEM[2] double side silicon detector with external quartz capacitors and are interfaced with the rest of the frontend electronics with a multi-layer ceramic hybrid.

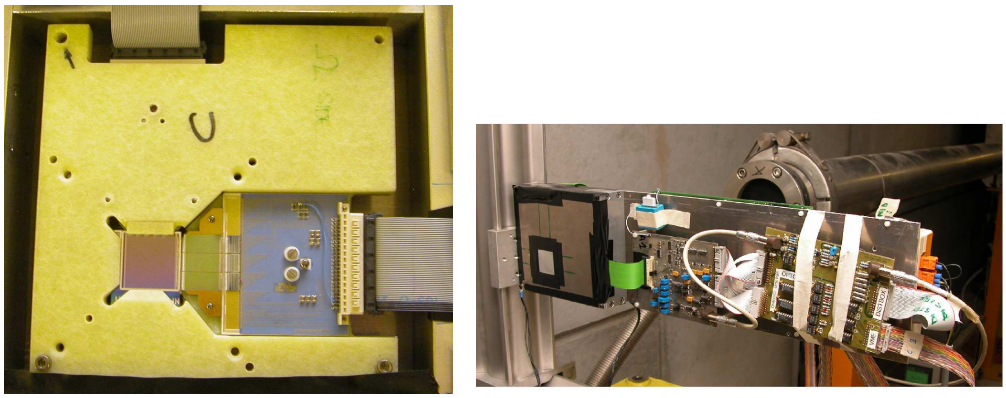

(a) (b)

Figure 2.4: Two photos of the double sided silicon detector: a) detail of the detector with the three VA2 ASICs connected to the ohmic side of the tile. b) The complete module, during its operation at the H8 beamline (CERN SPS, sec. 2.1.6).

Fig. 2.5 shows the distributions of the residual obtained on the CERN H8 beamline with a 400 GeV/c proton beam (see sec. 2.1.6) arranging the detectors one next to each other in order to evaluate their spatial resolution, minimizing the effect of the multiple scattering. The p-side, thanks to the presence of a floating strip, has a resolution of 6.4 μm which is better than the n-side one; therefore it has been used to measure the horizontal direction, the one in which the crystal deflection takes place. The n-side has a resolution of 10.5 μm.

The working principle of the setup presented in fig. 2.3 is the following: the first two silicon modules (**Ds**1-2) measure the incoming particle trajectory; this

[1] http://www.ideas.no/products/ASICs/pdf/VA2S2.pdf

[2] *Centre Suisse d'Electronique et de Microtechnique SA*, Rue Jaquet-Droz 1,CH-2002, Neuchâtel

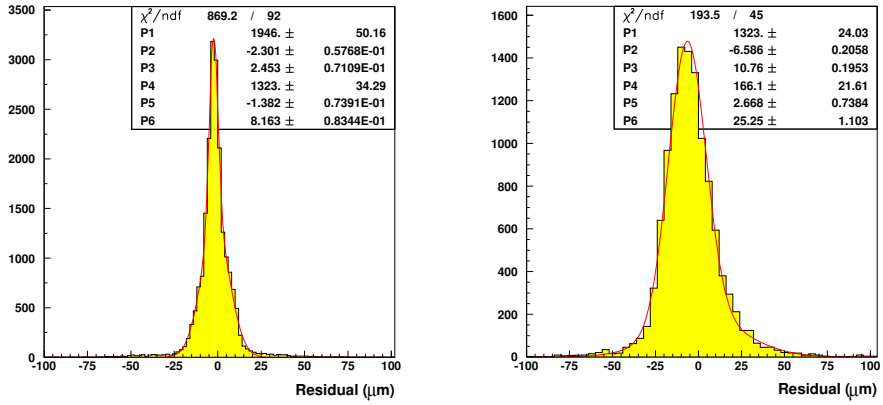

(a) (b)

Figure 2.5: The residual distribution of one of the silicon modules: the distribution is fitted with the sum of two gaussians; the average σ values (weighed on the gaussian areas) are 6.4 μm and 10.5 μm.

information allows to compute the position (x_c, y_c) on the crystal and the alignment (α) of the single particle with respect to the crystal; moreover, if integrated over a large number of particles, it provides the geometrical characteristics of the beam that is its dimensions and divergence (sec. 2.1.6).
Being the particle position at the crystal known, the **Ds**3 module allows to compute the outgoing angle (β) from the crystal and therefore the deflection angle ($\phi = \beta - \alpha$) produced by the crystal itself. The last silicon detector (**Ds**$_4$) is redundant: it measures the same information of **Ds**$_3$, thus averaging the two independent measurements the resolution can slightly improve. At the end of the line there are two scintillators whose coincidence generates the trigger for the tracking system.

The choice of a setup whose core is formed by only 3 detectors has been done to optimize the angular resolution, which is mainly determined by the multiple scattering that takes place in the material located between the first module and the last one. In this setup the material is mainly due to the central module (**Ds**$_2$), as the space between **Ds**$_1$ and **Ds**$_2$ and the one between the crystal and **Ds**$_3$ is "filled" by vacuum pipes to reduce the multiple scattering in the air.
To give an example, at 400 GeV/c on the H8 beamline, the detectors are mounted at a distance d of 10 m (fig. 2.6); if δx is the intrinsic resolution of one detector ($\sim$ 6.4 μm) (in the horizontal direction, see fig. 2.5a), the error propagation on the deflection angle (ϕ) will give an intrinsic resolution of $\sqrt{6} \cdot \delta x/d$, which means $\sim$ 1.6 μrad. If four detectors were used (fig. 2.6b), the intrinsic resolution on the deflection angle would be slightly better: $2 \cdot \delta x/d \simeq 1.3$ μrad. But taking into account the multiple scattering, the contribution of one silicon module (300 μm

of silicon) is about 1.5 μrad while it is about 2.2 μrad for two modules. Therefore, summing the two contributions, one concludes that the three module setup performs better than the four one; it should be also considered that 400 GeV is the maximum available energy and, since the multiple scattering increases at lower energy, the advantage of this setup becomes even more evident.

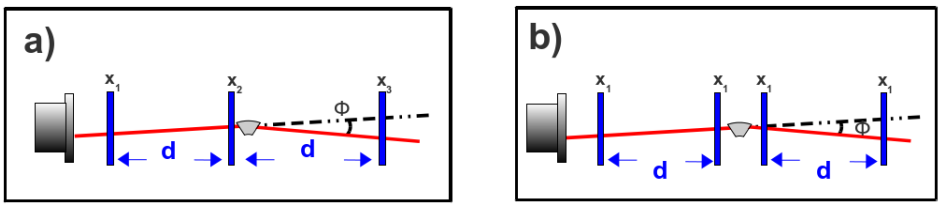

Figure 2.6: Schematics of two possible variants for a crystal channeling tracking system: a) with three detectors; b) with four detectors.

2.1.4 The DAQ

Fig. 2.7 shows the data acquisition chain that allows the operation of the elements described in the previous sections. The region enclosed by the dashed blue line contains detectors that have been used during the low energy measurement (sec. 2.2.5) and the radiation emission one (chap. 3). They are two large area silicon microstrip detectors (*silicon beam chambers*) and two electromagnetic calorimeters (*primary beam calorimeter*, sec. 3.2.1.2, and *γ-calorimeter*, sec. 3.2.1.3).

The system is based on the VME bus and the communication with the PC is provided by a SBS[3] Bit3 board, (a VME and a PCI one optically interlinked).
The DAQ software is written in C with Tcl/Tk[4] for the user graphical interface. The PC is also linked to the goniometer controller so that the DAQ program is able to move it and log the relevant information.

The trigger signals are generated by dedicated plastic scintillators in the deflection setup and by a combination of the scintillators and the primary beam calorimeter (sec. 3.2.1.2) in the radiation case. The signals are discriminated by NIM discriminators and sent to the VME trigger board (INFN Trieste). The trigger board is controlled by the DAQ program, allowing to choose the trigger mode (that can be the coincidence or the anticoincidence of the incoming signals) during the data taking.

[3]SBS Technologies, Inc., US.

[4]Tcl (Tool Command Language) is a dynamic programming language and Tk is its graphical user interface toolkit.

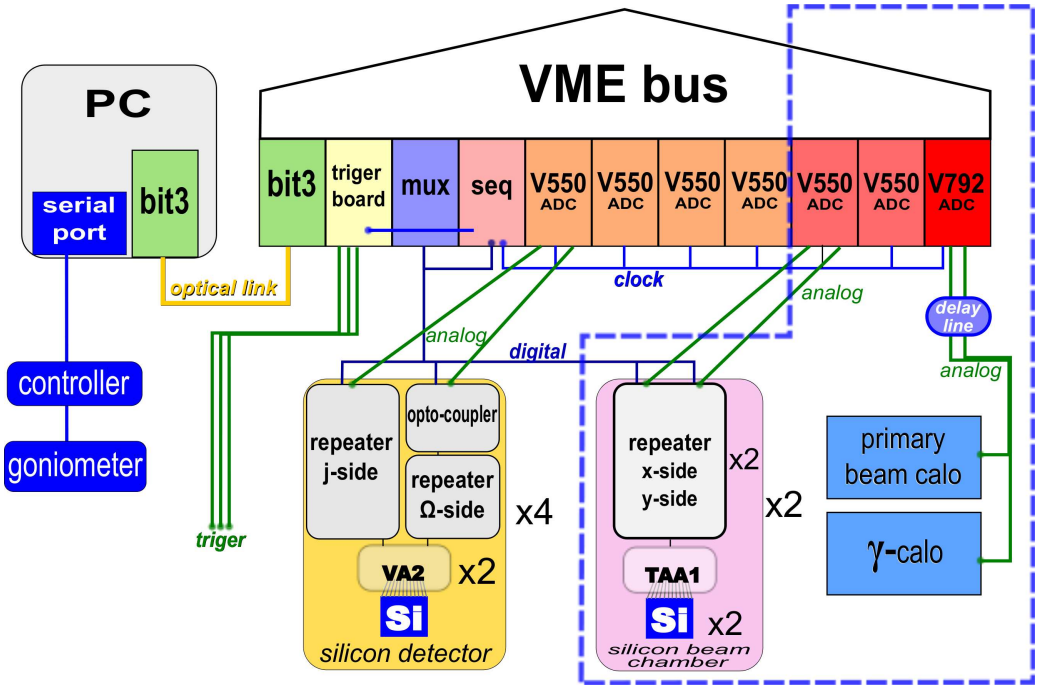

Figure 2.7: The DAQ chain; the elements inside the dashed blue line are not described in this section since they are not used during the high energy deflection measurements.

The resulting output trigger is sent to the sequencer (seq, INFN Trieste) that starts the DAQ sequence generating the ASIC control signals (carried out by a 16 pin scotchflex cable). Since the sequencer has a single output, a multiplexer (mux, INFN Trieste) is used to cope with all the modules, that are readout in parallel.
The interface between the frontend (the detector and the hybrid with the ASICs) and the readout (the VME board) is provided by the repeater boards that have the following tasks: to transform the RS422 differential signals to single ended ones as requested by the ASICs; to provide the bias, the power and the digital signals to the ASICs through 50 pin ERNI cables; to amplify the analog output of the hybrid.

The multiplexed analog output of the repeaters is digitized by the flash ADC boards (CAEN V550), which work in “zero suppression” mode: only the channels over a given threshold (set by the DAQ program) are readout, reducing the readout time.

The calorimeters are readout with an integrating ADC (CAEN V792) with 32 inputs; since their signals are very fast, a delay line is used to synchronize the signals themselves with the ADC gate which is generated by the trigger and starts $\sim$100 ns after the particle arrival.

The readout time is dominated by the transfer time from the VME to the PC that needs 5 μs (a VME cycle) per channel. If only the silicon detectors are used, about 300 μs per event are needed allowing to reach an acquisition rate of 3 kHz; when the silicon chambers and the calorimeters are readout, the time per event increases to 450 μs corresponding to 2.2 kHz.

2.1.5 The bent crystals

Two different types of crystals, characterized by a different bending technique, have been used in the measurements described in this work: the strip and the quasimosaic one. Fig. 2.8 shows a strip crystal (a) and a quasimosaic one (b) assembled on their holders.

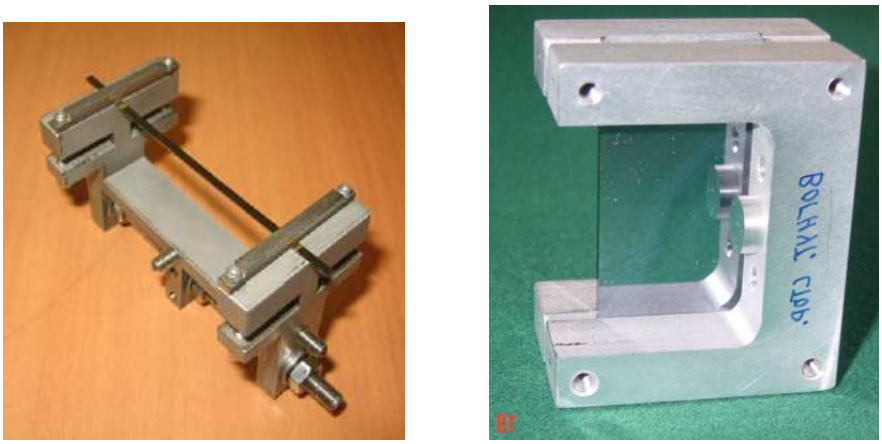

(a) (b)

Figure 2.8: Two examples of the crystals used during the experiment: a) a strip crystal; b) a quasimosaic one.

2.1.5.1 Strip crystals

The name strip comes from the shape of the crystal which is chosen to exploit the anticlastic curvature in order to obtain a uniform bending in the beam direction. Fig. 2.9a shows the curvature scheme of a strip crystal: a mechanical holder bends the strip (fig. 2.9b) along its major direction producing a primary curvature (indicated with P_c); the anticlastic forces generate a secondary curvature (indicated with A_c) which is used to deflect the charged particles. The silicon strips used in the experiment have been manufactured by the Sensors and Semiconductors Laboratory at Ferrara University [62] in collaboration with IHEP [63] (Institute of High Energy Physic, Protvino). The strip crystals are obtained dicing the silicon

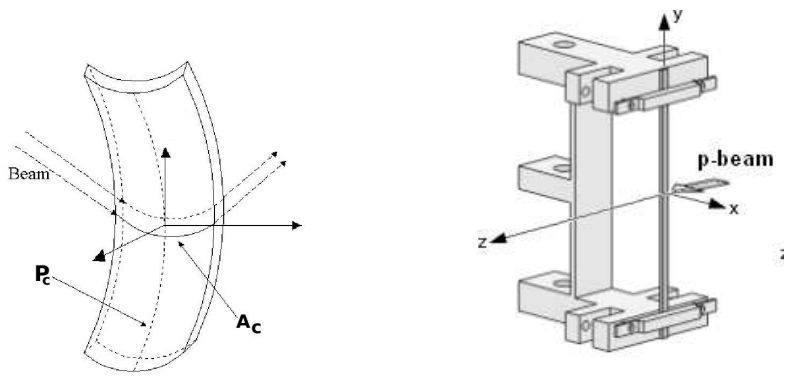

(a) (b)

Figure 2.9: a) The bending principle of the strip crystal (the arrows representing the beam follow the direction of the crystalline planes). b) A scheme of the strip crystal bending device (the crystal holder).

wafers with a fine grane-blade in order to induce minimal lattice damages; the residual lattice damage has been removed through wet isotropic chemical etching in acid solutions [64]. The surface characterization with the Rutherford Back Scattering technique in channeling mode demonstrated the quality of the etched surfaces [65].

2.1.5.2 Quasimosaic crystals

The second type of crystals has been prepared exploiting the elastic quasi-mosaicity effect. The crystals are built with the shape of small plates so that the (111) crystalline planes are normal to the large face of the crystal itself and parallel to its edges (as shown in fig. 2.10a). The bending device (shown in fig. 2.10b) exploits again the anticlastic effect: it is designed to bend the crystal in the *yz* plane conferring it the principal curvature (indicated with ρ in fig. 2.10b); the anticlastic forces produce a secondary curvature (indicated with ρ' in fig. 2.10b) in the *xz* plane which causes the quasimosaic curvature of the (111) atomic plane. The quasimosaic effect is due to the crystal anisotropy which depends on the selected crystallographic planes and on the orientation of the other crystalline direction with respect to the crystal plate. Fig. 2.11 shows the condition under which the quasimosaic effect takes place.

2.1.6 The beam

The data presented in this thesis work have been collected at CERN. CERN is the largest laboratory for high energy studies in the world; it is located in Geneva,

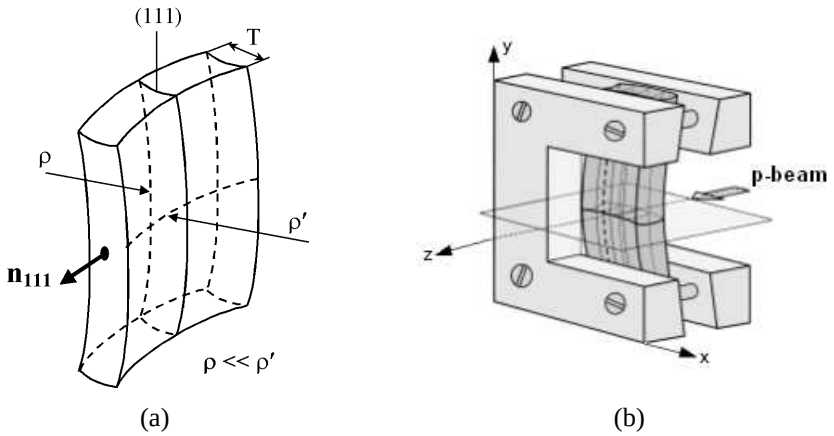

Figure 2.10: a) The bending principle of the quasimosaic crystal. b) A scheme of a quasimosaic crystal bending device (the crystal holder).

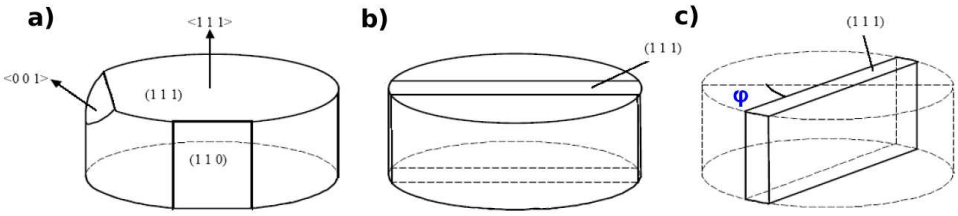

Figure 2.11: a) The silicon ingot before the cut with the interesting crystalline planes and axes indicated; b) a portion of the ingot to be cut is indicated; the corresponding crystal will not present the quasimosaic effect; c) if the cut is performed misaligned with respect to the (001) axis direction the quasimosaic effect will be present [66].

Switzerland and its main experimental structure is a wide complex of particle accelerators (fig. 2.12) able to provide many kinds of particle beams both to collider experiments and to extracted beamlines.

The tests described in this work have been performed on extracted beamlines: the **H8** and **H4** ones, located in the North Area experimental zone (fig. 2.12b) and the **T9** line, in the East Hall building.
The SPS accelerates the protons (actually it is also able to deal with ions and leptons) for the North Area, up to an energy of 400 GeV; this primary beam can be used directly or exploited to produce secondary beams of different particle kind and energy, using a combination of targets and magnets.
For what concerns the bent crystal characterization and the study of its different effects, the H8 line and the 400 GeV/c proton beam have been used. Although the geometric characteristics of the beam can slightly change in the different tests,

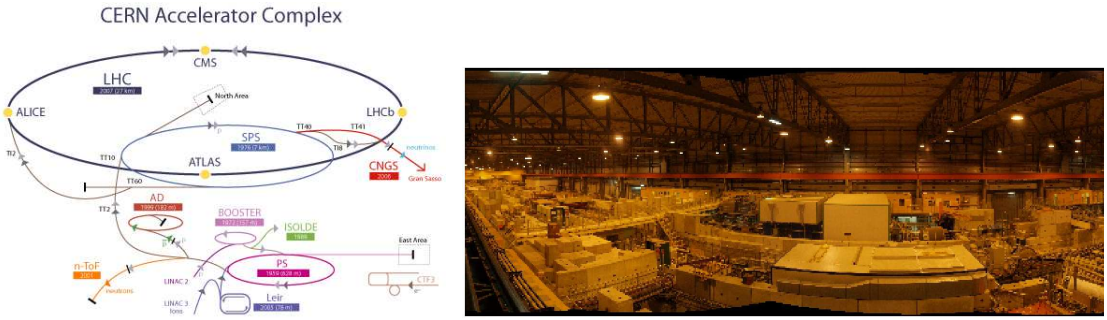

(a) (b)

Figure 2.12: a) The CERN accelerator complex: the beam for the measurements presented in this thesis has been provided by the PS and SPS accelerators. b) A photo of the North Area, the experimental zone in which most of the tests have been performed.

according to the different beamline settings, the beam dimension is in average 1 mm FWHM (in the horizontal and vertical plane) while the divergence is about 10 μrad RMS in both the directions; fig. 2.13 presents an example of the position and angular profile of the beam measured on the H8 line by the silicon tracking system, during a beam test in September 2009.

Even if the full tracking system described in sec. 2.1 allows the resolution of the measurements to be independent from the beam shape and divergence, a narrow and parallel beam is still preferable to maximize the statistics of good events. In this sense the quality of the H8 beam is good and, as it will be shown later, better than the H4 and T9 ones.

Concerning the H4 line, different kinds of beams have been used: a negative hadron one with an energy of 150 GeV and a light lepton one (electrons and positrons of 120 GeV/c) to measure the radiation emitted by bent crystals, as it is described in chap. 3.

On the other hand, the T9 line has been chosen to perform a test at lower energy; its injector, the PS accelerator, in fact, provides secondary beams generated by 24 GeV/c protons on a target with a resulting maximum energy that depends on the beamline. For the tests with the bent crystal, a hadron beam (of both positive and negative particles) with a momentum of 13 GeV/c has been used. Fig. 2.14 presents the geometric characteristics of this beam and in sec. 2.2.5 the procedure and the obtained results are summarized.

2.1.7 The experimental procedure

The standard experimental procedure to analyze a crystal is the following:

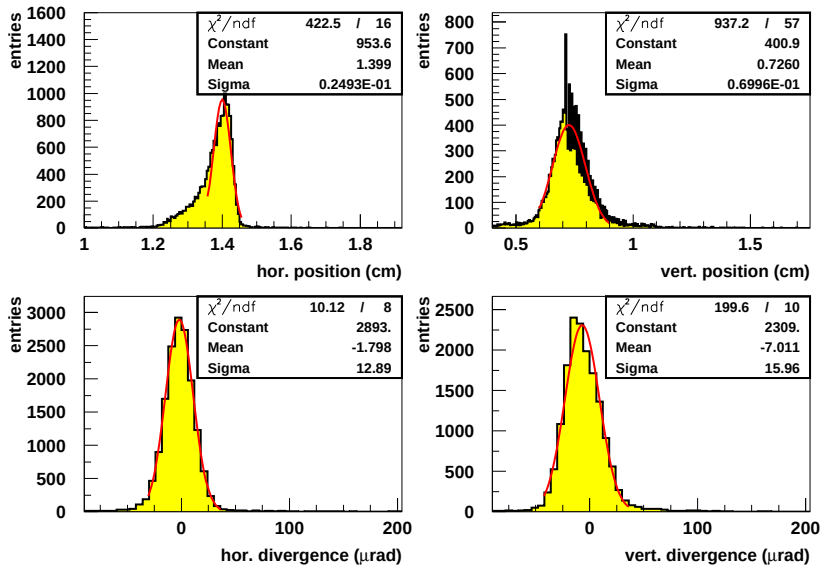

Figure 2.13: The 400 GeV/c proton beam measured on the H8 beamline: top) the beam profiles; bottom) the beam divergence; on the left the horizontal direction and on the right the vertical one.

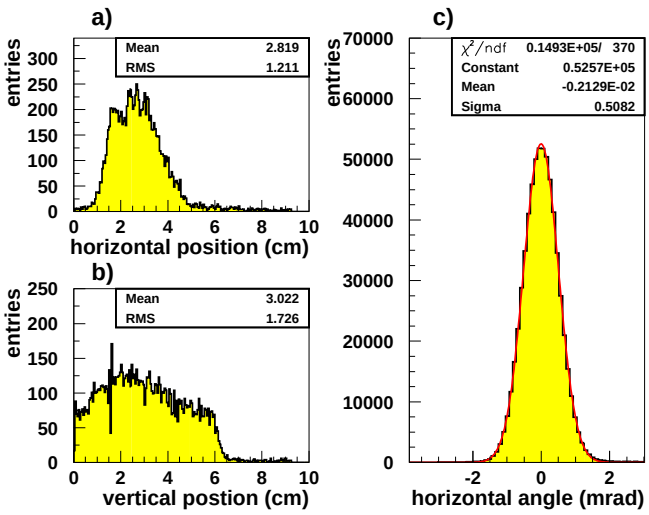

Figure 2.14: the T9 line: a-b) the beam profile; c) the horizontal beam divergence (0.5 mrad).

- the crystal is mounted on its holder and then on the goniometer.
- the crystal is pre-aligned with a laser beam (the procedure is described in fig. 2.15) with a precision of about 300 μrad.
- the crystal is placed on the beam trajectory with a lateral scan performed with the transversal movement of the goniometer acquiring data with the tracking system; the position of the crystal with respect to the beam can be inferred from its multiple scattering, as shown in fig. 2.16.
- since the critical angle is usually smaller than the precision of the laser prealignment, a fast angular scan with low statistics and large angular steps (one half of the channeling deflection angle is enough to observe the volume reflection) is performed, as shown in fig. 2.17.

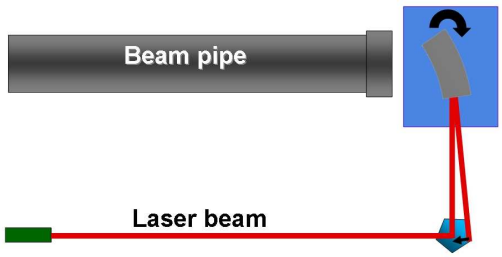

Figure 2.15: The laser pre-alignment technique: a laser beam is aligned with respect to the beam pipe and projected at 90° towards the crystal surface with a pentaprism; the crystal reflects the laser beam so that rotating it with the goniometer, once the incoming and the reflected beam overlap, the crystal is perpendicular to the proton beam; at this point a 90° rotation of the crystal aligns it for channeling.

Once the position and the orientation of the crystal with respect to the beam are known, the crystal is centered on the maximum of the beam profile to maximize the number of particles which cross the crystal itself over the total number of acquired events. At this point the crystal can be oriented in the desired position to acquire statistics.

2.2 Single crystal characterization

The setup and the experimental techniques described in the previous section have allowed an important step forward in the bent crystal studies field.
On one hand it has allowed to exploit beam conditions far from the ideal ones, making the measurement result independent from them; on the other one it has shown a lack of homogeneity in the crystal bending (the torsion, sec. 2.2.1) that explained the measured channeling efficiencies which were lower than the ones expected by theory.

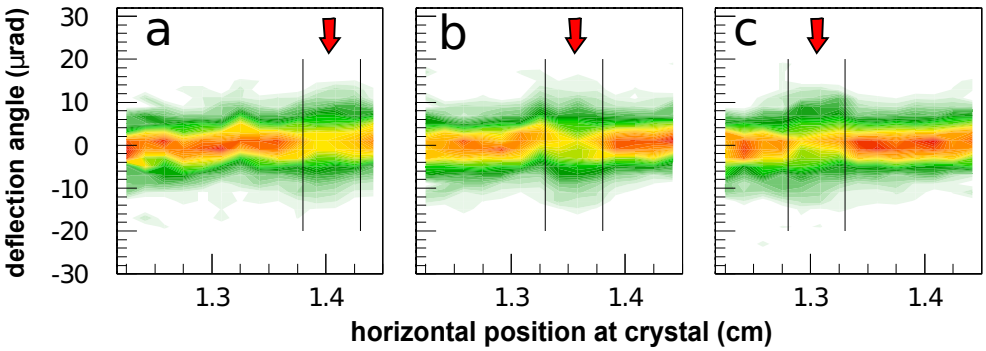

Figure 2.16: An example of a lateral scan performed moving a strip crystal (0.5 mm wide and 2 mm thick in the beam direction) in steps of 0.5 mm: from **a** to **c** the crystal is moving from the right to the left side of the beam profile (horizontal axis); it is recognizable since it increases the deflection angle due to multiple scattering.

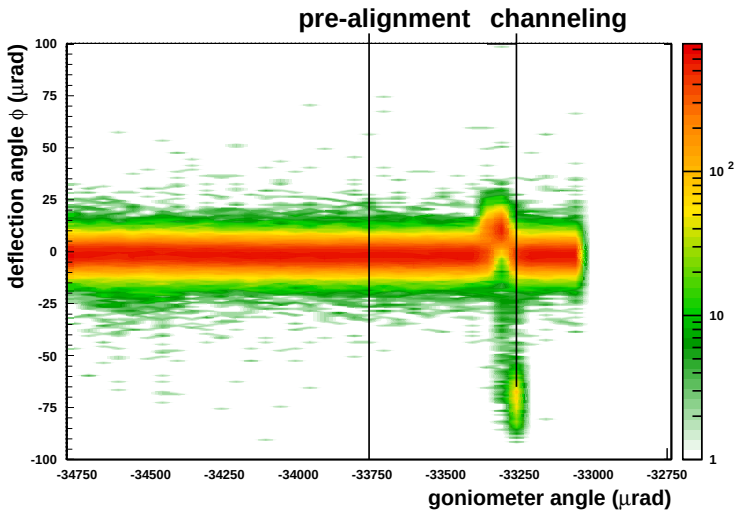

Figure 2.17: An example of a fast angular scan with the silicon telescopes; the channeling position (perfect alignment) is 500 μrad from the pre-alignment one. Once the channeling is found the run is stopped to start the large statistics data taking in the interesting positions.

This section will present an overview of the analysis methods used to characterize bent crystals oriented in planar condition.
Starting from the channeling effect (sec. 2.2.2) and the VR one (sec. 2.2.2), the interesting parameters, such as the deflection angle and efficiency, will be given at different beam energies (till the lower value of 13 GeV, sec 2.2.5) for positive and negative particles (sec. 2.2.4).

2.2.1 The crystal torsion

The crystal torsion is a deformation that characterizes both the quasimosaic crystal and the strip one. It consists of a rotation of the crystal along its vertical axis, originated by the non parallelism of the upper and lower part of the holder that bends the crystal, as schematically shown in fig. 2.18.

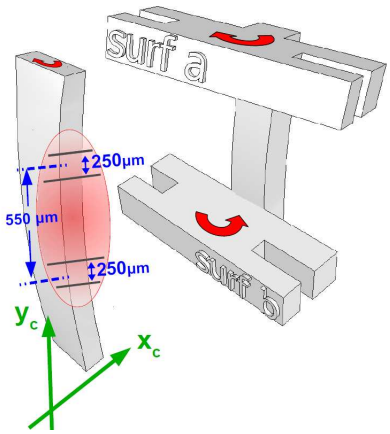

Figure 2.18: Schematics of a crystal holder that twists a strip crystal. The torsion is originated by the lack of parallelism of the surfaces (*a-b in the scheme*) which block the crystal. In front of the holder there is the strip (detached from it to make the scheme clearer); the red ellipse represents the beam; two 250 μm high horizontal slices at a distance of 550 μm are indicated.

The lack of parallelism of the holder surface depends on its mechanical imperfection which produces an asymmetric deformation when the holder itself is bent; therefore the torsion of the crystal is more evident in a crystal with a small curvature.
The torsion implies that the orientation of the crystal changes as a function of the local vertical impact position (y_c in fig. 2.18) of the beam. This is shown in fig. 2.19 where the result of a planar crystal scan is presented in two plots filled with the statistics of two 250 μm high horizontal slices at a distance of 550 μm from each other (schematically shown in fig. 2.18). The two plots are similar but shifted with respect to the horizontal axis that represents the orientation of the crystal: the position of the channeling peak in fact differs of 100 μrad.
Given that the distance between the slices is 550 μm, the crystal has an average torsion of 18.2 μrad/mm.

The crystal torsion can have a relevant impact on the performance of the crystal itself, either if the beam has a significant vertical dimension or if it presents a

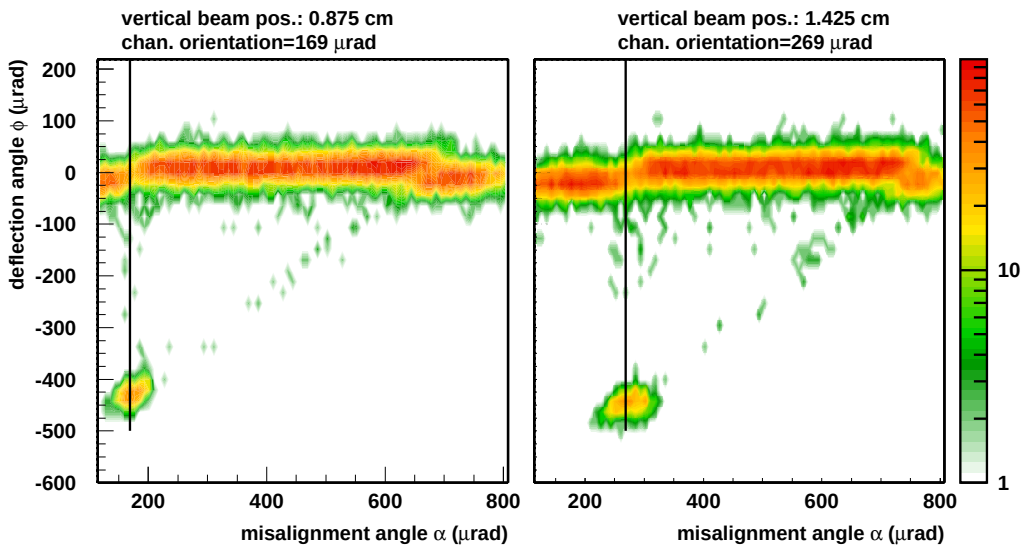

Figure 2.19: The planar scan of a strip crystal performed on the H4 line with a 120 GeV/c positron beam: the two plots are obtained selecting the particles crossing the crystal in two 250 μm high horizontal slices at a distance of 550 μm. The two plots are similar, apart from a horizontal shift due to the torsion of the crystal.

certain instability in the vertical position (in other words it moves during the run), for the following reasons:

- the channeling efficiency can appear much smaller than the nominal one. As shown in fig. 2.20, if the beam is extended in the vertical direction, the selection of a quasi parallel beam portion still corresponds to an integration over a wide alignment range; if the crystal is twisted, this means that the real number of particles aligned for channeling is small.

- if the beam changes its vertical position, the crystal operation changes in the same way as it happens when the crystal is rotated, thus producing an unpredictable behaviour, which may be a serious problem for several applications, such as beam extraction and collimation; in both of them in fact the efficiency and the direction of the extracted beam should be kept under control.

- the crystal characterization and the investigation of some peculiar axial effects (chap. 4) could become more difficult, as the torsion produces a mixing of the different orientations.

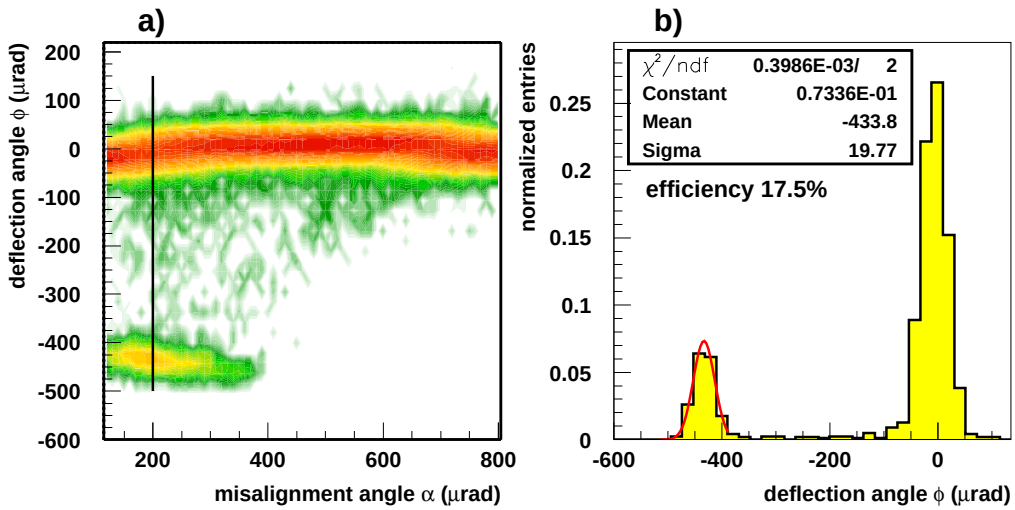

Figure 2.20: a) Same scan of fig. 2.19 but integrated over the whole beam: the transition between the amorphous and the volume reflection condition as well as the channeling acceptance are spread with respect to the horizontal axis due to torsion. b) The best channeling condition (marked with a line in the (a) plot); the channeling efficiency (17.5%) is very small due to torsion.

As mentioned above, the crystal torsion represents a problem in the crystal characterization mainly because the results obtained in these studies would be related with a beam condition that can change. A way of overcoming this problem is to select (off-line) a region of the beam (a horizontal slice) so thin that the influence of the torsion becomes negligible. This simple strategy is often used during the data acquisition but at the expense of statistics. Therefore during the analysis phase an alternative method has been developed computing a variable (α*), that represents the local alignment between the crystal and the particle: given that the torsion is constant along the vertical direction of the crystal (as it will be shown in fig. 2.22), the local alignment is:

$$\alpha^* = \alpha + (y_c - \bar{y}) \cdot t \tag{2.1}$$

where α is the standard misalignment (that is the sum of the goniometer angle and the incoming particle one), y_c is the vertical position on the crystal, $\bar{y}$ is the mean position of the beam (vertical direction), t is the torsion coefficient (for example 18.2 μrad/mm for the crystal of fig. 2.20). Fig. 2.21 shows how the same plots of

fig. 2.20 appear as a function of α* instead of α.

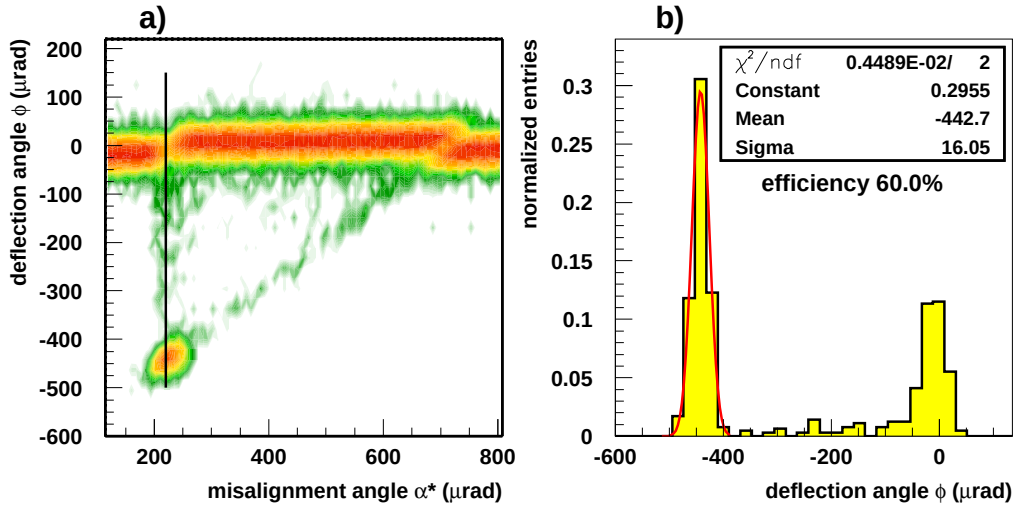

Figure 2.21: This figure is the equivalent of fig. 2.20 but with the torsion compensated via software. The separation of the different deflection effects is clearer (a) and the channeling efficiency corresponding to the best alignment is larger (b).

The compensation of the torsion operated via software is useful to study and characterize bent crystals, but obviously does not resolve the problems (of stability and low efficiency) connected with the applications. For this reason a procedure to straighten the twisted crystals has been developed.
The first step is a fast evaluation of the torsion: it requires just a single data acquisition in channeling and the evaluation of the deflection angle as a function of the vertical impact position on the crystal (y_c), as shown in fig. 2.22a. The histograms are filled with an almost parallel beam portion ($|\alpha|<1.5\mu$rad); if the crystal were straight, the angle of the channeling peak in this plot would be independent from y_c; if the crystal is twisted, the plot turns out to be equivalent to an angular scan, in which the misalignment angle is $\alpha = y_c \cdot t$, where t is the torsion coefficient. The trend of the channeling peak with respect to y_c (fig. 2.22) is linear and can be fitted with the following function:

$$\phi_{ch} = par2 \cdot y_c + par1 = par2 \cdot (\alpha/t) + par1 \tag{2.2}$$

where $par1$ and $par2$ are the fit parameters.
Considering an angular scan (scatter plot of ϕ vs α, fig. 1.3), the channeling peak

trend as a function of α is $\phi_{ch} = \alpha + const$. Combining the two equations: $\phi_{ch} = par2 \cdot (\alpha/t) + par1$ and $\phi_{ch} = \alpha + const$, it turns out that $par2/t = 1$, so that $par2$ gives the torsion coefficient t.

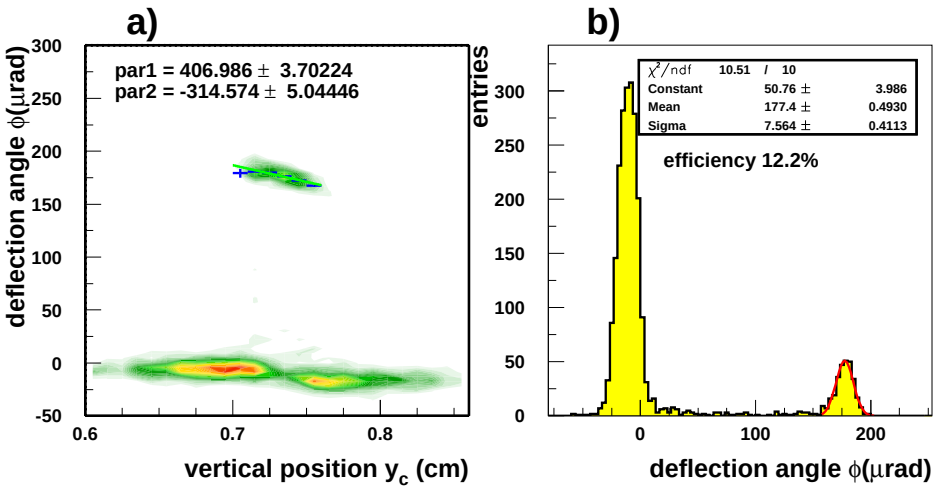

Figure 2.22: a) A fast method to evaluate the torsion of the crystal: the deflection angle is plotted as a function of the vertical position; the slope of the channeling peak measured with a linear fit gives the torsion coefficient, in this case 31.5 μrad/mm. The fit is performed on the profile histogram of the channeling peak superimposed on the contour plot. b) Confirming the large torsion coefficient, the channeling efficiency is very small: 12.2%.

Once the torsion is measured it can be corrected (fig. 2.23) acting on a screw which deforms one of the holder surfaces making it parallel to the other one; a laser impinging on the crystal surface and the goniometer give a feedback that allows to perform a precise deformation (the procedure is similar to the one used in the crystal prealignment, fig. 2.15).

Fig. 2.24 shows the result of a new torsion measurement on the same crystal of fig. 2.22 but after the torsion correction; as expected, in the left side plot no correlation between the deflection angle and the vertical position is present ($par2 \sim 0.95\mu$rad/mm) and the channeling efficiency is much larger reaching a value of 72.6%.

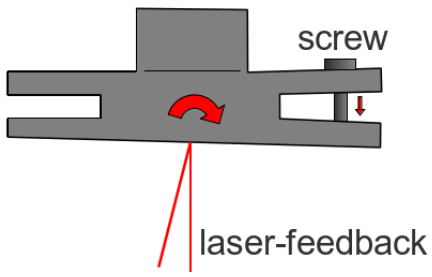

Figure 2.23: Schematic view of the upper part of a crystal holder; rotating a screw, one of the surfaces that block the strip is deformed to compensate the torsion. The rotation amplitude is measured with a laser.

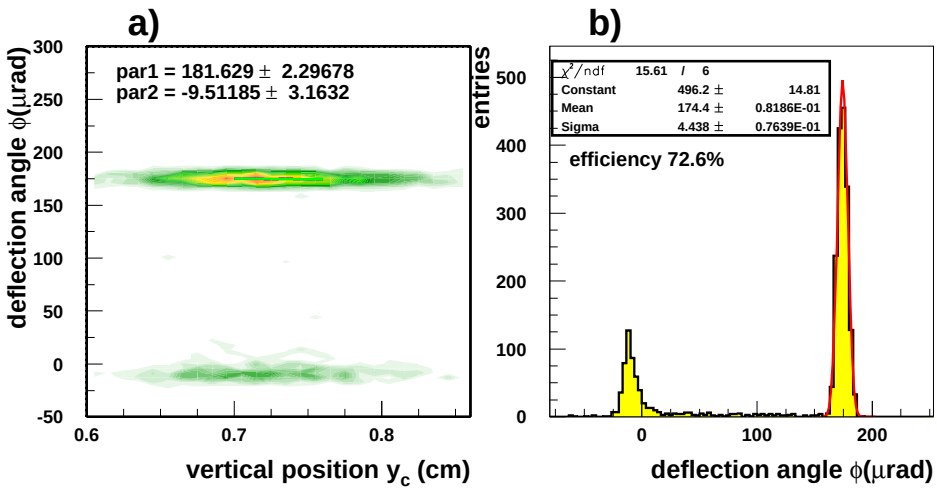

Figure 2.24: The equivalent of fig. 2.22 but after the torsion correction, whose residual value is just 0.95 μrad/mm; the channeling efficiency (72.6%) is much larger.

2.2.2 Channeling

The study of the planar channeling effect is important for two reasons: 1) even though many interesting alternative phenomena are being studied (chap. 3), channeling still represents the most concrete possibility for an application (such as beam extraction and collimation); 2) channeling allows the single crystal characterization in terms of crystalline quality (the channeling efficiency) and bending features (the precise measurement of the torsion and of the bending radius). For this reason each bent crystal study (including the ones addressed to the axial effect and the radiation emission) should start from the planar channeling investigation of which this section is a compendium.

The crystal used as a prototype in the following analysis has a strip shape with a length of 1.94 mm in the beam direction; it is bent along the (110) plane and it is 0.5 mm wide (fig. 2.25). The data have been taken on the H8 beamline with a 400 GeV/c proton beam (sec. 2.1.6).

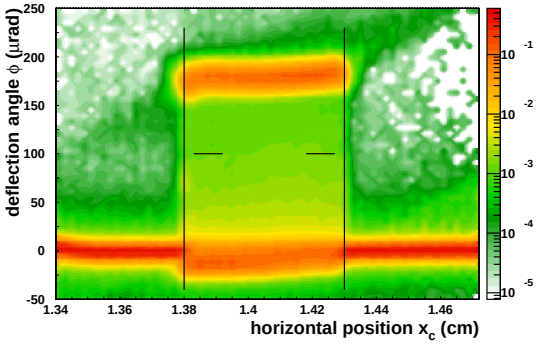

Figure 2.25: The deflection angle as a function of the horizontal position at the crystal coordinate. The presence of the crystal (0.5 mm wide) is underlined by the beam portion in channeling, shifted at $\phi \sim 180$ μrad. In the following analysis only the events in the region 1.385 cm$<$ $x_c < 1.415$ cm are considered.

The left side plot of fig. 2.26 shows the deflection angle ϕ as a function of the local misalignment one[5] α^*, near the channeling orientation. In the right side of the figure, two deflection angle profiles (corresponding to α^* =-5 μrad, bad alignment, and to α^* =1 μrad, good alignment) are shown to describe the fit procedure that allows the analysis of the channeling effect: the channeling peak and the undeflected beam are fitted with gaussian functions, while the region between them (dechanneling) with an exponential function.
Since the scatter plot in fig. 2.26-left has been normalized, its vertical slices, as a function of α^*, have been rescaled to have an integral equal to one. In this way the area of the gaussian function, that fits the channeling peak, directly represents the percentage of channeled particles for a given orientation α^*; this is shown in the top plot of fig. 2.27. The central part of this plot has been fitted with a parabolic function in order to obtain the following information on the channeling phenomenon:

- the maximum value of the channeling efficiency, corresponding to an almost parallel beam, perfectly aligned with the crystal. It is represented by the vertical position of the parabola vertex: in this case it is 75.2$\pm$0.1 % which is a value compatible with the theoretical one (sec. 1.3.3); this result represents a great achievement, indicating that the quality of the crystal is really close to the ideal one.

[5]computed taking into account the crystal torsion (sec. 2.2.1) that has been measured to be 5 μm/mm (which is the residual value after the hardware correction of the torsion, performed before the high statistics data taking).

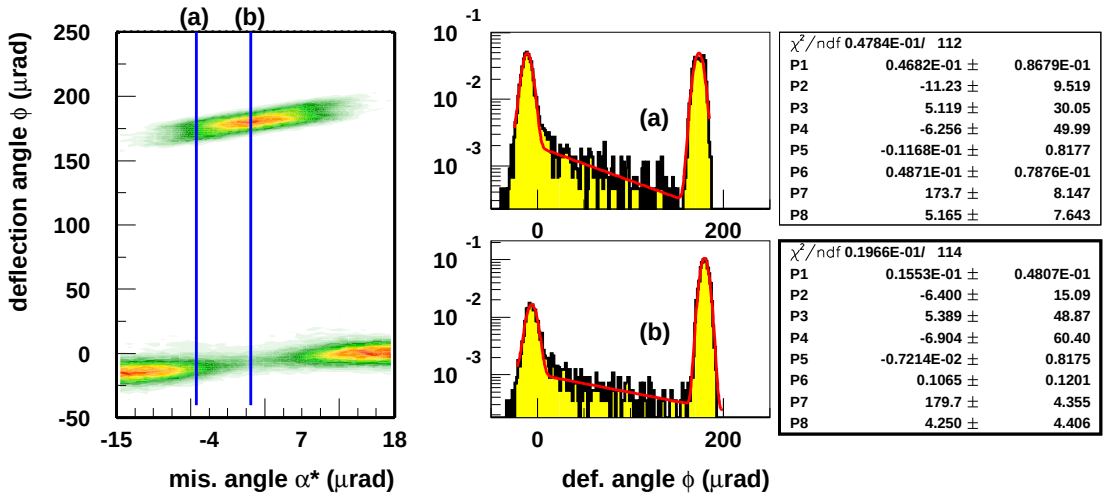

Figure 2.26: left) The deflection angle as a function of the local misalignment; the two blue lines correspond to the angular profiles shown on the right side of the figure; they are fitted with two gaussian and one exponential function.

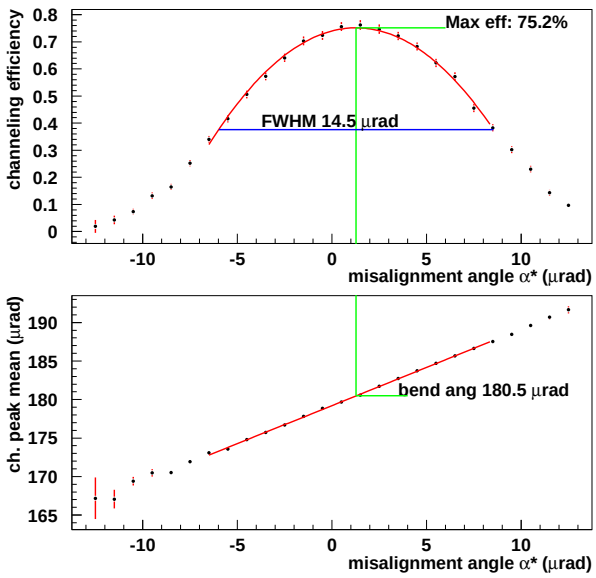

Figure 2.27: top) Channeling efficiency as a function of the angular alignment; the fit with a parabolic function identifies the maximum channeling probability that is 75.2% and also the best alignment orientation, exploited in the bottom plot (the mean channeling position as a function of α^*) to compute the crystal bending angle that is 180.5 μrad.

- the α^* orientation corresponding to the perfect alignment of the crystal, identified by the horizontal coordinate of the parabola vertex, α^* =1.28 μrad. This information is necessary to compute the channeling angle ϕ_c; in the bottom plot of fig. 2.27, the mean position of the channeling peak as a function of α^* is presented: the value 180.5±0.1μrad is the one corresponding to the perfect alignment. To be precise, this value should be compared with the position of the undeflected beam (outside the crystal) that depending on the detector alignment can differ from zero. In this case it is -1.63±0.01 μrad, so that $\phi_c = 182.1 \pm 0.1$ μrad. Given that the crystal length is l =1.94 mm, the crystal bending radius $R = l/\phi_c = 10.65 \pm 0.01$ m can be computed.

- the channeling angular acceptance: the FWHM of the curve has been chosen to evaluate the angular acceptance that is 14.5 μrad. According to the theory, channeling should not be possible in the region $\alpha^* < -\alpha_c, \alpha^* > \alpha_c$ but this cutoff is not sharp in the plot (because of the finite resolution on the α^* measurement). Therefore the angular acceptance curve is not the ideal method to evaluate the critical angle α_c, whose measurement will be described later in this section.

The sum of the channeling probability with the one of not being deflected is not equal to one, because of the particles that being dechanneled are in the region between the channeling peak and the "undeflected" one. For this reason the dechanneling probability is $P_{dc} = 1 - (P_{ch} + P_{un})$, where P_{ch} represents the channeling probability (given in fig. 2.27-top) and P_{un} the probability to be non deflected (computed as the integral under the "unchanneled" peak and shown in fig. 2.28). The bottom plot of fig 2.28 represents the dechanneling probability as a function of α^*. It is interesting to note that this probability is not constant with respect to α^*: its value is small for small and large α^* values (in the regions where the channeling probability is very small), it grows for intermediate α^* values (following the increase of the channeling probability) and then it decreases again, approaching the best alignment condition where it becomes about 10%. This reduction depends on the average value of the transversal energy of the channeled particles that, being small for a quasi perfect alignment, keeps the particles trajectories in the central region of the channel far away from the nuclei. This phenomenon can be interpreted as a confirmation of the hypothesis that the dechanneling in a short crystal depends on the interaction with the nuclei and thus acts only on the large transversal energy channeled particles.

It is also possible to measure the nuclear dechanneling length exploiting the information from the fits presented in the right side of fig. 2.26, where the dechanneling region is fitted with an exponential function. The "average lifetime" τ_α of this function is an angular value but, knowing the crystal length l and its bending

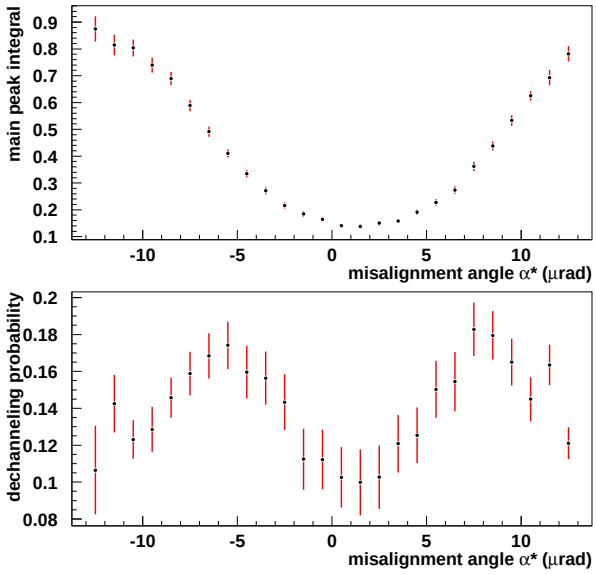

Figure 2.28: top) The portion of events under the "undeflected" peak as a function of α^*. bottom) The dechanneling probability as a function of α^*, corresponding to the events which are neither in the channeling peak (fig. 2.27 top) nor in the undeflected one (top plot of this figure).

angle ϕ_c, it can be converted in a length: $\tau_l = \tau_\alpha \cdot l/\phi_c$. Fig. 2.29 presents the result of this operation; the obtained average value for the nuclear dechanneling length is 1.68 ± 0.08 mm that is in good agreement with the one computed in sec. 1.3.2.1 and in [52].

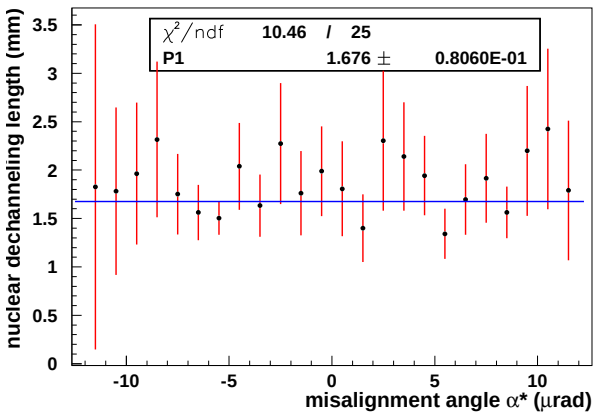

Figure 2.29: The nuclear dechanneling length as a function of the misalignment α^*. No defined trend can be recognized taking into account the experimental errors, thus the points are fitted with a constant function that returns an average value of 1.68 ± 0.08 mm.

If the shape of the channeling peak is observed in detail (fig. 2.30) a double peaked structure can be recognized for α^* values far from the best alignment condition: this is a macroscopic manifestation of the interplanar potential.
A particle in channeling with a misalignment $\alpha^* \sim \alpha_c$ should have a transversal

energy $E_t \sim U_{max}$; once it is captured, it will oscillate from side to side in the channel, changing its direction from 0 μrad (edge of the channel) to α_c (center of the channel) as schematically shown in fig. 2.31. When such a particle leaves the channel, it will assume the deflection given by the crystal bending plus a contribution given by the oscillation, ranging between 0 μrad and α_c. Although the precise value depends on the position of the particle, when it leaves the crystal the average value will be $0.5 \cdot \alpha_c$.
Two possibilities must be considered: if the oscillation takes place towards the external side of the crystal (increasing r, green trajectory in fig. 2.31) its contribution should be added to the deflection, whereas if it is towards the internal side of the crystal (red trajectory in fig. 2.31) it should be subtracted. Thus the channeled particles are divided in two deflected populations at an angular distance of α_c.

These two populations form the two peaks, that are fitted with the sum of two

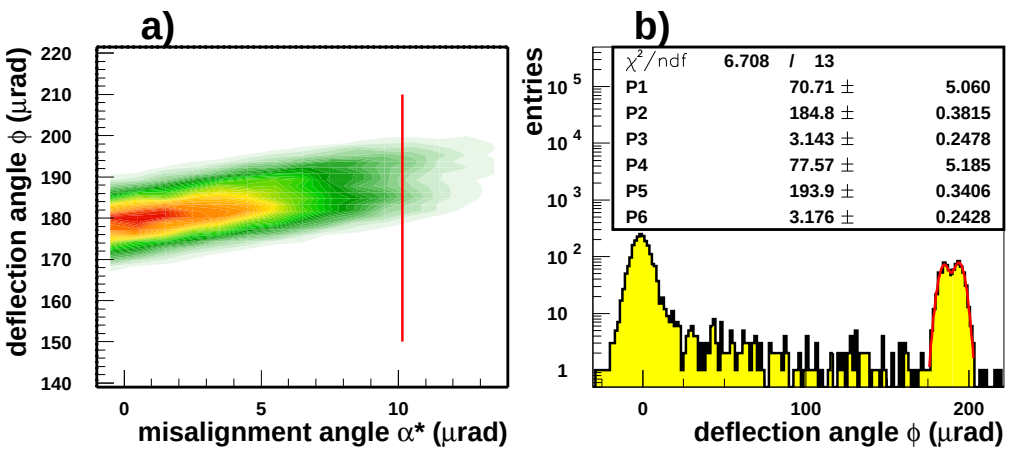

Figure 2.30: a) A detail of the channeling peak as a function of the misalignment angle α^*; in the region $\alpha^* > 7$ μrad, a double peaked structure can be seen. The red line indicates the profile of the deflection angle ϕ shown in the right plot; the channeling peak is fitted with the sum of two gaussian functions obtaining a distance between the means of 9.1±0.5 μrad which is a measurement of the critical angle α_c.

gaussian functions in fig. 2.30; the distance between their mean values is a measurement of the critical angle $\alpha_c = 9.1 \pm 0.5$ μrad. Inverting eq. 1.12, the maximum value of the interplanar potential is obtained, $U_{max} = 16.6 \pm 1.8$ eV, in agreement with the value given in sec. 1.3.2 for a silicon crystal aligned along the (110) plane.

Since the particle deflection through the oscillation in the channel should be

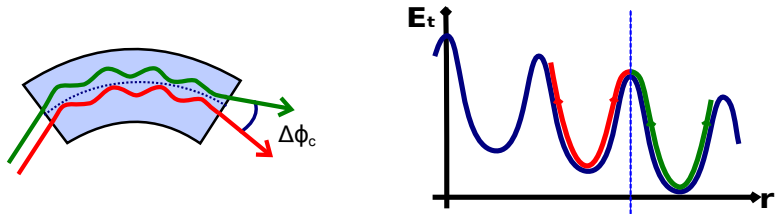

Figure 2.31: Two possible trajectories of large transversal energy channeled particles ($\alpha^* \sim \alpha_c$) in the laboratory reference frame (left side) and in the transversal energy - radius phase space (right side). The deflection angle is influenced by the oscillations in the channel providing a contribution that on average can be $\pm 0.5\alpha_c$, originating a separation of $\Delta\phi_c = \alpha_c$.

present also in straight crystals, this effect can be used to identify the channeling orientation (measuring the deflection angle) also in this case, in which the effect of bending is absent[6].

Fig. 2.32a presents the channeling effect (deflection angle ϕ as a function of the local misalignment α^*) at the energy of 120 GeV; the data were acquired on the H4 beamline (sec. 2.1.6) using a positron beam. Comparing this plot with the equivalent one taken at 400 GeV (fig. 2.27) the most visible difference is the broadening of the peaks, mainly due to the increase of the multiple scattering, that worsens the system resolution.

Fig. 2.32 shows the result of the analysis performed at 120 GeV obtained with a series of fits (like the one shown in fig. 2.26); the (b) plot presents the percentage of the beam in channeling as a function of the local misalignment α^*: this percentage reaches a maximum value of 66.7±11.4%. This value is smaller than the one recorded at 400 GeV and the one predicted by theory because of the increase of the multiple scattering contribution, that limits the efficiency with which the selection of the local misalignment angle α^* can be performed.

The horizontal blue line represents the FWHM of the parabolic function, whose value (28.8 μrad), following the trend of the critical angle α_c, is larger than the one recorded at 400 GeV (14.5 μrad); eq. 1.12, that defines α_c, provides a ratio $\alpha_c(120)/\alpha_c(400)$ =1.83 while the experimental value results to be slightly larger (1.99). This again depends on the multiple scattering and on the incoming angle selection.

Fig. 2.32c presents the mean position of the channeling peak as a function of α^*. The deflection angle $\phi = 170.8$ μrad, identified by the best alignment in

[6]The two peaked structures will appear superimposed to the un-channeled beam; therefore if the crystal is thin (low multiple scattering) channeling could be identified.

the top plot, allows to compute the channeling angle $\phi_c = 186.49 \pm 3.9$ μrad (a value obtained taking into account the detectors offset, -15.69 ± 0.01 μrad). The corresponding bending radius is 10.72±0.22 m.

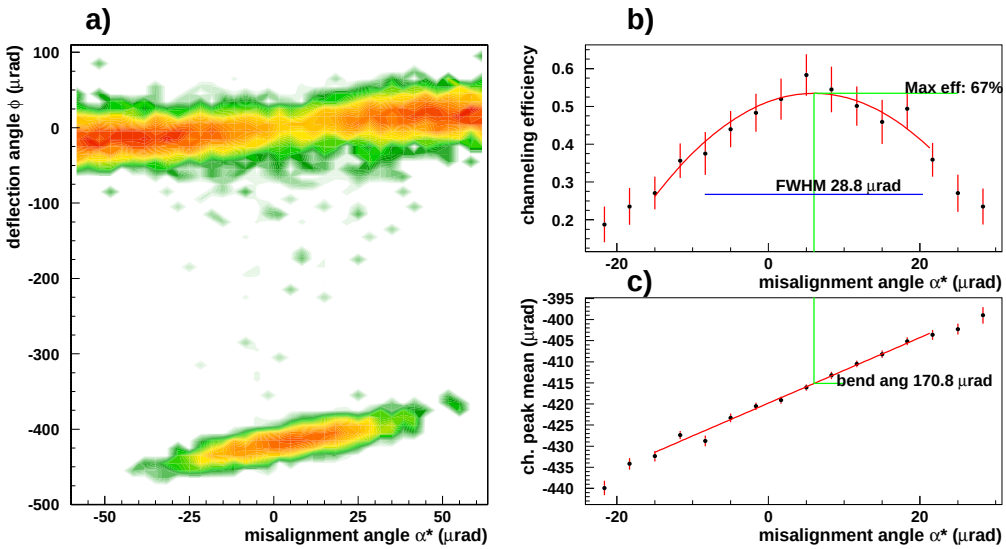

Figure 2.32: a) The deflection angle as a function of the local misalignment α^* in the channeling orientation at the energy of 120 GeV. b) Channeling efficiency as a function of the alignment; the fit with a parabolic function identifies the maximum, that is 66.7±11.4% and the best alignment. c) Mean channeling position as a function of α^*; the channeling peak angle, corresponding to the maximum efficiency, is 170.8±3.9 μrad.

2.2.3 Volume reflection

This section will describe the experimental characterization of the volume reflection effect at the energies of 400 and 120 GeV. The crystals are the same ones analyzed during the channeling characterization, in the previous section[7].
Fig. 2.33 shows the deflection angle as a function of the horizontal position with the crystal aligned in volume reflection: both the beam shift towards negative ϕ values (volume reflection) and the region filled with particles at $\phi \sim 60$ μrad (volume capture) are visible. The two plots on the right side of the picture compare the angular profiles in volume reflection (a) and without the crystal (b); the distributions are fitted with gaussian functions whose mean values distance gives the

[7]They are silicon strip crystals 0.5 mm wide and respectively 1.94 and 2 mm long for the one tested at 400 GeV and the one tested at 120 GeV. They are oriented along the (110) plane. The bending radii measured in sec. 2.2.2 are: 10.65 ± 0.01 m (400 GeV) and 10.72±0.22 m (120 GeV).

volume reflection angle $\phi_{VR} = 13.13 \pm 0.02$ μrad; this value is in good agreement with the one provided by theory (fig. 1.40a).

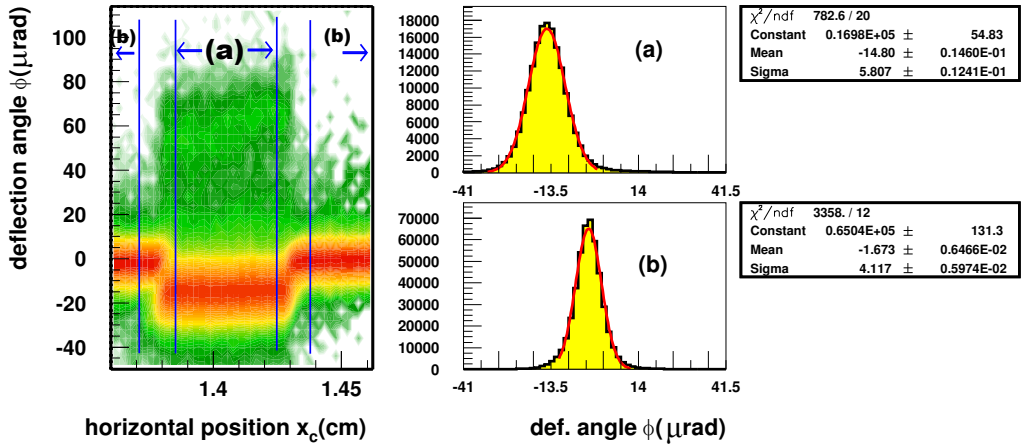

Figure 2.33: Left) The deflection angle as a function of the horizontal position; the crystal, aligned in volume reflection, is identified by the beam shift towards negative ϕ values. Right) The angular profile of the deflection angle: a) in volume reflection (region marked with (a) in the left plot); b) undeflected beam, outside the crystal (region marked with (b) in the left plot). The volume reflection angle $\phi_{VR} = 13.13 \pm 0.02$ μrad is given by the distance between the mean values of the two gaussian functions which fit the (a) and (b) angular distributions.

The same events, represented in fig. 2.33(region-(a)) are shown in the right side of fig. 2.34 as a function of the local misalignment α^*; this zoom provides a better identification of the volume capture region, whose average deflection angle depends on α^*. It is interesting to note that, as it happens for the channeling effect at large α^* angles (fig. 2.30), a double peaked structure can be recognized in the volume capture pattern.
The red lines in fig. 2.34a indicate the volume capture effect; the percentage of events contained in this slice gives the volume capture efficiency: 1.16±0.03%, a value in agreement with the theoretical one given in fig. 1.40b (ε_2 trend). This percentage does not represent the whole volume reflection inefficiency, since it is composed just by the particles that are captured and reach the end of the crystal in channeling without being dechanneled. Since the dechanneling probability for a captured particle is very large (these particles have a large transversal energy and thus they cross regions with a large nuclear density[8]), the contribution of this

[8]This has been experimentally verified for the channeling effect; as it is shown in fig. 2.28 the dechanneling probability grows for large misalignment angles α^*.

effect on the reflection efficiency is not negligible. For this reason the volume

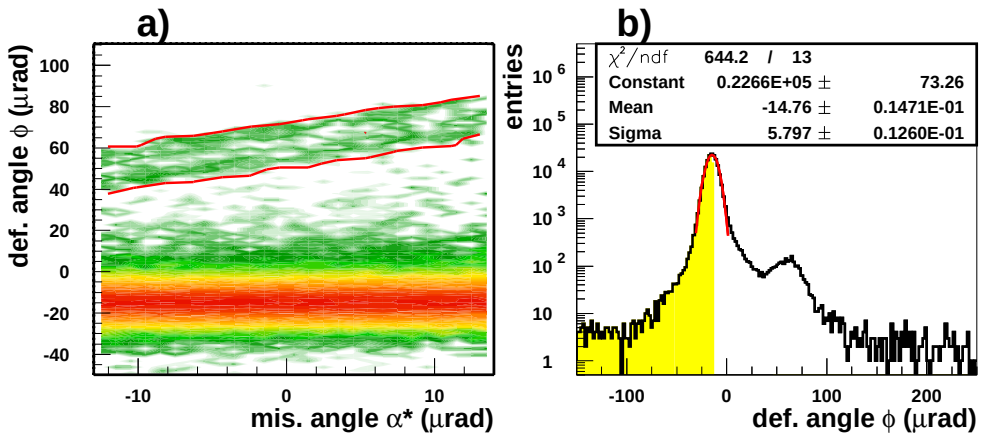

Figure 2.34: a) The deflection angle as a function of the local misalignment; the two red lines indicate the volume capture region (1.16±0.03% of the events). b) The deflection angle profile (all the events of the left plot) shown in logarithmic scale to make the volume capture peak visible; the region marked in yellow goes from $\phi = -\infty$ to the mean value of the main peak.

reflection efficiency has been estimated in a different way counting the number of events in the region $\phi < \phi_{VR}$ (given that the dechanneled particles fall on the opposite side of the distribution); these events represent half of the volume reflected particles. Doubling the number of events in the yellow histogram of fig. 2.34b the VR efficiency can be obtained, resulting to be 97.60±0.24 %. The VR inefficiency (2.4±0.24 %) should be compared with the ε_1 trend in fig. 1.40b; also in this case there is a good agreement.

The same kind of analysis has been performed at the energy of 120 GeV: fig. 2.35 shows the deflection angle as a function of α^* (a) and the corresponding profile (b). The mean deflection angle of the undeflected beam in this case is -15.69 ± 0.01 μrad, therefore the volume reflection angle is ϕ_{VR}=26.9±0.22 μrad. Due to the lower statistics and the worse resolution with respect to the 400 GeV case, it is not possible to effectively separate the volume capture events from the other ones; for this reason the volume capture probability has not been computed, while, selecting the events on the left side of the VR peak, the volume reflection efficiency has been measured to be 94.43±0.24 %.

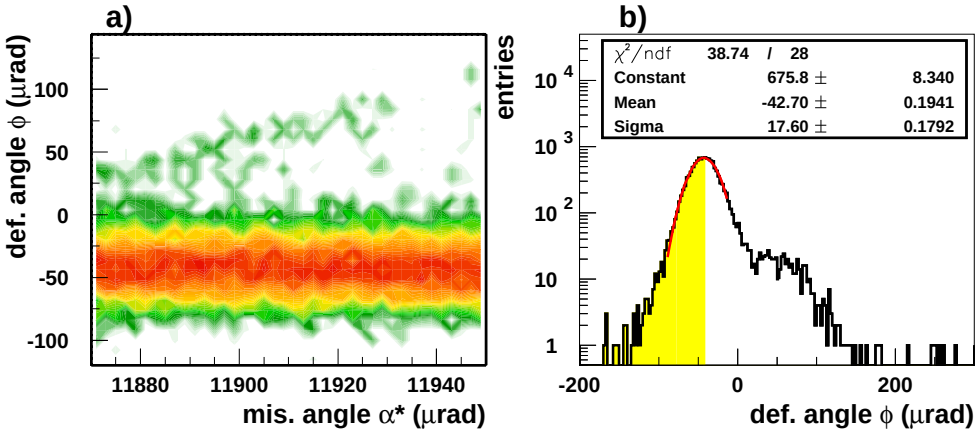

Figure 2.35: a) The deflection angle as a function of the local misalignment at 120 GeV. b) The deflection angle profile (all the events of the left plot) shown in logarithmic scale to make the volume capture peak visible; the region marked in yellow goes from $\phi = -\infty$ to the mean value of the main peak.

2.2.4 Negative particles

The coherent interaction of a negatively charged particle with bent crystals is different with respect to the positive particles one: a negative particle, in fact, being attracted by the crystalline planes where the nuclei are located, deals with an effective potential that is reversed with respect to the one felt by positive particles (fig. 2.36).
According to this, the potential wells that trap particles in channeling are located in the middle of the crystalline planes for a positive particle (fig. 2.36a) and across them for the negative ones (fig. 2.36b). In this way a negative channeled particle will travel in a crystal region with a large nuclear density, in which the large nuclear scattering probability does not allow a stable channeling condition.

In other words, although the bounded channeling state for negative particles is allowed, the dechanneling length is much shorter than for the positive ones[9]. For this reason it is practically not possible to obtain the full deflection of a negative particle in long crystals using channeling and thus, up to now, the coherent interaction between negative particles and bent crystals has not been investigated

[9]The reference is to the L_{De} electron dechanneling length (sec.1.3.2.1) that characterizes the motion of positive particles in stable channeling.

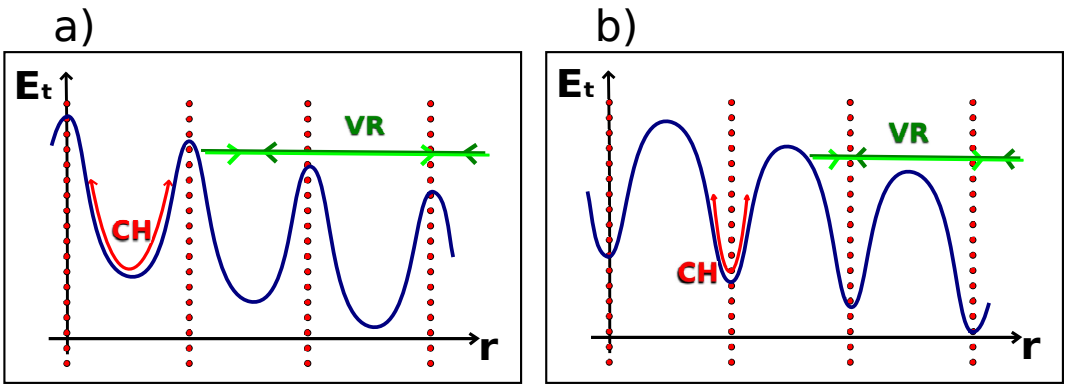

Figure 2.36: The effective potential in a bent crystal (transversal energy as a function of the radial coordinate) for positive (a) and negative (b) particles. The channeling trajectory (CH) and the volume reflection one (VR) are described by the red lines and the green ones.

in detail.

In the last years, the introduction of new bending techniques (sec. 1.3.3) that made short bent crystals available, together with the discovery of new deflection effects such as volume reflection (sec. 1.3.4.2) that have a lower dependence on dechanneling, have renewed the attention on negative particles.

This section presents the analysis performed on a silicon strip crystal 2 mm long in the beam direction, oriented along the (110) plane[10] mounted on the H4 beamline to be studied with a 150 GeV/c negative hadron beam (mainly π^- mesons).

Fig. 2.37 shows the result of a goniometer scan of the strip crystal, presented both in normal (a) and logarithmic scale (b) to underline the different deflection effects (channeling, dechanneling, volume reflection and volume capture) that are clearly identifiable.

Comparing this result with its equivalent positive particle one (fig. 1.3, acquired at a similar energy, 120 GeV/c, with an almost identical crystal) several differences can be listed: the channeling efficiency results to be very low while both dechanneling and volume capture are more pronounced; moreover, the volume reflection deflection angle is smaller.

To evaluate the deflection parameters of the crystal, two deflection angle profiles have been extracted from fig. 2.37. They correspond to the best channeling alignment (fig. 2.38a) and the middle of the VR angular region (yellow histogram in fig. 2.38b).

[10] It is similar to the crystals investigated in sec. 2.2.2 and 2.2.3 with positive particles of 400 and 120 GeV.

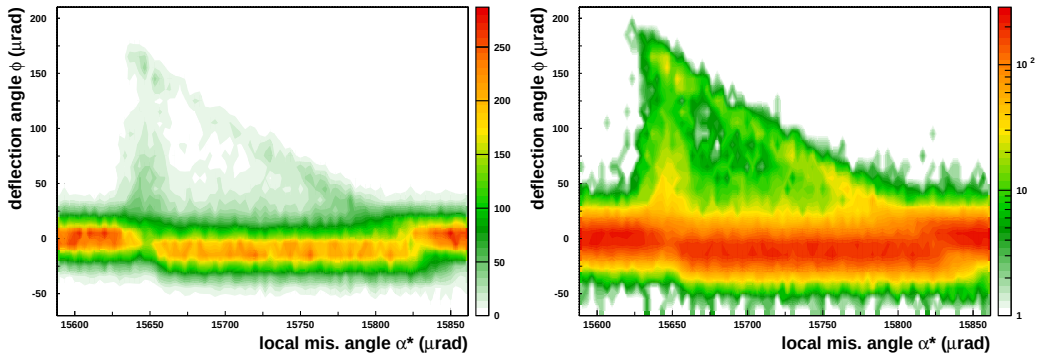

(a) (b)

Figure 2.37: Goniometer scan of the 2 mm strip crystal with 150 GeV/c negative particles in normal (a) and logarithmic scale (b). The scatter plots present the deflection angle ϕ as a function of the local misalignment α^*, computed after the torsion measurement (sec. 2.2.1), that has given a result of ~ 36 μrad/cm.

The angular profile in channeling (fig. 2.38a) shows how the channeling peak is reduced by the dechanneling increase, with respect to the positive particles case (fig. 1.5a). The plot has been fitted with the sum of two gaussian functions and an

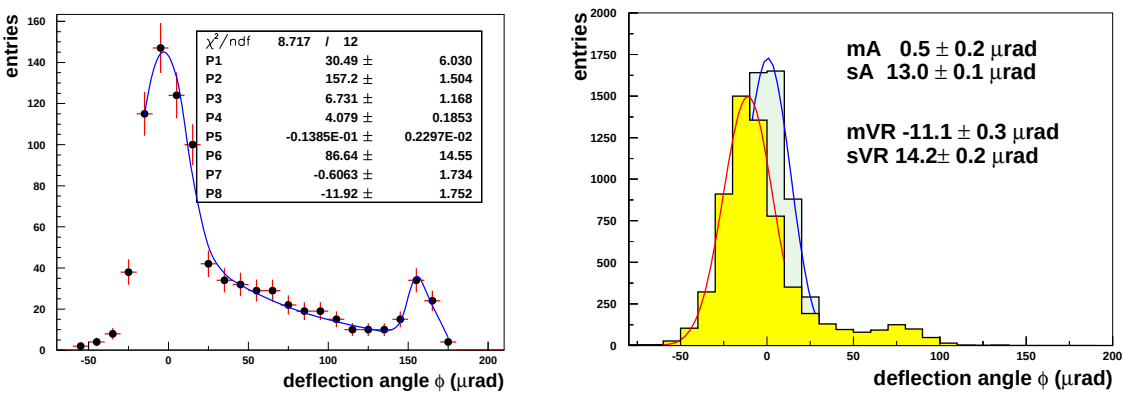

(a) (b)

Figure 2.38: a) The deflection angle profile corresponding to the channeling maximum efficiency; the plot has been fitted with the sum of two gaussian functions and an exponential one. b) The deflection angle distribution: in the middle of the VR acceptance (yellow histogram) and in the amorphous orientation (grey one).

exponential one, taking into account the different components of the distribution; the fit parameters allow to compute the following quantities:

- *channeling angle and bending radius.*
  The channeling angle ϕ_c is given by the difference between the channeling peak mean value ($P2$, fig. 2.38a) and the amorphous one (mA, fig. 2.38b); it is $\phi_c = 157.7 \pm 1.5$ μrad. According to this value, if $l = 2$ mm is the crystal length, the bending radius is $R = \phi_c/l = 12.7 \pm 0.1$ m.

- *channeling efficiency.*
  It is given by the integral of the gaussian that fits the channeling peak (number of channeled particles, $N_{ch} = 51.4 \pm 13.5$) divided by the whole statistics contained in the plot ($N_{tot} = 886$), resulting to be 5.8±1.52%.

- *dechanneling length.*
  It is given by the exponential slope ($P5^{-1}$, fig. 2.38a[11]) rescaled by the channeling angle and multiplied by the crystal length, as already done for positive particles (fig. 2.29). The resulting value is $D_{lneg} = \dfrac{l}{\phi_c \cdot P5} = 0.92 \pm 0.15$ mm. Given the dechanneling length is approximately proportional to the energy, D_{lneg} results to be close to the positive particles value ($D_{lpos} = 1.68 \pm 0.08$ mm at 400 GeV, fig. 2.29). However, it should be noted that D_{lpos} refers to the *nuclear* dechanneling length that concerns only the channeled particles with a large transversal energy (sec. 1.3.2.1) while D_{lneg} (determined by the nuclear interactions as well) characterizes the motion of all the channeled particles. For this reason, the dechanneling lengths are similar but the negative particles dechanneling probability is larger.

- *dechanneling probability.*
  The number of dechanneled particles can be computed integrating the exponential function which fits the dechanneling region between zero and the ϕ_c channeling angle. The integration gives 378.7±94.2 events, that correspond to a dechanneling probability of 42.7±7.4%. This value proves that using a shorter crystal it would be possible to increase the channeling efficiency. In fact, during the same H4 beam test a channeling efficiency of about 30% [67] has been reached using 1 mm long quasimosaic and strip crystals.

Fig. 2.38b shows the deflection angle profile in VR (yellow histogram) compared with the corresponding one in the amorphous orientation (grey histogram). The VR deflection angle is $\phi_{VR} = |mVR - mA| = 11.7 \pm 0.4$ μrad, a value, in

[11] The exponential function used in the fit is $e^{(P4+P5x)}$.

agreement with simulations and the measurements presented in [67], that corresponds to $\sim 0.7\alpha_c$, where α_c is the critical angle (eq. 1.12, $\alpha_c = 18.3$ μrad at 150 GeV). Compared with the positive particle one ($\phi_{VR} \simeq 1.4\alpha_c$), the VR deflection angle is smaller because of the shape of the effective interplanar potential (fig. 2.36b) [67].

The angular profile in volume reflection (fig. 2.38b) shows a tail on the right due to the volume captured particles: the ones that reach the end of the crystal in channeling, filling the peak at $\phi \simeq 80$ μrad, and the ones that are dechanneled and thus appear in the region between the two peaks.
The tail, that represents the VR inefficiency, is more populated than in the positive particles case (the equivalent plot is presented in fig. 2.35b).
The discrepancy is caused by the different impact of the multiple scattering on the transversal energy, that in turn depends on the shape of the effective potential.
The negative particles cross the crystalline planes (where the scattering with the nuclei takes place) at the minimum value of the interplanar potential, that is when the kinetic part of the transversal energy E_t is maximum ($E_t = E_k + U(x)$, where $E_k = \frac{pv\alpha^2}{2}$ is the transversal kinetic energy and $U(x)$ the periodic potential, eq. 1.11). According to this, an α_{ms} angular kick, caused by multiple scattering, makes the transversal energy $E_t = \frac{pv(\alpha+\alpha_{ms})^2}{2} + U(x)$, producing an increase of $\Delta E_t = \frac{pv(2\alpha\alpha_{ms}+\alpha_{ms}^2)}{2}$, that represents a larger change for negative particles which have a larger α value.

Using the method described in sec. 2.2.3, the volume reflection efficiency has been measured to be 87.4±1.4%, a value definitely smaller than the one recorded with positive particles (94.4±0.2% measured with 120 GeV positrons) that confirms the increased volume capture probability with negative particles.

2.2.5 Going to lower energy

This section describes a test performed on the CERN T9 line (sec. 2.1.6), with a 13 GeV/c hadron beam, coming from the PS accelerator. A silicon strip crystal with a size of 70×0.77×0.55 mm^3 and oriented along the (110) planes has been used.
The setup on the T9 line is shown in fig. 2.39, and it consists of the same elements of the high energy one, positioned in a much more compact way. At this energy, in fact, given the multiple scattering increase, the contribution of the intrinsic angular resolution (that worsens putting the detectors closer to each other) becomes negligible. Thus, it is convenient to simplify the setup, eliminating the vacuum pipes between the modules and reducing the air gap between them.

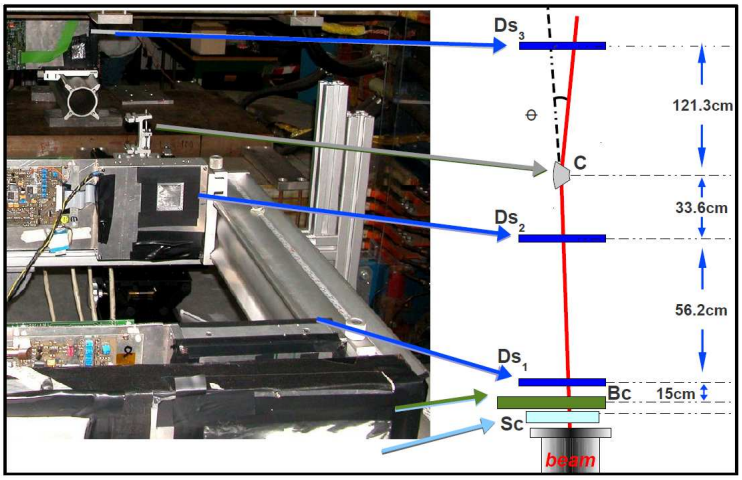

Figure 2.39: A photo of the setup installed at the T9 (CERN PS) beamline; the beam enters from the bottom. On the right side a schematic view of the setup is presented: Sc is a scintillator counter, Bc the beam chamber, DsX the silicon microstrip modules, C the crystal.

A second change in the setup has been determined by the beam size, which (fig. 2.14) in the horizontal direction exceeded 2 cm (FWHM), thus being about 40 times larger than the crystal width. For this reason, in order to increase the number of interesting events over the total acquired ones, an additional silicon microstrip detector has been added to the setup described in sec. 2.1.
It is a large area silicon beam chamber [68] (marked with Bc in fig. 2.39), consisting of two single sided 9.5×9.5 cm^2 410 μm thick silicon microstrip tiles [12], arranged in a x-y way; the strip physical pitch is 121 μm while the readout one is 242 μm; each tile is readout by three self-triggering TA1 ASICs[13]. The self-triggering capability of the silicon beam chamber has been used to select a narrow beam region, maximizing the number of the events that cross the crystal itself: fig. 2.40a shows the beam profile corresponding to the trigger region formed by the intersection of 4 horizontal strips and 50 vertical ones (∼0.12 cm^2).
The relative alignment between the trigger region and the crystal is checked by the silicon modules ($Ds_{1/2/3}$) that measure the deflection angle ϕ as a function of the particle horizontal position at the crystal (fig. 2.40b).
Fig. 2.40a shows that the trigger region is 1.5 cm in the vertical direction, which is much less than the crystal height (7 cm) but anyway covers a wide range. This wide vertical range makes the exact horizontal position of the crystal a function of

[12] Produced by *HAMAMATSU, Japan.*
[13] Produced by *Gamma Medica - IDEAS, Norway*.

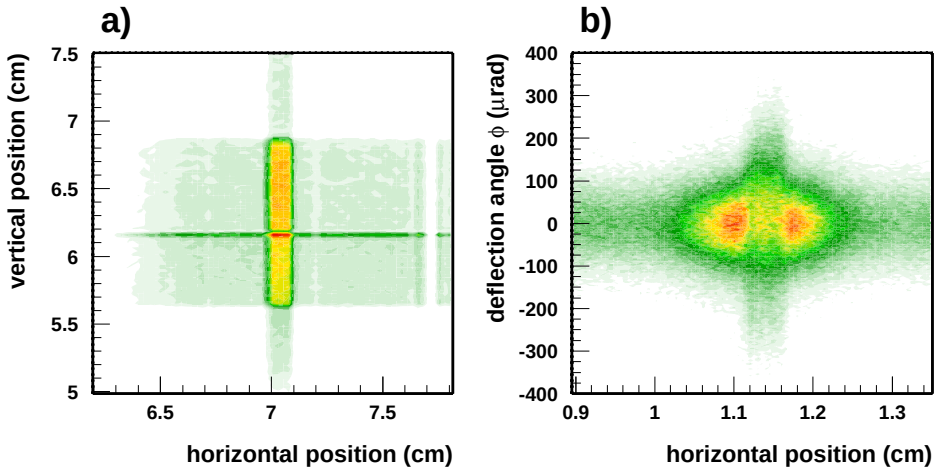

Figure 2.40: a) Bidimensional plot of the beam profile acquired triggering on a portion of the silicon chamber formed by 4 horizontal strips and 50 vertical ones. b) The deflection angle measured by the silicon modules as a function of the horizontal coordinate: in the central region the crystal presence is made visible by the multiple scattering it causes.

the particles vertical impact point, because of the principal curvature of the crystal.
For this reason either a hard cut on the particle horizontal position or the reconstruction of the crystal shape should be performed to ensure that the analysis takes into account only the particles impinging on the crystal.
To avoid the loss of good events, the second strategy has been applied in the following way: the beam has been divided in 6 vertical slices (two of them are shown in fig. 2.41a) measuring the crystal horizontal position in each slice, so that the average horizontal position of the crystal as a function of the vertical coordinate can be obtained (fig. 2.41b). As expected, the crystal describes a circular curve, from which it is possible to extract the crystal position at any given vertical coordinate, increasing the accuracy of the particles selection.

After the optical pre-alignment (sec. 2.1.7), the channeling orientation has been searched for exploiting the large divergence of the beam (~ 500 μrad RMS) and looking for an asymmetry in the scatter plot of the ϕ deflection angle as a function of the α misalignment angle, acquired at different goniometer angles. Fig. 2.42a shows the first channeling signature at $\alpha \sim 250$ μrad; it is interesting to note that the plot is much less clear than the equivalent one (fig. 2.17) acquired at 400 GeV.

Once the crystal is aligned, a long data taking is performed to accumulate

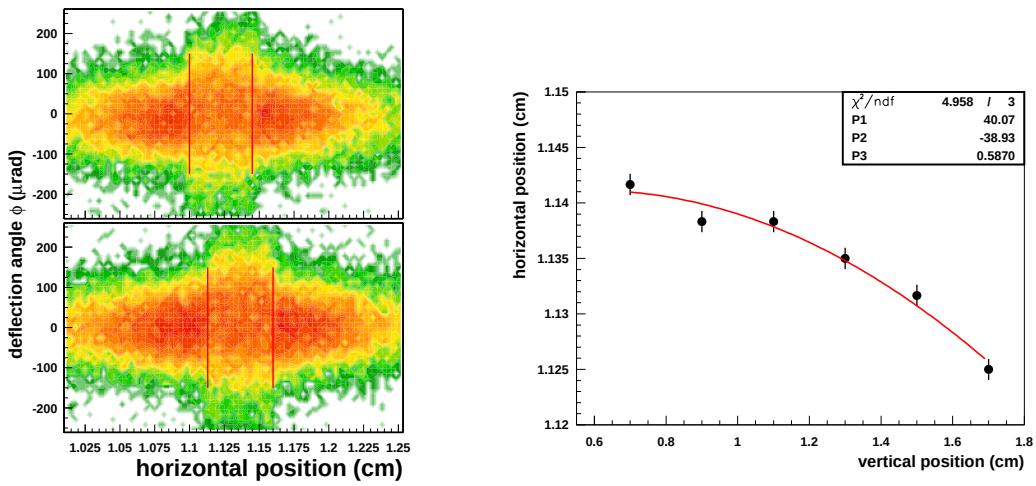

(a) (b)

Figure 2.41: The crystal is hit by an extended beam so that its position is a function of the vertical coordinate y_c. a) Two vertical beam slices 1 mm wide at a distance of 1 cm are taken into account; the plots show the deflection angle as a function of the horizontal position underlining the displacement of the crystal. b) The average position of the crystal entry face (on the y axis) as a function of the vertical position (x axis). The points are fitted with an arc of circumference whose radius is given by the parameter P_1 = 40.1 cm.

statistics. As the beam has a wide divergence, it is not necessary to rotate the goniometer, changing the alignment, to investigate the different deflection effects. Fig. 2.42b shows the result of $\simeq$10 hours of data taking during which 400k triggers have been recorded. Both the channeling and the VR effects can be identified.

The technique applied to measure the crystal torsion in this case slightly differs from the one presented in sec 2.2.1, given it is more difficult to determine the channeling orientation. A series of plots representing the deflection angle versus the misalignment at different vertical coordinates and their corresponding profiles[14] have been produced. Fig. 2.43a shows on the left two of these scatter plots, pointing out the channeling displacement due to torsion. In the corresponding profile (on the right) channeling corresponds to a valley and volume reflection to a "shoulder", so that the relative orientation can be determined with a parabolic fit of the valley.
Fig. 2.43b shows the result of a series of these parabolic fits performed at different vertical heights: the crystal has a torsion of 210.6$\pm$26.0 μrad/cm.

Once the torsion coefficient is known, the torsion can be compensated via

[14] A profile plot shows the average value of a variable as a function of another one.

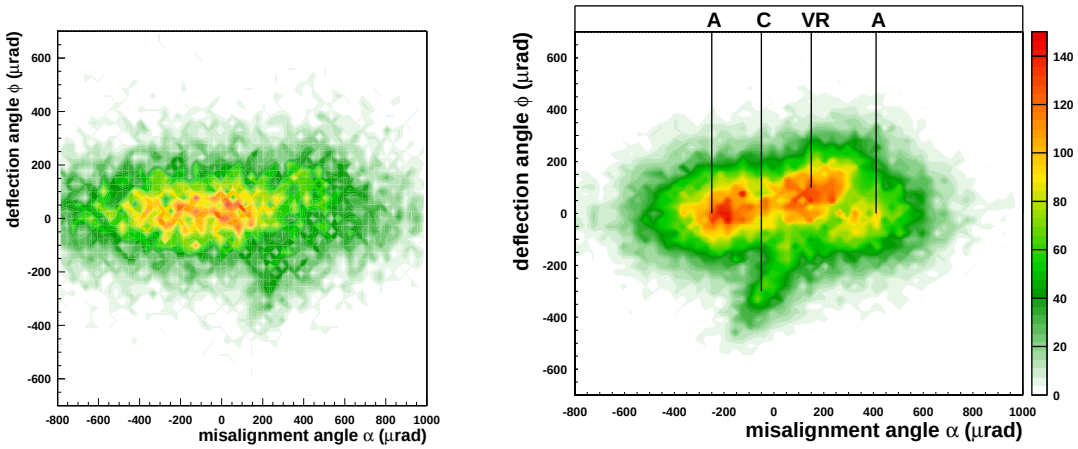

(a) (b)

Figure 2.42: (a) The result of a pre-alignment data taking, plotting ϕ as a function of α: the asymmetric structure that appears for $\alpha \simeq 250$ μrad reveals the channeling effect. b) The high statistics run with positive particles: both the channeling (C) and volume reflection (VR) effects are visible in comparison with the external regions (A) of the plot where the crystal behaves as an amorphous material.

software following eq. 2.1; the result of this operation is shown in fig. 2.44 where, in addition to the torsion correction, the number of events in each vertical bin of the histogram has been rescaled to one, to simplify the plot evaluation, given the collected statistics was not homogeneous with respect to α^*.

Fig. 2.45a shows the deflection angle distribution obtained for the best crystal alignment; the channeling peak and the undeflected one are fitted with the sum of two gaussian functions: the left side one has a mean value of 318.9±3.6 μrad which roughly corresponds to the crystal bending angle.
In fig. 2.45b the deflection angle profile of the beam portion in volume reflection is shown; two angular components are present: the reflected particles and the captured ones; they are fitted with the sum of two gaussian functions. The peak position of the right gaussian identifies the VR deflection angle which is ϕ_{VR} =69.4±4.7 μrad.

The fit procedure shown in fig. 2.45 can be repeated for several α^* angular slices; the integral of the gaussian function fitting each effect allows to compute the number of particles involved, as shown in the top plot of fig. 2.46a where the area of the gaussian distributions is plotted as a function of the misalignment angle α^* and the continuous black line represents the total number of events. For small and large α^* values, the whole beam is in an amorphous condition and the fit is performed using a single gaussian function which has an area corresponding

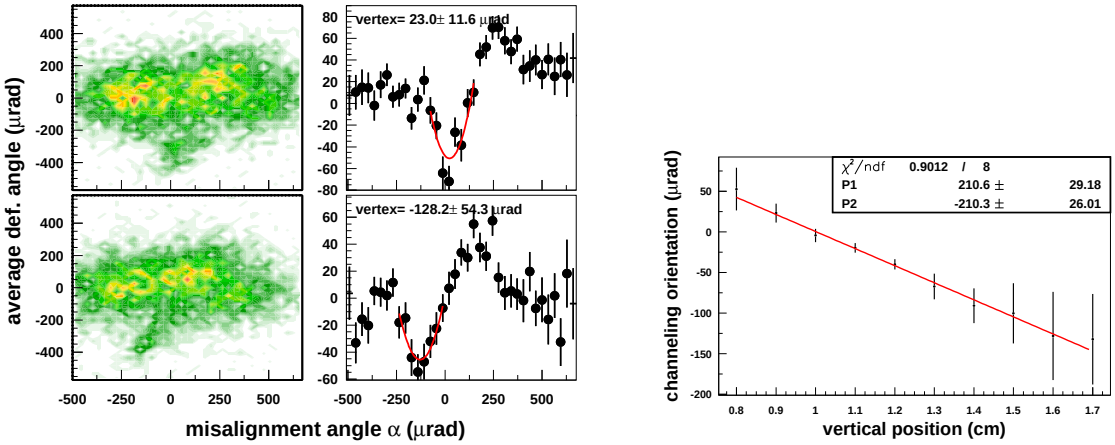

(a) (b)

Figure 2.43: a) Crystal deflection behaviour for two different vertical positions corresponding to two slices 1 mm high at a distance of 0.7 cm: the scatter plots (on the left) and corresponding profile ones (on the right) are presented. The channeling peak displacement caused by the crystal torsion is 151.2 μrad. b) The channeling peak α position as a function of the vertical position on the crystal. The torsion is linear and its value is 210.6$\pm$26.0 μrad/cm.

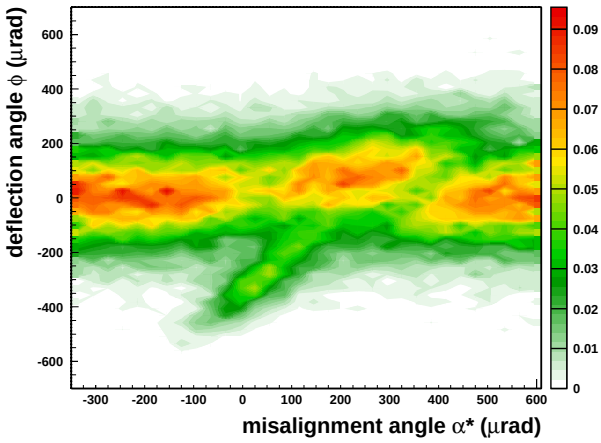

Figure 2.44: The ϕ deflection angle as a function of the α^* local misalignment between the crystal surface and the particles; each vertical bin has been normalized to one.

to the black line; in the central part of the plot the events are divided between channeling, volume reflection and volume capture.

A rough estimation of the angular acceptances of the channeling and the volume reflection regions has been performed: concerning channeling, the width of an

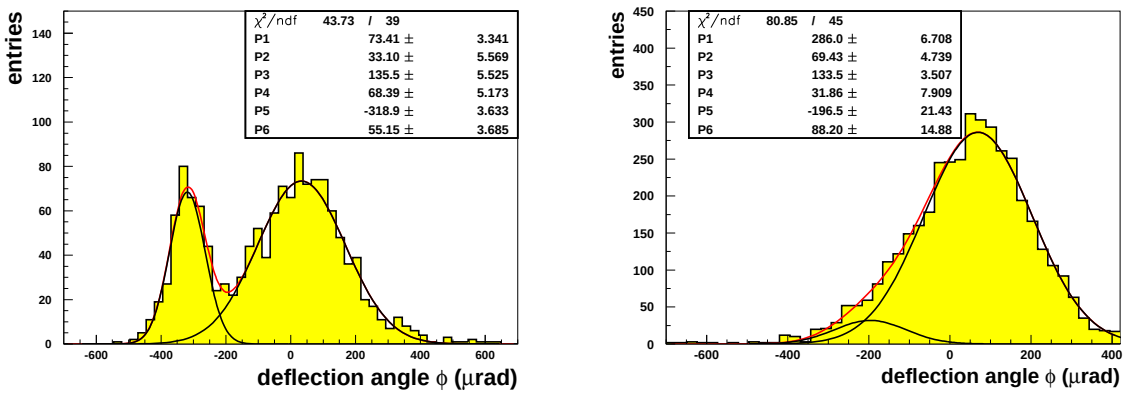

(a) (b)

Figure 2.45: a) The deflection angle ϕ distribution for a α^* value close to the ideal crystal alignment: the channeling and the undeflected beam are fitted with the sum of two gaussian functions. b) Deflection angle distribution in the volume reflection region: the two components (VR on the right and VC on the left) are fitted with the sum of two gaussian functions.

almost flat region has been considered, giving about 145 μrad; this value exceeds 2 critical angles ($2\alpha_c \simeq 110$ μrad) due to the multiple scattering that limits the α^* selection efficiency. For what concerns the VR region, it can be determined with higher precision considering the channeling central region as a start and the angle in which the "amorphous" efficiency overcomes the VR one as the end: the resulting value (300 μrad) is consistent with the crystal bending angle that is about 270 μrad, as will be shown.
To compute the efficiency of the different effects, a normalization is needed, and thus all the points have been rescaled with respect to the total number of events (bottom of fig. 2.46a). In the amorphous region the efficiency results to be 95% because of the events in the tail of the gaussian due to the large angular scattering inside the crystal or in the detectors. The efficiency of the crystal effects has thus been defined as the ratio between the number of the events which have undergone the effect and the one in the amorphous region. According to this definition the channeling efficiency is $28.4 \pm 1.3\%$ while the volume reflection one is $92.7 \pm 3.3\%$.

To determine the bending radius of the crystal the procedure described in sec. 2.2.2 can be applied: fig. 2.46b shows in the top plot the channeling angle ϕ as a function of α^* and in the bottom one the trend of the channeling efficiency as a function of α^*. This trend is fitted with a parabolic curve whose vertex horizontal position projected on the top plot, gives the value of the bending angle: ϕ_c=267.1

$\pm$ 12.2 μrad, which corresponds to a bending radius R = 280.8 $\pm$ 12.8 cm. This value can be compared with the principal crystal curvature measurement (presented in fig. 2.41b) that gives $R_{//} = 40$ cm. Being the ratio between the principal curvature and the anticlastic one about 6.1 [69], the expected bending radius $R_{\perp}$ is about 244 cm.

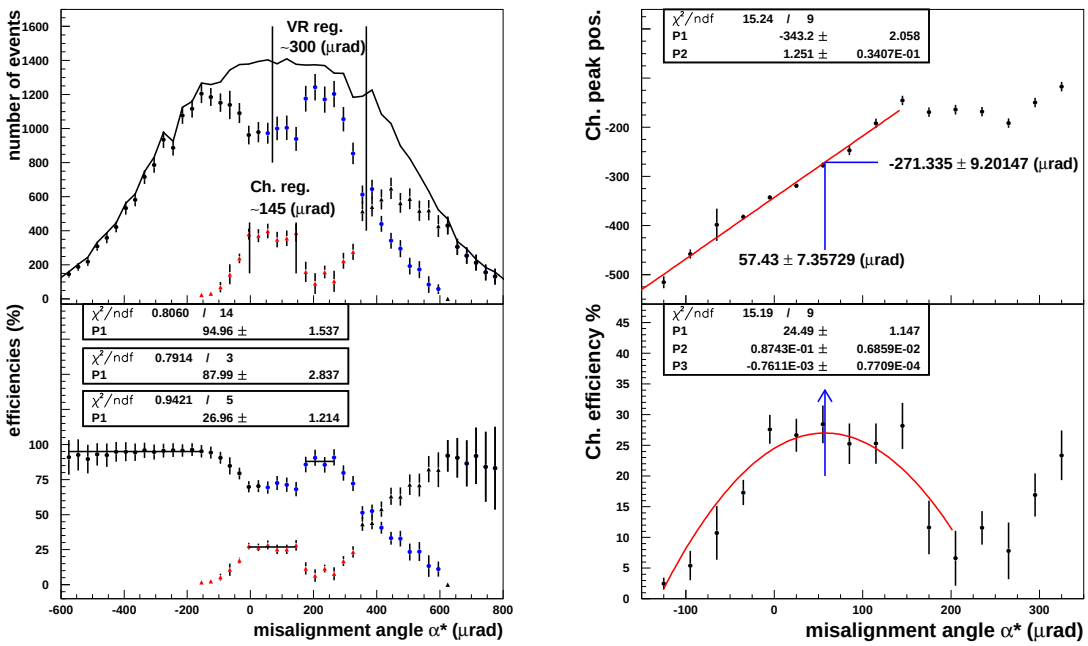

(a) (b)

Figure 2.46: a) In the top plot, the numbers of events in the different deflection effects are plotted as a function of α^*; the volume reflection and channeling regions are underlined. The black line represents the total number of events. The bottom plot is the equivalent of the top one but normalized to the acquired statistics: the constant fits give the percentage of events under the gaussian functions fitting the different effects. b) The mean angle of the channeling peak (top plot) and the channeling efficiency (bottom one), as a function of the local alignment α^*. The parabolic fit identifies the best crystal alignment and therefore the bending angle.

Once the positive particles measurement was concluded, an attempt to investigate the crystal at the same energy but with negative particles was performed. Since the identification of the channeling phenomenon with negative particles is more difficult, the goal was to exploit the previous (positive particles) investigation, changing the beam sign and nothing else: the spatial and angular alignment of the crystal, in fact, remains still valid being related with the detector position

and not with the beam features; moreover the crystal features such as the bending radius and the torsion coefficient do not need to be measured again.
Fig. 2.47a presents the ϕ deflection angle as a function of the α^* local misalignment for the whole statistics collected with 13 GeV/c negative hadrons (80.5k events). Differently from the positive case (fig. 2.42), neither channeling nor VR can be identified. The possibility of an unwanted crystal movement has been checked for, as shown in fig. 2.47b, that compares the average deflection angle as a function of α^* for positive and negative particles. The blue dots (positive particles) show the channeling and the VR effects in terms of two large asymmetries towards negative angles (channeling) and positive ones (VR). The same asymmetries are present also with the red dots (negative particles) but with a much lower intensity, thus confirming the correct alignment of the crystal.
The conclusion is that for this crystal the coherent deflection effect is negligible if compared to the incoherent amorphous one. To exploit a bent crystal in this condition, a much shorter crystal is needed to limit the dechanneling probability (the length of the tested crystal is of the order of the dechanneling one for negative particles) and to reduce the multiple scattering contribution to the deflection angle.

It is interesting to note that the unambiguity reached in the negative particle data taking was made possible by the previous measurement performed with positive particles that allowed to align the crystal and to study and compensate its torsion. This technique could be exploited in the future not only for the negative particle studies but also to perform further investigations at lower energy.

2.2.6 Summarizing

Tab. 2.2 collects the most relevant results (deflection angles (ϕ) and efficiencies (Ef) of channeling and volume reflection) for silicon strip crystals.
As described in the previous sections, the measurements summarized in tab. 2.2 have been performed at different energies, on different beamlines, with both positive and negative particles, using the same experimental setup and analysis techniques.

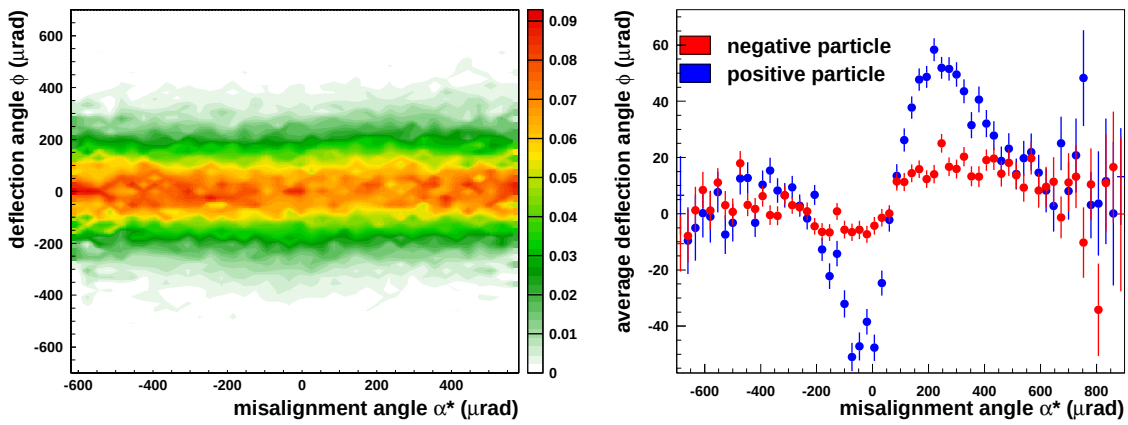

(a) (b)

Figure 2.47: a) Crystal behaviour with 13 GeV/c negative particles: the ϕ deflection angle is shown as a function of the α^* local misalignment; each vertical bin has been normalized to one. There is no clear evidence of channeling and volume reflection. b) Comparison between the positive and negative particle data taking: the dots represent the average ϕ deflection angle as a function of the α^* local misalignment. Although with different amplitudes, the red dots (negative particles) have the same trend of the blue ones (positive particles) demonstrating that the crystal has the same alignment in the two conditions.

E (GeV)	l (mm)	R (m)	ϕ_c (μrad)	$E\,f_c$ (%)	ϕ_{VR} (μrad)	$E\,f_{VR}$ (%)
400 pos.	1.94	10.65 ± 0.01	182.1±0.1	75.2±0.1	13.13±0.02	97.6±0.2
120 pos.	2	10.72 ± 0.22	186.5±3.9	66.7±11.4	26.9±0.2	94.4±0.2
150 neg.	2	12.7±0.1	157.7±1.5	5.8±1.52	11.7±0.4	87.4±1.4
13 pos.	0.77	2.81±0.13	267.1±12.2	28.4±1.3	69.4±4.7	92.7±3.3

Table 2.2: Summary of the deflection parameters for channeling and volume reflection for the studied crystals at different energies.

Chapter 3

Radiation emission in channeling and VR

This chapter is dedicated to the investigation of the radiation emission phenomena related to channeling and VR effects in bent crystals.
From the deflection point of view these effects are deeply different: channeling performs a slight deviation of the particle trajectory all along the crystal length, while reflection is a point-like event located in a small region of the crystal. When radiation emission is taken into account, their description becomes similar: in both cases the microscopic interaction with the interplanar potential plays the main role and the macroscopic deflection (the quantity whose measurement has been described in chap. 2) gives an almost negligible contribution.
Fig. 3.1 compares the trajectory of a channeled particle (red line) with one in VR (green line) with respect to the quasi harmonic interplanar potential; in both cases the interaction with the potential produces an oscillation in the transversal direction with respect to the motion. In channeling, the particle transversal energy is smaller than the potential barrier and the particle performs a quasi harmonic oscillation (box on the right in fig. 3.1) whose amplitude depends on the initial transversal energy value. In volume reflection, the transversal energy exceeds the potential barrier so that the particle crosses the crystalline planes in an almost regular sequence. These quasi harmonic oscillations and periodical interactions are responsible of the enhancement in the radiation emitted by channeled and reflected particles.

In the following sections the results of an experimental test performed with a 120 GeV/c positron beam on the CERN H4 beamline will be presented. The setup (sec. 3.2.1), based on the “deflection” one (sec. 2.1), has been developed to measure the energy lost by the charged particle during the crystal crossing using a spectrometer and an electromagnetic calorimeter. The analysis and the results (sec. 3.2.2) are in good agreement with the Montecarlo simulations and the ana-

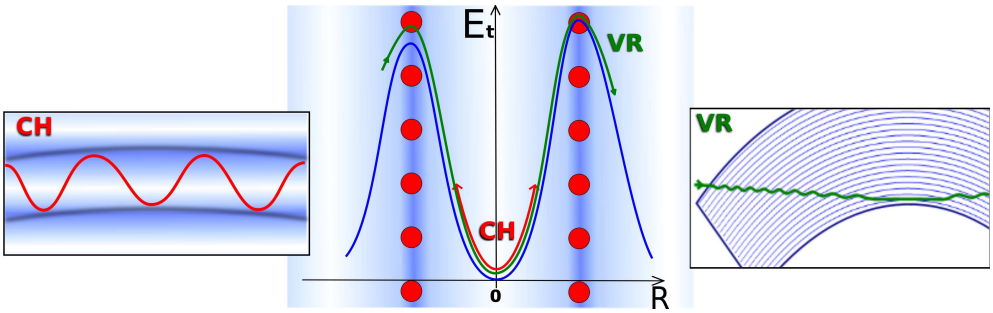

Figure 3.1: The central plot represents the region between two atomic planes inside the crystal: the channeled particle (red line) is confined in the potential well, its motion is an oscillation between the crystal planes (box on the left); the volume reflected particle (green line) has a transversal energy larger than the potential barrier, so that it crosses the crystal planes in sequence, while its transversal kinetic energy (and thus its trajectory) oscillates in the crystal (box on the right).

lytical calculations, whose basic principles are presented in sec. 3.1.

3.1 A physical model

This section has a twofold goal: to present a deeper look into the radiation emission phenomena in channeling and volume reflection and to describe the specific analytical techniques used to interpret the experimental results collected in sec. 3.2.

3.1.1 Channeling

A considerable number of theoretical [70] and experimental [71] studies have been dedicated to the channeling radiation investigation in straight crystals. The majority of these studies has been performed in the energy range from several hundreds of MeV to some tens of GeV.
At these energies the emitted radiation has an almost monochromatic character; in fact, its most relevant contribution is given by the first harmonic of the oscillation in the channel. An example is shown in fig. 3.2a in which the enhancement of the channeling radiation with respect to the bremsstrahlung one, measured with a 10 GeV positron beam, is presented. The peaks corresponding to the first and second harmonic contribution are clearly visible.
Fig. 3.2b shows the same enhancement obtained with an electron beam; in this case no structures are present given that the electrons are confined in a strongly

non-harmonic potential (sec. 2.2.4).

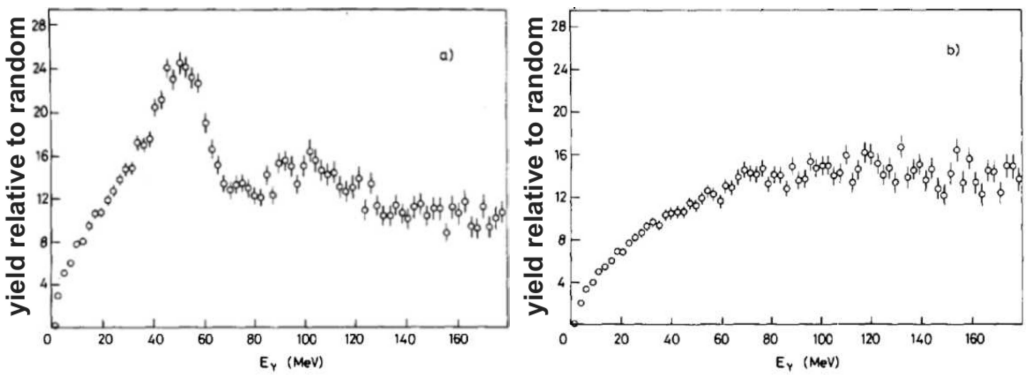

(a) (b)

Figure 3.2: Emitted photon energy spectra for a 10 GeV/c particle beam impinging on a silicon crystal ((110) plane, 0.1 mm thick) normalized to the incoherent bremsstrahlung spectra: a) positron beam, the first and second harmonics are clearly visible; b) electron beam, the spectrum shows an increase with respect to the incoherent bremsstrahlung but without any relevant structures [71].

At higher energy the monochromaticity of the radiation gradually decreases also for positive particles since the contribution of the higher harmonics increases and the spectrum becomes almost continuous.
The different radiation regimes can be distinguished with the help of the multipole parameter:

$$\rho = 2\gamma^2 \frac{\langle (v(t) - v_m)^2 \rangle}{c^2} \tag{3.1}$$

where $\langle (v(t) - v_m)^2 \rangle$ is the squared mean deviation of the transverse velocity from its mean value v_m.
Depending on ρ, two different situations can be recognized:

- $\rho \ll 1$: the radiation intensity is the result of the interference on a large part of the particle trajectory and thus depends on the peculiarities of the particle motion.

- $\rho \gg 1$: the particle radiates during a small part of the trajectory and the interference between distant parts can be neglected.

Concerning channeling radiation, the value of the ρ parameter at a given energy depends on the single particle trajectory (that is on its transversal energy). At low energy (up to a few tens of GeV) ρ is smaller than one, meaning that the emitted radiation is the result of the interference along the particle trajectory (undulator

radiation [72]) and thus the dipole approximation can be used to compute the radiation emission.
It should be noted that when the crystal is bent, a circular motion is superimposed on the oscillations, with two consequences: 1) the interference (undulator radiation) is reduced since the particle trajectory drifts away from the straight line; 2) a low energy continuous component (synchrotron radiation) generated by the circular motion adds to the spectrum.
The influence of bending on emitted radiation is shown in the simulation presented in fig. 3.3 for a 5 GeV positron beam: as the curvature increases, the middle and high energy part of the spectrum decreases (undulator radiation, curves 3-4) while a low energy component (synchrotron, curve 2) appears.

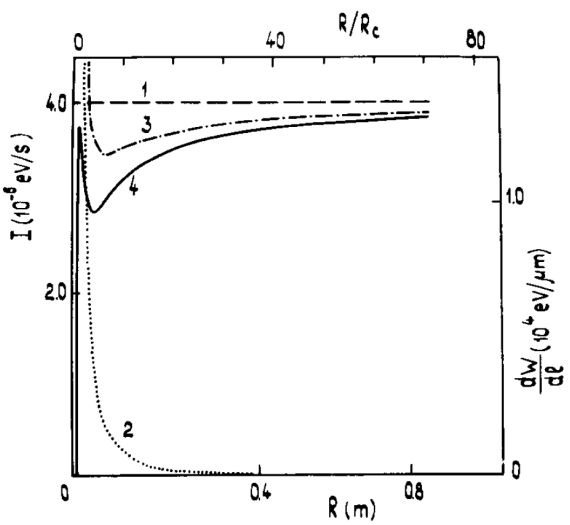

Figure 3.3: The intensity of the radiation emitted by relativistic positrons (the Lorenz factor is $\gamma = 10^4$, with $\gamma \equiv \frac{c}{\sqrt{c^2 - v^2}}$, where c is the speed of light and v the particle velocity) in bent crystals as a function of the crystal curvature expressed both in absolute terms (R) and as a function of the critical radius (R/R_c): curve 1 refers to the radiation emitted in a straight crystal, curve 2 describes the synchrotron contribution, curve 3 is the intensity spectrum for a bent crystal and curve 4 takes into account the quasi-channeled particle contribution [72].

To identify which aspect dominates between the undulator and the synchrotron one, the oscillation period in channeling λ (given in eq. 1.16) should be compared with the radiation formation length $l_{coh} = R\gamma^{-1}$ (R is the bending radius and γ the Lorentz factor). If $l_{coh} \gg \lambda$, the interference takes place along many oscillation periods and the radiation has the features of a quasi-undulator type; when $l_{coh} \ll \lambda$, it is a quasi-synchrotron one.

The previous argument can be used at a relatively low energy ($\rho < 1$), while in the hundreds of GeV range ρ exceeds the unity value, so that the dipole approximation is no more valid and other methods should be considered to compute the radiation emission. Fig. 3.4 presents the computed ρ trend as a function of the normalized oscillation amplitude ξ_m[1] in the channel (that in turn depends on the

[1] ξ_m represents the oscillation amplitude in the channel normalized to the interplanar distance

initial transversal energy of the particle) for a 100 GeV positron beam: ρ exceeds 20 for a considerable portion of the channeled particles.

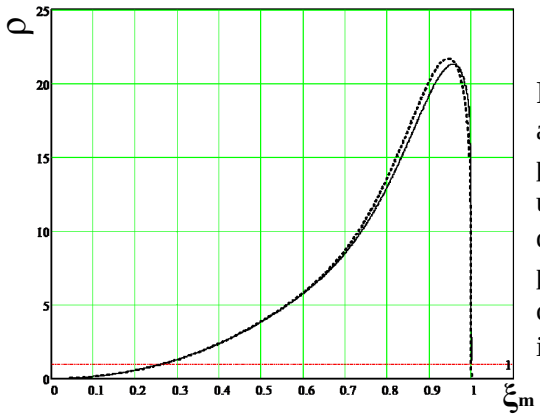

Figure 3.4: The multipole parameter ρ as a function of the normalized oscillation amplitude ξ_m in channeling [73]. The continuous line is the exact calculation while the dotted one is computed in the harmonic approximation; the potential used for the calculations (fig. 3.5) will be described later on in this section.

As underlined in [73], two approaches can be used to describe the radiation emission phenomenon in channeling at this energy:

- **method 1** is based on quasi-classical considerations [74] and is able to describe the quasi-periodic particle motion for all the possible ρ values but, taking into account the interference phenomenon, should be applied in straight crystals or at least when $l_{coh} \gg \lambda$.

- **method 2** uses a synchrotron like approach (based on the equation of classical electrodynamics [75]); it neglects the interference between the distant parts of the trajectory and therefore should be used when the particle direction changes faster than the characteristic radiation angle (that approximately goes as the inverse of the Lorentz factor, $\sim \gamma^{-1}$), thus when $\rho \gg 1$ or $l_{coh} \ll \lambda$.

The second method should be preferred being valid in a large curvature range, but since an interference contribution at this energy could not be excluded a priori, its validation, comparing the two methods in straight crystals, is necessary.

Before being applied, both the methods need a common physical modeling of the channeling phenomenon that goes from the analytical description of the interatomic potential to the main features of the particles motion:

- an accurate description of the *interplanar potential* [70], based on the X-ray measurements of the atomic form factor, can be obtained, reaching an accuracy of 1%. Fig. 3.5a shows the obtained potential as a function of the normalized amplitude ξ.

d_p so that $\frac{2\xi_m}{d_p} = 1$.

- given the interplanar potential, the *oscillation frequency* as a function of the normalized amplitude $\omega(\xi_m)$ can be computed. Fig. 3.5b shows the trend of the normalized frequency $\Omega(\xi_m) = \omega(\xi_m)/\omega_0$, where ω_0 is the oscillation frequency for $\xi_m \longrightarrow 0$. $\Omega(\xi_m)$ is constant for small oscillations and increases for larger amplitudes as the non-harmonic region of the potential is taken into account.

- figg. 3.5b and 3.4 show that the motion features depend on the oscillation amplitude ξ_m in the channel; thus its probability distribution $p(\xi_m)$ should be computed. Given that in short crystals the scattering on the electrons has a negligible effect (sec. 1.3.2.1), the transversal energy is almost conserved and the oscillation amplitude depends just on the initial conditions of the motion described by the α and x parameters that are the particle misalignment and position with respect to the planes. Since the position x has an equiprobable distribution (the beam has a macroscopic dimension compared with the channel width), $p(\xi_m)$ depends only on the angular divergence of the particle impinging on the crystal. Fig. 3.6 shows the amplitude probability distribution $p(\xi_m)$ for different ($\pm\alpha$) values.

- the last consideration is addressed to the character of the particle trajectories; in fig. 3.7 the amplitude ξ is shown as a function of time, for two amplitude values close to one ($\xi_m = 0.98$ and $\xi_m = 0.995$). The real trajectories are compared with a sinusoidal function, showing that the harmonic approximation is quite good up to large amplitudes ($\xi_m = 0.98$); beyond this level the approximation gets worse but, since these amplitudes are populated by a small number of particles (due to nuclear dechanneling, sec. 1.3.2.1), the harmonic approximation can be used to compute the spectrum emitted by the channeled particles.

Summarizing, the used technique is based on an accurate representation of the interplanar potential, that allows to compute exactly the multipole parameter ρ and the oscillation frequency ω as a function of the oscillation amplitude ξ_m whose distribution depends only on the particle incoming angle α and can be computed.
Assuming the previous results, the radiation emission spectrum[2] per positron per unit length can be determined for both the methods in the harmonic approximation (the details of the calculations can be found in [73]).

[2]Expressed by $\frac{d^2E}{dE_\gamma ds}(E_\gamma^0)$, where dE is the energy irradiated (in the energy range $E_\gamma < E_\gamma^0 < E_\gamma + dE_\gamma$) by a charged particle crossing the crystal length ds.

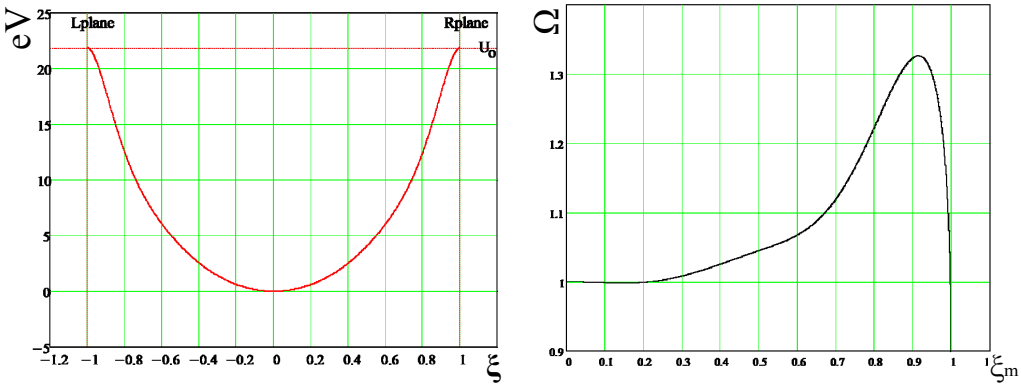

(a) (b)

Figure 3.5: a) The interplanar potential computed for a straight silicon crystal oriented along the (110) plane. b) The normalized oscillation frequency of a channeled particle, Ω, as a function of its normalized oscillation amplitude ξ_m [73].

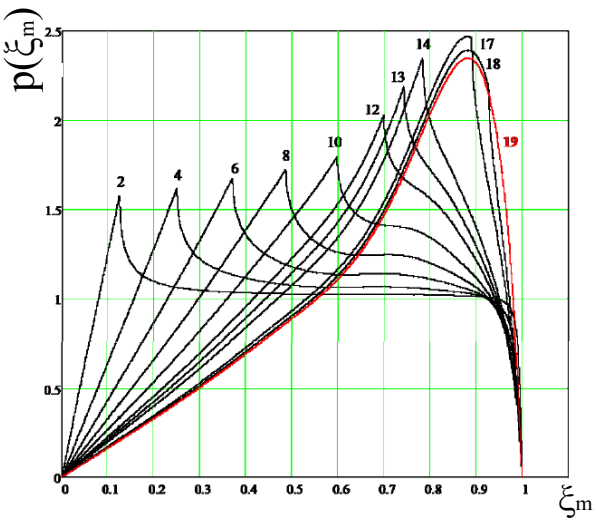

Figure 3.6: The probability distribution of the normalized amplitude ξ_m for different values of the misalignment angle α expressed in μrad near the corresponding curve [73].

Fig. 3.8 shows the spectra obtained with method 1 (a) and method 2 (b) for two values of α (4 and 19 μrad) for a charged particle crossing 1 cm of crystal. The interference effect in the first method, whose presence should be indicated by the recognizable contribution of the different harmonics, is small for two reasons: the presence of a larger number of high and close harmonics and the integration over a distribution of amplitude values ξ_m (fig. 3.6) that smears the contribution of the harmonics themselves. For these reasons the agreement with the second method (that shows a smooth distribution) is substantially good (better than 10% comparing the positions of the spectra maximum).

This comparison demonstrates that the second more general method can be ap-

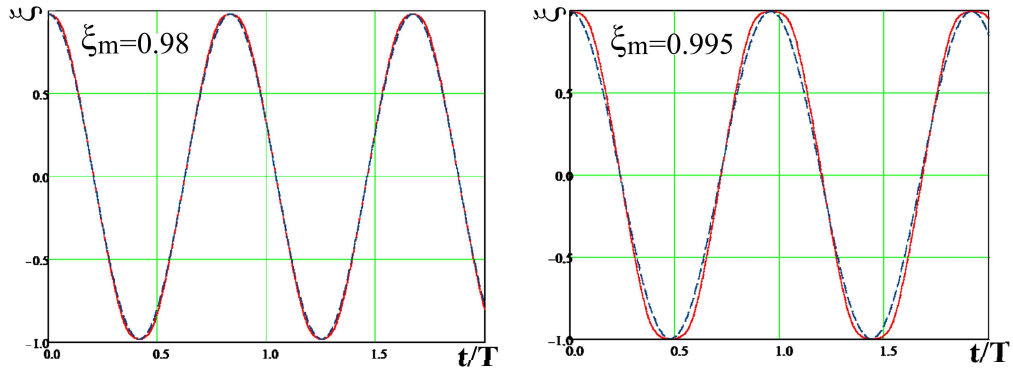

(a) (b)

Figure 3.7: Particles trajectories in channeling for two large oscillation amplitudes: a) $\xi_m = 0.98$; b) $\xi_m = 0.995$. The continuous red lines represent the exact solutions and the dotted ones the harmonic approximation [73].

plied to compute channeling radiation but its final validation needs the comparison with the experimental results (sec. 3.2.2).

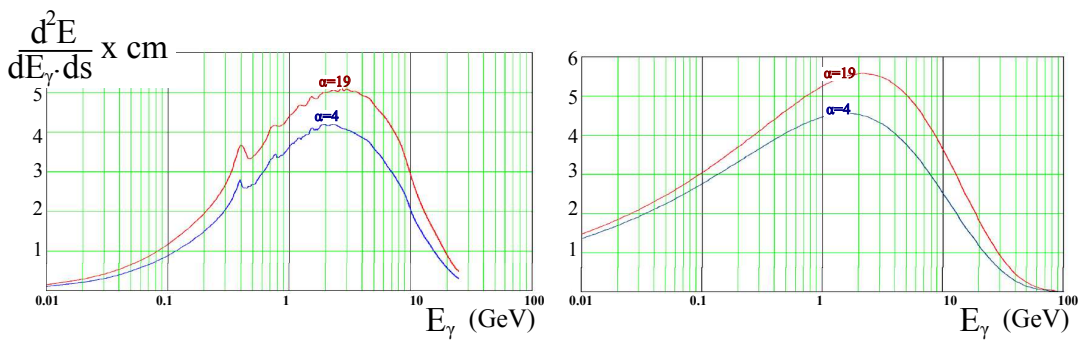

(a) (b)

Figure 3.8: The channeling radiation spectra obtained with method 1 (a) and 2 (b) for two values of the misalignment angle $\alpha = 4, 19$ μrad, for a 120 GeV positron, crossing 1 cm of crystal.

To allow this last step, two further contributions should be taken into account:

- *the curvature of the crystal.*
  The agreement between method 1 and method 2 demonstrates that the channeling radiation (at 120 GeV) has a synchrotron like character which means that the interference is weak and the different radiation processes can be considered independently. The contribution given by the crystal curvature

can be estimated starting from the equation describing a particle moving along a circular trajectory [70]:

$$I = \frac{2e^2\gamma^4}{3R^2} \tag{3.2}$$

where I is the energy loss per unit length, e is the particle charge, R the curvature radius and γ the Lorentz factor. The smallest tested bending radius (sec. 3.2) is 4.74 m giving $I = 1.315$ GeV/cm (its spectrum has a maximum at 235 MeV and a cut-off at 1 GeV). Since the energy loss due to the oscillation in the channel (corresponding to the integral of the spectrum in fig. 3.8) is about 80 GeV/cm, the contribution given by the crystal curvature can be neglected.

- *the multi-photon emission probability for a single positron.*
  The spectra shown in fig. 3.8 allow to estimate the single photon emission probability for a positron crossing a crystal length ds; but when a positron crosses a macroscopic crystal (the crystal length along the beam is 2 mm) the probability of multi-photon emission has to be taken into account. To introduce this effect, a Montecarlo simulation has been performed: particles are generated with a random position in the channel ($\pm d_p$) and a random alignment ($-\alpha_{ref} < \alpha < \alpha_{ref}$ with an equiprobable distribution). Using these variables the transversal energy and thus the oscillation amplitude ξ_m are computed, so that the particle is tracked along the crystal associating an emission probability to every step of the trajectory (only photons in the energy interval 50 MeV$< E_\gamma <$50 GeV have been considered): the result is the total spectrum of the emitted radiation.

In sec. 3.2.4 the spectra obtained with the described simulation for two 2 mm long strip crystals will be shown and compared with the experimental results.

3.1.2 Volume reflection

The description of the channeling radiation phenomenon in bent crystals (sec. 3.1.1) started from the simpler case of straight crystals; in the same way volume reflection radiation emission presents a straight crystal counterpart: *the coherent bremsstrahlung*.

Coherent bremsstrahlung takes place when a particle crosses a crystal at an angle α with respect to its planes larger than the critical one α_c (so that channeling is not allowed) and small enough for the continuum approximation (sec. 1.3.1) to be valid. In this condition the particle crosses the crystal planes periodically (every d_p/α, where d_p is the interatomic distance, fig. 3.9); thus, for selected frequencies, the electromagnetic radiation emitted at the passage through a plane adds

coherently, increasing the total emitted radiation with respect to the incoherent bremsstrahlung [2].

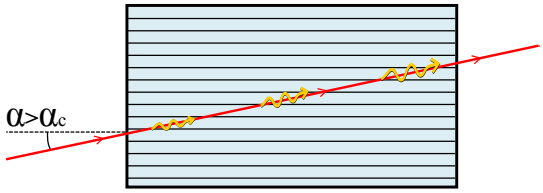

Figure 3.9: A particle crossing a straight crystal at an angle $\alpha > \alpha_c$.

Fig. 3.10 shows the enhancement of the radiation emitted by a straight crystal (0.1 mm thick) crossed by a 10 GeV/c positron beam as a function of its misalignment α with respect to the beam direction [71]. For $\alpha \sim 0$ (perfect alignment) positrons are channeled and the channeling radiation (sec. 3.1.1), characterized by a relatively low photon energy (E_γ) and high intensity, is emitted. As the misalignment α increases, the coherent bremsstrahlung appears as two tails of higher photon energy and lower intensity. Increasing even more the misalignment with the planes, the spectrum becomes harder because the periodicity of the planes crossing (d_p/α) is shortened and the coherent interference selects higher frequencies corresponding to higher photon energies.

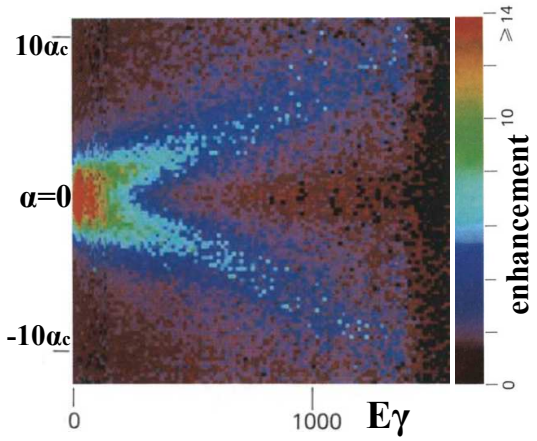

Figure 3.10: The enhancement of the radiation emitted by a straight crystal (0.1 mm thick) crossed by a 10 GeV/c positron beam as a function of its misalignment with the beam direction (α, vertical axis) and of the emitted photons energy (E_γ, horizontal axis) [71]. Both the channeling radiation and the coherent bremsstrahlung are present.

The condition of a volume reflected particle is similar to the coherent bremsstrahlung one: the transversal energy exceeds the potential barrier value so that the particle crosses in sequence the different crystalline planes. In both the cases the particle trajectory oscillates due to the interaction with the interplanar potential; the peculiar feature of volume reflection is given by the crystal curvature, that varies the average misalignment between the particle trajectory and the planes, $\alpha(t)$, during the crystal crossing.
For this reason the analytical expression to determine the radiation emission properties developed in the coherent bremsstrahlung framework cannot be directly ap-

plied to bent crystals. Therefore two strategies have been proposed to describe the volume reflection phenomenon from the radiation point of view:

- the first one uses the quasi classical approach in which the probabilities of QED processes are determined computing the classical trajectories of the particles in the interplanar potential [76]; this method takes into account the details of the motion in volume reflection and thus is complicated and very time consuming from the CPU point of view.

- the second one considers the radiation emission in volume reflection as the sum of sub-processes in which $\alpha(t)$ varies of a negligible amount so that the coherent bremsstrahlung formalism can be applied locally [77]. This method is faster and somehow more complete than the first one since it allows to include the multiple scattering contribution; it is suitable for a wide energy range till about 150 GeV. A more detailed description of the method will be given in this section and its good agreement with the experimental results will be shown in sec. 3.2.2.

Defining $I(\alpha,E)ds$ as the coherent bremsstrahlung radiation [74] emitted by a charged particle (of energy E) which is crossing a crystal length ds ($ds \simeq cdt$), misaligned with respect to the crystal planes of an angle α, the "local" application of the bremsstrahlung theory to bent crystals can be expressed in the following way:

$$\frac{d^2E_l}{dE_\gamma}(t) = \frac{dI}{dE_\gamma}(\alpha(t))cdt \tag{3.3}$$

where $\frac{d^2E_l}{dE_\gamma}$ (the variation of the differential energy loss along a distance $ds \simeq cdt$) matches the radiation intensity due to coherent bremsstrahlung which in turn depends on the angle $\alpha(t)$ between the particle trajectory and the crystal planes.
The evolution of this angle before the reflection ($t < t_c$ where t_c is the time of the reflection) is described in fig. 3.11, providing the following expression:

$$\alpha(t) = \alpha_0 - \frac{ct}{R} \tag{3.4}$$

where R is the bending radius and c the light speed.

Fig. 3.12 shows that eq. 3.4 well approximates the $\alpha(t)$ angle for $t < t_c$, comparing its average value with the instantaneous oscillatory one, computed according to the interplanar potential [78].
For $t = t_c$ (reflection time), a discontinuity corresponding to the reflection is present; note that it is centered in $\alpha = 0$ because the particle is parallel with the crystal

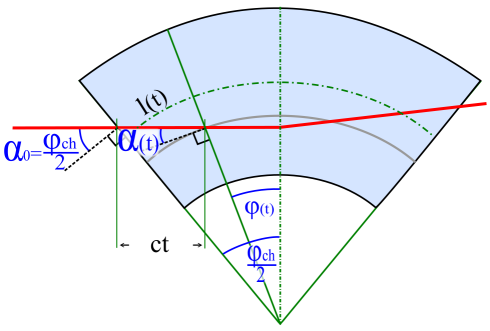

Figure 3.11: The evolution of the misalignment between the crystal planes and the particle trajectory $\alpha(t)$ in VR (before the reflection). To simplify the scheme, the starting angle $\alpha_0 = \frac{\phi_{ch}}{2} = \frac{l}{2R}$ has been chosen. After a time t the particle crosses a distance ct ($\beta \simeq 1$) so that $\alpha(t) = \alpha_0 - \phi(t) = \alpha_0 - \frac{l(t)}{R}$. Since $\phi_{ch} \ll 1$, $l(t) \simeq ct$ giving $\alpha(t) \simeq \alpha_0 - \frac{ct}{R}$.

plane. The minimum α value before the reflection is $\alpha_c = \alpha_0 - \frac{ct_c}{R}$; thus for symmetry, just after the reflection, $\alpha = -\alpha_c = \frac{ct_c}{R} - \alpha_0$ and, for continuity, in the region $t > t_c$ the following expression for $\alpha(t)$ holds:

$$\alpha(t) = \alpha_0 - \frac{2ct_c}{R} - \frac{ct}{R} \tag{3.5}$$

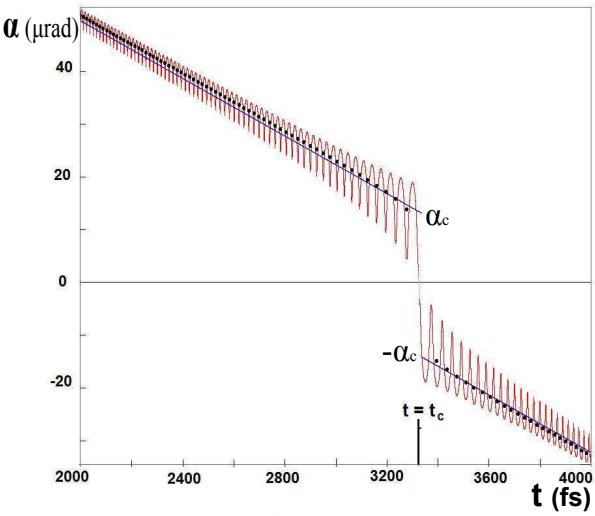

Figure 3.12: The behaviour of the $\alpha(t)$ angle near the reflection time t_c: the red curve represents the instantaneous value, the black points the one averaged every oscillation and the blue line the linear approximation presented in this section.

Once the $\alpha(t)$ behaviour is known, eq. 3.3 can be integrated with respect to α eliminating the explicit dependence on time, given that $\frac{d\alpha}{dt} = -\frac{c}{R}$:

$$\frac{dE_l}{dE_\gamma}(E_\gamma) = R\int_{\alpha_0}^{\alpha_c} \frac{dI}{dE_\gamma}(\alpha)d\alpha + R\int_{-\alpha_c}^{\alpha_{out}} \frac{dI}{dE_\gamma}(\alpha)d\alpha \tag{3.6}$$

where the integral has been split in two parts corresponding to the intervals $t < t_c$ and $t > t_c$ respectively; α_c and α_{out} can be determined, according to [78], being characteristic angles of the volume reflection trajectory.
The function $I(\alpha)$ is the standard expression for coherent bremsstrahlung [74] in a straight crystal; in this situation the average energy loss of a particle crossing a crystal of length l is just $I(\alpha)l$ while in bent crystals a non trivial dependence from the crystal length and curvature is present.

Eq. 3.6 gives the energy lost by a volume reflected particle emitting a single photon but, as for channeling radiation (sec. 3.1.1), the multiphoton emission probability is not negligible. Computations show in fact that in a 2 mm long crystal (like the used one, sec. 3.2.2), the average photon multiplicity above 1 GeV is 1.5. The multiphoton emission could be treated in two ways: with a Montecarlo simulation (as for channeling, sec. 3.1.1) or including its effect in the analytical calculation. As will be shown in sec. 3.2.2, the second method has been chosen for the volume reflection case; the details of the calculation can be found in [79].

3.2 The experimental test

This section describes a test performed in August 2009 on the H4 beamline at the CERN SPS with a 120 GeV/c positron beam. The main goal of the test was the bent crystal characterization from the radiation point of view in channeling and volume reflection. To do this, the experimental setup described in sec. 2.1 has been modified in order to measure the energy lost by the positron which is equivalent to the irradiated one.

3.2.1 A setup add-on for the radiation tests

Fig. 3.13 shows the scheme of the experimental setup used on the H4 beamline; it can be divided in two functional parts: the one called “deflection” (sec 2.1) dedicated to the beam monitoring and the study of the bent crystal deflection properties and the one called “radiation” to measure the energy radiated by the crystal.
A spectrometer (sec. 3.2.1.1) and two electromagnetic calorimeters (secc. 3.2.1.2, 3.2.1.3) compose the “radiation” part of the setup, whose working principles can be described as follows:

- a charged particle[3] crosses the crystal, with a certain probability of emitting a photon travelling in parallel with it; the silicon modules (DsX) provide the information on its outgoing trajectory from the crystal.

[3]The beam is not a pure positron one; it contains positive muons and hadrons.

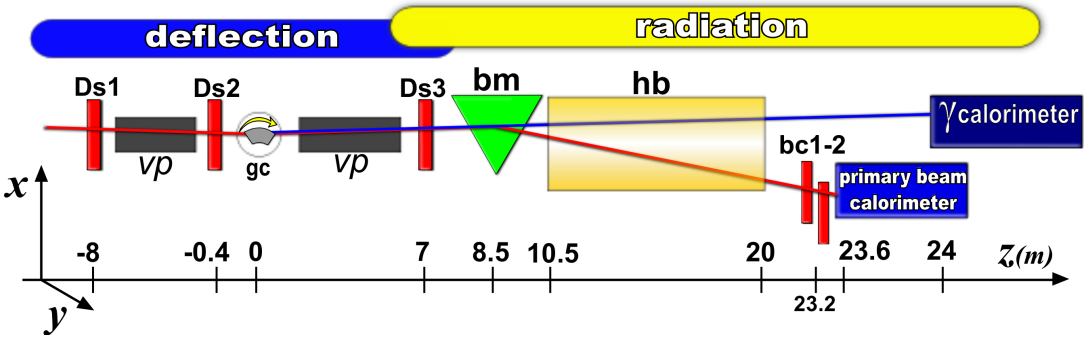

Figure 3.13: The H4 setup. "Deflection part": 3 silicon modules (DsX) separated by vacuum pipes and the high precision goniometer (gc). "Radiation part": a bending magnet (bm), a helium bag (hb), the 9.5×9.5 cm^2 silicon beam chambers (bc1-2), two electromagnetic calorimeters measuring the primary beam energy and the photon one.

- the 3.6 Tm bending magnet separates the charged beam from the neutral photon one.
- after having crossed a helium bag (whose goal is the multiple scattering reduction), the positron reaches two large area silicon microstrip chambers which allow to measure the deflection angle produced by the bending magnet and thus the particle momentum.
- beyond the silicon chambers, the charged particle impinges on an electromagnetic calorimeter that is used to separate positrons from hadrons and muons (given these last ones do not generate a shower in the calorimeter itself).
- the emitted photons travel on a straight line eventually impinging on a second electromagnetic calorimeter that measures their energy.

3.2.1.1 Spectrometer

The spectrometer is designed to measure the momentum and the energy ($\gamma \gg 1$, $E \simeq pc$) E_p of the charged particle after the crystal. The energy lost during the crystal crossing thus will be $E_l = E_b - E_p$, where E_b is the beam energy (120 GeV in this case).
As shown in fig. 3.14, the core of the spectrometer is a bending magnet (green triangle) that deflects the particle depending on its momentum according to:

$$p\phi_b = 0.3BL \tag{3.7}$$

where p is the particle momentum, ϕ_b the bending magnet deflection angle, B the magnetic field and L the magnet length. The magnet used in the test has a maximum BL value of 3.6 Tm; thus $\phi_b = 9$ mrad at 120 GeV/c. Considering eq. 3.7, the measurement of ϕ_b gives the momentum (and thus the energy) of the charged particle.

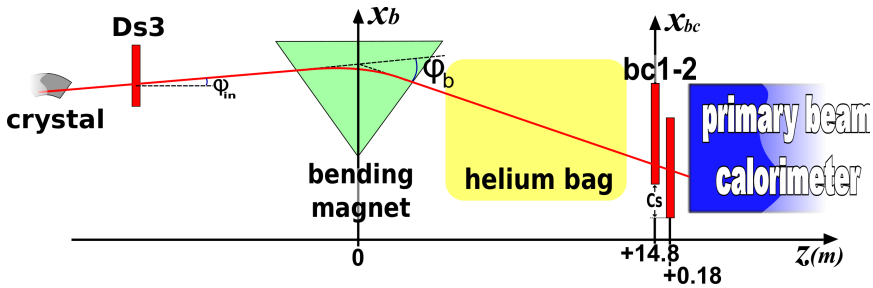

Figure 3.14: Schematic view of the spectrometer: the bending magnet (green triangle), the helium bag (yellow square) and the silicon beam chambers (bc1-bc2) are its main elements. The red line represents the charged particle trajectory; the measured quantities are: the incoming angle towards the magnet, ϕ_{in}; the position inside the magnet, x_b; the position measured by the silicon chambers, x_{bc} and the deflection angle produced by the bending magnet, ϕ_b.

To measure this angle the charged particle trajectory is reconstructed using the silicon miscrostrip detectors:

- the DsX silicon modules (sec. 2.1) track the particle before the magnet allowing to measure the incoming angle to the magnet, ϕ_{in}, and the horizontal position in its center, x_b.
- after the magnet, the particle travels for a distance of about 15 m; this distance acts both as a lever arm to increase the angular resolution and allows to separate in space the photon and the charged beam of $\phi_b \cdot 15$ m=13.5 cm, to measure the photons and the charged beam with two independent calorimeters (avoiding contamination). Most of this space is covered by a 9.6 m long helium bag, to reduce the multiple scattering in air.
- at the end of the line two large area (9.5×9.5 cm^2) silicon chambers[4] measure the particle position, x_{bc}, so that the outgoing angle from the magnet ϕ_{out} can be computed; thus the resulting deflection angle produced by the magnet is $\phi_b = \phi_{out} - \phi_{in}$.

[4]The same detectors have been previously used to perform the low energy measurement, sec. 2.2.5.

The silicon chambers are displaced one with respect to the other in the horizontal direction to increase the angular acceptance of the spectrometer that, in this way, results to be limited by the dimension of the trigger detector; the primary beam calorimeter (which is included in the trigger, sec. 3.2.1.2) in fact has a horizontal acceptance of 15 cm.
Fig. 3.15a presents the comparison of the beam profile measured by the two chambers (taking into account their relative shift): the yellow histogram is the one corresponding to the first chamber (bc1) while the red one to the second chamber (bc2). The peak on the right ($x_{bc} \sim 8$ cm) represents the unperturbed beam ($\phi_b \sim 9$ mrad and $E_l = 0$ GeV); the tail extending to the left is due to the lower energy particles deflected of a larger angle by the magnet.

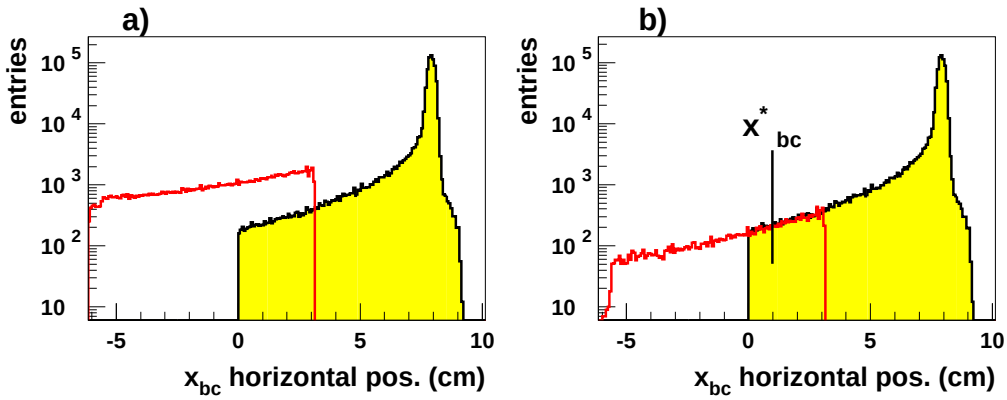

Figure 3.15: The charged particle horizontal position, x_{bc}, measured by the silicon chambers. The yellow histograms are measured with the first chamber and the red ones with the second one: a) all the events are taken into account; b) only the events which satisfy the "vertical residual condition" (fig. 3.17) are considered.

In the region where the chambers overlap ($0 < x_{bc} < 3$ cm), the beam intensity measured by the two detectors is different. This effect has been ascribed to the presence of the primary beam calorimeter that, being too near to the chambers, causes random hits on the chambers themselves because of backscattering. The second chamber being closer to the calorimeter is more subject to this contamination and thus measures a beam profile more intense than the real one. It should be noted that the effect of the "random" hits seems more important since it acts on a region where the intensity of the "good" events is low.
Fig. 3.16 proves the existence of the "random" hits showing the vertical residual

on the second chamber, that is the difference between the vertical position computed using the DsX silicon modules information and the one measured by bc2. Two components populate the distribution: a peaked one that collects the "good" events and a flat one that is not correlated with the incoming beam and thus is random.

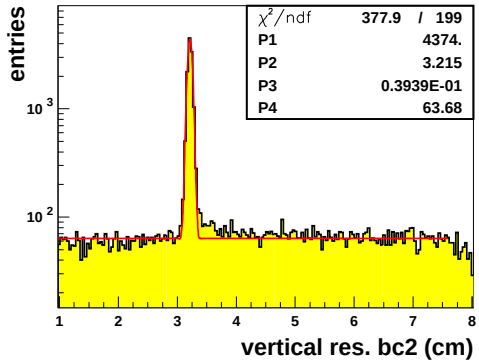

Figure 3.16: The vertical residual on the second chamber that is the difference between the particle position extrapolated from the DsX silicon modules and the one measured by the silicon chambers.

The vertical residual can be used for these studies because the vertical direction is not perturbed by the magnet that acts only in the horizontal plane. This means that the vertical residual can be used to separate the "good" events from the "random" ones. In fact, according to fig. 3.16, if the region within $\pm 3\sigma$ from the peak mean is considered, the percentage of random events becomes very small ($< 2.5\%$).
Fig. 3.17 shows how the vertical residual cut has been implemented for bc-1 (a) and bc-2 (b). The plots show a slight correlation between the vertical residual and the horizontal position, probably generated by a non perfect rotational alignment between the detectors. To take into account this effect the edges of the residual cut are placed at $\pm 3\sigma$ from a mean value that in turn is a function of the horizontal position. The overlapped contour histograms of fig. 3.17 are filled only with the events in the region defined by the residual cut.

Fig. 3.15b shows the result of the "vertical residual cut": the beam profiles measured by the two chambers are overlapping.
Once the two chambers "see" the same beam shape, a single x_{bc} value for each incoming particle is selected in the following way: if the first chamber measures a position $x_2 > x^*_{bc}$ (where x^*_{bc} is a given position, belonging to the chambers overlapping region) $x_{bc} = x_1$, otherwise, the second chamber is checked and if it presents an event $x_2 < x^*_{bc}$, $x_{bc} = x_2$.

The beam profile produced with this algorithm is presented in fig. 3.18a; the valley corresponding to $x_{bc} = x^*_{bc}$ (which in fact should be a delta in the x^*_{bc}

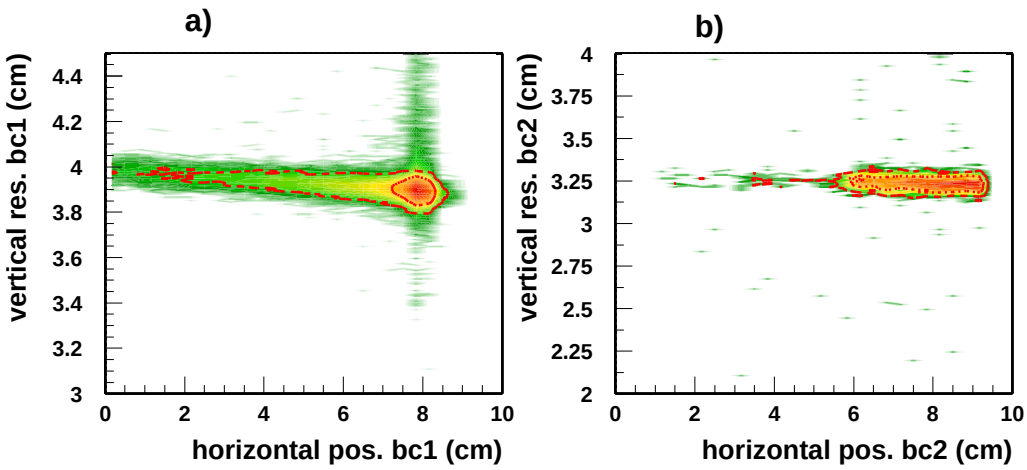

Figure 3.17: The plots show the vertical residual of bc1 (a) and bc2 (b) as a function of the horizontal position measured by the chamber itself. The colored histogram collects all the statistics while the red contour plots are filled only in a region of $\pm 3\sigma$ from the mean residual value.

position) depends on the fact that the beam crosses the chamber with an angle ($\phi_{out} > 9$ mrad) and thus a "shadow" region appears: when the beam profile is converted in the deflection angle ϕ_b distribution (fig. 3.18b), the hole disappears; note that the chamber alignment has been performed so that the peak on the left corresponds to $\phi_b = 9$ mrad (equivalent to 120 GeV).
Considering eq. 3.7, the angle ϕ_b gives the particle momentum after the crystal crossing, p, and assuming $E_p \simeq pc$ (where E_p is the particle energy), the energy loss $E_l = E_b - E_p$ (E_p =120 GeV) can be computed: its distribution is presented in fig. 3.19a.

To estimate the spectrometer intrinsic resolution (at E_p =120 GeV), only the heavy particles (muons and hadrons) should be selected to eliminate the broadening of the distribution by the low energy radiation emission.
This can be done exploiting the particle identification performed by the primary beam calorimeter (sec. 3.2.1.2). The result is presented in fig. 3.19b: the high E_l tail disappears and a fit of the peak with a gaussian function gives a resolution value of 350 MeV (RMS) at 120 GeV that corresponds to about 0.3% of the primary particle energy.

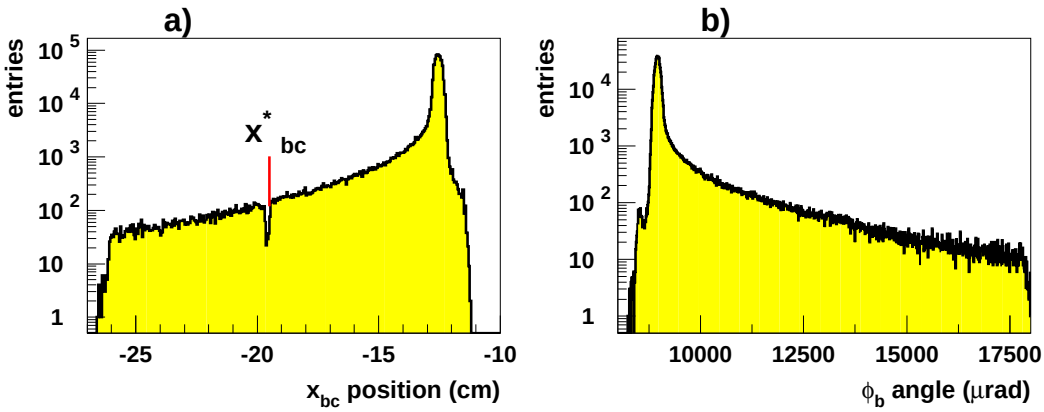

Figure 3.18: a) The x_{bc} position reconstructed using the information of the two chambers. b) The deflection angle ϕ_b produced by the magnet, computed combining the DsX information given by the silicon modules (x_b and ϕ_{in}) with the x_{bc} position measured by the bc1-2 beam chambers (fig. 3.14).

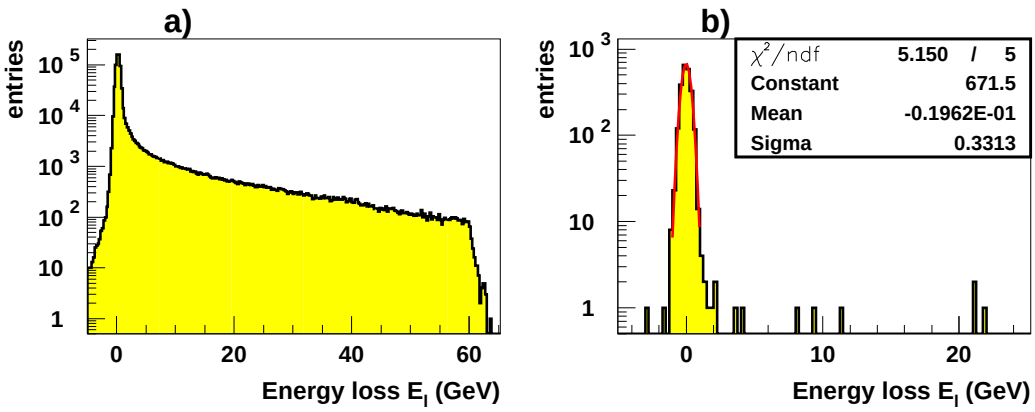

Figure 3.19: The energy loss distributions measured with the spectrometer: a) the whole beam; b) only muons and hadrons (selected with the primary beam calorimeter, sec. 3.2.1.2); the fit with a gaussian function gives a resolution value (RMS) of ∼350 MeV at 120 GeV.

3.2.1.2 Primary beam calorimeter

The H4 beam is produced by the interaction of a primary proton beam with a target; for this reason it is not pure containing a mixture of particle kinds. Acting on the beamline settings (targets and magnet parameters) it is possible to maximize the desired particle kind (positrons in this case); nonetheless a contamination of other particles (muons and hadrons) will be present.
The test on the crystal radiation emission needs the primary particle identification, since the measured radiation spectrum should be evaluated considering the total number of positrons. For this purpose an electromagnetic calorimeter is used exploiting the fact that muons and hadrons do not generate a shower (rarely in case of hadrons) in the calorimeter itself. The calorimeter is shown in fig. 3.20 and is called DEVA. It is a sampling calorimeter composed of 12 plastic scintillator tiles

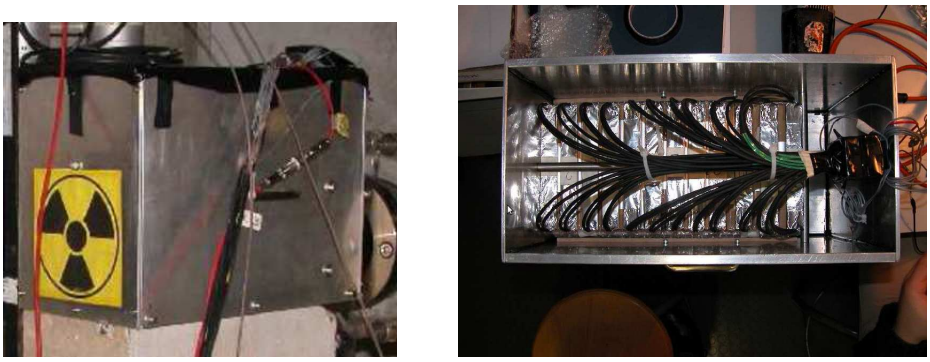

(a) (b)

Figure 3.20: The DEVA calorimeter in its aluminum vessel: the sensitive area is shown by a yellow stick with the radioactive material symbol. b) The DEVA calorimeter from the top (without cover); it is composed of 12 plastic scintillator tiles and 11 lead tiles for a total of 13 X_0. The light produced in the scintillators is carried by WLS fibers to a 16 channel PMT.

interleaved with 11 lead tiles (eight tiles 0.5 cm thick and three 1 cm thick) for a total of about 13 X_0. Each plastic scintillator tile measures $15 \times 15 \times 2$ cm^3. The light is carried by wave-length shifter (WLS) fibers to a multi-anode photomultiplier tube[5] (PMT). During the 2009 beam test, the signal from two consecutive scintillator tiles was read by a single ADC channel to limit the number of channels (the DAQ scheme allowing the DEVA readout is described in sec. 2.1.4).

A typical energy spectrum measured by DEVA is presented in fig. 3.21 showing how the different beam populations can be identified. The positron percentage is around 88%.

[5]HAMAMATSU 16 anode PMT (R5600-M16).

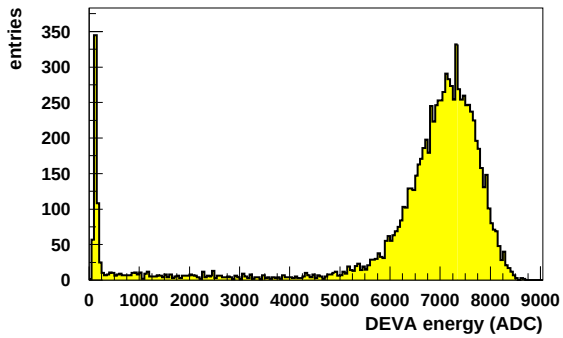

Figure 3.21: The spectrum measured by DEVA (sum of the single tiles signal): the first peak corresponds to the MIPs (Minimum Ionizing Particles) which are mainly muons; the central region is populated by hadrons while the last peak consists of positrons.

Fig. 3.22a shows the longitudinal trend of the energy released in DEVA: while the MIP "region" is constant at about 1100 ADC (the pedestal, that is the baseline measured when no events are present, has not been subtracted in the plot), the energy released by positrons is larger and changes in the different tile pairs according to the shower depth.
To increase the data acquisition efficiency, DEVA may be used in the trigger. In fact, discriminating with a high threshold the signal produced by the tiles in which the energy deposit is maximum (tile pair number 5, $\sim$3500 ADC), a trigger that excludes the muons and part of the hadrons is obtained. Fig. 3.22b shows the primary beam spectrum measured by DEVA when the high threshold trigger is active. The positron percentage increases to 92%.
A further selection on the particle type is then performed during the off-line analysis: an event which has an energy deposit in the 4th tile pair smaller than $\sim$2500 ADC and at the same time does not radiate energy (as measured by the spectrometer or the γ-calorimeter) is not identified as a positron and thus is excluded.

3.2.1.3 The γ-calorimeters

The bending magnet of the spectrometer on one hand allows to measure the particle momentum (sec. 3.2.1.1) and on the other it separates the charged beam from the photon one, so that two independent calorimeters are able to detect the two components.
The primary beam calorimeter is used for the positron identification, while an independent measurement of the photon beam energy with respect to the spectrometer one is useful for three reasons:

- to cross-check immediately that the spectrometer works properly.

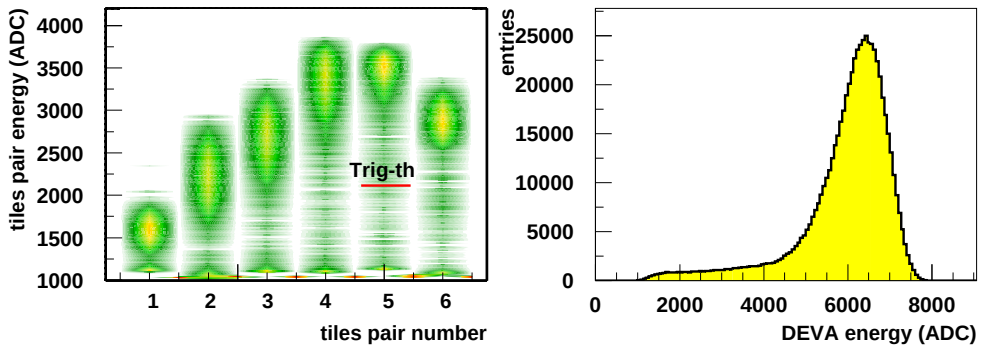

Figure 3.22: a) The longitudinal trend of the energy release in DEVA: on the horizontal axis, the tile number (every number corresponds to a tile pair); on the vertical one, the signal in ADC (without the pedestal subtraction). b) The total spectrum measured by DEVA with a DAQ trigger including the high threshold one on the 5th pair (marked in red in (a)).

- to integrate the spectrometer measurement in the medium-high energy loss range, where its resolution worsens (the multiple scattering contribution to the ϕ_b angle increases as the primary particle energy decreases) and the calorimeter resolution becomes better (sec. 3.2.1.5).

- to measure the photon spectrum in the high energy loss range (till the nominal energy of the beam, $E_l = E_b$). In this range the primary particle energy E_p is small and thus the deflection ϕ_b induced by the magnet becomes too large to be measured in a spectrometer geometry like the one presented in sec. 3.2.1.1 (unless the surface covered by the silicon detectors is greatly increased).

A calorimetric system able to satisfy the previous requirements has been developed in three steps corresponding to three different apparatuses that will be described in the following sections. As it will be shown, the system has been completed only in the 2010 beam test (using the "Jack"[6] calorimeter, sec. 3.2.1.6); thus in 2009 the γ-calorimeter has been used just to cross-check the spectrometer behaviour without limiting anyway the experimental study, since in channeling and VR, the interesting energy loss range is the low-medium one (sec. 3.2.2).

[6]Jack is a conventional name chosen to identify the detector.

3.2.1.4 The Rino calorimeter

The first calorimeter used in the crystal radiation test performed on the H4 beam-line, shown in fig. 3.23, is called “Rino”.
It is a homogeneous calorimeter consisting of 4 NaI blocks with a sensitive area

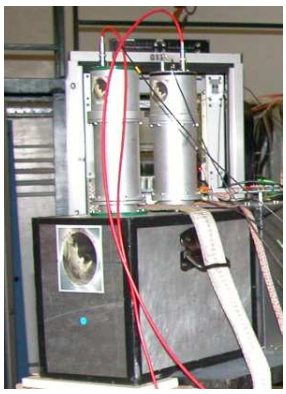

Figure 3.23: A photo of the Rino calorimeter. The bottom vessel contains 4 $20 \times 20 \times 5$ cm^3 NaI blocks; the aluminum tubes contain two photomultipliers.

of 20×20 cm^2 and a thickness of 5 cm for a total length of 20 cm, corresponding to 7.7 X_0. The light readout is performed by two photomultiplier tubes, one each couple of blocks.
Figg. 3.24a-b show the photon beam energy spectrum in the calorimeter, after the pedestal subtraction. In both cases the spectrum extends up to about 3000 ADC corresponding to the saturation of the ADC board.

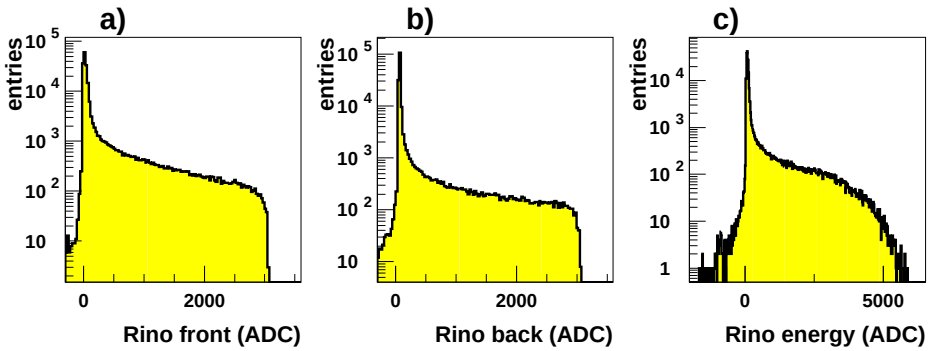

Figure 3.24: a-b) The energy spectrum in the two parts of Rino-cal; c) the total energy deposited in Rino determined as the normalized sum of the two channels (a+b).

The saturation affects of course also the total spectrum that is obtained as the

sum of the two channels (once normalized considering the MIP signal) and is presented in fig. 3.24c.
The ADC saturation does not represent a crucial problem, given that the Rino calorimeter would anyway not be able to measure the total energy released by the high energy photons being too short; for example the shower of a 25 GeV photon would deposit the maximum energy at about 7.7 X_0, a value corresponding to the whole length of the Rino calorimeter.
For this reason the Rino calorimeter has been used just to cross-check the spectrometer behaviour as confirmed by the scatter plot of fig. 3.25a in which the proper photon energy measured by Rino-cal is presented as a function of the energy loss value provided by the spectrometer, showing the expected linear correlation between the two observables.

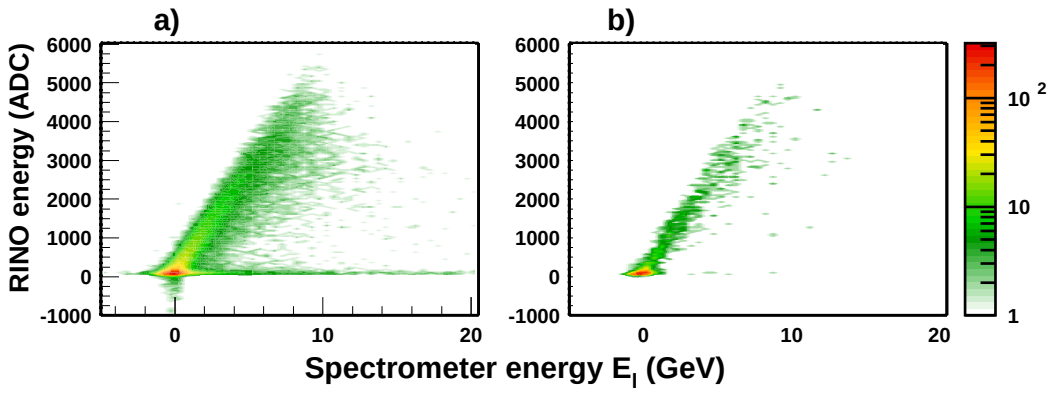

Figure 3.25: The energy measured by Rino-cal as a function of the one measured by the spectrometer; the two measurements are linearly correlated as expected. a) The whole beam; b) only the particles impinging on the crystal.

Fig. 3.25 underlines also that besides the events properly correlated (filling the central region of the plot), there is a second, less populated, event class, filling the bottom of the plot and consisting of the events detected by the spectrometer and not by the calorimeter. These events are probably correlated with particles belonging to the beam tails that for some reasons are not correctly tracked. In fact, once the same plot is produced only for the particles impinging on the crystal (fig. 3.25b), these events disappear.

3.2.1.5 The Willie calorimeter

During the 2009 beam test, Rino-cal has been substituted with another calorimeter with the twofold aim of testing an innovative calorimetric system (with a Silicon PhotoMultiplier readout [80]) and extending the energy range covered by the γ-calorimeter itself.
This second calorimeter is a "shashlik" one called Willie [81]. Willie is composed of 41 tiles of plastic scintillator and 40 tiles of lead; each tile has an area of 8×8 cm^2 and is 3.27 mm thick for a total of 24 X_0.
The word "shashlik" refers to the scintillation light collection and transport method, consisting in 64 0.8 mm WLS fibers[7], that cross the whole calorimeter longitudinally, so that each fiber collects the light of all the scintillator tiles.
Fig. 3.26a presents a photo of the calorimeter contained in a 1 cm thick aluminum vessel and of its back side; the WLS fibers are bundled together in groups of 4 fibers each bundle, with a SiPM for each group. Each SiPM consists of a matrix

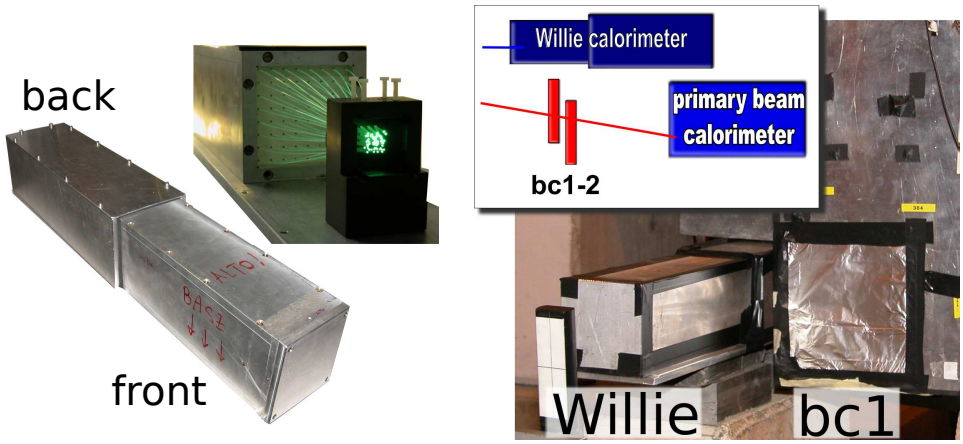

(a) (b)

Figure 3.26: a) Two photos of the Willie calorimeter: its front part contains the active region while fibers and SiPMs are interfaced together in the back (top photo). b) The Willie calorimeter in the H4 line near the silicon chamber (bc1); the top box shows a schematic of this layout section.

of pixels, acting as passive-quenched silicon avalanche photodiodes operated in limited Geiger-mode. Each pixel (with a typical size of 20×20 - 100×100 μm^2) gives the same current response when hit by a photon (a Geiger-like discharge): the SiPM output signal, which is given by the analog sum of all the pixels since they are connected together, is proportional to the number of incoming photons.

[7] Produced by Kuraray (model Y11).

The SiPMs used in Willie are manufactured by FBK-irst (Trento, Italy) and have a sensitive area of $\sim$1 mm^2 corresponding to 688, 40$\times$40 μm^2 pixels; their output signal was not amplified in order to simplify as much as possible the readout electronics.

Fig. 3.26b shows the calorimeter installed on the H4 beamline next to the bc-1 silicon beam chamber. Unfortunately this proximity has generated an interference problem with the spectrometer (noted only during the off-line analysis): the lateral leakage has generated ghost hits on bc-1 which do not allow to determine the position of the primary particle unambiguously.
This effect can be observed in fig. 3.27 where the beam profiles measured by the two chambers are compared before (a) and after (b) the cut on the vertical residual (sec. 3.2.1.1). Even after the cut, the plots are not equalized; the first chamber apparently measures a lower intensity.
This happens because the plots are filled with the events presenting a single particle, that is only one cluster[8] on each detector, to make the ϕ_b angle measurement possible. But when a high energy photon is emitted and the first chamber sees a multi-cluster event (originated by the calorimeter leakage) this is excluded from the analysis causing the under-estimation of the number of the events as in fig. 3.27b.
This phenomenon is also proved by the increase of the number of the multi-cluster (rejected) events measured by the first chamber after the Willie-cal installation.

The installation of the Willie calorimeter has compromised the spectrometer use; nevertheless the analysis on the crystal can be performed using the calorimeter itself that, as will be shown, has proven to work properly.
The energy deposit in Willie-cal is obtained as the sum of the different channels, after the equalization of their response to the MIP signal. Fig. 3.28a presents the resulting value as a function of the energy loss computed using the spectrometer (the multi-cluster events have been excluded).
The linearity is good up to 10 GeV, but at higher energies a clear saturation effect appears due to the relatively small number of pixels in the 1 mm^2 SiPMs compared to the large flux of optical photons produced at this energy. The SiPM saturation, that can be reduced with larger area SiPMs (sec. 3.2.1.6), worsens the calorimeter performances in terms of resolution but does not prevent from using it to measure the energy loss E_l in place of the spectrometer. To do this a calibration is needed, which can be performed using the information of the spectrometer.

Fig. 3.28b shows two vertical slices of fig. 3.28a, corresponding to $E_l = 13$ GeV and $E_l = 55$ GeV: the distributions are fitted with a gaussian function. Once this procedure has been repeated on all slices, the gaussian mean ADC values give the curve presented in fig. 3.29 whose parameters (it is fitted with a 4 degree polyno-

[8] A cluster is a set of contiguous strips detecting the energy deposited by a particle.

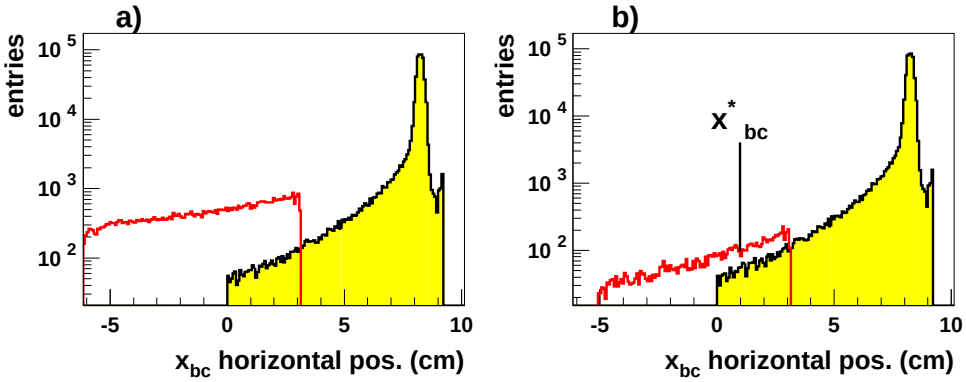

Figure 3.27: The primary particle horizontal position x_{bc} measured by the silicon chambers after the Willie-cal installation. The yellow histograms are measured by the first chamber (bc1) and the red ones by the second chamber (bc2): a) all the events are taken into account; b) only the events which satisfy the cut on the vertical residual (sec. 3.2.1.1) are considered. The data presented in these plots and in the following analysis refer to a run in which the "background" (photons generated by the detectors and along the beamline) is the prevalent component.

mial function) give a one to one relation between the E_l value measured by the spectrometer and the ADC one recorded by Willie.

Fig. 3.29b presents the trend of the calorimeter resolution $\Delta E/E$ (where ΔE and E are respectively the σ and mean of the gaussian fit) as a function of the energy loss E_l. Even in the low energy range (where the calorimeter has a lower resolution with respect to the spectrometer) the resolution value is acceptable for the study to be performed on crystal radiation production (no fine structure in the spectrum is expected).
To give an example, at 10 GeV the plot gives a resolution of 6% corresponding to a RMS uncertainty of 600 MeV (ΔE_{tot}). Given that the spectrometer has a RMS error of about 350 MeV (ΔE_{sp}), the calorimeter intrinsic resolution can be computed as $\Delta E_w = \sqrt{E_{tot}^2 - E_{sp}^2} \simeq 490$ MeV comparable with the spectrometer one.

Once the calorimeter has proven to be a valid alternative to the spectrometer, its output should be "linearized" and rescaled using the inverse of the function that fits fig. 3.29a. The validity of this operation is shown in fig. 3.30a where there is a perfect linearity between the "reconstructed" calorimetric energy and the measured spectrometer one.

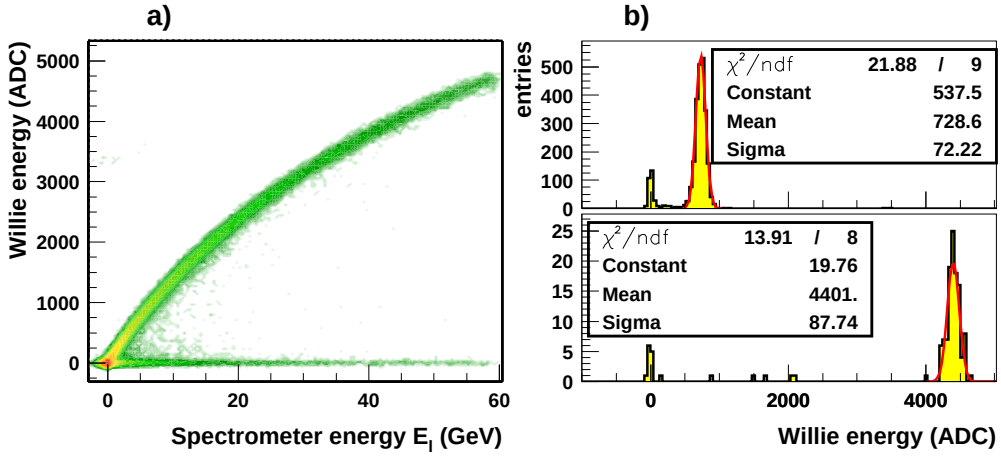

Figure 3.28: a) The energy deposit in Willie-cal as a function of the one measured by the spectrometer. b) Two slices of plot (a) corresponding to $E_l = 13$ GeV and $E_l = 55$ GeV; the mean and σ parameters provided by the gaussian fits are used to calibrate the calorimeter and measure its resolution.

Fig. 3.30b presents the resulting energy spectrum; note that in this case also the events with more than one cluster on the chambers can be considered, so that the spectrum has a continuous and smooth shape.

3.2.1.6 The 2010 beam test (the Jack calorimeter)

In June 2010 a new beam test on the H4 beam has been performed to go on with the radiation emission study extending it to the axial effects characterization and to negative particles; some of the results will be described in chap. 4.
This section presents the novelties introduced in the experimental setup with respect to 2009:

- *a new trigger system.*
  The old trigger logic was based on the high threshold discrimination of the DEVA calorimeter signal (sec. 3.2.1.2) to increase the percentage of acquired positrons. Since the intrinsic beam purity proved to be high ($\sim 88\%$ of positrons), this strategy has been abandoned using a couple of scintillators (s1-2, scheme in fig. 3.31a) placed in front of the Ds1 silicon detector (fig. 3.31b). In this way, the incoming particles trigger the DAQ also when they do not reach DEVA, being deflected too much by the bending magnet

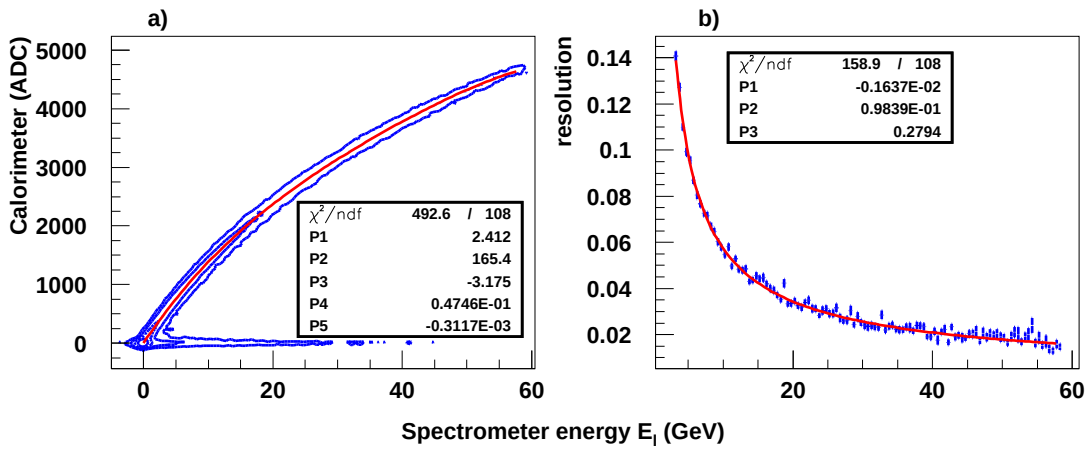

Figure 3.29: a) The energy deposit in Willie as a function of the one measured by the spectrometer with the polynomial function, which fits the trend, superimposed; b) the calorimeter resolution as a function of the energy loss E_l measured by the spectrometer (the values include the spectrometer contribution).

($E_l > 60$ GeV). The s2 scintillator has a hole and it can act as an anti-coincidence, so that two trigger logics are available: the single trigger on s1 to detect the whole beam acquiring statistics fast during the setup commissioning and the anti-coincidence ($s1 \wedge \overline{s2}$) one to acquire a beam portion that matches the crystal shape thus increasing the number of events impinging on the crystal itself. The anti-coincidence has been preferred to a coincidence because in this way only one scintillator (7 mm thick) is crossed during the "crystal physics" runs limiting the background contribution due to bremsstrahlung.

- *a different arrangement of the beam chambers and the calorimeters.*
  The 2009 beam test was affected by the interference problems between the calorimeters and the spectrometer due to the calorimeter leakage that creates ghost hits on the silicon beam chambers. This problem has been solved increasing the distance between the different elements so that the chambers are placed before the γ-calorimeter that in turn is located before DEVA as it is shown in fig. 3.32a.

- *a new γ-calorimeter (Jack-cal) readout with 3 mm^2 SiPMs.*
  The most remarkable novelty of the 2010 beam test has been the introduc-

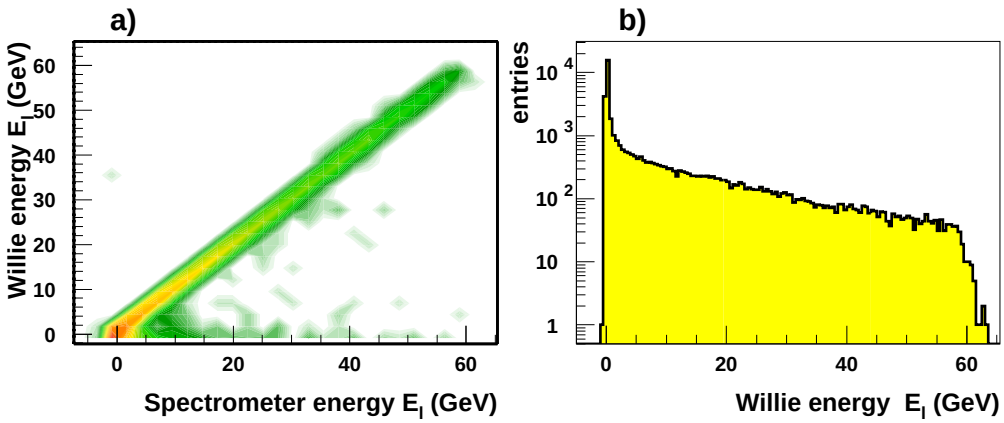

Figure 3.30: a) The energy released in Willie-cal, after the calibration as a function of the one measured by the spectrometer; b) the overall spectrum measured by the calibrated Willie-cal.

tion of a new γ-calorimeter; it is called Jack (fig. 3.32b). As well as Willie (sec. 3.2.1.5), Jack is a "shashlik" calorimeter, composed of 70 tiles, 4 mm thick, of plastic scintillator and 69 tiles, 1.5 mm thick, of lead, for a total of 19 X_0. Each tile has an area of 12×12 cm^2; the scintillation light is brought by 1.2 mm WLS fibers [9] to 16 silicon photomultipliers[10] with an active area of 9 mm^2.

Fig. 3.33a shows the Jack output in ADC counts as a function of the energy loss given by the spectrometer; the blue lines represent the scatter plot, while the overlapped red line is the fit of the mean Jack energy, obtained with a series of gaussian fits (the procedure has been described in sec. 3.2.1.5). Comparing the plot with the equivalent one produced with the Willie calorimeter (fig. 3.29) the Jack linearity improvement obtained using larger area SiPMs can be noted. Fig. 3.33b shows the Jack-cal resolution trend as a function of E_l.

The trigger strategy used during the 2010 beam test allows to acquire particles with an energy loss value larger than what the spectrometer can measure (due to the finite dimensions of the bc1-2 silicon chambers). The energy lost by these positrons should be measured by the γ-calorimeter. For this reason the calorimeter calibration has been extended to the region $E_l > 63$ GeV, beyond the spectrometer

[9] BCF-9224, produced by Saint-Gobain.
[10] Produced by FBK-irst, Trento, Italy.

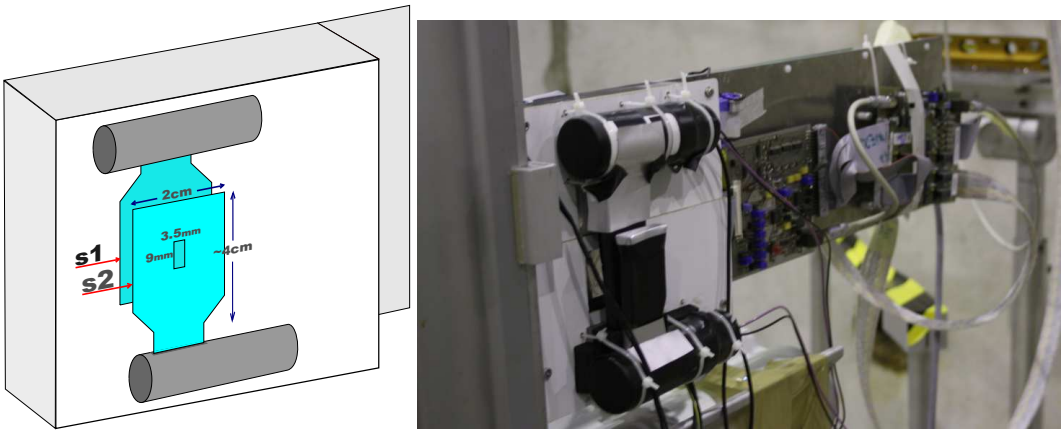

(a) (b)

Figure 3.31: a) A schematic drawing of the s1-2 scintillators mounted on the Ds1 detector; each of them is 2×4 cm^2 with a thickness of 7 mm and it is readout by a single anode 931-B photomultiplier, produced by HAMAMATSU. b) A photo of the s1-2 scintillator in the H4 beamline.

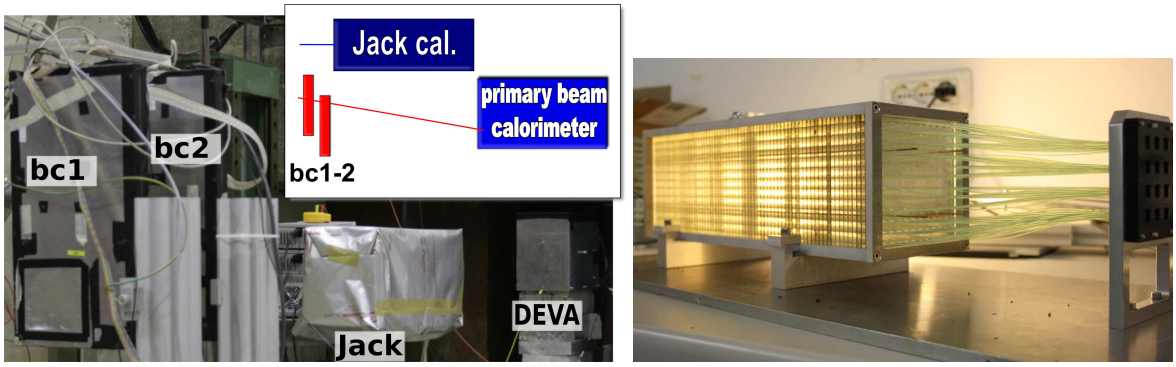

(a) (b)

Figure 3.32: a) The Jack calorimeter in the H4 beamline during the 2010 beam test; it is located after the silicon chambers as shown in the top box scheme. b) A photo of the calorimeter: its front part contains the active region while fibers and SiPMs are interfaced in the back.

limit.

Fig. 3.34 presents the energy deposited in Jack by the primary beam (the bending magnet was switched off) with an energy of 80 GeV (a), 100 GeV (b) and 60 GeV (c). The peak representing the positron population has been fitted with a gaussian to obtain the corresponding mean value in ADC.

Fig. 3.35 shows the Jack calibration curve obtained using the spectrometer information at low energy (fig. 3.33a) and the direct primary beam detection

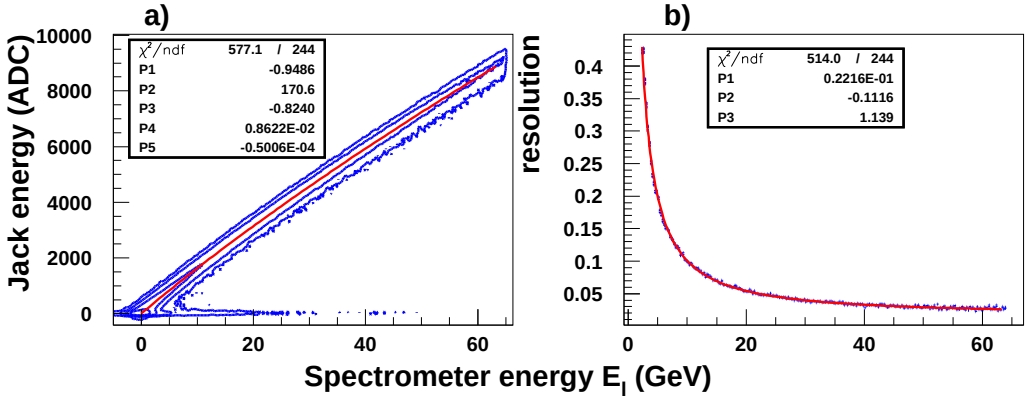

Figure 3.33: a) The energy deposit in Jack-cal as a function of the E_l energy loss measured by the spectrometer (scatter plot in blue) with the polynomial function which fits the trend (red line); b) the calorimeter resolution as a function of the energy loss E_l measured by the spectrometer (the values include the spectrometer contribution).

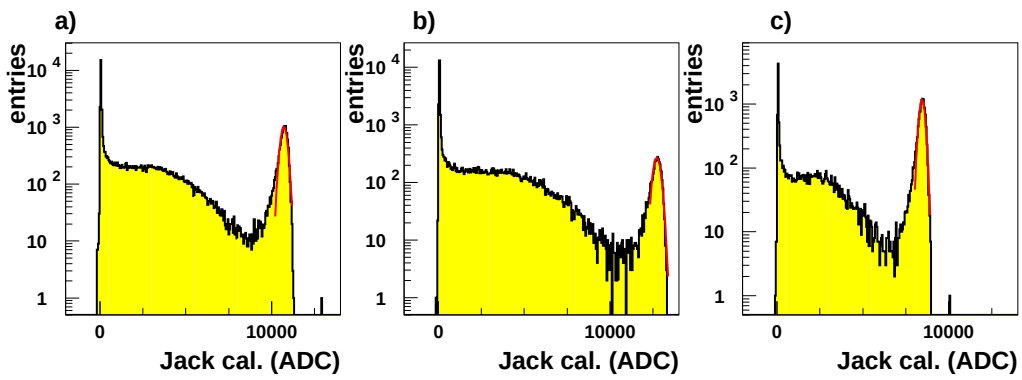

Figure 3.34: The energy spectrum of the primary beam measured by Jack-cal for a 80 GeV (a), 100 GeV (b) and 60 GeV (c) beam.

(fig. 3.34a) at high energy. The point at 60 GeV demonstrates the agreement between the two measurements. The information provided by the fit parameters allows to obtain the E_l energy loss in GeV.

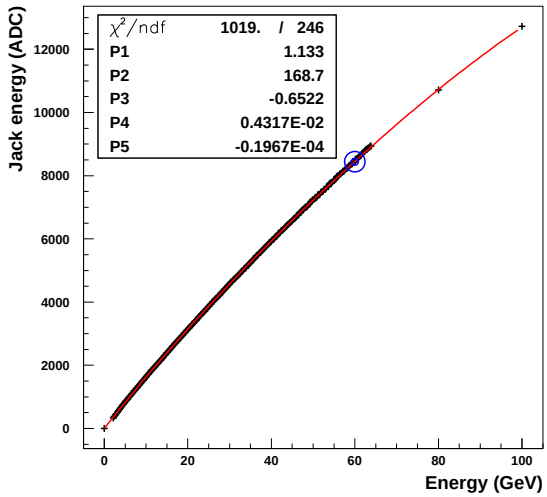

Figure 3.35: Jack calibration obtained using the E_l measurement performed by the spectrometer for an energy$<$ 62 GeV and the direct measurement of the primary beam energy for the points at 80 GeV and 100 GeV. The blue point, corresponding to a primary beam energy of 60 GeV, is used to cross-check the two independent measurements.

3.2.2 Analysis and results

The 2009 beam test on the H4 beamline has been dedicated to the development of the experimental setup and to the investigation of channeling and volume reflection from the radiation emission point of view.
This section will start (sec. 3.2.3) presenting the characteristics of the crystals, measured following the methods described in chap. 2 and the evaluation of the background radiation contribution and of the amorphous one. Then the emitted radiation in channeling (sec. 3.2.4) and volume reflection (sec. 3.2.5) will be measured and compared with the theoretical models presented in sec. 3.1.

3.2.3 Crystals and background

The channeling and VR radiation emission investigation has been performed using two silicon strip crystals bended with curvatures radii of about 5 m and 10 m. These crystals have been fully characterized following the procedure presented in chap. 2 and their features are summarized in tab. 3.1.

Crystal	orientation	length (mm)	torsion $\left(\frac{\mu\text{rad}}{\text{cm}}\right)$	ϕ_c (μrad)	R(m)
StR5	(110)	2	181.8	403.5±1.3	4.96±0.02
StR11	(110)	2	52.7	186.5±3.9	10.72±0.22

Table 3.1: Characteristics of the strip crystals investigated during the 2009 H4 beam test.

The experimental setup presented in sec. 3.2 has been designed to measure the radiation emitted by the crystal; anyway a background contribution, produced by the detectors placed before the bending magnet (the DsX silicon telescopes) and along the beamline, is present.
In sec. 3.2, the spectra of the background contribution have been used to show the behaviour of the spectrometer (fig. 3.28) and of the γ-calorimeter (fig. 3.19). Fig. 3.36 presents the passage from raw data to a normalized distribution:

- the first plot is the raw histogram, that is the number of events $\Delta N(E_{l0})$ acquired in the range $E_{l0} < E_l < E_{l0} + \Delta E_{l0}$.

- rescaling ΔN for the total number of incoming positrons N_{tot} (well approximated by the number of the entries of the histogram) and dividing it by the bin size of the histogram ΔE, the photon spectrum $\frac{dn}{dE_l}$ is obtained (fig. 3.36b).

- to extract the energy loss distribution $\frac{dn}{dE_l} \cdot E_l$ (fig. 3.36c), each point of the (b) plot should be multiplied by the corresponding E_l value.

Integrating the energy loss distribution presented in fig 3.36c, the average energy loss per positron without crystal (background) is obtained. The integration interval is $3 < E_l < 60$ GeV; the low threshold ($E_l = 3$ GeV) has been chosen to exclude the low energy peak caused by the finite resolution on E_l. The integral gives an average background energy loss of $\bar{E}_l^{Bg}$=1.72$\pm$0.02 GeV.

Fig. 3.37 shows the photon (a) and the energy loss (b) spectra, measured selecting the particles impinging on the crystal, that is misaligned of 4 mrad with respect to the channeling orientation and thus behaves as an amorphous material. The obtained spectra represent the sum of the crystal contribution and the background one; this last one has been superimposed (green points) for comparison.
Since the probability for a positron to lose more than 3 GeV (computed as the integral of fig. 3.37a) is much lower than one ($\sim$19%), the crystal contribution and the background one can be considered independent, so that the amorphous contribution can be obtained subtracting the background, as shown in fig. 3.37c. The plot fit with a constant function gives the percentage of energy lost by a positron crossing the crystal in an amorphous condition: 2.10$\pm$0.17% that is compatible with the expected value of 2.05% (computed as $1 - e^{(-l/X_0)}$ where l and X_0 are the crystal length and the silicon radiation one). According to the measurement, the average energy loss in the amorphous condition is $\bar{E}_l^{Am} = 1.20 \pm 0.1$ GeV (for $3 < E_l < 60$ GeV).

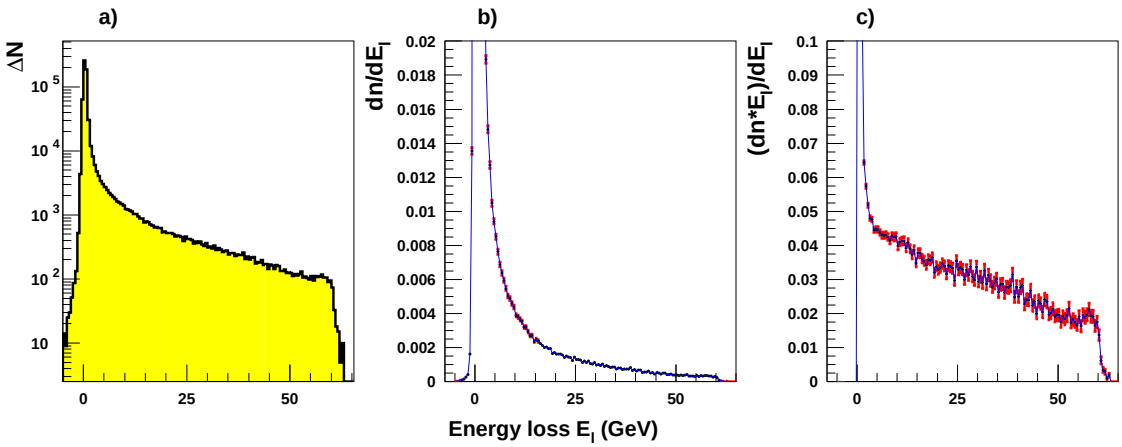

Figure 3.36: Spectra of the background (without crystal) radiation contribution: a) the number of acquired events (ΔN); b) the photon spectrum $\frac{dn}{dE_l}$; c) the energy loss spectrum $\frac{dn}{dE_l} \cdot E_l$.

3.2.4 Channeling

The combination of the "deflection" and the "radiation" part of the setup presented in sec. 3.2 allows to measure the radiation spectra emitted by the crystal in a given incoming deflection angle range.
For what concerns channeling, it is possible to take into account only the channeled particles selecting also the desired incoming divergence.
Fig. 3.38 shows the plots involved in the channeling radiation study, collecting the statistics of a single DAQ performed with the StR5 crystal oriented in channeling:

- a) the distribution of the local divergence (sec. 2.2.1) impinging on the crystal, $p(\alpha^*)$.
- b) the scatter plot of the deflection angle ϕ as a function of α^*; in the central part of the plot the channeling peak is present.
- c) the energy loss distribution ($\mathrm{d}nE_l/\mathrm{d}E_l$) of the channeled particles as a function of α^*, obtained selecting the particle with $\phi < -300$ μrad (note that the statistics is present only in correspondence of channeling).

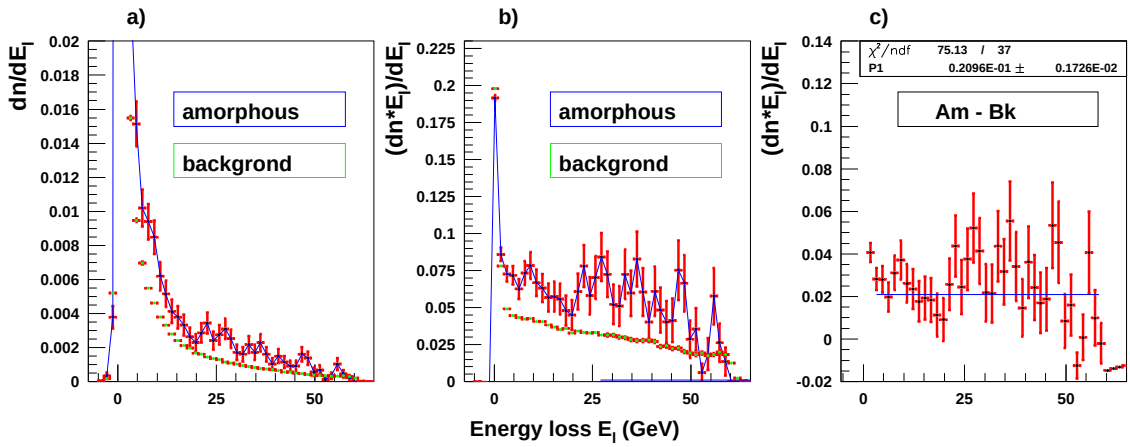

Figure 3.37: The photon spectrum $\frac{dn}{dE_l}$ (a) and the energy loss one $\frac{dn}{dE_l} \cdot E_l$ (b): the blue lines represent the particles impinging on the crystal oriented in amorphous condition and the green points the beam portion outside the crystal (background). c) Subtracting the background contribution, the energy loss produced only by the crystal is obtained.

Fig. 3.38c shows that in principle it is possible to obtain the energy loss spectrum for any arbitrary value of α^* but in practice a finite angular range should be considered due to the limited statistics. Doing so, the shape of the α^* distribution could influence the obtained spectrum, thus a procedure to obtain the spectra independently from the incoming angle distribution shape has been implemented:

- the histogram presented in fig. 3.38c is divided in vertical slices representing the spectral distribution before the normalization ($\Delta N(E_l) \cdot E_l$ or $\Delta N(E_l)$) as a function of α^*. For each slice (called s_j) the number of incoming positrons $p(\alpha^*)_j$ (fig. 3.38a) is computed.

- a new spectrum (s_{tot}) is obtained summing the s_j slices weighting their contribution for the number of the incoming positrons related to slice $p(\alpha^*)_j$,

$$s_{tot} = \sum \frac{s_j}{p(\alpha^*)_j} \tag{3.8}$$

  In this way, after the normalization, s_{tot} will correspond to the spectrum produced by an equiprobable α^* distribution. Depending on the j values taken into account in the sum, the analyzed α^* interval is chosen.

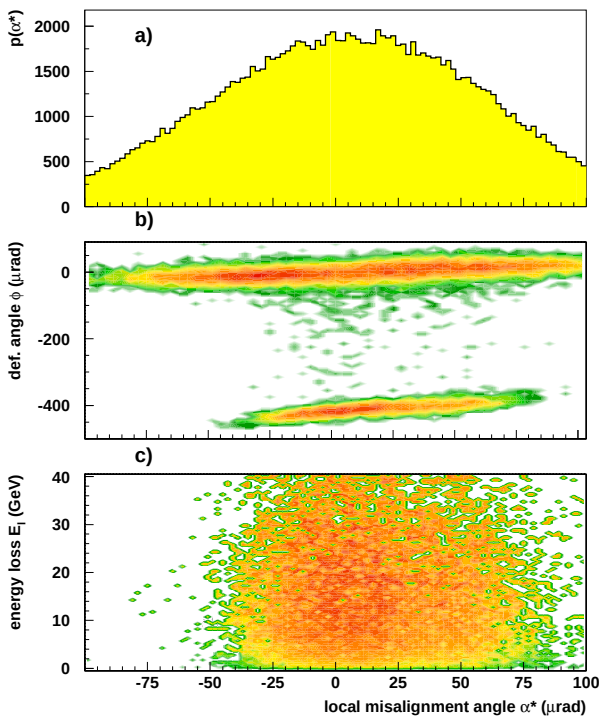

Figure 3.38: The whole statistics collected during a single DAQ with the StR5 crystal in channeling. The following quantities are plotted as a function of the local misalignment α^*: a) the α^* distribution itself $p(\alpha^*)$; b) the deflection angle ϕ; c) the energy loss E_l weighted on E_l itself to obtain $\frac{dn}{dE_l} \cdot E_l$ (only for the channeled particles, that is $\phi < -300$ μrad).

- to define the α^* ranges, the angle corresponding to the best crystal alignment should be identified (using the procedure shown in fig. 2.27); for the StR5 crystal (fig. 3.38b) this angle is $\alpha_0^* \sim 6.6$ μrad.

- once α_0^* is known, the angular ranges, symmetric with respect to this value, can be defined taking into account: the central region of the channeling peak ($|\alpha^* - \alpha_0^*| < \alpha_{r1}^*$) or the external one ($|\alpha^* - \alpha_0^*| > \alpha_{r1}^*$ and $|\alpha^* - \alpha_0^*| < \alpha_{r2}^*$ with $\alpha_{r1}^* < \alpha_{r2}^*$, where $\alpha_{r1}^*, \alpha_{r2}^*$ are the parameters determining the range size).

Fig. 3.39 shows the energy loss spectrum of the particles channeled by the StR11 (a) and the StR5 (b) bent crystals: the red points correspond to the central region of the channeling peak ($|\alpha^* - \alpha_0^*| < 3$ μrad) while the black ones to the external portion of the peak ($|\alpha^* - \alpha_0^*| > 5$ μrad and $|\alpha^* - \alpha_0^*| < 20$ μrad).

Fig. 3.39 shows a similar behaviour of the two crystals with different curvature radii, confirming the negligible effect of the crystal bending on the radiation emission (sec. 3.1.1).
Comparing the different angular ranges, no clear differences are recognizable; probably the high uncertainty (due to the low statistics) does not allow to identify the slight discrepancies that should be caused by the difference in the transversal energy distribution.

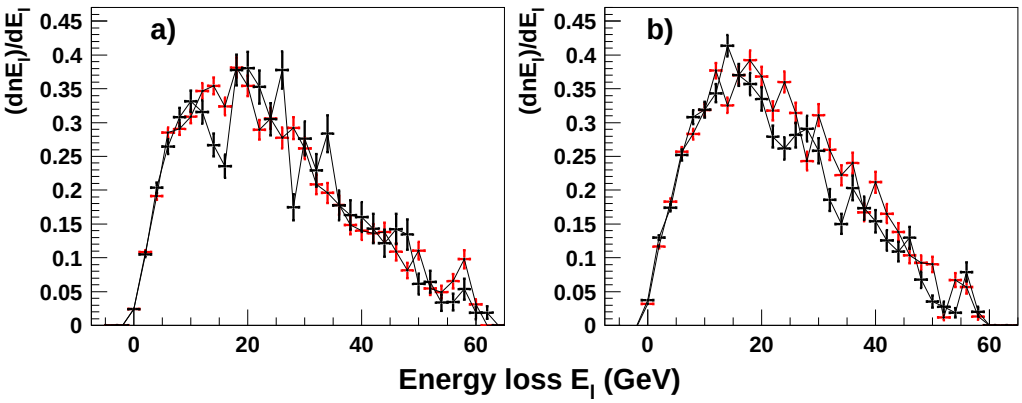

Figure 3.39: The energy loss spectra in channeling for: a) the StR11 crystal (using the spectrometer) and b) the StR5 one (using the Willie calorimeter). The red points correspond to the range $|\alpha^* - \alpha_0^*| < 3$ μrad while the black ones to $|\alpha^* - \alpha_0^*| > 5$ μrad and $|\alpha^* - \alpha_0^*| < 20$ μrad.

Fig. 3.40a for the StR11 crystal (and b for the StR5 one) presents the comparison between the measured energy loss spectrum in channeling (black points with the red error bars) and the one obtained with the simulation described in sec. 3.1.1 (blue lines). The angular range taken into account is $|\alpha^* - \alpha_0^*| < 20$ μrad; the green line represents the radiation emission in the amorphous condition (background subtracted, sec. 3.2.3). The agreement with the simulation (within the experimental errors) is rather good; the measured average energy loss is $\bar{E}_l^{ch}$ =11.69±0.08 GeV for the StR11 crystal and $\bar{E}_l^{ch}$ =11.67±0.07 GeV for the StR5 one, while the value provided by the simulation is $\bar{E}_l^{ch}$ =11.98 GeV.

3.2.5 Volume Reflection

Sec. 3.1.2 describes the radiation emission in volume reflection extending the coherent bremsstrahlung model to bent crystals. Fig 3.10 has been used to present the straight crystal radiation emission as a function of its misalignment with the beam: in addition to the channeling radiation, for $\alpha \sim 0$ two external tails represent the coherent bremsstrahlung.
The equivalent of that plot for a bent crystal (the StR11 one) has been recorded during the 2009 H4 beam test and is shown in fig. 3.41.

The top plot of fig. 3.41 presents the deflection angle ϕ as a function of the

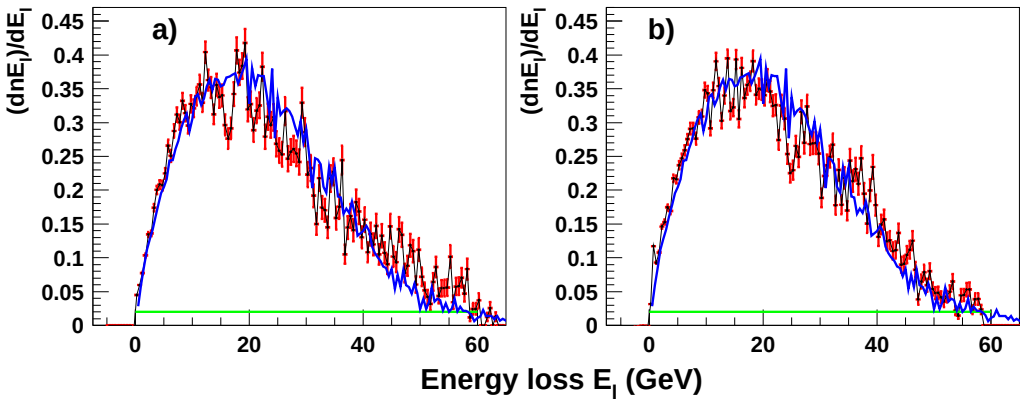

Figure 3.40: Comparison between the measured (black points) and simulated (blue line) energy loss spectra for the StR5 crystal (a) and the StR11 one (b); the green lines represent the radiation emission in the amorphous condition.

misalignment one α^* as a reference to identify the channeling alignment ($\alpha^* \sim$ 12025 μrad) and the volume reflection region (11825 μrad$< \alpha^* <$ 12025 μrad). The second plot shows the photon spectrum (dn/dE_l) and the third one the energy loss spectrum $\left(\frac{dn}{dE_l} \cdot E_l\right)$.
The enhancement in the radiation emission can be clearly defined and some qualitative differences with respect to the straight crystal (fig 3.10) can be recognized: the angular region, interested by the radiation enhancement, is no more centered around the best alignment (channeling) and its acceptance is larger being approximately determined by the VR one, that depends on the crystal curvature (an adjustable parameter). Moreover the spectral shape is almost uniform with respect to the misalignment angle; this is due to the crystal curvature that changes the angle between the particle trajectory and the crystal planes during the crystal crossing, producing a “mixed”, more uniform effect.

Fig. 3.42 shows the comparison between the measured energy loss spectrum in volume reflection (black points with the red error bars) and the one provided by the analytical calculation as described in sec. 3.1.2 (blue lines).
Fig. 3.42a refers to the StR11 crystal while the StR5 crystal spectrum is shown in (b). Both plots have been produced using the procedure described in sec. 3.2.4 to emulate an equiprobable incoming angle distribution.

Defining α_1^* as the middle point of the VR angular acceptance, the ranges

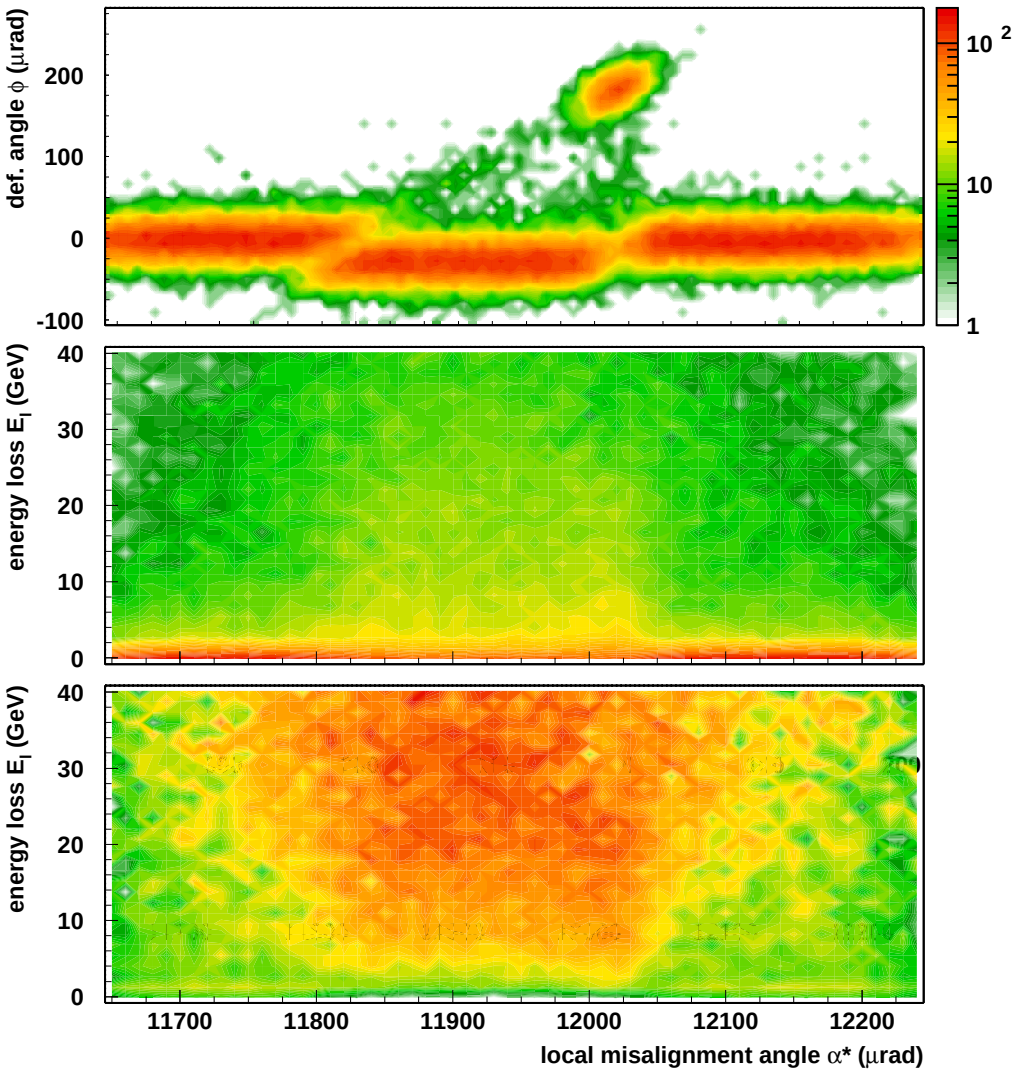

Figure 3.41: The scatter plots present as a function of the local misalignment α^* the ϕ deflection angle and the energy loss E_l. In the bottom plot each histogram entry is weighted for the energy loss value itself so that the intensity color scale represents the energy loss spectrum $\frac{dn}{dE_l} \cdot E_l$.

considered in fig. 3.42 are: $\alpha_1^* - 60$ μrad$< \alpha^* < \alpha_1^* + 20$ μrad for the StR11 crystal (a) and $\alpha_1^* - 200$ μrad$< \alpha^* < \alpha_1^* + 200$ μrad for the StR5 one (b).

Differently from channeling, in VR both the shape and the intensity of the

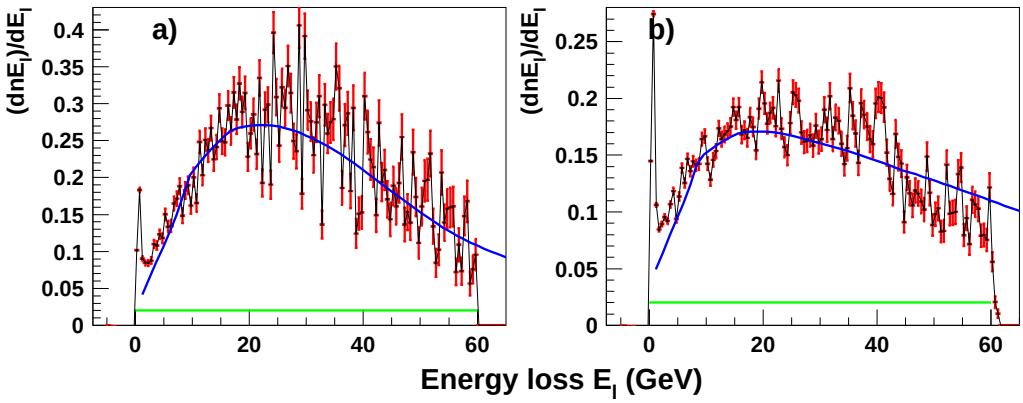

Figure 3.42: Comparison between the measured (black points) and calculated energy loss spectra for the StR11 crystal (a) and the StR5 one (b); the green lines represent the radiation emission in the amorphous condition.

spectrum depend on the bending radius; in fact the StR5 crystal (b) being more bent, presents a lower radiation intensity and a more broaden distribution.
This depends on the increase of the angular range experienced by the positron during the crystal crossing, that causing the interaction with planes that are misaligned more, adds a harder but less intense component to the energy loss spectrum.

The agreement with the analytical calculation (within the experimental errors) is rather good; the measured average energy loss is $\bar{E}_l^{vr}$ =12.29±0.12 GeV for the StR11 crystal and $\bar{E}_l^{vr}$ =8.53±0.05 for the StR5 one while the values provided by the simulation are $\bar{E}_l^{vr}$ =11.64 GeV (StR11) and $\bar{E}_l^{vr}$ =8.27 GeV (StR5).

3.2.6 Conclusion

This chapter has described channeling and volume reflection from the radiation emission point of view from the theoretical characterization to the measurements, performed on two 2 mm long strip crystals, with different curvature radii (tab. 3.1). The obtained results are summarized in tab. 3.2; the third column gives the average energy loss (background subtracted, $\bar{E}_l - \bar{E}_l^{bg}$), for the amorphous, channeling and volume reflection orientation, in the investigated energy range ($3 < E_l < 60$ GeV). If compared with the amorphous condition, both channeling and VR produce a more intense radiation emission, with an enhancement ranging from 5.7±0.6

(StR5 VR) to 8.8±0.9 (StR11 VR), with an intermediate 8.3±0.8 value for channeling (both crystals).

	$\bar{E}_l$ GeV	$\bar{E}_l - \bar{E}_l^{bg}$ GeV	$\bar{n}\gamma$	Accept. μrad	Efficiency
Amorphous	2.92±0.1	1.20±0.1			
StR11					
channeling	11.69±0.08	9.97±0.08	4.14	34	67.7±11.4
V. R.	8.53±0.08	6.81±0.08	1.5	186.5±3.9	94.4±0.24
StR5					
channeling	11.67±0.07	9.95±0.07	4.14	34	97.3±1.1%
V. R.	12.29±0.12	10.57±0.12	1.5	403.5±1.3	53.4±2.4%

Table 3.2: Results for the strip crystals investigated during the 2009 H4 beam test.

Considering the average energy loss per positron, channeling and VR have a similar behaviour but there are differences between these effects that should be underlined:

- *average photon multiplicity or single photon spectrum.*
  The obtained results have proven that a positron, crossing a bent crystal, loses a similar amount of energy, both in channeling and in volume reflection but this does not imply the emitted photon beam to be similar as well. In other words, the single photon spectrum[11] can be different as expected by theory (sec. 3.1). The theoretical (it has not been measured) parameter that allows to estimate this difference is the $\bar{n}\gamma$ average number of emitted photons per positron (fourth column of tab. 3.2); this number in channeling is about 3 times larger than in VR so that the single photon spectrum in channeling is much softer than in VR.

- *dependence from curvature.*
  As theoretically described in sec. 3.1.1 and experimentally verified in sec. 3.2.4, the radiation emission in channeling (at the investigated energy) is determined by the oscillation inside the channel with a negligible contribution given by the crystal curvature. On the other hand, considering VR, there are big differences between its straight crystal counterpart, the coherent bremsstrahlung, and the bent crystal behaviour. These differences originate in the variation of the angle between the particle and the crystalline planes during the crystal crossing. Moreover, since this angle average value increases with

[11]The single photon spectrum refers to $\frac{\mathrm{d}n_\gamma}{\mathrm{d}E_\gamma}$ as a function of E_γ, where E_γ is the photon energy and n_γ is the number of emitted photons per positron, in the dE_γ energy range.

the curvature and so does its distribution spread, the VR energy loss distribution can be modified acting on the crystal curvature. Finally it should be noted that, although the curvature has no effect on the emitted radiation in channeling, the use of bent crystals has been fundamental to find the correct alignment and to tag the channeled particles separating them from the undeflected beam.

- *efficiency and angular acceptance.*
  To measure the energy loss values (reported in tab. 3.2) only the particles subject to the effect under study have been considered but, when the overall crystal behaviour is evaluated, the efficiency of the given effect should be taken into account, since it provides the number of the "effective" positrons (the channeled or reflected ones) over the total one. When the efficiency is taken into account, VR "naturally" overcomes channeling (the measured values in this case are 96% for VR and 60% for channeling) even if the most significant difference is the angular acceptance, that for VR is much larger than for channeling and can also be adjusted, depending on the bending radius. The angular acceptance, in fact, becomes crucial when the "practical parameters" such as the beam divergence, the alignment precision and the crystal torsion, are taken into account.

Chapter 4

Advanced bent crystals

This chapter will go beyond the standard channeling and volume reflection effects, describing some innovative bent crystal deflection schemes. Experimental results obtained with both positive and negative particles will be presented for every effect, after a brief theoretical introduction.

Sec. 4.1 will focus on the multi volume reflection in a series of crystals that is not a new effect but rather a technological development, based on VR, to obtain large deflection angles with high efficiency and large angular acceptance.

Sec. 4.2 will uncover the "second bent crystal dimension" given by the crystal rotation along the vertical direction. Moving in this dimension, new elements such as the skew planes (sec. 4.2.1) and axes will come on the scene, revealing the possibility to drive particles that are spinning around the axes (axial channeling, sec. 4.2.2) or to reflect particles in several planes inside a single crystal (MVROC, sec. 4.2.3).

4.1 Multi VR in a sequence of crystals

As described in sec. 2.2.3, volume reflection has a large angular acceptance and a high efficiency, properties that make it a channeling competitor in applications such as collimation and beam extraction.
Compared with channeling, VR is limited by the deflection angle, that, being determined by the intrinsic crystal properties, is small and fixed, differently from the channeling one, that depends on the crystal length and curvature.
To increase the deflection produced by VR, a system of many crystals, aligned between each other, has been developed so that the particle, crossing the crystals, is subject to a series of reflections, resulting in a larger deflection angle, as shown schematically in fig. 4.1.

The first experimental test of multi volume reflection in a series of crystals [82]

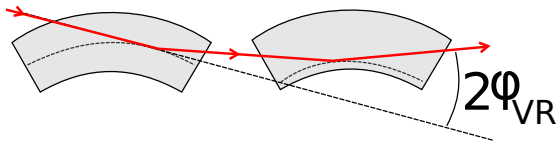

Figure 4.1: Scheme of the multi volume reflection in two subsequent crystals.

has been carried out in 2007 using two quasimosaic crystals (fig. 4.2a) that were originally designed to work separately. Fig 4.2b shows the result of a goniometer scan performed with the double crystal system: in the region 0 μrad< α <70 μrad, two overlapping channeling peaks can be noted, while a double reflection of the beam is present for 40 μrad< α <110 μrad, which provides a deflection angle $\phi_{VR} = 23.4 \pm 0.3 \mu$rad, reaching a maximum efficiency of 95.7±0.4%.

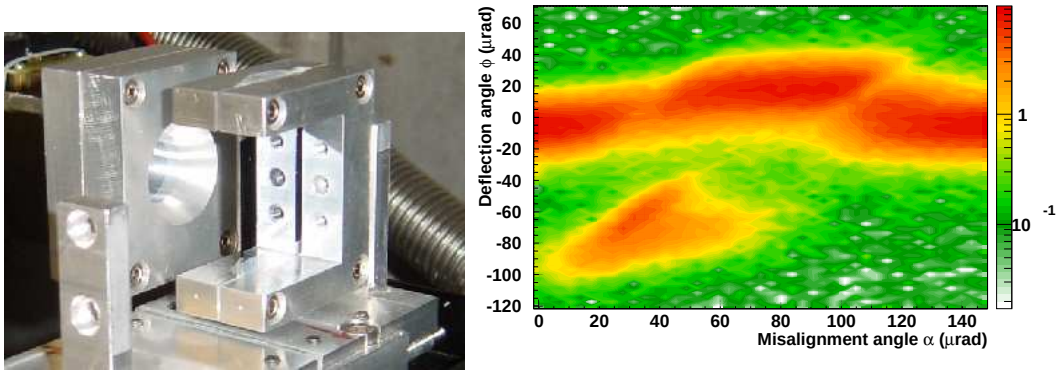

(a) (b)

Figure 4.2: a) The quasimosaic bent crystals aligned between each other and mounted on the goniometer. b) The result of the goniometer scan performed with the two crystal assembly: on the horizontal axis the misalignment angle with respect to the beam and on the vertical one the deflection angle produced by the crystals.

Fig. 4.2 demonstrates the feasibility of multi volume reflection, revealing at the same time its main difficulty: the need of an accurate alignment between the crystals in order to preserve the large VR acceptance. The misalignment between the crystals causes in fact the increase of the angular region interested by channeling, in which volume reflection and thus multi volume reflection (MVR) present a low efficiency.

There are two possible strategies to improve the relative alignment between crystals: one is based on the active control of the alignment of each crystal, that can be obtained using piezoelectric motors (fig. 4.3a) and the other requires the development of holders able to keep the crystals parallel between each other, as in the case presented in fig. 4.3b.

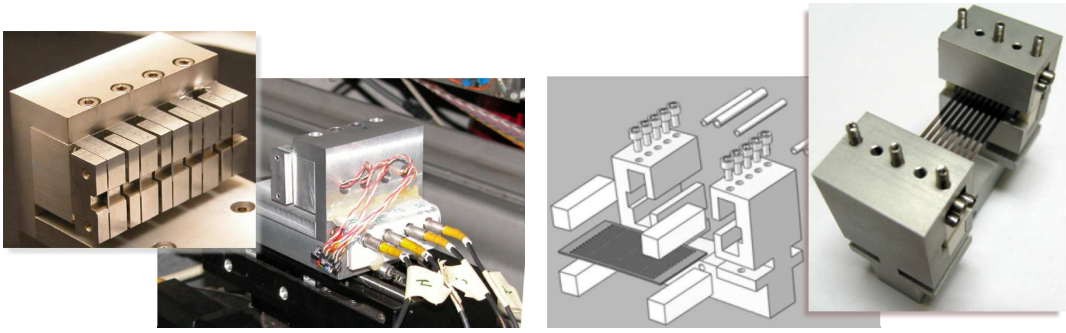

(a) (b)

Figure 4.3: Two examples of multi-crystal systems: a) two photos of an ensemble of 5 quasimosaic crystals mounted on a holder that allows to adjust their relative alignment through piezoelectric motors (developed by the Petersburg Nuclear Physics Institute, PNPI [83]); b) a photo and the schematics of an array of 9 silicon strips, bent by a holder designed to ensure the parallelism between the strips, balancing the forces applied to them by the screws that fix their positions (produced by the Physics Department of the University of Ferrara [62]).

Both techniques have been tested producing positive results (see [84] for what concerns the active alignment and [85] for the "passive" one) but, at the moment, most of the efforts are directed towards the improvement of the passive alignment system since the active one, though offering excellent performances in terms of angular acceptance and efficiency, introduces practical complications. Multi-crystals, in fact, are developed in the framework of beam collimation whose main request is the reliability; the presence of electronics and motors close to the beam could be a problem. In addition to this, all the elements placed next to the beam (crystals, holders and goniometer) should fit the ultra high vacuum requirements so that the development of an active multi-crystal system becomes more expensive in terms of cost and time.

The next section will present as an example the results obtained with a multi-strip crystal (without active alignment) tested in 2008, with positive and negative charged particles.

4.1.1 The measurements

This section presents the experimental results obtained with a multi-strip crystal (fig. 4.4) composed by 8, 2.2 mm long silicon strips, oriented along the (111) plane; it has been developed at IHEP.

Fig. 4.5a presents the result of a goniometer scan performed with the IHEP multi-crystal in 2008, on the H8 beamline, with a 400 GeV/c proton beam (sec. 2.1.6).

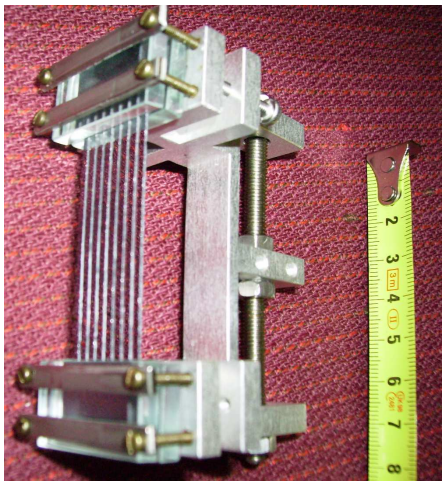

Figure 4.4: A photo of the multi-strip crystal (8 (111) silicon crystals) produced at the IHEP laboratory. The strips are held in position by two layers of glass that, thanks to their high planarity, keep them parallel.

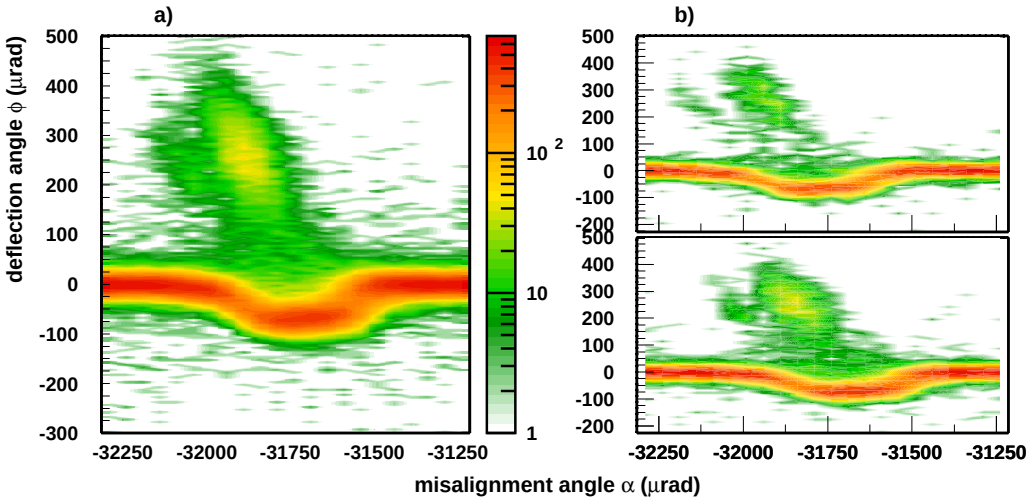

Figure 4.5: a) Goniometer scan of the IHEP multi-strip crystal: the deflection angle as a function of the misalignment one (sum of the goniometer angle and the incoming particle angle measured by the DsX silicon detectors). b) Same as (a) but selecting the events that fall in two horizontal beam slices (0.25 cm high), at a distance of 0.5 cm one from the other.

The torsion phenomenon, described for the single crystal (sec. 2.2.1), is also present in a multi-crystal, as proven by fig. 4.5b, whose two plots are produced

with particles falling in two horizontal beam slices at a distance of 0.5 cm one from the other: they show that the torsion generated by the holder propagates to all the strips as a rigid shift with respect to the horizontal axis (α). This displacement can be measured comparing the position of the channeling peaks and of the reflection regions in the two plots: they differ of around 100 μrad, corresponding to a torsion of 200 μrad/cm.

Once the torsion coefficient has been measured, the deflection angle as a function of the local misalignment α^* (sec. 2.2.1) can be obtained (fig. 4.6a). This compensation of the torsion allows to observe a more detailed plot, with the channeling peaks fine structure, demonstrating a good alignment between all the strips except for the first one whose channeling peak is separated from the other ones. The position of the channeling peaks with respect to the vertical axis allows to estimate an average channeling angle ϕ_{ch} ~250 μrad, corresponding to a bending radius of about 9 m.

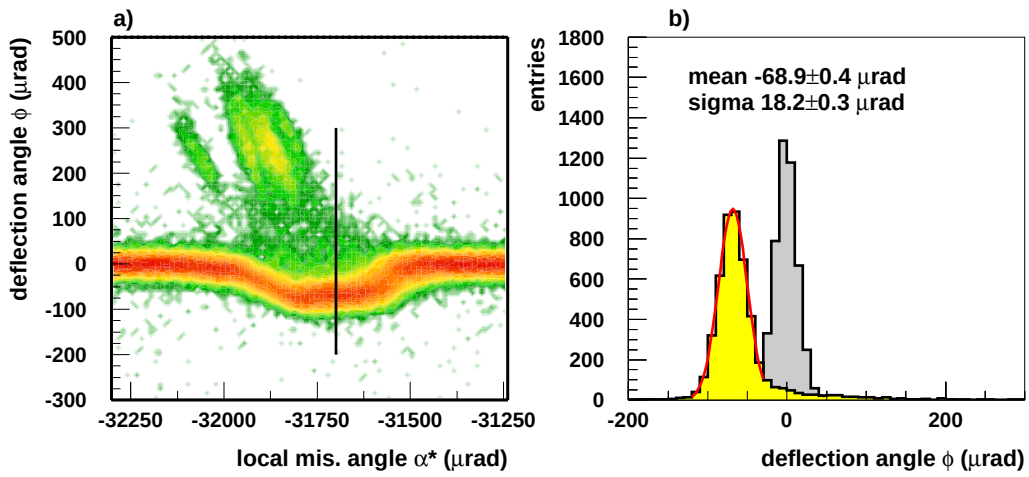

Figure 4.6: a) Goniometer scan of the IHEP 8 strip crystal with the torsion compensated via software. b) The yellow histogram represents a slice of the (a) scatter plot (whose position is indicated by the black line) showing the multiple reflection of the beam compared with the gray histogram (amorphous orientation).

Fig. 4.6b compares the deflection angle profile acquired in the middle of the multi volume reflection region (black line in fig. 4.6a) with the amorphous one. Once the detectors offset is taken into account, a deflection angle $\phi_{MVR} = 67.5 \pm 0.5$ μrad is obtained. Such a deflection corresponds to 5 consecutive reflections

(consider that a single VR should give $\phi_{VR} = 13.6\ \mu$rad, fig. 1.40a). This means that not all the crystals are simultaneously in VR which is not surprising [85] and depends on the non perfect alignment between the crystals.

The top plot of fig. 4.7 presents the percentage of events contained in the main peak (range $-\infty < \phi < \bar{\phi} + 3\sigma$, with $\bar{\phi}$ the mean deflection angle value) of the deflected beam, as a function of the effective misalignment α^*; the bottom plot (deflection angle as a function of α^*) is used just to provide an angular reference. Three regions can be identified: on the left, a valley, corresponding to the channeling peaks; in the middle, the multi volume reflection and on the right the amorphous orientation. The multi volume reflection and amorphous ranges are fit with a constant function providing the corresponding average percentage of events.

As already done in sec. 2.2.5 for a single crystal, the MVR efficiency can be

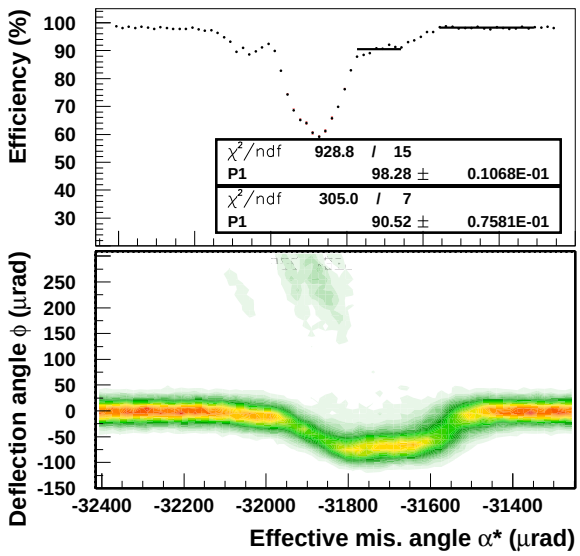

Figure 4.7: The top plot shows the percentage of events that are in the main peak of the deflection angle distribution, within the range $-\infty < \phi < \bar{\phi} + 3\sigma$, where $\bar{\phi}$ is the mean deflection angle value, obtained with a series of gaussian fits, like the one presented in fig. 4.6. The scatter plot at the bottom (deflection angle as a function of α^*) is used to give a reference.

obtained rescaling the percentage of events under the MVR peak for the corresponding amorphous one (that is smaller than 100% because of the deflection angle distribution tails that are not perfectly gaussian). The efficiency results to be 92.1±0.1%.

It is interesting to note that the single VR efficiency is about 97.4% (fig. 1.40b); assuming 5 independent reflections, this would cause a MVR efficiency of 87.7%, a value definitely smaller than the measured one. As pointed out in [85], this happens because the particles that are not reflected by one of the crystals, being

volume captured, are then reflected by the other ones thus increasing the total MVR efficiency.

The same multi-strip crystal tested with the 400 GeV/c beam was brought on the H4 beamline to be investigated with a negative hadron beam of 150 GeV/c. Fig. 4.8a shows the result of the goniometer angular scan performed in this condition and fig. 4.8b the comparison between the deflection angle profile acquired in the middle of the multi volume reflection region (black line in fig. 4.8a) with the amorphous alignment. Taking into account the angular offset (given by the imperfect detector alignment), the average deflection angle can be computed: $\phi_{MVR} = 79.5 \pm 1.0$ μrad. Comparing fig. 4.8 with its equivalent positive parti-

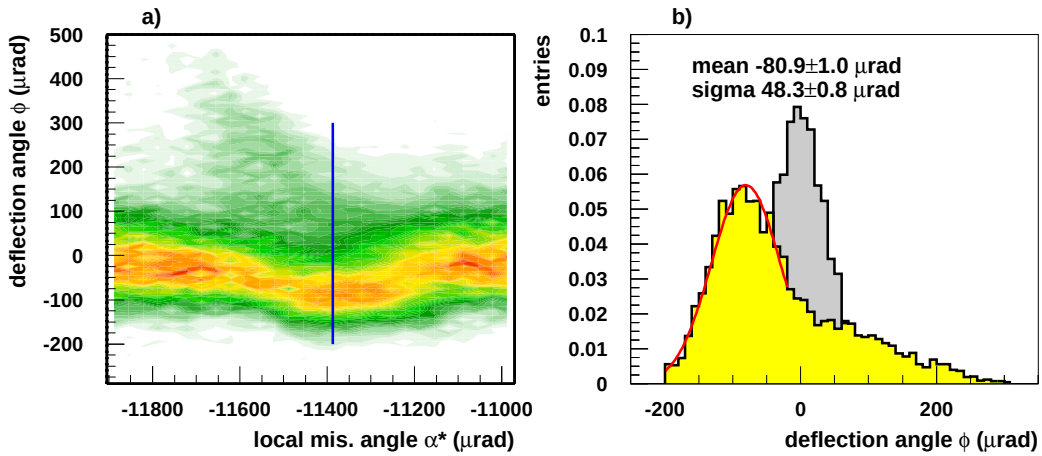

Figure 4.8: a) Goniometer scan of the IHEP 8 strip crystal performed with a 150 GeV/c negative hadron beam showing the deflection angle produced by the crystals as a function of the effective misalignment. b) The yellow histogram represents a slice of the (a) scatter plot (whose position is indicated by the black line) while the gray histogram allows the comparison with the amorphous orientation.

cle one (fig. 4.6), several differences due to the charge sign and the energy of the particles appear: the lower energy is mainly responsible of the ϕ distribution broadening due to the increase of the multiple scattering, while the disappearing of the channeling peaks and the increase of the volume capture probability is caused by the negative sign of the particles, in agreement with what has been measured for the single crystal (sec. 2.2.4).

Fig. 4.9 presents the number of events under the main peak as a function of the

effective misalignment α^*. The value corresponding to the amorphous alignment (not shown in figure) is 98.56±0.02%.

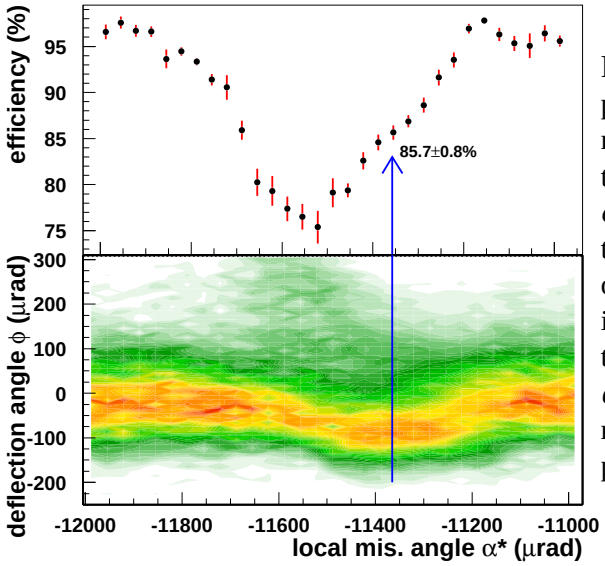

Figure 4.9: The top plot shows the percentage of events that are in the main peak of the deflection angle distribution, within the range $-\infty < \phi < \bar{\phi} + 3\sigma$, where $\bar{\phi}$ is the mean deflection angle value, obtained with a series of gaussian fits, like the one presented in fig. 4.8b. The scatter plot at the bottom (deflection angle as a function of α^*) is used to give a reference. The arrow indicates the position of the slice plotted in fig. 4.8b.

Fig. 4.9 indicates that it is not possible to identify an angular region (in MVR) characterized by a stable efficiency as was the case for positive particles. This is caused by the broadening of the ϕ distribution and the increase of the channeling acceptance due to the lower energy. Thus, to estimate the MVR efficiency, a thin alignment region, corresponding to the angular profile shown in fig. 4.8b (middle point of the MVR acceptance) will be taken into account; once rescaled for the corresponding amorphous percentage, this gives an efficiency of 87.0±0.8%.

It should be noted that, for what concerns negative particles, VR and MVR represent very interesting methods to deflect particles using bent crystals. The lower channeling efficiency in fact on one hand does not allow to obtain large deflection angles with high efficiency using channeling while on the other one, favours MVR limiting the maximum value of its inefficiency. This last statement is confirmed by the comparison between the positive (fig. 4.7) and negative (fig. 4.9) efficiency trends: in both cases the minimum is reached in correspondence of the channeling peaks but its value is much larger for the negative particles ($\sim$ 76%) with respect to the positive ones ($\sim$ 60%).

4.2 Axis related effects

This section will show the possibilities offered by the crystal rotation in the vertical plane. First of all, new elements such as the skew planes, will be introduced (sec. 4.2.1) and then the axial channeling (sec. 4.2.2) and MVROC (sec. 4.2.3) phenomena will be described both from the theoretical and experimental point of view.

4.2.1 Skew planes

In the continuum approximation (sec. 1.3.1), a crystal has been described as a series of parallel planes that interact with the charged particles as a continuum periodic potential.
According to the continuum approximation, the crystalline planes are seen as such by a charged particle when its trajectory forms a small angle with respect to the planes themselves.
Up to now, the presented measurements have considered only the crystal planes aligned along one direction that, for design choice, is the one perpendicular to the bending. This is schematically shown in fig. 4.10a, in which the curvature lies in the $(x-z)$ plane while the particle is aligned with respect to the crystalline planes parallel to the $(y-z)$ orientation.

In this framework, the misalignment angle between the particle momentum

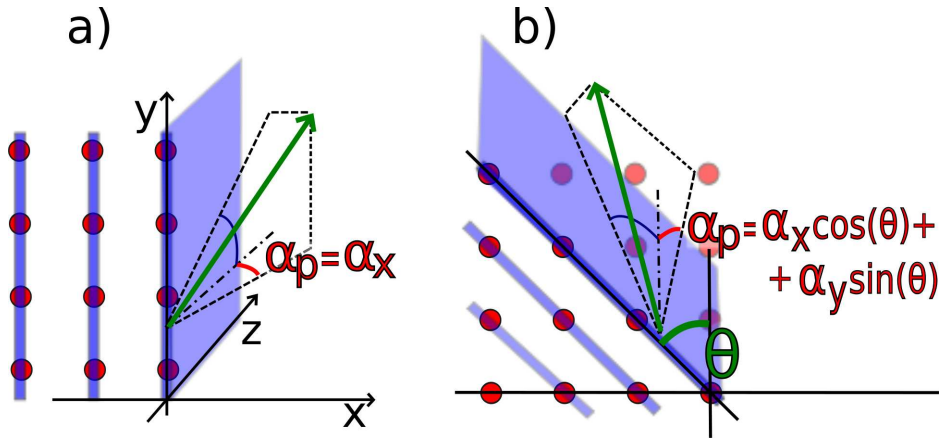

Figure 4.10: Two schemes of a crystal: the red dots represent the nuclei, the blue lines the crystalline planes and the green arrow the direction of a charged particle that forms a $\alpha_p \ll 1$ angle with respect to a vertical plane (a) and to a secondary skew one (b).

(green arrow) and the z axis (black arrow) can be decomposed in a α_x horizontal

component and a α_y vertical one, so that the misalignment between the particle and the crystalline planes, α_p, is given by α_x (that in turn corresponds to the α angle used in this thesis to indicate the misalignment between the particle trajectory and the crystal). The crystalline planes perpendicular to the bending direction are the main ones but secondary skew planes are also present, as shown in fig. 4.10b. Considering a skew plane, the α_p misalignment angle with respect to the particle trajectory becomes a composition of the horizontal and vertical misalignment with respect to the axis: $\alpha_p = \alpha_x sin(\theta) + \alpha_y cos(\theta)$, where θ represents the skew plane slope with respect to the vertical direction (fig. 4.10b).

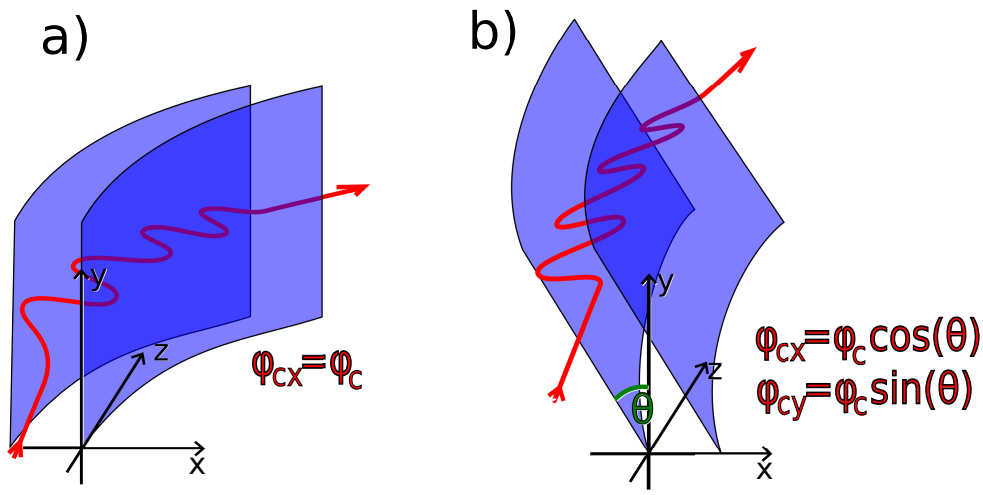

Figure 4.11: The trajectory of a particle channeled by the vertical planes (a) and by the skew ones (b).

As well as the main ones, the skew planes are able to trap particles in channeling and reflect them in the crystal volume, but the deflection angle produced by them rotates in space according to the orientation of the plane.
Fig. 4.11a shows the trajectory of a particle channeled by the main planes of a bent crystal; if the ϕ deflection angle is decomposed in a ϕ_x horizontal component and a ϕ_y vertical one, the ϕ_c channeling deflection acts only in the horizontal plane meaning that its horizontal projection corresponds to the full bending angle, $\phi_{cx} = \phi_c$, while the vertical one is absent, $\phi_{cy} = 0$. When the skew planes are taken into account (fig. 4.11b), both the horizontal component and the vertical one of the deflection have a non zero value resulting to be $\phi_{cx} = \phi_c cos(\theta)$ and $\phi_{cy} = \phi_c sin(\theta)$.

Fig. 4.12a presents a goniometer scan of a silicon strip crystal, in which both the main planes and the skew ones give a contribution: the top plot (the ϕ_x horizontal component of the deflection angle as a function of the α^* misalignment)

presents two channeling peaks while, in the bottom one (the ϕ_y vertical component of the deflection angle as a function of the α^* misalignment), only the skew peak is visible given that it has a non zero vertical deflection angle.

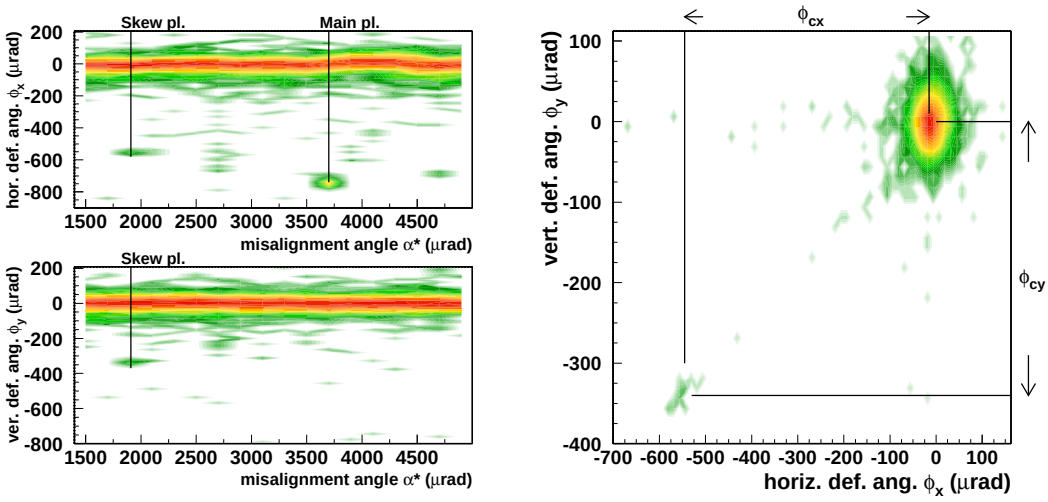

(a) (b)

Figure 4.12: The experimental evidence of a skew plane compared with the main one. a) The goniometer scan of a (110) silicon strip crystal: the ϕ_x horizontal deflection angle (top) and the ϕ_y vertical one (bottom) as a function of the local misalignment α^*; two channeling peaks can be recognized but only the skew one is present in both plots. b) Scatter plot of the ϕ_y vertical deflection angle as a function of the ϕ_x horizontal one, filled with the events in the angular region corresponding to the skew plane that is 1700 μrad$<$ $\alpha^* < 2200$ μrad; the projections of the channeling peak on the two axes ϕ_{cx} and ϕ_{cy} are indicated.

Fig. 4.12b shows the ϕ_y vertical deflection angle as a function of the ϕ_x horizontal one, considering the events in the angular region corresponding to the skew peak (1700 μrad$<$ $\alpha^* < 2200$ μrad, fig. 4.12a). Measuring the position of the channeling peak with respect to the two axes it is possible to recognize the inclination of the plane that is $\theta = \text{atan}\left(\frac{\phi_{cy}}{\phi_{cx}}\right) = 30^{\text{o}}$ in this case.
It should be noted that the decomposition of the deflection angle described for the channeling effect is valid also for the VR one but in this case the ϕ_{VR} deflection angle changes depending on the "strength" of the skew plane[1]. Therefore it can have a very small value compared to the main one. For this reason it is not possible

[1] ϕ_{VR} depends on the depth of the potential well, that in turn depends on the geometric characteristics of the plane itself (eq. 1.5).

to recognize a VR deflection associated to the skew channeling peak in fig. 4.12.

4.2.2 Axial channeling

In the previous sections, the continuum approximation has always been applied to the crystalline plane that behaves as a continuous planar charge distribution with respect to the aligned particles ($\alpha_p \ll 1$, fig. 4.10).
This section will describe the case in which a charged particle, moving at a small angle with respect to the crystal atomic strings (z axis in fig. 4.10), feels the electric field generated by the atoms of the string as if it were produced by a charge distribution with a cylindrical symmetry, as schematically shown in fig. 4.13.

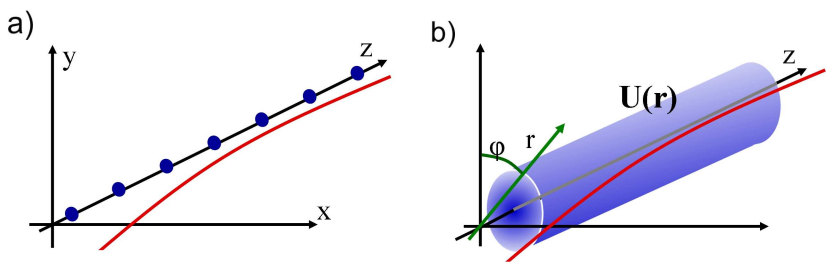

Figure 4.13: a) A particle moving at a small angle with respect to a crystal axis. b) The continuum potential with radial symmetry as it is felt by the aligned particle.

The potential of an isolated atomic string $U_A(r)$ in the Lindhard approximation (eq. 1.4) is:

$$U_A(r) = \frac{Z_i Z e^2}{a_i} \ln\left(1 + \frac{3a_{TF}^2}{r^2}\right) \tag{4.1}$$

where a_i is the interatomic spacing in the string, r is the distance between the particle and the axis, a_{TF} is the Thomas Fermi screening radius ($a_{TF} = 0.8853 \cdot a_B \cdot Z^{-1/3}$, $a_B = 0.529$ Å).
The transverse electric field generated as the sum of the fields produced by the single atomic strings shows a rather complicated structure (fig. 4.14), in which the negative charged particles can be trapped by the strong field of the atomic string and, being attracted by the positive nuclei, be confined near them while the positive ones may be captured in the well of a minor potential placed between the atomic strings.

The particle motion in the $U(r)$ field with cylindrical symmetry [87] is characterized by two conserved quantities, the angular momentum J and the energy in the transverse plane E_t, which can be decomposed into a radial component and a circular one. In fact, the angle between the particle trajectory and the crystal axis

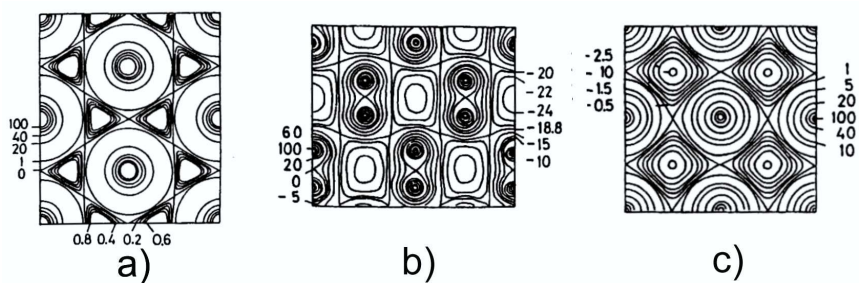

Figure 4.14: Axial potential computed [86] with the use of the Molière approximation, in the following orientations: a) (111) Si; b) (110) Si; c) (100) Si. The numbers give the potential in eV.

z, which is $\alpha_a = \sqrt{\mathrm{d}x^2 + \mathrm{d}y^2}/\mathrm{d}z^2$, can be expressed in the cylindrical coordinate system:

$$\alpha_a = \sqrt{\left(\frac{\mathrm{d}r}{\mathrm{d}z}\right)^2 + \left(\frac{r\mathrm{d}\phi}{\mathrm{d}z}\right)^2} = \sqrt{\alpha_r^2 + \alpha_\phi^2} \tag{4.2}$$

According to this and taking into account that the angular momentum is $J = p \times r = pr\alpha_\phi$, eq. 1.11, which gives the transversal energy value and was computed for the planar channeling case, becomes:

$$E_t = \frac{pv}{2}\alpha^2 + U(r) = \frac{pv}{2}\alpha_r^2 + \frac{J^2}{2M\gamma r^2} + U(r) \tag{4.3}$$

where the last two terms are the effective potential in which $\dfrac{J^2}{2M\gamma r^2}$ represents a centrifugal term whose effect is to move the effective potential minimum aside from the channel center ($r = 0$), where the real $U(r)$ has the minimum; so, as J increases, the effective potential minimum moves farther from the atomic string for the negative particles and nearer to them for the positive ones.

As in the planar channeling case, the condition for axial channeling is that the transversal energy E_t does not overcome the maximum value of the potential well U_0. This condition can be transformed in the request for the particle angle with respect to the axis (α_a) to be smaller than a critical value $\alpha_{ac} = \sqrt{2U_0/pv}$, as already shown in sec. 1.3.2 for the planar case.
The U_0 values for the most important axes in Si, Ge, W crystals are given in tab. 4.1. Comparing these U_0 values with the planar ones, the axial channeling critical angle results to be $2-3$ times larger. According to this, the axial channeling condition could seem favoured with respect to the planar one but two distinct states characterizing the axial channeling should be taken into account [88]:

crystal	Si			Ge			W		
axis	100	110	111	100	110	111	100	110	111
U_0 (eV)	89	114	105	157	203	185	842	979	979

Table 4.1: The potential well depth of some axial channels of silicon, germanium and tungsten crystals, calculated in the Molière approximation at room temperature.

- *the hyperchanneling*, fig. 4.15a.
  It is the confinement of a particle in a single axial channel; given that the potential barrier separating the different axial channels is rather low (6 eV and 1 eV respectively for a silicon crystal aligned along the $\langle 110 \rangle$ axis and the $\langle 111 \rangle$ one) only a small fraction of the aligned particles is trapped in this state, during the whole crystal crossing.

- *the doughnut scattering*, fig. 4.15b.
  It is the motion of a particle aligned with respect to the crystal axis but not confined in a single channel. In this condition the transversal momentum of the particle changes its direction due to the multiple scattering with the atomic string so that particles with an initial misalignment α_a are distributed along an arc (circle) with a radius α_a, from which the name doughnut scattering derives. The scattering process is completed after the particle has crossed the so called equalization length:

$$\lambda(\alpha_{ac}) = \frac{4}{\pi^2 N d a_{TF} \alpha_{ac}} \tag{4.4}$$

  where a_{TF} is the Thomas Fermi constant and d the interatomic distance.

In previous experiments on axial channeling [89, 90], only the hyperchanneling [91] phenomenon has been observed resulting in a very small deflection efficiency. But if some limitations on the crystal bending and length are taken into account, the doughnut scattering does not significantly smear out the trajectories transversely, so that the channeled particles, proceeding along the bent axis, can be deflected of the crystal bending angle ϕ_c. The condition for the particles deflection through the axial channeling doughnut scattering [91] is the following:

$$k = k_1 k_2 < 1 \quad \text{with} \quad k_1 = \frac{\lambda}{R\alpha_{ac}} \quad \text{and} \quad k_2 = \frac{l}{R\alpha_{a_{TF}c}} \tag{4.5}$$

where l is the crystal length, R the bending radius, α_{ac} the axial channeling critical angle, λ the equalization length, a_{TF} the Thomas Fermi constant and d the

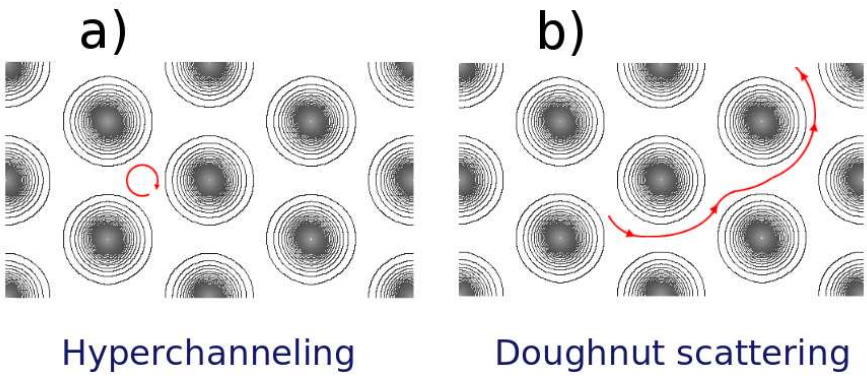

Figure 4.15: The trajectory (red arrow) of a particle trapped in the axial potential: a) the particle is confined in a single potential well, hyperchanneling; b) the particle overcomes the axial channeling potential well moving around the axes, doughnut scattering.

interatomic distance.
The experimental results presented in the next section will show that when eq. 4.5 is satisfied, axial channeling becomes an effective way of deflecting both positive and negative charged particles.

4.2.2.1 Results with positive and negative particles

This section will present the experimental results on the axial channeling deflection investigation performed on the H4 beamline at CERN. The analyzed data are taken from two beam tests, one carried out in 2009 with 120 GeV/c positrons and one with 150 GeV/c negative hadrons (mainly π^-) during 2008.

The crystal tested with positive particles is a silicon strip one oriented along the (110) planes and $\langle 111 \rangle$ axis; its features are summarized in tab. 3.1 (StR11) while a horizontal goniometer scan is presented in fig. 1.3.
To align the crystal axis with respect to the beam, a two step procedure has been used: the crystal was rotated around the vertical axis (horizontal scan, fig. 1.3) aligning it in planar channeling ($\alpha_x^* = 0$, fig. 1.3) and then the craddle stage of the goniometer (sec. 2.1.2) was used to find the alignment with the axis (vertical scan, fig. 4.16).

Fig. 4.16 shows the ϕ_x horizontal deflection angle (a) and the ϕ_y vertical one (b) as a function of the α_y vertical misalignment. Two structures (one at $\phi_x \sim -10$ μrad, undeflected beam, and one at $\phi_x \sim +180$ μrad, channeled one) can be seen in the external regions of the (a) plot while in the range $3890 < \alpha_y < 3960$ a third component at $\phi_x \sim 30$ μrad appears, identifying the alignment with the axis. The (b) plot reveals that this position is characterized by two channeling

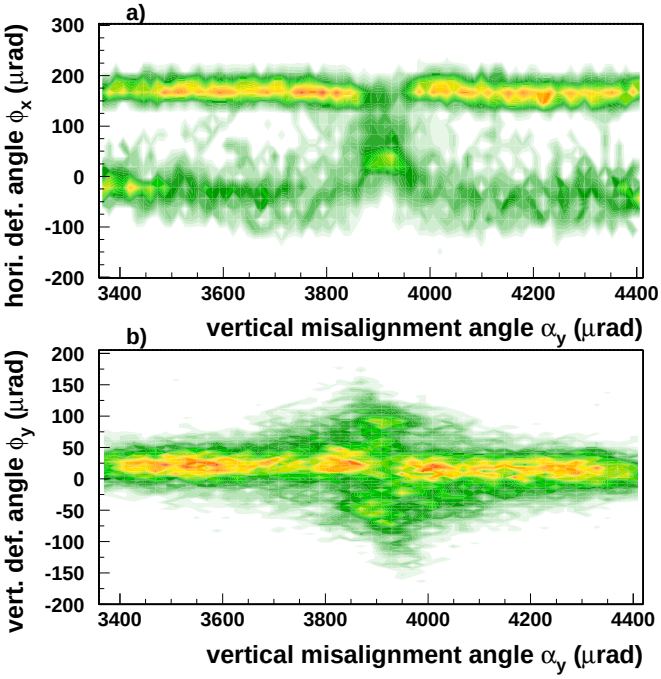

Figure 4.16: Vertical goniometer scan performed with the silicon strip aligned in planar channeling with respect to the horizontal misalignment ($\alpha_x^* = 0$ μrad, fig. 1.3). The plots present as a function of α_y: the ϕ_x horizontal deflection (a) and the ϕ_y vertical one (b).

peaks that, having a vertical deflection component, can be identified as produced by skew planes.

Once the axial alignment has been found, a single DAQ was acquired in this position. The scatter plot of fig. 4.17a (the vertical deflection angle as a function of the horizontal one) is obtained selecting a narrow beam portion (a ~ 30 μrad width on the α_x horizontal direction and a ~ 40 μrad width on the vertical one) and allows the identification of three channeling peaks: the one on the right, that does not present any vertical component, is due to axial channeling, while the two symmetric ones on the left are originated by the particles that, dechanneled from the axial potential, are captured in the (011) skew planes.

Fig. 4.17b presents the deflection angle distribution on the two axes (yellow histograms) compared with the same distribution obtained in the amorphous position. The red boxes in fig. 4.17a enclose a region at $\pm 3\sigma$ from the mean position of the channeling peaks so that, counting the number of particles falling into them, the efficiency of the different effects can be estimated. It turns out that 26.2 ± 0.3 % of the particles fill the axial channeling peak while 56.2 ± 0.4 % the skew ones.

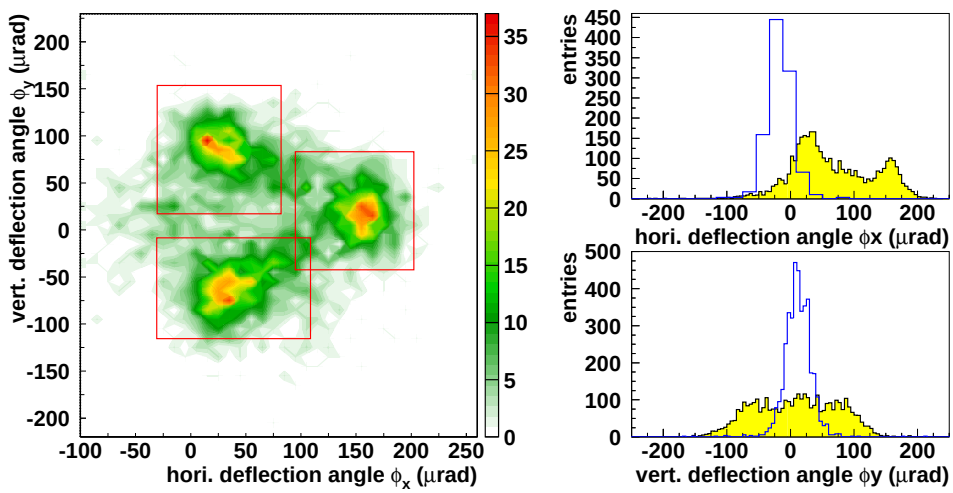

(a) (b)

Figure 4.17: Single DAQ with the crystal aligned in axial channeling ($\alpha_y = 3910$ μrad in fig. 4.16). a) The vertical deflection angle as a function of the horizontal one; the red boxes around them represent a region at $\pm 3\sigma$ with respect to the mean channeling position. b) The horizontal (top) and vertical (bottom) deflection angle profiles in axial channeling (yellow histograms) compared with the amorphous alignment (blue histograms).

The interesting feature of axial channeling is the almost complete absence of undeflected beam, that could be exploited in applications such as beam collimation (sec. 1.2.1) to increase the efficiency.
The study of the axial channeling performed with 400 GeV protons on the H8 beamline is described in [88] where the results, in agreement with the ones presented in this work, are compared with a Montecarlo simulation that well reproduces the experimental data.

Concerning negative particles [92], the used crystal was a silicon strip one, oriented along the (110) plane, 0.98mm long in the beam direction and 500 μm wide in the horizontal one. Fig. 4.18 shows a scan of this crystal in the horizontal plane (which means as a function of the α_x^* misalignment angle). The crystal has been characterized according to the procedure described in sec. 2.2.2, providing the following parameters: a channeling angle $\phi_c = 42.1 \pm 0.9$ μrad, a bending radius $R = 23.3 \pm 0.5$ m and a torsion of 10 μrad/cm.

As for the positive particle case, once the planar alignment has been found ($\alpha_x = -12600$ μrad, fig. 4.18), a vertical scan was performed to orient the crystal with respect to the axis, so that the ϕ_x horizontal deflection angle and the ϕ_y vertical one as a function of the α_y vertical misalignment have been obtained,

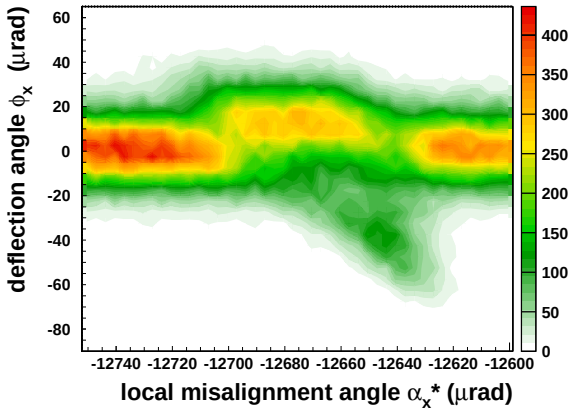

Figure 4.18: The goniometer scan of the (110) silicon strip used in the negative particles axial channeling investigation. The plot presents the ϕ_x horizontal component of the deflection angle as a function of the local misalignment α_x^*.

(fig. 4.19). The axis position can be identified as the center of symmetry of both plots, corresponding to $\alpha_y = 6322$ μrad.

A high statistics single DAQ was acquired with the crystal axis aligned with

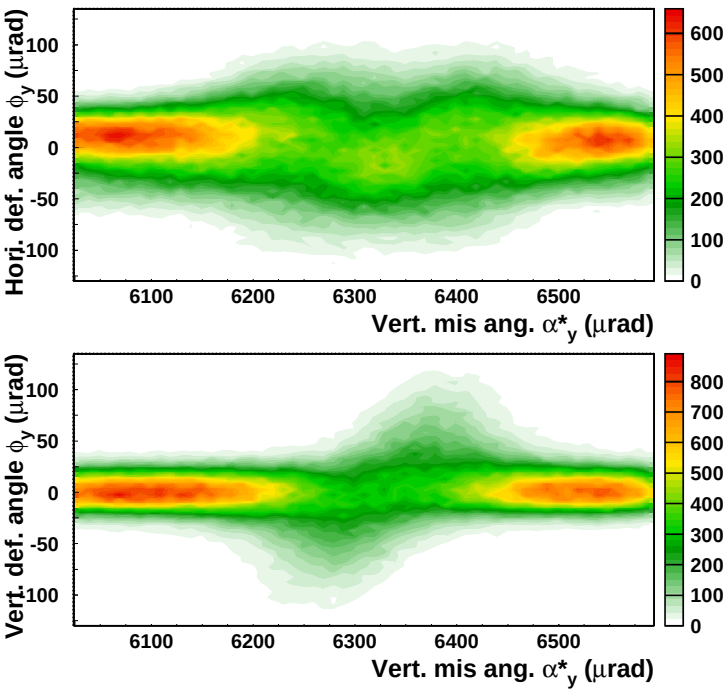

Figure 4.19: Vertical goniometer scan performed with the silicon strip aligned in planar channeling with respect to the horizontal misalignment ($\alpha_x^* = -12600$ μrad, fig. 4.18). The plot presents as a function of α_y: a) the ϕ_x horizontal deflection; b) the ϕ_y vertical one.

the beam. Given the beam divergence ($\sigma_{\alpha x} = 30$ μrad, $\sigma_{\alpha y} = 35$ μrad), the data contain a set of different alignments as presented in fig. 4.20, in which the ϕ_x horizontal deflection angle (a-c) and the ϕ_y vertical one (b-d) are plotted as a function of the α_y misalignment (left side) and the α_x^* one (right side).
These plots can be used to select the angular region of the incoming beam providing the best axial channeling alignment, as it is indicated by the vertical red lines. The angular profiles in fig. 4.21 (yellow histograms) have been obtained

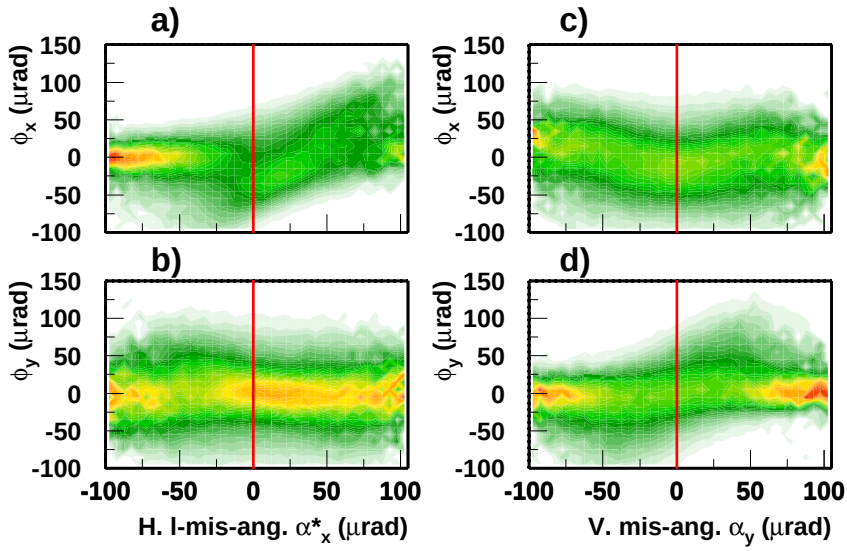

Figure 4.20: Single DAQ in axial channeling with negative particles. The ϕ_x horizontal deflection angle (a-c) and the ϕ_y vertical one (b-d) are plotted as a function of the α_x^* misalignment (left side) and the α_y one (right side); each vertical bin of the plots has been normalized to one to eliminate the dependence from the shape of the beam angular distribution. The vertical red lines indicate the optimal axial channeling alignment.

selecting the events falling into two ~ 10 μrad wide bands around these positions. They represent the projections of the deflection angle distribution on the horizontal plane (a) and the vertical one (b) and are plotted with the corresponding planar channeling distributions (red histograms). This comparison reveals that the maximum of the ϕ_x distribution in axial channeling (fig. 4.21a) corresponds to the planar channeling mean position and thus to the full crystal bending angle. Moreover it is interesting to note that the undeflected beam component, that dominates the planar channeling distribution, almost disappears in axial channeling, increasing the deflection efficiency. To give a parameter, the percentage of particles with $\phi_x < \phi_{0x}$ (vertical blue line in fig. 4.21a) is about 82%. Fig. 4.21

shows also a considerable broadening of the deflection angle distribution; this is due to the multiple scattering of the particles with the atomic strings and the incoherent multiple scattering on the nuclei enhanced by the proximity of the particle trajectories and the crystal axis.

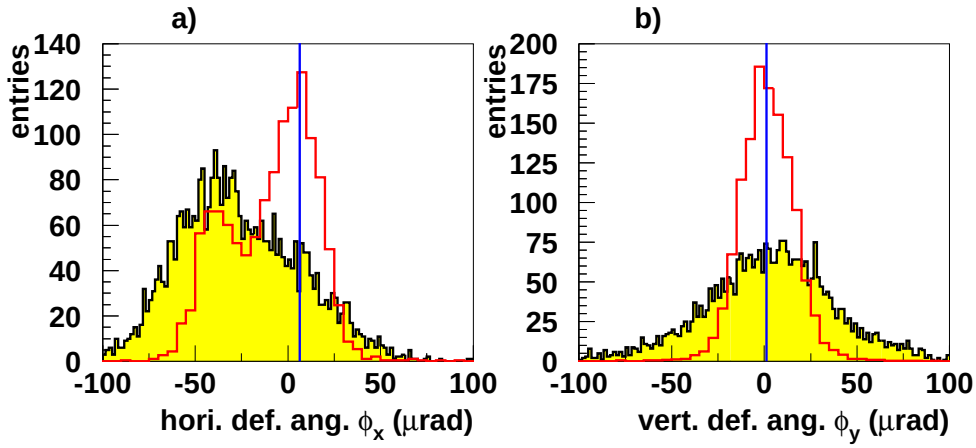

Figure 4.21: The yellow histograms represent: a) the horizontal deflection angle profile and b) the vertical one corresponding to the alignment regions indicated by the red lines in fig. 4.20. The superimposed red histograms show the comparison with the corresponding planar channeling position. The vertical lines indicate the (ϕ_{0x}, ϕ_{0y}) zero deflection angles.

4.2.3 Multi VR in One Crystal (MVROC)

This section will show that it is possible to increase the VR deflection angle through a multiple reflection inside one crystal, exploiting the so called MVROC (Multiple VR in One Crystal) effect. The name is used to distinguish the phenomenon from the MVR obtained using an array of crystals (sec. 4.1).

MVROC has been theoretically described in 2007 [93] and experimentally verified on the H8 beamline with 400 GeV protons in 2009 [94]. It is based on the possibility that, under proper alignment conditions, using a crystal with specific geometric characteristics, the volume reflections due to the vertical plane and the skew ones take place subsequently during a single crystal crossing thus increasing the final value of the deflection.

Fig. 4.22 shows the trajectory of a charged particle in a bent crystal in the phase space of the vertical α_y and the horizontal α_x misalignment with respect to the $\langle 111 \rangle$ axis, whose position is identified by the intersection of the blue lines (representing the crystalline planes), whose direction is perpendicular to the sheet.

Given the crystal is bent, this coordinate system rotates following the curvature, so that a charged particle (green line), entering the crystal in the $(\alpha_{x0}, \alpha_{y0})$ angular position, will move towards smaller α_{x0} values while approaching the crystalline planes (as it happens in the single VR).
If the α_{y0} angle is small enough, the particle trajectory becomes tangent with a skew plane sooner than with the vertical one. These planes ($(110)_{sk}$ and $(112)_{sk}$ in fig. 4.22) give both a horizontal and vertical ϕ_{VRx} and ϕ_{VRy} VR deflection angles to the particle trajectory.
After these interactions, the reflection by the $(110)_v$ main plane (acting only in the horizontal direction) takes place followed by the deflection induced by the skew planes, giving a positive ϕ_{VRx} horizontal deflection and a negative ϕ_{VRy} vertical deflection.
In this way the ϕ_{VRx} horizontal deflection angles of the different reflections add coherently producing a ϕ_{MVROCx} deflection angle larger than the single VR one while the ϕ_{VRy} vertical deflection angles, compensating each other, make a zero deflection in the vertical plane, as well as the single VR does.

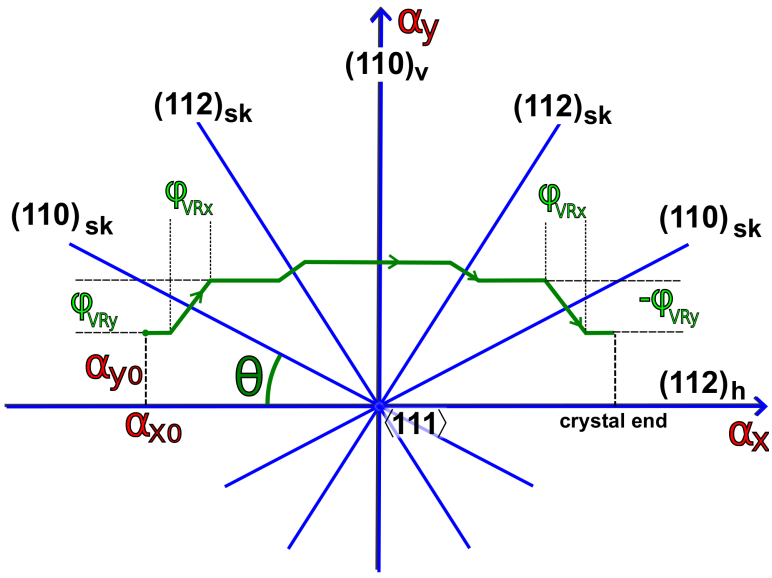

Figure 4.22: The angular space around the $\langle 111 \rangle$ axis of a silicon crystal oriented along the (110) plane. The blue lines represent the crystalline planes (only the main ones are represented to simplify the scheme) and the green arrow is the trajectory of a particle that having an initial misalignment $(\alpha_{x0}, \alpha_{y0})$ with respect to the axis, is subject to MVROC.

A way to better understand the MVROC is to consider the goniometer scan of fig. 4.12a, where both a skew plane and the main one are present at an angular distance of $\delta\alpha_x \sim 2500\ \mu$rad. Considering the alignment condition with a skew plane

($\alpha_p = \alpha_x cos(\theta) + \alpha_y sin(\theta) = 0$, fig. 4.10), this angular distance is determined by the misalignment with respect to the vertical direction: $\delta\alpha_x = \alpha_y \tan(\theta)$. Reducing the vertical misalignment of the crystal, the skew planes are "compressed" in a small angular region, so that the ϕ_c amplitude of the crystal curvature is enough for some of the particles to interact during the crystal crossing.
For this reason, the α_{y0} value should be small to involve the largest number of skew planes increasing the deflection.
If the α_{x0} initial horizontal misalignment is set to be equal to half of the crystal bending angle ($\frac{1}{2}\phi_c$, in order to preserve the symmetry with respect to the $(110)_v$ plane), a skew plane, characterized by a θ inclination, will be involved in MVROC if:

$$\alpha_{y0} < \frac{1}{2}\phi_c \mathrm{cotg}(\theta) \tag{4.6}$$

To give an example, if $\alpha_{y0} = \frac{1}{2}\alpha_{x0} = \frac{1}{4}\phi_c$, the planes characterized by $\theta < 26.6^o$ will be involved in the MVROC process.
However α_{y0} has also a low limit because if it is too small particles are captured by the axial potential. The most suitable value of α_{y0} can be determined by simulations depending on the specific crystal and the energy of the beam but a good approximation is $\sim 5\alpha_{cA}$, where α_{cA} is the axial channeling critical angle (sec. 4.2.2).

4.2.3.1 Experimental meausurements on MVROC

This section presents the experimental results obtained during the MVROC investigation performed in 2010 on the H4 beamline with a 120 GeV/c positron and electron beam.
The used crystal was a silicon strip one, oriented along the (110) plane, 2 mm long in the beam direction and 300 μm wide in the horizontal one. Fig. 4.23 shows a scan of this crystal in the horizontal plane (as a function of the α_x^* misalignment angle). The crystal has been characterized according to the procedure described in sec. 2.2.2, providing the following parameters: a channeling angle $\phi_c = 734.6 \pm 22.3$ μrad, a bending radius $R = 2.72 \pm 0.08$ m and a torsion of 150μrad/cm.
Once the crystal has been characterized from the planar point of view, the MVROC orientation is searched for with a scan of the vertical misalignment angle α_y that is changed using the cradle stage of the goniometer (sec. 2.1.2). Fig. 4.24 shows the resulting scan, obtained keeping the horizontal alignment of the crystal in the middle of the VR angular acceptance ($\alpha_x^* = 3600$ μrad). The (a) plot presents the ϕ_x horizontal projection of the deflection angle and the (b) one the ϕ_y vertical one. The center of symmetry of both plots, $\alpha_y \sim 8900$ μrad, corresponds to the perfect

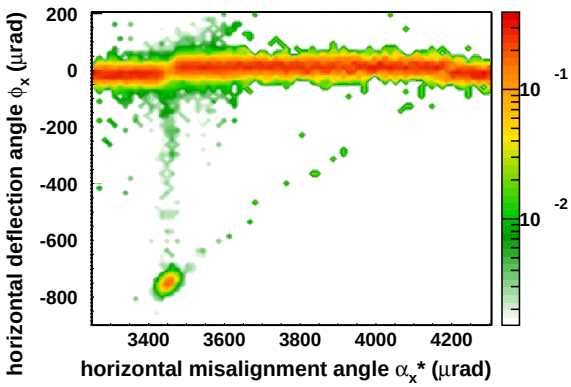

Figure 4.23: The goniometer scan of the (110) silicon strip used in the MVROC investigation. The ϕ_x horizontal component of the deflection angle is plotted as a function of the local misalignment α_x^*. Note that in this plot and in the following ones the VR and MVROC deflections are towards positive angles and the channeling one is towards negative angles.

alignment with the $(112)_h$ crystalline horizontal plane ($\alpha_{y0} = 0$ in fig. 4.22) and, as expected, this position is characterized by the particles capture by the axial potential, represented by the events in the angular region $\phi_x < 0$ μrad (fig. 4.24a).

The main peak in fig. 4.24a is aligned in VR with respect to the horizontal mis-

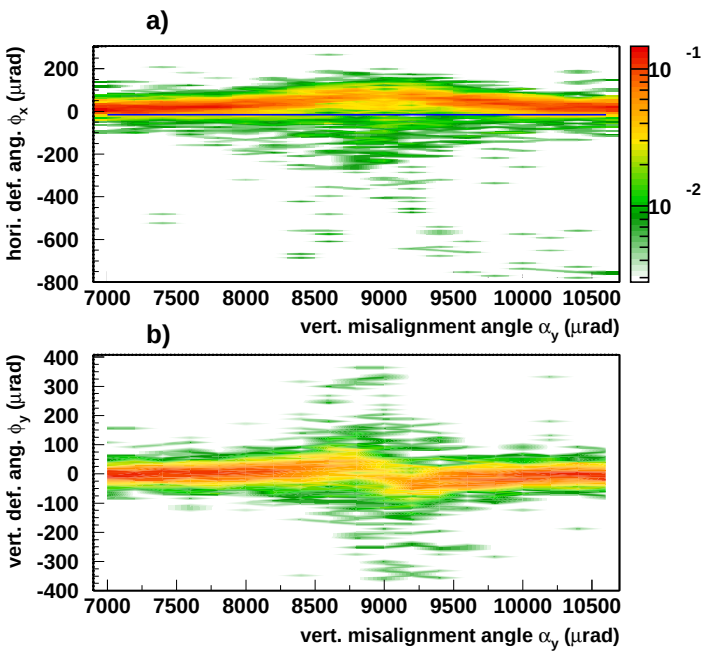

Figure 4.24: Vertical goniometer scan performed with the silicon strip aligned in VR with respect to the horizontal misalignment ($\alpha_x^* = 3600$ μrad, fig. 4.23). The plots present as a function of α_y: a) the ϕ_x horizontal deflection; b) the ϕ_y vertical one.

alignment in the whole plot (the blue horizontal line gives the reference of the "zero deflection angle"). The MVROC produces the further beam shift towards positive angles, observed in the central region of the plot.
Once the fast angular scans have determined the optimal MVROC horizontal orientation ($\alpha_x^* = 3600$ μrad, fig. 4.23) and a vertical one ($\alpha_{y0} = 9070$ μrad, fig. 4.24), a high statistics run in these goniometer positions was acquired. Given the vertical beam divergence ($\sigma_{\alpha y} = 79$ μrad), a single DAQ contains a set of different alignments as shown in fig. 4.25, where the ϕ_x horizontal deflection angle (a) and the ϕ_y vertical one (b) are plotted as a function of the α_y misalignment, corresponding to the incoming vertical angle measured by the silicon detectors.
The two vertical lines indicate the angular region in which the MVROC deflection is maximum and the capture by the skew planes and the axes is minimum, that is about 80 μrad wide.
Considering the events falling in this region, the scatter plot of the ϕ_x horizontal

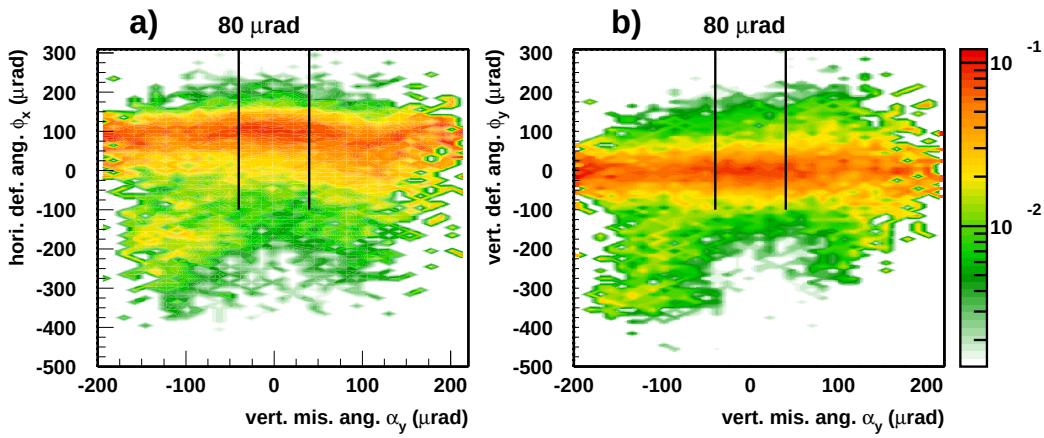

Figure 4.25: Single DAQ in MVROC: a) the ϕ_x horizontal deflection angle and b) the ϕ_y vertical one as a function of the α_y vertical misalignment, corresponding to the single particle incoming angle. The black lines indicate the optimal angular region for MVROC, which is 80 μrad wide. Each vertical bin of the plots has been normalized to one to eliminate the dependence from the shape of the beam angular distribution.

deflection angle and the ϕ_y vertical one has been produced (fig. 4.26); the blue lines in the figure, that represent the zero deflection with respect to the two axes, point out the beam shift towards positive angles in the horizontal direction due to MVROC. The left tail is formed by the particles captured by the skew planes and for this reason it has a non-zero ϕ_y vertical deflection component.

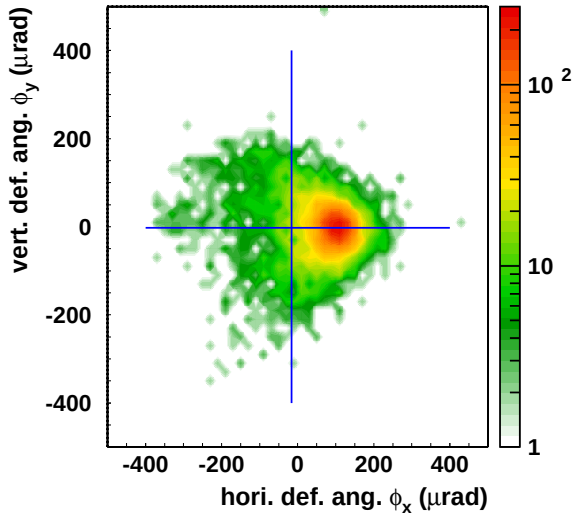

Figure 4.26: The ϕ_y vertical deflection angle as a function of the ϕ_x horizontal one in MVROC (events in the region between the black vertical lines in fig. 4.25). The orthogonal blue lines give the reference of the zero deflection angles along the two axes.

Fig. 4.27 presents the horizontal (a) and vertical (b) projections of fig. 4.26 (yellow histograms), corresponding to the deflection angle profiles in the two directions. They are compared with their VR (blue histograms) and amorphous (black histograms) counterparts to underline the MVROC effect.
The deflection angle, computed as the difference between the mean of the gaussian function (fig. 4.27a) and the zero-deflection position ($\phi_x = -16$ μrad) turns out to be $\phi_{MVROCx} = 116.2 \pm 1.6$ μrad, that corresponds to about 5 single VR deflections[2] in agreement with the previous 400 GeV/c measurement and the simulation [94].
The MVROC efficiency has been estimated considering the percentage of events under the MVROC peak (within the range $-\infty < \phi < \bar{\phi} + 3\sigma$, where $\bar{\phi}$ and σ are the mean deflection angle and the sigma values given by the gaussian fit, fig. 4.27a) providing the following result: 79.4±0.2%.

The H4 beamline (sec. 2.1.6) allows to switch the particle sign fast, therefore the same strip crystal used to investigate the MVROC with positive particles (120 GeV/c positrons) has been tested also with negative ones (120 GeV/c electrons).
Fig. 4.28 presents the result of the vertical scan with the crystal aligned in the middle of the VR angular acceptance: the (a) plot shows the ϕ_x horizontal projection of the deflection angle and the (b) one the ϕ_y vertical one. The perfect alignment with the $(112)_h$ crystalline plane does not correspond to the center of symmetry of the plots as it was for the positive particle ones but can be identified

[2]The single VR deflection angle for this crystal has been measured to be $\phi_{VR} = 25.1 \pm 0.5$ μrad.

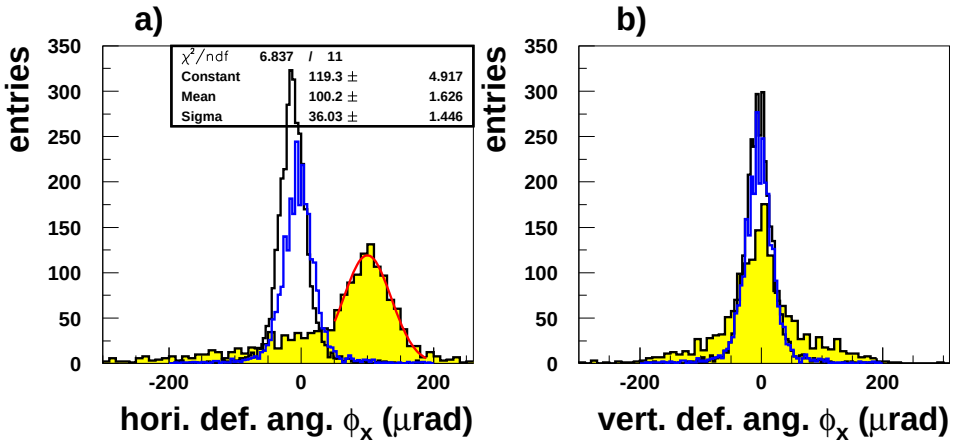

Figure 4.27: The horizontal (a) and vertical (b) deflection angle profiles in MVROC represented by the yellow histograms. The black histograms and the blue ones are the ones obtained in the amorphous and single volume reflection alignment measured with the same crystal.

at $\alpha_y \sim 8900$ μrad. Around this position the MVROC can be observed, underlined by the displacement of the main peak from the horizontal blue line giving the zero deflection reference.

Once the effect was identified, a high statistics run has been acquired and the result is shown in fig. 4.29 where the ϕ_y vertical deflection angle is plotted as a function of the ϕ_x horizontal one. The blue lines, that represent the zero deflection with respect to the two axes, point out the beam shift towards positive angles in the horizontal direction due to MVROC. Fig. 4.30 presents the projections of fig. 4.29: the yellow histograms are the horizontal (a) and vertical (b) deflection angle profiles. They are compared with their VR (blue histograms) and amorphous (black histograms) counterparts.

The deflection angle, computed as the difference between the mean of the gaussian function (fig. 4.30a) and the zero-deflection position ($\phi_x = -23.1$ μrad) is $\phi_{MVROCx} = 40.4 \pm 2.65$ μrad, that corresponds to about 4 single VR deflections[3]. The MVROC efficiency has been estimated considering the percentage of events under the MVROC peak (within the range $-\infty < \phi < \bar{\phi} + 3\sigma$, where $\bar{\phi}$ and σ are the mean deflection angle and the sigma values given by the gaussian fit, fig. 4.27a) providing the following result: $88.65 \pm 0.05\%$.

[3]The single VR deflection angle for this crystal has been measured to be $\phi_{VR} = 10.9 \pm 0.6$ μrad.

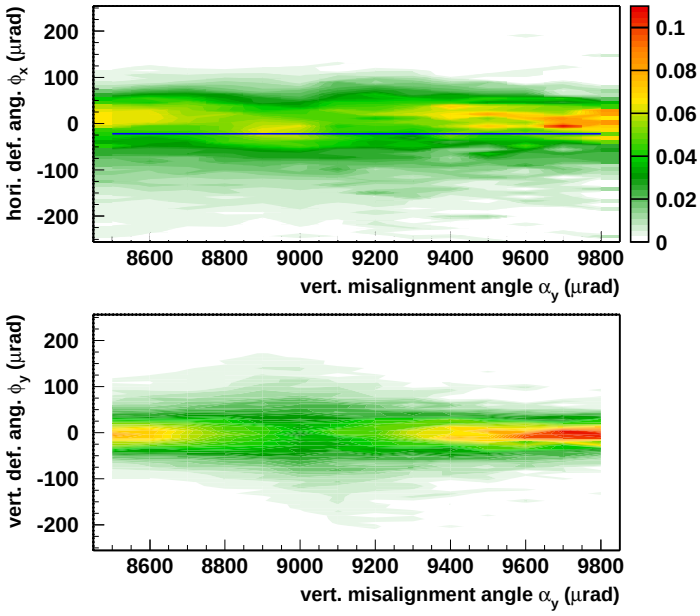

Figure 4.28: Vertical goniometer scan performed with the silicon strip aligned in VR with respect to the horizontal misalignment ($\alpha_x^* = 3600$ μrad, fig. 4.23). The plots present as a function of α_y: a) the ϕ_x horizontal deflection; b) the ϕ_y vertical one. The plots are the negative particles counterparts of fig. 4.24; in this case the color intensity scale is linear to allow a better identification of the different structures.

4.2.4 Summarizing

This chapter and chap. 2 have shown several effects that exploit bent crystals to deflect positive and negative particles. Some techniques, as planar channeling and VR (chap. 2), have been studied in detail and are already used; other ones, like MVR and axial channeling, are relatively new thus needing further developments and optimizations.

Presently, a hierarchical scale that classifies these phenomena according to their performances cannot be established, because several aspects should be taken into account with their own pros and cons. These aspects can be divided in three main categories: *deflection*, that is the possibility to obtain large and adjustable deflection angles; *efficiency*, that is the percentage of deflected particles; *angular acceptance*, which refers to the complexity of the alignment procedure and to the possibility of using the crystals with low collimated beams. According to these parameters, tab. 4.2 summarizes pros and cons of the different deflection effects.

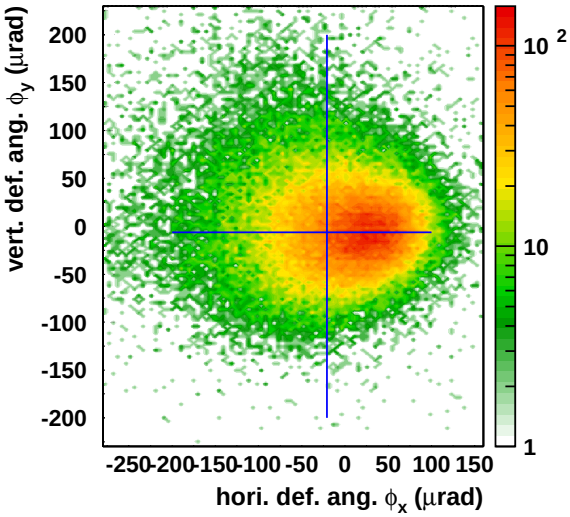

Figure 4.29: The ϕ_y vertical deflection angle as a function of the ϕ_x horizontal one in MVROC. The orthogonal blue lines give the reference of the zero deflection angles along the two axis.

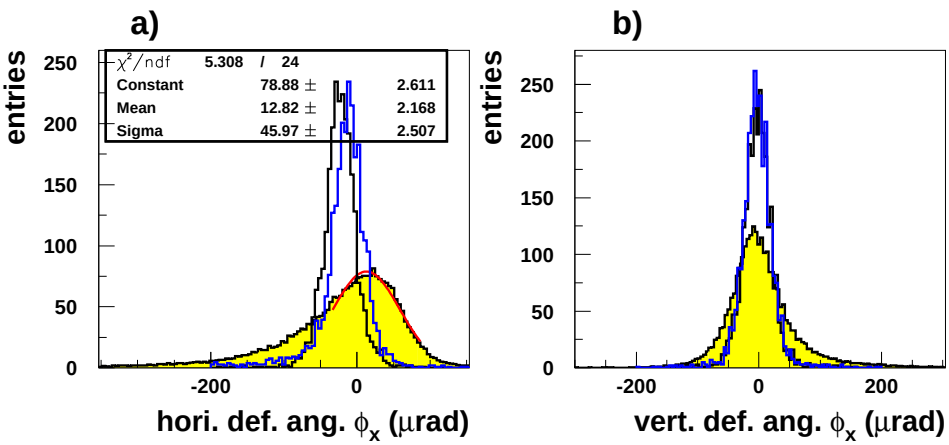

Figure 4.30: The horizontal (a) and vertical (b) deflection angle profiles in MVROC represented by the yellow histograms. The black histograms and the blue ones represent the amorphous and single volume reflection alignment conditions measured with the same crystal.

EFFECT	PROS	CONS
PLANAR CH.		
deflection	large and adjustable deflection angle, independent from the energy	
efficiency	it can reach 80% (positive particles)	it depends on the alignment and the torsion; for negative particles it is much lower
alignment	needs to control one rotation axis	it is limited by the critical angle that depends on the energy
VR		
deflection		small and fixed deflection angle with a rather complicated dependence on the energy
efficiency	efficiency close to 100% (for negative and positive particles); it is independent from torsion and fine alignment tuning	
alignment	large angular acceptance; needs to control one rotation axis	
MVR		
deflection	large and adjustable deflection angle	deflection angle dependence on the energy
efficiency	efficiency close to 100% (for negative and positive particles)	lower than the single VR one
alignment	large angular acceptance, needs to control one rotation axis	needs to control the relative alignment between the crystals
AXIAL CH.		
deflection	large deflection angle	presence of limits on the crystal length and bending
efficiency	efficiency close to 100% (for negative and positive particles)	presence of skew channeling peaks (positive particles), broadening of the deflection angle distribution (negative ones)
alignment		small angular acceptance; needs to control two rotation axes
MVROC		
deflection	large deflection angle	fixed deflection angle dependent on the energy
efficiency	high efficiency with negative and positive particles	
alignment	large angular acceptance	needs to control two rotation axes

Table 4.2: Comparative table between the different deflection effects studied in this thesis.

Conclusions and outlooks

This thesis work has been written with the aim to provide a complete and updated overview on the bent crystal research field. Starting from the basic physical principles, it guides the reader through a detailed description of the experimental techniques developed to study bent crystals, concluding with the analysis of the phenomena discovered in recent years.
For this reason, the different chapters form a unitary path that progressively reveals the details and the novelty of the bent crystals physics. Nevertheless they have been written to focus on a well-defined topic both from the theoretical and experimental point of view, so that, apart from chap. 1 which is introductory, the other ones deserve their own conclusions.

Chap. 2 presents the state of the art of the bent crystal deflection properties in planar alignment. Its first part is dedicated to the description of the experimental setup, that being based on a high resolution silicon microstrip tracking system, is able to measure the single particle incoming angle towards the crystal, the impact position on its surface and the deflection angle. The second part presents the single crystal characterization, providing a description of the analysis procedure, that has become a standard one, to measure crystal properties such as the bending radius, the torsion coefficient and the deflection efficiency. This description provides also a complete study of the channeling and volume reflection phenomena for different beam energies, with positive and negative particles.
These planar phenomena result to be clearly understood from the theoretical and experimental point of view, so that in the future only technical improvements, such as the reduction of the torsion deformation, are foreseen as long as silicon crystals are concerned. Possible novelties, in fact, can come from the test of different materials as germanium or tungsten, that, having a larger atomic number, present a deeper interplanar potential that in turn should provide a larger channeling acceptance and VR deflection angle.
From the measurement point of view, the future goal can be represented by the investigation of the sub GeV range, whose results could have a deep impact on the application field.

The focus of the third chapter is still on channeling and VR but they are treated

under a different angle, that is investigating the radiation emission properties.
As pointed out in the theoretical introduction of the chapter, both in the channeling and VR condition, particles are subject to a quasi periodic motion that is represented by the oscillation between the crystalline planes for channeling and by the almost periodic crossing of them for VR. Compared to bremsstrahlung, these peculiar trajectories generate a substantial enhancement in the emitted radiation, whose theoretical description can be obtained extending the theory on straight crystals.
After the theoretical introduction, chap. 3 describes the additions to the standard deflection angle setup necessary to measure the irradiated energy. They consist in a spectrometer, based on large area silicon microstrip detectors and in two electromagnetic calorimeters allowing to measure the energy lost by the crossing particles due to radiation and to select the positrons of the incoming beam. In the extended setup, the deflection angle information can be used to tag the different crystal effects obtaining the relative energy loss spectra.
These spectra have been measured both for the channeling and VR conditions for two bending radius values and the obtained results are in good agreement with the simulations and theoretical calculations. The measurements have been performed with 120 GeV/c positrons, recording an emitted energy enhancement of about an order of magnitude with respect to bremsstrahlung both in channeling and VR (in the covered energy loss range 3-60 GeV).

Concerning radiation emission, several further investigations can be carried out; among them the most interesting ones aim at the characterization of the emitted photon beam, measuring the single photon spectra (which gives the photon multiplicity per single incoming positron) as well as the degree of polarization. Moreover the radiation studies can be extended to negative particles.

The last chapter goes beyond planar channeling and VR showing the most innovative techniques developed to extend the bent crystal deflection capabilities. Its first section presents the results of the technological effort spent to produce arrays of bent crystals aligned with each other in order to multiply the deflection angle provided by the volume reflection effect. The results point out that this is a method able to partially mix the large angular acceptance, that characterizes VR, with large channeling deflection angles for both positive and negative particles, with a high deflection efficiency.
The second section reveals what happens when the crystal is aligned along two directions, meaning with respect to the crystalline axes. The first surprise is the appearance of the skew planes that, as well as the main vertical ones, are able to channel and reflect particles. The second interesting phenomenon is the axial channeling, a well known effect in straight crystals, that, under some limitations on the bending angle, can be used to deflect particles. Its peculiarity is represented by the almost total disappearance of the undeflected beam both for positive and

negative particles.
The last section is dedicated to one of the newest and most intriguing effects in the bent crystal field, the so called MVROC (Multi Volume Reflection in One Crystal). Its macroscopic behaviour is similar to the bent crystal arrays one but, in this case, the subsequent reflections take place inside a single crystal exploiting the contribution of the skew planes, thus simplifying the crystal construction.
As remarked at the end of the fourth chapter, these new effects open the way to further developments, such as the study of their performances as a function of the bending radius to optimize the deflection capabilities. They also allow to figure out new opportunities in the application field that will require studies and simulations.

This thesis work has presented bent crystals as innovative devices that could bring many novelties in the future, but has also described a scenario in which the bent crystal physics is well understood and characterized by a very good agreement between the theoretical and experimental results and in which the technological know-how has proven successful. These facts lead us to consider bent crystals as reliable tools in particle accelerator physics and to support their use in several applications, starting from the LHC collimaton.

List of Figures

1.1 A bending magnet and a bent crystal. 8
1.2 The basic principle of channeling in bent crystals 9
1.3 The angular scan that characterizes a bent crystal. 10
1.4 Schematic description of the different deflection effects in a bent crystal. 11
1.5 Deflection angle profile in channeling and volume reflection. . . . 11
1.6 Scheme of the crystal-based collimation system. 13
1.7 Stored beam energy for various past, present and future high power accelerators. 14
1.8 The layout of the UA9 experiment. 15
1.9 Photos of the main UA9 experiment elements. 16
1.10 The crystal alignment technique in the UA9 experiment. 16
1.11 The channeling efficiency measured in the UA9 experiment. . . . 18
1.12 Crystal collimation driven by volume reflection. 18
1.13 Crystal extraction efficiency recorded by the RD22 experiment on the SPS and in the IHEP laboratory. 20
1.14 Crystal extraction at the IHEP laboratory. 21
1.15 The scheme of the first crystal beam-split station installed at the IHEP laboratory. 22
1.16 Layout of the NA48 kaon beams production setup. 23
1.17 A standard method to produce a light ion microbeam. 25
1.18 Beam focusing using a bent crystal. 26
1.19 Schematic view of a multi-wall nanotube. 26
1.20 The continuous potential inside a nanotube. 27
1.21 Simulation of the nanotube efficiency compared with the silicon crystal one. 27
1.22 Experimental results of the PICH program. 30
1.23 The crystalline positron source used at KEKB compared with a standard one. 31
1.24 The undulator crystal working principle. 32
1.25 Planes and axes in a crystal depending on its orientation. 32

1.26 Schematic description of a quasi aligned motion inside a crystal. . 34
1.27 Representation of a particle trapped in the interplanar potential. . . 34
1.28 Miller indices in the cubic lattice system. 36
1.29 The interplanar Molière potential for the (110) and the (111) Si channel. 36
1.30 Schematic description of the interplanar potential. 38
1.31 Dechanneling length: measurements in long crystals. 42
1.32 The bent crystal working principle and an example of a bending device. 42
1.33 Scheme of the channeling motion of a particle which enters a bent crystal aligned with its planes. 43
1.34 The interplanar silicon ((110) planes) potential computed in the Molière approximation for different bending radii. 44
1.35 Dechanneling and feed-in mechanisms in straight and bent crystals. 48
1.36 The volume capture process in bent crystals. 48
1.37 Reflection of a charged particle in the crystal volume. 50
1.38 Detailed trajectory of a volume reflected particle. 51
1.39 The influence of bending on the volume reflection process. 52
1.40 Experimental result of the volume reflection properties as a function of the bending radius. 53

2.1 The strategies to perform a crystal channeling test. 57
2.2 The goniometric system. 58
2.3 Scheme of the tracking system used for the crystal channeling measurements. 59
2.4 Photos of a silicon microstrip detector. 60
2.5 The residual distribution of one of the silicon modules. 61
2.6 Two possible variants for a crystal channeling tracking system. . . 62
2.7 The DAQ chain. 63
2.8 Two examples of the crystals used during the experiment. 64
2.9 The bending principle of the strip crystal and a scheme of its bending device. 65
2.10 The bending principle of the quasimosaic crystal and a scheme of its bending device. 66
2.11 The origin of the quasimosaic curvature. 66
2.12 The CERN accelerator complex and the North Area. 67
2.13 The geometric characteristics of the H8 beamline proton beam . . 68
2.14 The geometric characteristics of the T9 beamline positive hadron beam. 68
2.15 The laser pre-alignment procedure. 69
2.16 An example of a crystal lateral scan 70

2.17 An example of a fast angular scan. 70
2.18 Schematics of a crystal holder that twists a strip crystal. 71
2.19 The effect of the crystal torsion. 72
2.20 The behaviour of a twisted crystal 73
2.21 The software compensation of the torsion effect 74
2.22 A fast method to evaluate the torsion of the crystal. 75
2.23 The mechanism to correct the torsion. 76
2.24 The performances of a straight crystal. 76
2.25 The channeling effect as a function of the horizontal position. . . . 77
2.26 A summary of the channeling analysis. 78
2.27 Channeling angular acceptance and efficiency at 400 GeV. 78
2.28 Dechanneling probability as a function of the alignment. 80
2.29 Measurement of the nuclear dechanneling length. 80
2.30 The critical angle identified from the channeling peak. 81
2.31 Trajectories of high transversal energy channeled particles. 82
2.32 Channeling angular acceptance and efficiency at 120 GeV. 83
2.33 Volume reflection at 400 GeV. 84
2.34 Volume reflection and volume capture efficiency at 400 GeV. . . . 85
2.35 Volume reflection and volume capture efficiency at 120 GeV. . . . 86
2.36 Effective potential for positive and negative particles. 87
2.37 Goniometer scan of a 2 mm silicon strip crystal with 150 GeV/c negative particles. 88
2.38 Channeling and VR deflection angle profiles with 150 GeV/c negative particles. 88
2.39 The experimental setup used on the T9 beamline. 91
2.40 The trigger region used on the T9 beamline. 92
2.41 Measurement of the principal strip crystal curvature. 93
2.42 Fast and high statistics crystal angular scan on the T9 beamline. . 94
2.43 The crystal torsion at 13 GeV/c. 95
2.44 High statistics crystal scan at 13 GeV. 95
2.45 Deflection angle profiles at 13 GeV in channeling and VR. 96
2.46 Deflection efficiency at 13 GeV in channeling and VR. 97
2.47 Bent crystal investigation with 13 GeV/c negative hadrons on the T9 beamline. 99

3.1 Radiation emission in channeling and volume reflection. 102
3.2 Emitted photon energy spectra for a 10 GeV/c particle beam impinging on a silicon crystal. 103
3.3 Synchrotron radiation in bent crystals at low energy. 104
3.4 The multipole parameter ρ as a function of the oscillation amplitude in channeling. 105

3.5 The interplanar potential and the corresponding frequency distribution in channeling. 107
3.6 The channeled particles amplitude distribution $p(\xi_m)$. 107
3.7 Comparison between the exact trajectories and the harmonic approximation in channeling. 108
3.8 Channeling radiation spectra computed with the two methods. . . 108
3.9 Schematic of the motion in coherent bremsstrahlung. 110
3.10 The channeled particles amplitude distribution $p(\xi_m)$. 110
3.11 The evolution of the misalignment between the crystal planes and the particle trajectory in VR. 112
3.12 Misalignment $\alpha(t)$ in VR; comparison between the instantaneous value and the average one. 112
3.13 Scheme of the H4 “deflection” and “radiation” setup. 114
3.14 The scheme of the spectrometer. 115
3.15 The beam profile measured by the silicon chambers at the end of the line. 116
3.16 The vertical residual on the second chamber. 117
3.17 The “vertical residual cut” applied on the silicon beam chambers. . 118
3.18 Position and angle obtained combining the two chambers information. 119
3.19 The energy loss distribution obtained with the spectrometer. . . . 119
3.20 Photos of the DEVA calorimeter. 120
3.21 The H4 primary beam composition measured by DEVA. 121
3.22 The DEVA high threshold trigger. 122
3.23 A photo of the Rino calorimeter. 123
3.24 Energy deposited in the Rino calorimeter. 123
3.25 The energy measured by Rino-cal as a function of the one measured by the spectrometer. 124
3.26 Photos of the Willie calorimeter. 125
3.27 The Willie-cal interference on the silicon beam chambers. 127
3.28 The energy deposited in Willie-cal as a function of the one measured by the spectrometer. 128
3.29 The Willie-cal calibration. 129
3.30 The energy spectrum measured by the Willie calorimeter. 130
3.31 The trigger scintillators used in the 2010 beam test. 131
3.32 Photos of the Jack calorimeter. 131
3.33 The energy deposit in Jack-cal as a function of the one measured by the spectrometer and its resolution. 132
3.34 The energy deposit in Jack-cal by a 60-80-100 GeV beam. 132
3.35 The Jack-cal calibration curve. 133
3.36 Photon and energy loss spectra of the background. 135

3.37 Crystal radiation emission in the amorphous condition. 136
3.38 Selection of the channeled particles. 137
3.39 Channeling energy loss spectrum for different misalignment regions. 138
3.40 Channeling energy loss spectrum comparison with the simulation. 139
3.41 The radiation emission of a bent crystal as a function of its alignment. 140
3.42 Volume reflection energy loss spectrum: comparison with the analytical calculation. 141

4.1 Schematic example of a double VR in two crystals. 146
4.2 Double volume reflection in two crystals. 146
4.3 Examples of multi-crystal systems. 147
4.4 A photo of the multi-strip crystal produced at the IHEP laboratory. 148
4.5 Goniometer scan of the IHEP 8 strip crystal. 148
4.6 The IHEP 8 strip crystal goniometer scan with torsion compensation (positive particles). 149
4.7 The IHEP 8 strip crystal reflection efficiency with positive particles. 150
4.8 The IHEP 8 strip crystal goniometer scan with torsion compensation (negative particles). 151
4.9 The IHEP 8 strip crystal reflection efficiency with negative particles. 152
4.10 The alignment condition between a charged particle and a skew plane. 153
4.11 The trajectory of a particle channeled by the main planes and the skew ones. 154
4.12 The experimental evidence of a skew plane, compared with the main one. 155
4.13 Schematic of a particle moving at a small angle with respect to a crystal axis. 156
4.14 Axial potential computed [86] with the use of the Molière approximation 157
4.15 The trajectory of a MVROC particle in the phase space of the horizontal and vertical misalignment. 159
4.16 Vertical goniometer scan of the (110) strip crystal to find the axial alignment, with positive particles. 160
4.17 The axial channeling alignment obtained with positive particles. . 161
4.18 Horizontal scan of the (110) silicon strip used in the negative particle axial channeling investigation. 162
4.19 Vertical goniometer scan of the (110) strip crystal to find the axial alignment, with negative particles. 162
4.20 A single DAQ in axial channeling acquired with 150 GeV/c negative hadrons. 163

4.21 The horizontal and vertical deflection angle profiles in axial channeling, with negative particles. 164
4.22 The trajectory of a MVROC particle in the phase space of the horizontal and vertical misalignment. 165
4.23 Horizontal scan of the (110) silicon strip used in the MVROC investigation. 167
4.24 Vertical goniometer scan of the (110) strip crystal to find MVROC. 167
4.25 A single DAQ in MVROC with 120 GeV/c positrons. 168
4.26 Scatter plot of the ϕ_x horizontal deflection angle versus the ϕ_y vertical one in MVROC. 169
4.27 Horizontal and vertical deflection angle profiles in MVROC. . . . 170
4.28 Vertical goniometer scan of the (110) strip crystal to find MVROC, with negative particles. 171
4.29 Scatter plot of the ϕ_x horizontal deflection angle versus the ϕ_y vertical one in MVROC for negative particles. 172
4.30 Horizontal and vertical deflection angle profiles in MVROC for negative particles. 172

List of Tables

2.1 Performances of the goniometric system. 59
2.2 Summary of the deflection properties of the studied crystals. . . . 100

3.1 Characteristics of the strip crystals investigated during the 2009 H4 beam test. 133
3.2 Results for the strip crystals investigated during the 2009 H4 beam test. 142

4.1 The potential well depth of some axial channels of silicon, germanium and tungsten crystals, in the Molière approximation. 158
4.2 Comparative table between the different deflection effects studied in this thesis. 173

List of acronyms

AC	Alternate Current
ADC	Analog to Digital Converter
AGILE	Astro Rivelatore Gamma a Immagini LEggero
ASIC	Application Specific Integrated Circuit
BLM	Beam Loss Monitor
BNL	Brookhaven National Laboratory
CERN	European Organization for Nuclear Research
CH	CHanneling
CMOS	Complementary Metal Oxide Semiconductor
CPU	Central Processing Unit
DC	Direct Current
DAQ	Data AcQuisition
FWHM	Full Width Half Maximum
FNAL	Fermi National Accelerator Laboratory
IHEP	Institute for High Energy Physics
INFN	Istituto Nazionale di Fisisca Nucleare
JINR	Joint Institute for Nuclear Research
LET	Linear Energy Transfer
MSE	Multiple Scattering on Electrons
MSN	Multiple Scattering on Nuclei
MVR	Multi Volume Reflection (in a sequence of crystals)
MVROC	Multi Volume Reflection in One Crystal
MWNT	Multi Wall Nano Tube
NA48	Particle experiment at CERN
LET	Linear Energy Transfer
LHC	Large Hadron Collider
MIP	Minimum Ionising Particle
NIM	Nuclear Instrumentation Module
PC	Personal Computer
PICH	Particle Identification with CHanneling radiation

PIXE	Particle Induced X-ray Emission
PMT	PhotoMultiplier Tube
PNPI	Petersburg Nuclear Physics Institute
PS	Proton Synchrotron
QED	Quantum ElectroDynamics
RBE	Radio Biological Effectiveness
RHIC	Relativistic Heavy Ion Collider
RMS	Root Mean Square
SSC	Superconducting Super Collider
SWNT	Single Wall Nano Tube
SiPM	Silicon PhotonMultiplier
SPS	Super Proton Synchrotron
TRD	Transition Radiation Detector
VC	Volume Capture
VME	Versa Module Eurocard
VR	Volume Reflection
WLS	Wave Length Shifter

Bibliography

[1] O. S. Brüning *et al.*. *LHC Design Report Volume I: the LHC Main Ring*. http://cdsweb.cern.ch/record/782076, 2004.

[2] V. M. Biryukov, Y. A. Chesnokov, and V. I. Kotov. *Crystal channeling and its application at high energy accelerators*. Springer, 1996.

[3] A. G. Afonin *et al.*. High-efficiency beam extraction and collimation using channeling in very short bent crystals. *Phys. Rev. Lett.*, 87(9):094802, 2001.

[4] E. Tsyganov. Some aspects of the mechanism of a charged particle penetration through a monocrystal. *Fermilab preprint TM-682*, 1976.

[5] E. Tsyganov. Estimates of cooling and bending processes for charged particle penetration through a monocrystal. *Fermilab preprint TM-684*, 1976.

[6] A. F. Elishev *et al.*. Steering of charged particle trajectories by a bent crystal. *Phys. Lett. B*, 88:387–391, 1979.

[7] Joint Institute for Nuclear Research, Dubna, Moscow region, Russia. URL `http://lrb.jinr.ru/`.

[8] K. Jukka. Proton extraction from a high energy beam with bent crystals. *PhD Thesis*, 1998. URL `http://care-hhh.web.cern.ch/care-hhh/CrystalCollimation/papers/jklem_ Thesis.pdf`.

[9] M. A. Maslov *et al.*. The SSC beam scraper system. *SSCL*, 484, 1991.

[10] R. P. Fliller. Results of bent crystal channeling and collimation at the relativistic heavy ion collider. *Phys. Rev. ST Accel. Beams*, 9:013501, 2006.

[11] D. Still. Tevatron bent crystal studies. *Workshop talk: Crystal Channeling for Large Collider: Machine and Physics Application*, 2007. URL `http://indico.cern.ch/contributionDisplay.py?contribId=5&sessionId=6&confId=12959`.

[12] R. W. Aßmann *et al.*. Requirements for the LHC collimation system. *LHC-project-report-599*, 2002.

[13] R. W. Aßmann *et al.*. The final collimation system for the LHC. *Proceedings PAC06*, 2006.

[14] J. Resta Lòpez. Design and performance evaluation of nonlinear collimation systems for CLIC and LHC. *PhD Thesis, Valencia Univ., CERN-THESIS-2008-018*, 2007.

[15] V. M. Biryukov *et al.*. Crystal collimation as an option for the large hadron colliders. *Nucl. Instr. and Meth. B*, 234:23–30, 2005.

[16] W. Scandale *et al.*. First result on the SPS beam collimation with bent crystals. *Phys. Lett. B*, 692:78–82, 2010.

[17] B. Goddard. Injection and Extraction. *Lecture presented at CAC 2010, http://cas.web.cern.ch/cas/Bulgaria-2010/Talks-web/Goddard-1-web.pdf*.

[18] S. I. Baker *et al.*. First operation with a crystal septum to replace a magnet in a charged particle beam. *Nucl. Instr. and Meth. A*, 234:602–605, 1985.

[19] A. A. Asseev *et al.*. Extraction of 50 GeV protons from the IHEP accelerator by the bent crystal. *Nucl. Instr. and Meth. A*, 2:283–284, 1993.

[20] R. A. Carrigan *et al.*. Beam extraction studies at 900 GeV using a channeling crystal. *Phys. Rev. ST Accel. Beams*, 5:043501, 2002.

[21] V. Biryukov *et al.*. On the theory of proton beam multiturn extraction with bent single crystals. *Nucl. Instr. and Meth. B*, 53:202–207, 1991.

[22] A. G. Afonin *et al.*. High-efficiency multipass extraction of 70-GeV protons from an accelerator with a short bent crystal. *Phys. Lett. B*, 435:240, 1998.

[23] A. G. Afonin *et al.*. The schemes of proton extraction from the IHEP accelerator using bent crystals. *Nucl. Instr. and Meth. B*, 234:14–22, 2004.

[24] G. D. Barr *et al.*. Proposal for a precision measurement of ε'/ε in CP-violating $K^o \to 2\pi$ decays. *CERN/SPSC/90-22/P253*, 1990.

[25] N. Doble *et al.*. A novel application of bent crystal channeling to the production of simultaneous particle beams. *CERN/SL/95-16, NA48 Note*, 1995.

[26] A. Baurichter *et al.*. Channeling of high-energy particles in bent crystals experiments at the CERN SPS. *Nucl. Instr. and Meth. B*, 27:164–165, 2000.

[27] M. Folkard *et al.*. The use of radiation microbeams to investigate the bystander effect in cells and tissues. *Nucl. Instr. and Meth. A*, 280:446–450, 2007.

[28] D. Durante *et al.*. Preparatory study of investigations into biological effects of radiation. *European Space Agency - ESA-ESTEC*, 2008.

[29] J. Kennedy *et al.*. Elemental analysis of urban stormwater particulate matter by PIXE. *Nucl. Instr. and Meth. B*, 258:435–439, 2007.

[30] R. Cambria *et al.*. A methodological test of external beam PIXE analysis on inks of ancient manuscripts. *Nucl. Instr. and Meth. B*, 75:488–492, 1993.

[31] V. A. Andreev *et al.*. Spatial focusing of 1-GeV protons by a curved single crystal. *JETP Lett.*, 41:500–502, 1985.

[32] V. I. Smirnov *et al.*. First results from a study of a 70 GeV proton beam being focused by a bent crystal. *Nucl. Instr. and Meth. B*, 69:382–384, 1992.

[33] V. M. Biryukov *et al.*. Channeling technique to make nanoscale ion beams. *Nucl. Instr. and Meth. B*, 231:70–75, 2005.

[34] J. F. Bak *et al.*. Measurement of average electron densities in Si and Ge using MeV -rays produced by channelled high-energy projectiles. *Nucl. Phys. A*, 389:533–556, 1982.

[35] G. N. Greaves and C. R. A. Catlow. *Applications of synchrotron radiation*. Chapman and Hall, 1990.

[36] J. A. Clarke. *The science and technology of undulators and wigglers*. Oxford University Press, 2004.

[37] M. Chiba *et al.*. 200-MeV bremsstrahlung tagged photon beams at Sendai. *Nucl. Instr. and Meth. A*, 564:100–107, 2006.

[38] D. Aston *et al.*. The 25-50 GeV tagged photon facility at CERN. *Nucl. Instr. and Meth.*, 197:287–296, 1982.

[39] P. J. Bussey *et al.*. A polarized high energy tagged photon beam. *Nucl. Instr. and Meth.*, 211:301–308, 1983.

[40] M. A. Kumakhov *et al.*. On the theory of electromagnetic radiation of charged particles in a crystal. *Phys. Lett. A*, 57:359–360, 1976.

[41] M. Brigida *et al.*. Application of the channeling radiation for particle identification. *Proceedings of the Conference on Astroparticle, Particle and Space Physics, Detectors and Medical Physics Applications, Como, Italy*, 2007.

[42] C. Favuzzi *et al.*. Particle identification by means of channeling radiation in high collimated beams. *Nucl. Instr. and Meth. A*, 617:402–404, 2010.

[43] R. Chehab *et al.*. *Proceedings of PAC'89 Chicago, IL, USA*, page 283, Mar 1989.

[44] X. Artru *et al.*. Axial channeling of relativistic electrons in crystals as a source for positron production. *Nucl. Instr. and Meth. A*, 10:246–252, 1996.

[45] K. Yoshida *et al.*. Positron production in tungsten crystals by 1.2-GeV channeling electrons. *Phys. Rev. Lett.*, 7:1437–1441, 1998.

[46] T. Suwada *et al.*. First application of a tungsten single-crystal positron source at the KEK b factory. *Phys. Rev. ST Accel. Beams*, 10:073501, 2007.

[47] S. Bellucci *et al.*. Experimental study for the feasibility of a crystalline undulator. *Phys. Rev. Lett.*, 90:034801, 2003.

[48] J. Lindhard. Motion of swift charged particles, as influenced by strings of atoms in crystals. *Phys. Lett.*, 12:126–128, 1964.

[49] G. Molière. *Z. Naturforsh A.*, 2(133), 1974.

[50] J. S. Foster *et al.*. Deflection of GeV particle beams by channeling in bent crystal planes of constant curvature. *Nucl. Phys. B*, 318:301–318, 1989.

[51] V. E. Biryukov. Computer simulation of beam steering by crystal channeling. *Phys. Rev. E*, 51(4):3522–3528, 1995.

[52] W. Scandale *et al.*. Observation of nuclear dechanneling for high-energy protons in crystals. *Phys. Lett. B*, 680:129–132, 2009.

[53] A. M. Taratin *et al.*. Volume reflection of high-energy protons in short bent crystals. *Nucl. Instr. and Meth. B*, 262:340–347, 2007.

[54] Particle physics booklet. chap. 27, sec 3, 2006.

[55] S. P. Møller. Crystal channeling or how to build a 1000 tesla magnet. *CERN*, 94(05), 1994.

[56] A. M. Taratin and S. A. Vorobiev. Deflection of high-energy charged particles in quasi-channeling states in bent crystals. *Nucl. Instr. and Meth. B*, 26: 512–521, 1987.

[57] Yu. M. Ivanov *et al.*. Volume reflection of a proton beam in a bent crystal. *Phys. Rev. Lett.*, 97(14):144801, 2006.

[58] W. Scandale *et al.*. Volume reflection dependence of 400 GeV/c protons on the bent crystal curvature. *Phys. Rev. Lett.*, 101:234801, 2008.

[59] W. Scandale *et al.*. Apparatus to study crystal channeling and volume reflection phenomena at the SPS H8 beamline. *Rev. Sci. Instr.*, 79:023303, 2008.

[60] S. Bellucci *et al.*. Using a deformed crystal for bending a sub-GeV positron beam. *Nucl. Instr. and Meth. B*, 252:3–6, 2002.

[61] L. Celano *et al.*. A high resolution beam telescope built with double sided silicon strip detectors. *Nucl. Instr. and Meth. A*, 381:49–56, 1996.

[62] Sensors and Semiconductors Laboratory, Ferrara University, Italy. URL `http://ws.fe.infn.it/lab/`.

[63] Institute of High Energy Physics, Protvino, Moscow region, Russia. URL `http://www.ihep.su/index-e.html`.

[64] V. M. Biryukov *et al.*. Crystal deflector for highly efficient channeling extraction of a proton beam from accelerators. *Rev. Sci. Instr.*, 73(9):3170–3173, 2002.

[65] S. Baricordi *et al.*. Low-energy-channeling surface analysis on silicon crystals designed for high-energy-channeling in accelerators. *Appl. Phys. Lett.*, 87:094102, 2005.

[66] Yu. M. Ivanov *et al.*. *JETP Lett.*, 81:99, 2005.

[67] W. Scandale *et al.*. Observation of Channeling and Volume Reflection in Bent Crystals for High-Energy Negative Particles. *Phys. Lett. B*, 681:233–236, 2009.

[68] M. Prest *et al.*. The AGILE silicon tracker: an innovative γ-ray instrument for space. *Nucl. Instr. and Meth. A*, 501:280–287, 2003.

[69] V. Guidi *et al.*. Tailoring of silicon crystals for relativistic-particle channeling. *Nucl. Instr. and Meth. B*, 234:40–46, 2010.

[70] V. A. Maisheev *et al.*. Model-independent description of planar channeling at high energies. *Nucl. Instr. and Meth. B*, 119:42–47, 1996.

[71] J. Bak *et al.*. Channeling radiation from 2-55 GeV/c electrons and positrons. *Nucl. Phys. B*, 254:491–527, 1984.

[72] A. M. Taratin *et al.*. Radiation of high-energy positrons channeled in bent crystals. *Nucl. Instr. and Meth. B*, 254:551–557, 1988.

[73] V. A. Maisheev *et al.*. Channeling radiation of positrons with energy in the region of 100 GeV in single crystals, 2009. http://web.ihep.su/library/pubs/prep2009/09-21-e.htm.

[74] V. N. Baier, V. M. Katkov, and V.M. Strakhovenko. *Electromagnetic Processes at high energies in oriented single crystals*. Singapore World Scientific, 1998.

[75] L. D. Landau and E. M. Lifshitz. *The classical theory of fields*. Pergamon, Oxford, 1979.

[76] W. Scandale *et al.*. Experimental study of the radiation emitted by 180 GeV/c electrons and positrons in a bent crystal. *Phys. Rev. A*, 79:012903, 2009.

[77] V. A. Maisheev. Contribution to the 4th Crystal Channeling Workshop, March 2009. URL `http://indico.cern.ch/conferenceDisplay?confId=50840`.

[78] V. A. Maisheev *et al.*. Volume reflection of ultrarelativistic particles in single crystals. *Phys. Rev. SP AB*, 10(084701), 2007.

[79] V. A. Maisheev. Photon emission and photoproduction processes in bent single crystals. *Contribution to Channeling 2010, October 3 - 8, 2010 Ferrara (FE), Italy*. URL `http://www.lnf.infn.it/conference/channeling2010/presentations/101004/ch2010_maisheev.pdf`.

[80] B. Dolgoshein *et al.*. Status report on silicon photomultiplier development and its applications. *Nucl. Instr. and Meth. A*, 563:129–132, 2006.

[81] A. Berra *et al.*. Silicon photomultipliers as a readout system for a scintillator-lead shashlik calorimeter. *Transaction on Nuclear Science*, DOI: 10.1109/TNS.2011.2117440.

[82] W. Scandale *et al.*. Double volume reflection of a proton beam by a sequence of two bent crystals. *Phys. Lett. B*, 658:109–111, 2008.

[83] Petersburg Nuclear Physics Institute, Petersburg, Russia. URL `http://www.pnpi.spb.ru/index.html.en`.

[84] W. Scandale *et al.*. Observation of Multiple Volume Reflection of Ultrarelativistic Protons by a Sequence of Several Bent Silicon Crystals. *Phys. Rev. Lett.*, 102:084801, 2009.

[85] W. Scandale *et al.*. Multiple volume reflections of high-energy protons in a sequence of bent silicon crystals assisted by volume capture. *Phys. Lett. B*, 688:284–288, 2010.

[86] V. G. Baryshevsky and V. V. Tikhomirov. *Usp. Fiz. Nauk*, 159(527), 1989.

[87] L. D. Landau and E. M. Lifshits. *Mechanika (Mechanics)*, Nakua, Moscow 1973.

[88] W. Scandale *et al.*. High-Efficiency deflection of high-energy protons through axial channeling in a bent crystal. *Phys. Rev. Lett.*, 101:164801, 2008.

[89] J. F. Bak *et al.*. Detailed investigation of the channeling phenomena involved in bending of high-energy beams by means of bent crystals. *Nucl. Phys. B*, 242:1–30, 1984.

[90] A. Baurichter *et al.*. New results from the CERN-SPS beam deflection experiments with bent crystals. *Nucl. Instr. and Meth. B*, 119:172–180, 1996.

[91] N. F. Shul'ga and A.A. Greenenko *et al.*. Multiple scattering of ultrahigh-energy charged particles on atomic strings of a bent crystal. *Phys. Lett. B*, 353:373–377, 1995.

[92] W. Scandale *et al.*. High-Efficiency deflection of high-energy negative particles through axial channeling in a bent crystal. *Phys. Lett. B*, 680:301–304, 2009.

[93] V. Tikhomirov *et al.*. Multiple volume reflection from different planes inside one bent crystal. *Phys. Lett. B*, 655:217–222, 2007.

[94] W. Scandale *et al.*. First observation of multiple volume reflection by different planes in one bent silicon crystal for high-energy protons. *Phys. Lett. B*, 682:274–277, 2009.

Acknowledgement

It is a pleasure to thank those who made this thesis possible: all the people who I collaborated with during these years sharing discussions, knowledge, stressful situations as well as moments of happiness.
I have worked with people from all over the world and, among them, a special thank goes to the Ferrara group, that had a key role in spreading the knowledge about bent crystals among the italian scientific comunity, and to the Protvino one: Dr. Yury Chesnokov and Dr. Vladimir Maisheev, it was an honor for me to visit your laboratory working with you.
I am indebted to many of my colleagues to support me. It was a real pleasure to be member of the Insulab group, a team of friends working together; although our careers probably will take different ways I hope we will never lose our friendship.
The last and most important acknowledgement obviously goes to the leaders of this group: Michela and Eric; thank you to believe that through the every day work we can give a contribution for a better world, starting from an University, that educate people as you did with me.